MODELING AND CHARACTERIZATION OF HBT TRANSISTOR AND ITS APPLICATION TO EBG MULTIBAND ANTENNA

CHEN BO

NATIONAL UNIVERSITY OF SINGAPORE

2005

MODELING AND CHARACTERIZATION OF HBT TRANSISTOR AND ITS APPLICATION TO EBG MULTIBAND ANTENNA

CHEN BO

A THESIS SUBMITTED

FOR THE DEGREE OF DOCTOR OF PHILOSOPHY

DEPARTMENT OF ELECTRICAL & COMPUTER ENGINEERING

NATIONAL UNIVERSITY OF SINGAPORE

2005

Acknowledgment

I would like to express my greatest gratitude and indebtedness to my supervisors, Professor Ooi Ban Leong, Professor Kooi Pang Shyan and Dr Lin Fujiang, for their tremendous help, inspiring guidance, stimulating and invaluable advices throughout the entire course of my candidature and the writing of this thesis, without which this thesis would not have been completed.

I appreciate Professor Leong Mook Seng and Professor Li Lewei for their expert technical assistance, constructive suggestions and unceasing encouragement to my work.

Deep appreciation also goes to all my colleagues and friends at the MMIC Modeling and Packaging Lab of the National University of Singapore for their valuable discussions, kind help and the wonderful time we spent together.

Additional appreciation is extended to Mr. Sing C. H., Ms. Lee S. C., Mr. Teo T. C. and their colleagues of Microwave Laboratory for their technical assistance.

Finally, I would like to thank my wife and my parents for their endless support and encouragement.

Summary

Heterojuction bipolar transistor (HBT) is widely used in many microwave circuits, such as low noise amplifier, power amplifier and active antenna. This thesis involves the small-signal, large-signal, noise modeling and characterization of microwave heterojunction bipolar transistor for the application of multi-band active integrated slot antenna with novel electromagnetic bandgap (EBG) feed. As the first step to obtain an accurate large-signal model, small-signal modeling based on the PI-equivalent circuit is carried out. The uniqueness of the approach taken in this thesis is that it accurately determines the parameters of the small-signal model by the bi-directional optimization technique, thus reducing the number of optimization variables. Moreover, to accurately determine the parasitic resistance by eliminating the thermal effect, a fast and accurate method to extract the thermal resistance is proposed and experimentally verified. The accuracy of the HBT small-signal model has been further validated by the measured bias-dependent S-parameters.

Due to the uncertainties caused by the S-parameter measurement, the planar circuit approach and resonance-mode technique are, for the first time, extended to investigate the HBT parasitic inductive effect and its accurate determination. Comparison with optimized values from measurement results shows that this technique is a valid method to extract the parasitic inductance without the tedious process of de-embedding and S-parameter measurements.

On the basis of a HBT small-signal model, the noise behavior is studied thoroughly. Following the comparison of current available noise models, the wave approach combined with the contour-integral method is applied to analyze the HBT

noise properties. To reliably perform the noise modeling by the wave approach, the equivalent noise temperatures must be known. Therefore, a novel method to determine the equivalent noise temperature by using the HBT small-signal model and minimum noise figure is proposed here.

Based on the Gummel-Poon model and the Vertical Bipolar Inter-Company model, large-signal modeling including self-heating effects is performed. The model is then compared with the measurement data in terms of DC IV and small-signal transit parameters. Due to the complex nature of HBT breakdown behavior in the high current region, most available avalanche models cannot predict the HBT breakdown behavior accurately up to the high current density. In view of this, this piece of work presents an empirical modification on the VBIC avalanche model which is valid up to the high current breakdown region. The validity of the proposed model is verified by the good agreement between the simulation results and the measurement data obtained.

Taking the inherent advantage of the coplanar waveguide, the planar slot antenna fed by coplanar waveguide is selected for the integration of an active antenna. A novel feeding technique is proposed here to simultaneously improve the impedance bandwidth of the multi-band slot antenna. The new antenna feed makes use of an electromagnetic/photonic bandgap (EBG/PBG) structure which effectively enhances the impedance bandwidth of the multi-band slot antenna. Finally, based on the DC and the small-signal verifications of the HBT model, a wideband power amplifier is designed using the load-pull technique and integrated with the EBG-fed slot antenna. The measurements on the power amplifier and the active integrated antenna show the validity of the proposed approaches.

Table of Contents

List of Figures

List of Tables

Chapter 1

Introduction

1.1 Motivation

The active integrated antenna has been a growing area of research in recent years [1]-[4] as the microwave integrated circuit and monolithic microwave integrated circuit technologies become more mature allowing for high-level integration. Active integrated antennas are antennas incorporating one or more active solid-state devices and circuit to amplify or generate radio frequency. A typical active integrated antenna consists of active devices such as Gunn diodes or three-terminal devices, MESFET or HBT, to form an active circuit, and planar antennas such as dipoles, microstrip patches, bowties, or slot antennas [5].

Present existing active antennas are only working on a single frequency band. Recently, multi-band operation becomes favorable due to the development of multi-standard communication transceivers. This work is, therefore, concerned with HBT modeling for the development of multi-band active antennas.

An important issue in the design of an active antenna is the development of accurate and efficient computer-aided design tools. While many high-quality commercial packages are currently available for the analysis and design of complicated microwave and millimeter-wave circuits and various types of antennas, a

unified full-wave simulation tool, which can take into account the tight circuit-antenna coupling effects within an active integrated antenna environment, remains an open challenge. Fortunately, recent efforts to include nonlinear active devices into full-wave simulations based on transmission-line matrix (TLM) [6], finite-difference time-domain (FDTD) [7]-[9], and finite-element time-domain (FETD) [10] techniques have shown impressive progress. Continued research activities in this direction should lead to the establishment of accurate and reliable analysis and design tool for active integrated antennas in the foreseeable future.

1.2 Objectives of this Work

A multi-band active antenna can be partitioned into two parts: an active circuit, such as a wideband amplifier, and a multi-band antenna with reasonable impedance bandwidth. The HBT has rapidly gained acceptance for commercial applications, and is currently the device of choice for many active microwave circuits, such as power amplifiers, low noise amplifiers, and oscillators. To design a power amplifier for wideband operation, an accurate device model valid for a wide range of operating biases and signal frequencies is critical. Existing bipolar models used in most commercial circuit simulators, which are based on the Gummel-Poon model, do not take into account several effects important for the prediction of large-signal HBT performance. For example, the self-heating effect and avalanche breakdown are omitted, which have been recognized as important factors in determining HBT operations at high power dissipations. Therefore, the purpose of this work is to investigate the modeling and parameter extraction of the HBT devices, e.g., the accurate extraction and determination of small-signal HBT equivalent circuit

parameters, the self-heating effect on the parameter extraction and the improvement on the avalanche breakdown model.

The multi-band antenna forms another part of a multi-band active antenna. It is well-known that one drawback of the planar antenna is its inherent narrow impedance bandwidth. Therefore, this work has also studied the simultaneous bandwidth enhancement for multi-band slot antenna by a novel feeding scheme, namely, the electromagnetic bandgap (EBG) structure.

1.3 Organization of the Thesis

Chapter 2 discusses the HBT small-signal equivalent circuit and parameter extraction. Following the discussion of typical parameter extraction method for HBT small-signal models, a new extraction method based on optimization with multi-plane data fitting and bi-directional search has been carried out to extract the equivalent circuit elements of the HBT small-signal model. In addition, to eliminate the self-heating effect on the parameter extraction, new methods to extract thermal resistance and parasitic resistance are proposed.

Due to the importance of parasitic inductance on the extraction of small-signal intrinsic element and noise matching, Chapter 3 discusses the modeling of the parasitic elements using the contour-integral method. It is demonstrated that the planar circuit approach is a very efficient way to determine the equivalent circuit element as well as to model the overall small-signal behavior of the HBT device.

Chapter 4 investigates the HBT noise model, which is based on the small-signal model in Chapter 2. The S-wave approach combined with the contour-integral method is, for the first time, applied to model the noise behavior of the HBT device and a new method to determine the equivalent noise temperatures has also been employed.

Based on the small-signal models discussed in Chapter 2, Chapter 5 is devoted to the HBT large-signal models. Both the Gummel-Poon model and the VBIC model are applied to HBT devices and a new extraction flow is implemented to extract the large-signal model parameters. As the current VBIC avalanche model suffers the drawback of poor modeling on high-current density breakdown, an empirical modification is proposed to improve its accuracy.

To effectively enhance the impedance bandwidth of a planar antenna, Chapter 6 proposes a new feeding technique using an electromagnetic/photonic bandgap (EBG/PBG) lattice. Analysis and design of an EBG structure and an EBG-fed multi-band slot antenna is presented. Finally, a multi-band active slot antenna with EBG feed is designed, fabricated and tested. The measurement results show the validity of our approaches throughout this work.

1.4 Major Contributions

The above modeling approaches lead to the following major contributions of this research:

1. For HBT small-signal modeling, a new parameter extraction method based on the two-directional search and multi-plane optimization has been proposed and demonstrated.
2. A fast and accurate method to extract the thermal resistance is proposed and the thermal effect on the emitter and collector resistance extraction is investigated.
3. The parasitic inductance of an one-finger HBT device can be accurately calculated by the resonance-mode technique without S-parameter measurements.

4. The contour-integral method is employed to extract the parasitic elements of a HBT device. It is demonstrated that the planar circuit approach combined with multi-connect method can accurately predict the overall small-signal behavior of the HBT device.
5. For the first time, the noise wave approach, combined with the contour-integral method, is applied to analyze the HBT noise behavior. The calculation results obtained from the wave approach are found to be more accurate than the existing SPICE noise model.
6. The HBT equivalent noise temperatures are extracted from the analysis of the HBT small-signal equivalent circuit model and the minimum noise figure.
7. The effect of various doping concentrations on HBT high-current avalanche breakdown behavior is explained by the change of maximum electric field in the intrinsic junction.
8. A modified VBIC avalanche breakdown is proposed which can be used to improve the fitting of the high-current breakdown region.
9. A novel feeding scheme is proposed to effectively increase the impedance bandwidth of the multi-band slot antenna. An EBG-fed multi-band slot antenna is designed and fabricated. The measurement results show that the bandwidth enhancement for all the operating frequency bands is achieved simultaneously.

Journal Papers:

[1] F. Lin, B. Chen, T. Zhou, B. L. Ooi, P.S. Kooi**, "**Characterization and Modeling of Avalanche Multiplication in HBTs," *Microelectronics Journal*, pp. 39-43, Apr. 2002.

[2] F. Lin, T. Zhou, B. Chen, B. L. Ooi, P. S. Kooi, "Extraction of VBIC Model for SiGe HBTs Made Easy by Going through Gummel-Poon Model," *Microelectronics Journal*, pp. 45-54, Apr. 2002.

[3] B. L. Ooi, B. Chen, F. Lin, P. S. Kooi, "A Fast and Practical Approach to the Determination of Junction Temperature and Thermal Resistance for BJT/HBT Devices," *Microwave and Optical Technology Letters.* vol. 35, No. 6, pp.499-502, Dec. 20, 2002.

[4] B. L. Ooi, D. Xu, B. Wu, and B. Chen, "A novel type of two-layer LTCC combiner," accepted for publication in *Microwave and Optical Technology Letters.*

[5] B. L. Ooi, M. S. Leong, K. Y. Yu, Y. Wang, and B. Chen, "Experimental investigation of novel multi-fingered antenna," accepted for publication in *Microwave and Optical Technology Letters.*

[6] B. L. Ooi, and B. Chen, "Simultaneous matching technique for multi-band antenna design through EBG structures," submitted for publication in *IEEE Trans. Antenna and Propagation*.

Conference Papers:

[1] B. Chen, F, Lin, B. L. Ooi, "HICUM Parameter Extraction Using IC-CAP," *HICUM User's Meeting, IEEE Bipolar/BiCMOS Technology Meeting, Sep. 2001, MN USA.*

[2] F. Lin, B. Chen, T. Zhou, B. L. Ooi, P.S. Kooi**, "**Characterization and Modeling of Avalanche Multiplication in HBTs," *International Symposium on Microelectronics and Assembly*, Dec. 2000, Singapore.

[3] F. Lin, T. Zhou, B. Chen, B. L. Ooi, P.S. Kooi, "Extraction of VBIC Model for SiGe HBTs Made Easy by Going through Gummel-Poon Model," *International*

Symposium on Microelectronics and Assembly, Dec. 2000, Singapore.

[4] F. Lin, B. Chen, T. Zhou, B. L. Ooi, P.S. Kooi**, "**Characterization and Modeling of Avalanche Multiplication in HBTs," *Agilent IC-CAP User's Meeting, Dec. 2000, Washington DC, USA.*

[5] F. Lin, T. Zhou, B. Chen, B. L. Ooi, P.S. Kooi, "Extraction of VBIC Model for SiGe HBTs Made Easy by Going through Gummel-Poon Model," *Agilent IC-CAP User's Meeting, Washington DC, Dec. 2000, USA.*

[6] B. Chen, B. L. Ooi, M. S. Leong and F. Hong, "Bandwidth enhancement for multi-band slot antenna by PBG feed," accepted by *IEEE AP-S Int. Symp*. 2004.

[7] B. Chen, B. L. Ooi, M. S. Leong, and F. Hong, "Active slot antenna by PBG-fed," accepted by *The IASTED International Conference on Antennas, Radar and Wave Propagation, ARP 2004*, Banff, AB, Canada, July 2004.

[8] B. Chen, B. L. Ooi, P. S. Kooi, and M. S. Leong, "Simultaneous signal and noise modeling of HBT by wave approach," accepted by *Progress in Electromagnetics Research Symposium (PIERS 2004)*.

[9] B. Chen, B. L. Ooi, L. Li, M. S. Leong, and S. T. Chew, "Planar antenna design on LTCC multiplayer technology," accepted by *Progress in Electromagnetics Research Symposium (PIERS 2004)*.

Chapter 2

Extraction of HBT Small-Signal Model Parameters

2.1 Introduction

As the range of HBT's applicability constantly widens, the need for accurate small-signal and large-signal models is critical to ensure the success of the design of nonlinear microwave circuits, such as amplifiers, oscillators, mixers, receivers and synthesizers [11]-[16]. Specifically, to design a power amplifier for wideband operation and to integrate it with an antenna for multi-band application, the accurate determination of the model parameters valid for a wide range of operating conditions and signal frequencies is even more critical. Therefore, an accurate parameter extraction procedure of the linear equivalent circuit is highly desirable.

Parameter extraction by fitting the model responses to measurements is the primary method to obtain the model parameter values of equivalent circuit models. Conventionally, parameter extraction is based on DC, S-parameter and large-signal measurements [17]-[19]. The most commonly used small-signal parameter extraction technique is numerical optimization of the model generated S-parameters to fit the measured data [18]. It is well-known, however, that optimization techniques may

result in nonphysical and/or non-unique values of the components. Also the optimized parameters are largely dependent on the initial values of the optimization process. In order to avoid this problem, several authors have proposed some analytical parameter extraction techniques. Costa *et al.* [20] have used several specially designed test structures to systematically de-embed the intrinsic HBT from surrounding extrinsic and parasitic elements. However, this method requires three test structures for each device size on the wafer. It ignores the non-uniformity across the wafer, and may involve an additional processing mask in some self-aligned technologies. The frequency dependence of the equivalent circuit model parameters was discussed by Pehlke and Pavlidis in [21], allowing a direct extraction of certain parameters. The remaining parameters (r_π, C_π, R_e and L_e) were extracted using numerical optimization. An alternative approach for small-signal modeling of HBT was also proposed in [22], where certain assumptions and optimization steps were used. Another elegant direct extraction procedure for HBTs was developed in [23], where the effect of pad capacitances was neglected and the measured S-parameters under open collector bias conditions were utilized to determine the extrinsic parameters. An approach combining analytical and optimization routines for parameter extraction purposes was reported in [24], in which DC and multi-bias RF measurements were used in conjunction with a conditioned impedance-block optimization approach. Finally, Li *et al.* [25] proposed a parameter extraction approach that combined analytical and empirical optimization procedures. In this approach, the derived circuit equations are simplified by neglecting some terms depending on the frequency range (low-middle-high frequency) where the model parameters are extracted.

Most of these techniques are based on the use of the device's frequency behavior, but some assumptions and approximations are made in order to derive the

equivalent circuit equations. This introduces an uncertainty in the obtained parameter values depending on the accuracy and validity of the assumptions. In practice, due to the diversity of the process technology and device geometry, these assumptions and approximations need to be modified and adjusted for different processes and devices. In order to design both analog and digital applications, an accurate and systematic extraction technique is essential to precisely model the device performance from DC to millimeter-wave frequencies [26].

This chapter discusses the combination of the analytical extraction and optimization-based extraction of the HBT small-signal model. Following the discussion of the analytical extraction procedure, the methodology of extracting HBT small-signal model parameters, based on the optimization of multi-plane data fitting and bi-directional search, is suggested by the author. This method has been applied to MESFET device with good success. Making use of the similarity of HBT and MESFET equivalent circuits, this work, for the first time, extends the optimization of multi-plane data fitting to extract the HBT small-signal element values. Moreover, due to the uncertainty introduced by the device self-heating effect, a novel extraction method to determine the emitter resistance value from flyback method is proposed by the author. Meanwhile to eliminate the self-heating effect on the emitter resistance extraction, a simple but accurate method to extract the thermal resistance will also be discussed for the first time by the author.

2.2 Parameter Extraction of the HBT π-Equivalent Circuit

The HBT small-signal equivalent circuit is shown in Figure 2.1. This circuit is divided into two parts, i.e., the outer part contains the extrinsic elements, considered as bias independent, and the inner part (in the dashed box) contains the intrinsic

elements, which are considered to be bias dependent. In order to facilitate the extraction of the intrinsic parameters, the intrinsic part of the device equivalent circuit can be re-grouped into Figure 2.2, using the well-known Tee-to-PI transformations shown in Figure 2.3. The final circuit is shown in Figure 2.4.

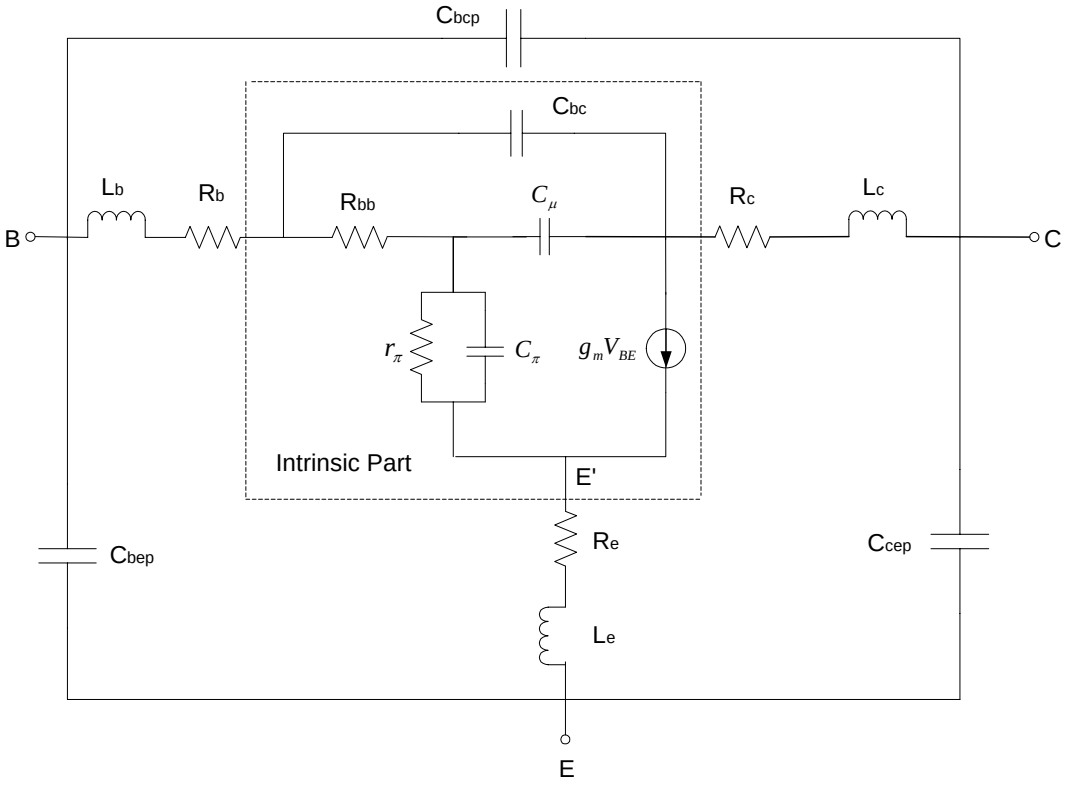

Figure 2.1 PI small-signal equivalent circuit of HBT device.

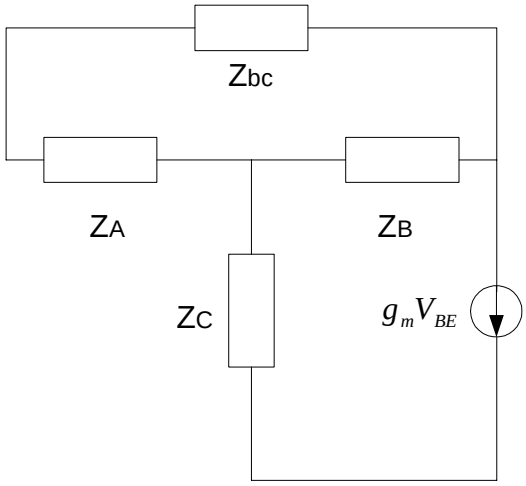

Figure 2.2 Intrinsic part of the HBT small-signal Tee model.

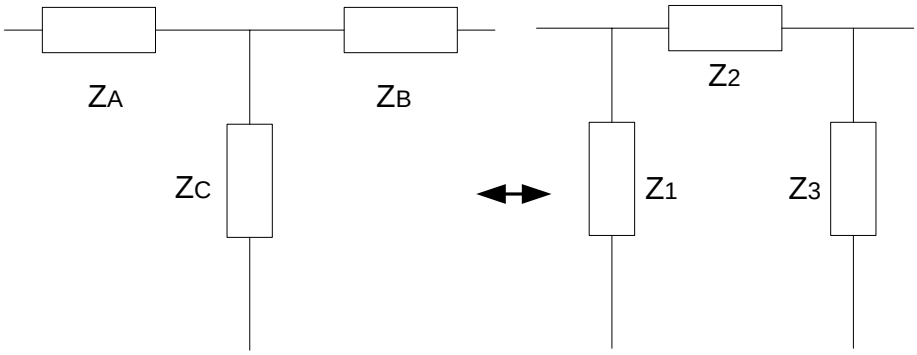

Figure 2.3 Tee-PI transformation of the HBT intrinsic part.

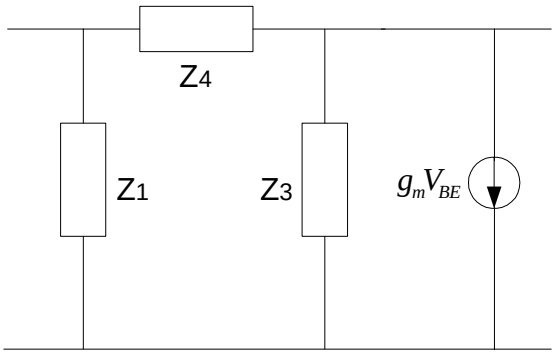

Figure 2.4 Compacted equivalent circuit of the intrinsic HBT small-signal model.

Since the intrinsic device exhibits a PI topology, it is convenient to use the admittance *Y*-parameters to characterize its electrical properties. These parameters can be defined as follows:

$$Y_{11} = \frac{Z_1 + Z_4}{Z_1 \cdot Z_4}, \tag{2.1}$$

$$Y_{12} = -\frac{1}{Z_4}, \tag{2.2}$$

$$Y_{21} = X \cdot \frac{Z_3}{Z_1} - \frac{1}{Z_4}, \tag{2.3}$$

$$Y_{22} = \frac{Z_4 + Z_3}{Z_4 \cdot Z_3} + X, \tag{2.4}$$

with $$X = B \cdot g_{m0} \cdot \exp(-j\omega\tau),$$

$$Z_A = R_{bb},$$

$$Z_B = \frac{1}{j\omega C_\mu},$$

$$Z_C = \frac{r_\pi}{1 + j\omega r_\pi C_\pi},$$

$$Z_{bc} = \frac{1}{j\omega C_{bc}},$$

$$Z_1 = \frac{D_2}{Z_B},$$

$$Z_2 = \frac{D_2}{Z_C},$$

$$Z_3 = \frac{D_2}{Z_A},$$

$$Z_4 = \frac{Z_2 Z_{bc}}{Z_2 + Z_{bc}},$$

$$D_2 = Z_A Z_B + Z_B Z_C + Z_A Z_C,$$

and $$B = \frac{(Z_1)^2 Z_2 Z_3}{(Z_2)^2 Z_1 Z_3 + (Z_3)^2 Z_2 Z_1 + (Z_1)^2 Z_3 Z_2}.$$

2.2.1 Extraction of Parasitic Elements

The first step in determining the equivalent circuit elements is the accurate extraction of extrinsic element values. The pad capacitances, pad inductances and contact resistances are relatively small, but have significant influence on the extraction of the intrinsic elements. Thus, their values have to be determined with great accuracy. As reported in [27], the extraction of parasitic elements is made by biasing the device first in forward operation (high current I_b) in order to extract the parasitic resistances (R_c, R_e and R_b) and inductances (L_c, L_e and L_b). The device is then

biased in the cutoff operation mode, thus, permitting the extraction of the parasitic capacitances (C_{bep}, C_{bcp} and C_{cep}). This method is also called “cold modeling technique”.

2.2.2 Extraction of Parasitic Inductances and Access Resistances

These parameters are determined from open collector bias conditions [23], where the base-collector and base-emitter junctions are in such forward condition that the collector current is cancelled out. As high base current densities, the base-emitter and base-collector junction capacitances have low impedances and low junction dynamic resistances. This is why the imaginary parts of Z-parameters of the equivalent circuit are dominated by the parasitic inductances of the device. In such an operation mode, the HBT equivalent circuit is shown in Figure 2.5. This circuit is more valid than that used in [27] since it is not perfectly symmetric and more physical.

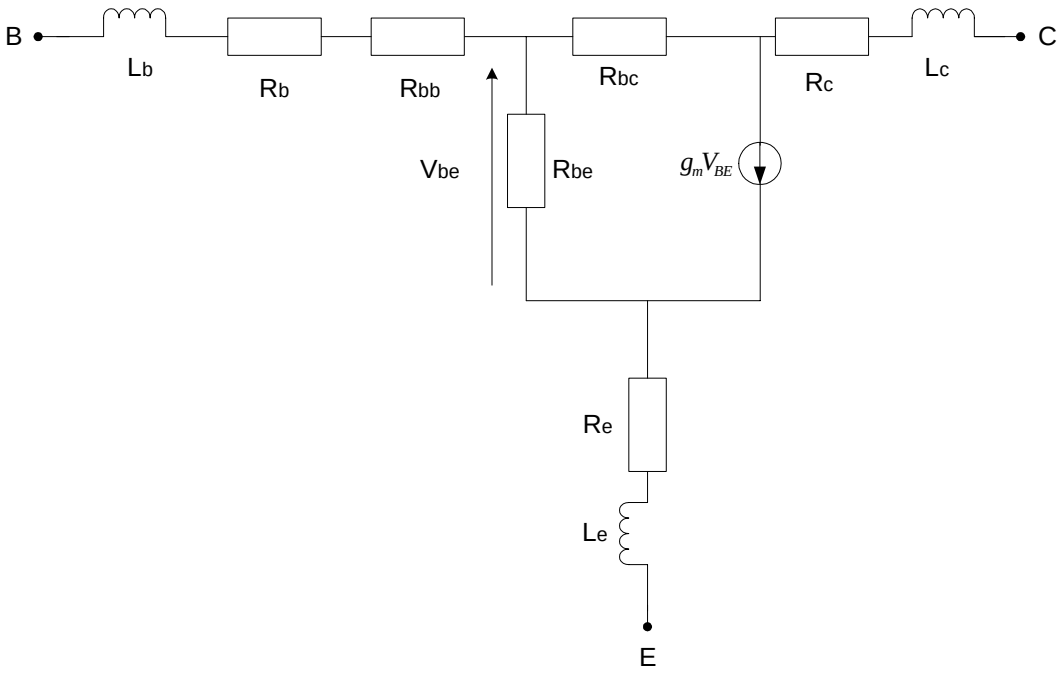

Figure 2.5 Equivalent circuit of the HBT device at open-collector bias condition.

The Z-parameters of this circuit are defined by the following equations:

$$Z_{11} = R_{bTotal} + R_e + \frac{R_{be}}{1 + g_{m0} R_{be}} + j\omega(L_b + L_e), \tag{2.5}$$

$$Z_{12} = R_e + \frac{R_{be}}{1 + g_{m0} R_{be}} + j\omega L_e, \tag{2.6}$$

$$Z_{21} = R_e + (1 - g_{m0} R_{bc}) \frac{R_{be}}{1 + g_{m0} R_{be}} + j\omega L_e, \tag{2.7}$$

$$Z_{22} = R_c + R_e + \frac{R_{be}}{1 + g_{m0} R_{be}} (1 + \frac{R_{bc}}{R_{be}}) + j\omega(L_c + L_e), \tag{2.8}$$

where R_{be} and R_{bc} are bias-dependent resistances of the base-emitter and base – collector junctions, respectively, and their expressions are given as follows:

$$R_{be} = \frac{n_{be} KT}{q I_{be}}, \tag{2.9}$$

$$R_{bc} = \frac{n_{bc} KT}{q I_{bc}}. \tag{2.10}$$

where g_{m0} is the dc transconductance and R_{bTotal} is the total base resistance, which is the sum of parasitic series resistance and intrinsic bias dependent resistance. The intrinsic base resistance depends on the injected forward base current I_b.

The extrinsic resistances are determined at low frequency from the real parts of the calculated Z-parameters and are given as follows:

$$\text{real}(Z_{11}\text{-}Z_{12}) = R_{bTotal}, \tag{2.11}$$

$$\text{real}(Z_{12}) = R_e + \frac{R_{be}}{1 + g_{m0} R_{be}}, \tag{2.12}$$

$$\text{real}(Z_{22}\text{-}Z_{21}) = R_c + \frac{1}{1 + g_{m0} R_{be}} (R_{bc} + g_{m0} R_{bc} R_{be}). \tag{2.13}$$

At high base current densities, the total base resistance R_{bTotal} tends asymptotically to the base resistance R_b, as shown in Figure 2.6. Also at these high current densities, R_{be}

and R_{bc} become very small $(R_{be} \approx 0, R_{bc} \approx 0)$ and the real parts of Z_{12}, Z_{21} and Z_{22}-Z_{21} increase linearly as a function of $1/I_b$, as shown in Figure 2.7. The extrapolated intercepts at the ordinate $(I_b \approx \infty)$ of these lines give the values of parasitic R_e and R_c. However, this method suffers from one drawback. As R_e and R_c must be extracted at the high base current, the self-heating effect may become pronounced. Figure 2.7 also shows that the values of R_e extracted from the expressions of real(Z_{12}) and real(Z_{21}) are roughly the same, and the extrinsic discrepancy between the evolution of these two expressions versus $1/I_b$ is explained by the fact that the device at the considered bias condition is not perfectly symmetric as predicted by equations (2.6) and (2.7). For the parasitic inductances L_b, L_e and L_c, using expressions (2.5)-(2.8), we can get their values from the imaginary parts of Z_{11}-Z_{12}, Z_{12} and Z_{22}-Z_{21}, respectively, as shown in Figure 2.8.

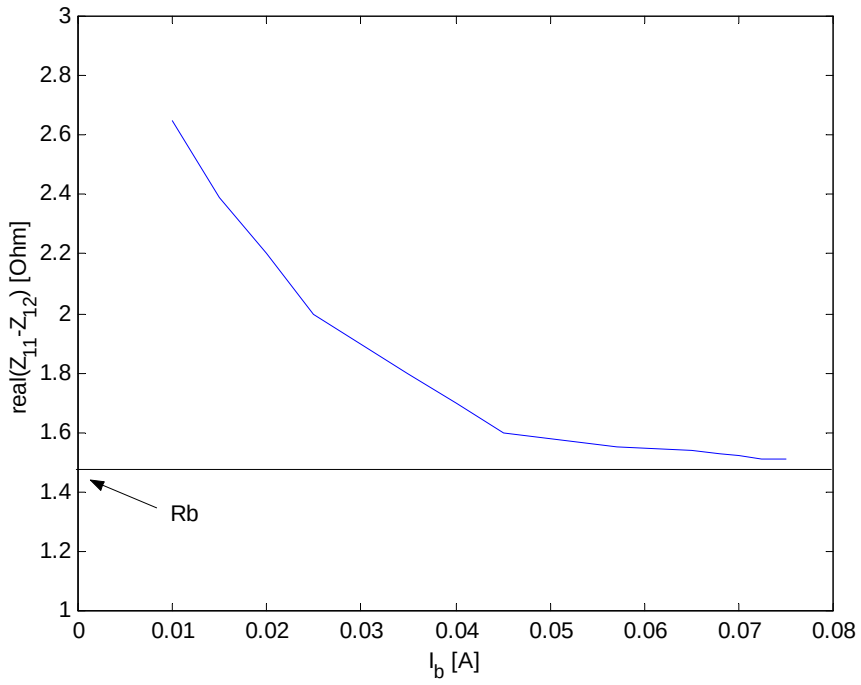

Figure 2.6 Evolution of the total base resistance from the measured real(Z_{11}-Z_{12}) as a function of the current I_b, freq=2 GHz.

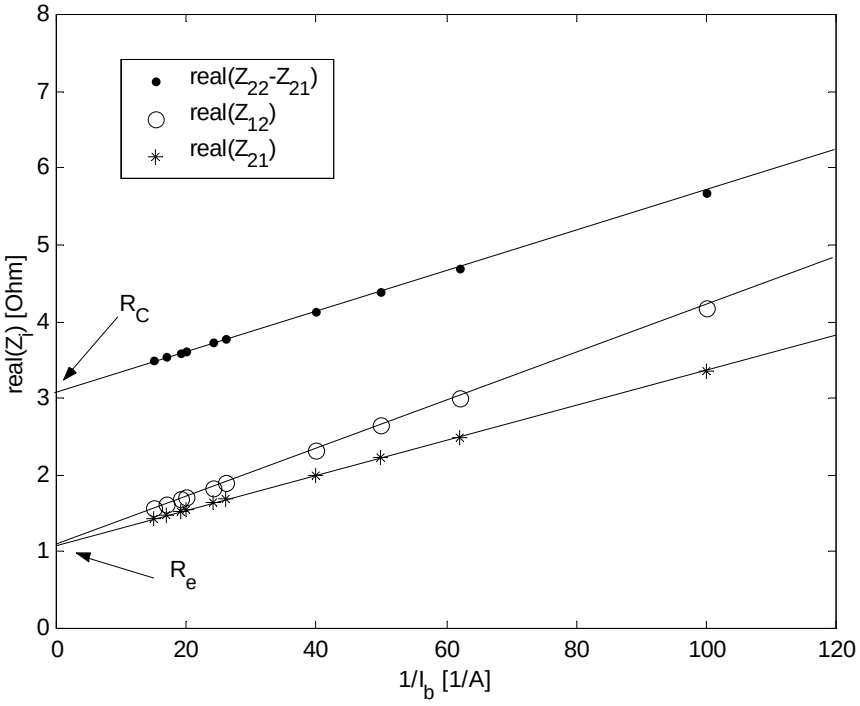

Figure 2.7 Plot of measured real(Z_{12}), real(Z_{21}) and real(Z_{22}-Z_{21}) versus *1/I_b*, freq=2 GHz.

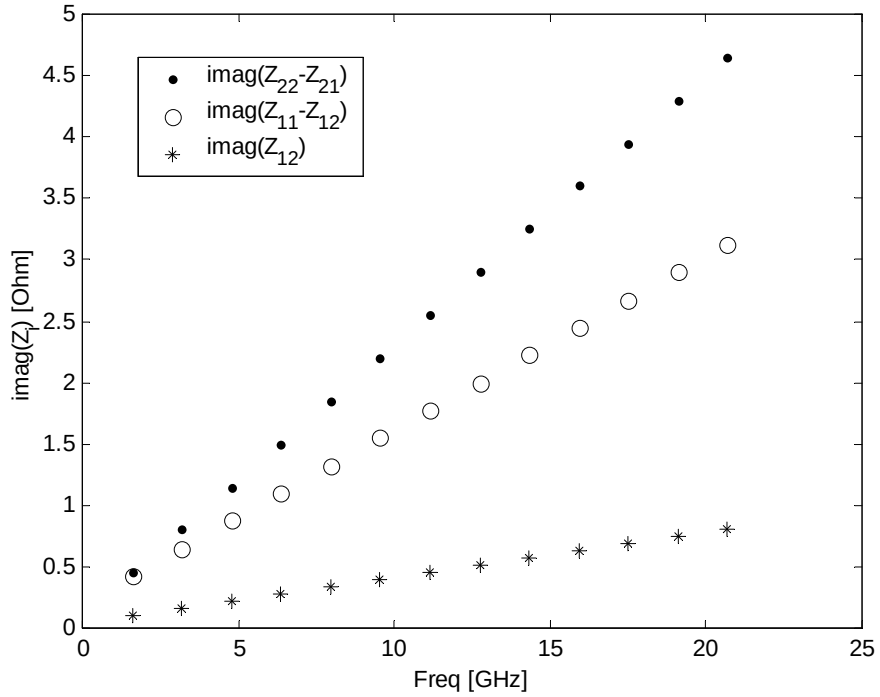

Figure 2.8 Evolution of the imaginary part of the measured Z-parameters versus frequency when the device is forward biased.

2.2.3 Extraction of Parasitic Capacitances

The pad capacitances can be extracted by the cold modeling technique from the HBT operating at cutoff [27]. The cold modeling technique was proposed to extract the parasitic elements of the MESFET device. As Diamant and Laviron have suggested, the S-parameter measurements at zero drain bias voltage can be used for the evaluation of device parasitics because the equivalent circuit is simpler. The cutoff operation of HBT refers to the bias condition that both B-E junction and B-C junction are reverse-biased or zero-biased. Under such bias condition, the HBT equivalent circuit can be simplified if the influence of the inductances and resistances can be negligible. Thus the cutoff operation is similar to the “cold FET modeling” used for MESFET’s. In cutoff mode, the intrinsic part of the HBT device can be modeled by simple passive circuit consisting of the B-E and B-C depletion capacitances, because B-E and B-C junctions are reverse-biased together with the probe-pattern parasitics. Under such conditions, the HBT equivalent circuit of Figure 2.1 is reduced to capacitance elements only, and this can be represented by the circuit shown in Figure 2.9.

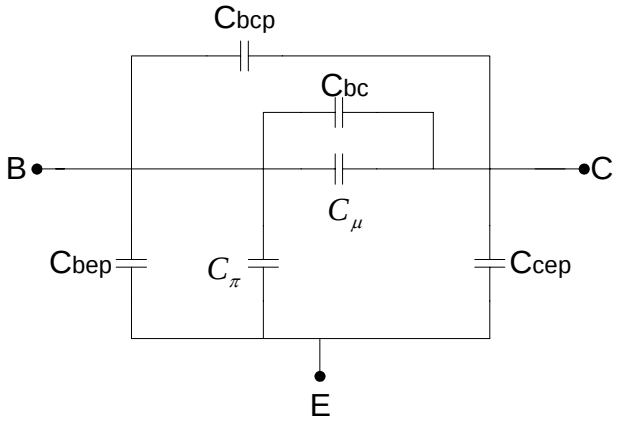

Figure 2.9 Equivalent circuit of the reverse-biased HBT device.

From the *Y*-parameters of this circuit, we have

$$\omega(C_{bep} + C_{\pi}) = \text{imag}(Y_{11}+Y_{12}), \tag{2.14}$$

$$\omega(C_{bcp} + C_{bc} + C_{\mu}) = \text{imag}(Y_{22}+Y_{12}), \tag{2.15}$$

and

$$\omega(C_{cep}) = -\text{imag}(Y_{12}). \tag{2.16}$$

Figure 2.10 shows the *Y*-parameters of the circuit as a function of the frequency. In the above equations, the parameters C_{bep}, C_{bcp} and C_{cep} are considered to be bias independent, whereas C_{π} and $C_{bc}+C_{\mu}$ are bias-dependent elements. Both the base-emitter and base-collector junction capacitances can be described by the following well-known expression:

$$C_j = \frac{C_{j0}}{\left(1 - \frac{V_{be}}{V_{bi}}\right)^{m_j}}. \tag{2.17a}$$

Taking the log of equation (2.17a), we arrive:

$$In(C_j) = In(C_{j0}) - m_j In\left(1 - \frac{V_{be}}{V_{bi}}\right). \tag{2.17b}$$

This equation can be interpreted as a linear function of the form:

$$y = b + m\,x \tag{2.17c}$$

where

$$y = In(C_j),$$

$$b = In(C_{j0}),$$

$m = m_j$ is the slope,

and

$$x = In\left(1 - \frac{V_{be}}{V_{bi}}\right).$$

Equation (2.17b) shows that $In(C_j)$ is a linear function of $In\left(1-\frac{V_{be}}{V_{bi}}\right)$ with the slope m_j. Ideally it is a straight line while the extrapolated intercepts at the ordinate of these lines gives the values of parasitic capacitance. Therefore, the extraction of the parasitic capacitances C_{bep} and C_{bcp} are carried out by fitting (C_π+C_{bep}) and (C_μ+C_{bc}+C_{bcp}) to the equation (2.17b), and this can be done by varying iteratively the parameter values of m_j and V_{bi} until the resulting curve is a straight line. Thus, the extrapolated intercepts at the ordinate of the lines give the values of the parasitic capacitances. However, in reality, and as discussed in [24], it is difficult to distinguish between these parasitic capacitances and their corresponding junction capacitances. That is why their values are considered to be absorbed by the junction capacitances and final optimization is employed to separate them from junction capacitances.

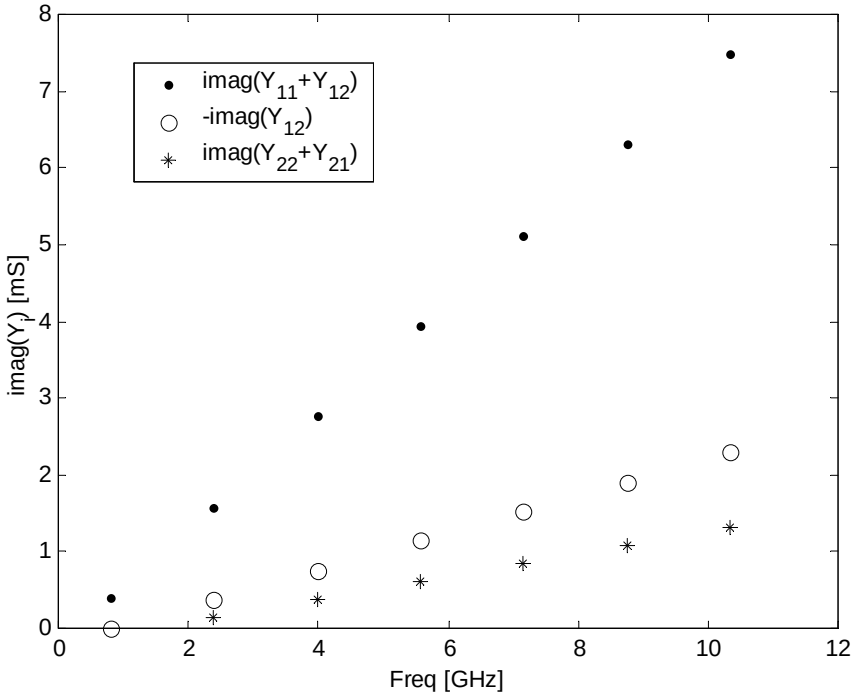

Figure 2.10 Evolution of the imaginary part of the measured Y-parameter versus frequency when the device is reverse biased.

2.2.4 Extraction of Intrinsic Elements

The calculated extrinsic parameters are then used to de-embed the measured *S*-parameters of the device and deduce the intrinsic *Y*-parameters defined by equations (2.1)-(2.4). After *S-to-Y* transformations, and using the following equations:

$$Z_1 = \frac{1}{Y_{11} + Y_{12}}, \tag{2.18}$$

$$Z_3 = \frac{Y_{21} + Y_{11}}{(Y_{11} + Y_{12})(Y_{22} + Y_{12})}, \tag{2.19}$$

$$Z_4 = -\frac{1}{Y_{12}}, \tag{2.20}$$

$$X = Y_{22} - \frac{(Y_{11} + Y_{12})(Y_{22} + Y_{12})}{Y_{21} + Y_{11}} + Y_{12}, \tag{2.21}$$

the intrinsic parameters can be determined analytically for each bias point as follows:

(1) $r_\pi = {n_{be}KT}\big/{qI_b}$, where n_{be} is the ideality factor of base-emitter junction.

(2) $\omega R_{bb}C_\mu = imag(Z_1/Z_3)$. The value of $R_{bb}C_\mu$ is then calculated from the slope of this expression when plotted versus frequency, as shown in Figure 2.11.

(3) $imag(Z_1) = -\dfrac{r_\pi(r_\pi\omega C_\pi - \omega R_{bb}C_\mu)}{1+(\omega C_\pi r_\pi)^2}$. This relation represents a second degree equation as a function of ωC_{bc} and it has the following solution:

$$\omega C_\pi = \frac{-r_\pi^2 - \sqrt{r_\pi^4 - 4(imag(Z_1) - \omega R_{bb}C_\mu r_\pi)imag(Z_1)r_\pi^2}}{2imag(Z_1)r_\pi^2}. \tag{2.22}$$

The other solution is usually nonphysical or negative. The value of C_π is then calculated from the slope of this expression when plotted against frequency.

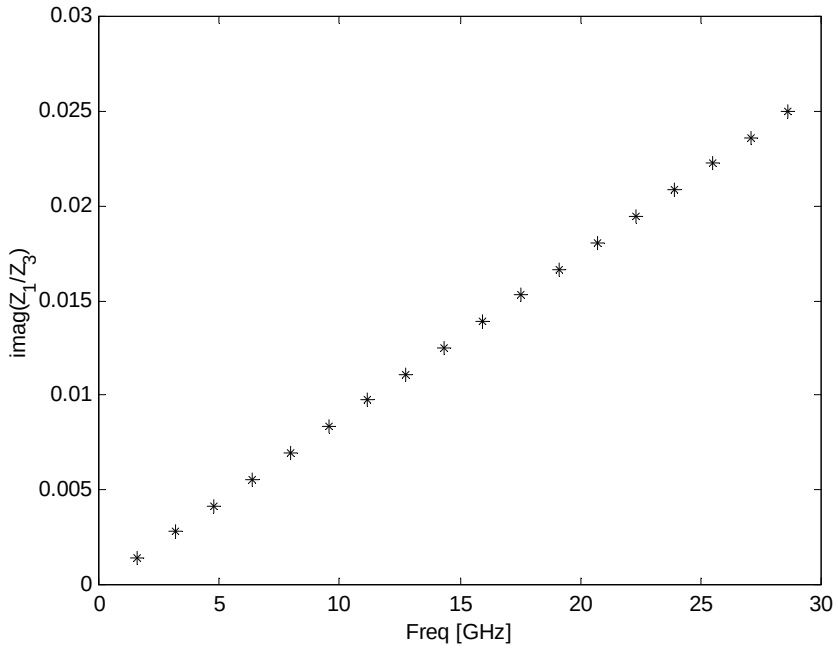

Figure 2.11 Plot of the measured imag(Z1/Z3) versus frequency for the calculation of $R_{bb}C_{\mu}$..

(4) From the real part of Z_1, we get

$$\omega R_{bb} = \frac{\omega(real(Z_1)\cdot(1+(\omega C_{\pi} r_{\pi})^2) - r_{\pi} - R_{bb}C_{\mu}r_{\pi}^2 C_{\pi}\omega^2)}{(1+C_{\pi}^2 r_{\pi}^2\omega^2)}. \tag{2.23}$$

The value of R_{bb} is calculated from the slope of this expression when plotted against frequency.

Once the values of R_{bb}, C_{μ}, C_{π} and r_{π} are calculated, we can evaluate the Z_2 and B, and then followed by the values of C_{bc}, τ and g_{m0} from the slope of their corresponding expressions:

$$\omega C_{bc} = imag(\frac{1}{Z_4} - \frac{1}{Z_2}), \tag{2.24}$$

$$\omega\tau = tg^{-1}\left(\frac{-imag\left(\frac{X}{B}\right)}{real\left(\frac{X}{B}\right)}\right), \tag{2.25}$$

and $$\omega g_{m0} = \omega \sqrt{\left(real\left(\frac{X}{B} \right) \right)^2 + \left(imag\left(\frac{X}{B} \right) \right)^2} \,. \qquad (2.26)$$

2.3 HBT Model Parameter Extraction Based on Optimization with Multi-plane Data Fitting and Bi-directional Search

The analytical approach in Section 2.2 suffers from two drawbacks. One is that the self-heating effect cannot be eliminated, which affects the accuracy of the R_e and R_c values, thus further affecting the intrinsic element values. The other drawback is, in the final optimization, that only one error criterion is examined for all circuit elements in the error function. While we will discuss the self-heating effect during the parasitic resistance extraction in the next section, let us examine the optimization issue in this section.

The method discussed in this section can still be categorized into the analytical optimizer based data-fitting technique. However, in contrast to the traditional ones, the new algorithm fits the measured data to the equivalent circuit model in two reference planes and minimizes the objective function by using a bi-directional search technique. In such a way, the number of optimization variables is reduced significantly. Every effort is made to diminish the searching space optimization as much as possible.

2.3.1 Data-fitting Carried Out in Two Reference Planes

The determination of the HBT equivalent circuit elements with an optimization based approach is carried out traditionally by minimizing an error function in such a way that starting from the initial values, all elements are changed independently and simultaneously by the optimizer until the error function reaches a minimum [28].

During the optimization process, only one error criterion is examined for all circuit elements in the external measurement reference plane. Because physically based microwave HBT equivalent circuit models comprise a large number of network elements, the optimization may terminate in any local minima. To reach the global minima, suitable starting values are usually necessary. In [29] and [30] efforts have been undertaken for mathematical separation of the variables, dividing the optimization into several successive steps. During each step, only some elements are changed by the optimizer to match the measured data. This kind of approach is partially successful. The search space is not diminished significantly, since the successive steps are not linearly independent. Another approach, focusing on the reduction of the number of optimization variables is known, which calculates the single frequency values of the intrinsic elements over some frequency range directly from the de-embedded device response and then averaging the values [31]. This approach is only successful if the starting values for the extrinsic equivalent circuit model elements are chosen very close to the true values.

In order to reduce the searching space effectively, but still maintain the matching purpose, a new optimization technique is proposed [32] and applied to the MESFET device successfully. In this method, the data-fitting is performed not only in the external measurement reference plane, but also in an additional internal one. Figure 2.12 illustrates this idea of decomposing a complex problem into easy solvable sub-problems.

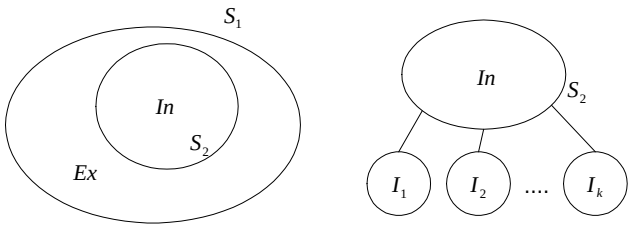

Figure 2.12 Illustration of data-fitting carried out in two reference planes and the definition of sub-problem within the intrinsic plane.

Referring to Figure 2.12, the second internal reference plane $\mathbf{S}_2$ is chosen in such a way that the objective of data-fitting in this plane can be divided into independent sub-problems I_1, I_2, …, I_k. Each sub-problem is easily solved by means of data fitting. To reduce the searching space most effectively, the number of extrinsic elements between the two planes (region **Ex**) should be as small as possible and the subdivisions of intrinsic area (**In**) must be independent from each other.

Regarding the conventional optimization and direct analytical extraction methods, the approach to the objective is performed only in one directional search. The common optimization algorithms begin with an initial value vector for all variables and approach to the objective of data-fitting (forward search). Conversely, analytical methods start directly with the measured data and general useful values of model elements (reverse search). Regarding the unavoidable errors in the measurements and idealized method topology with inherent model mismatching, both methods are not always establishing satisfying results in the model parameter extraction process. This can be explained by the large searching space in such a case. The searching space can be significantly reduced with simultaneously by means of a bi-directional search. Variables (model element) are divided into two groups and optimized simultaneously by means of a two directional search. In addition to the reduction of the searching space the bi-directional search establishes a sharp bend of

the search boundary close to the object node, which yields an increased possibility in finding the global minima. In the proposed new technique, extrinsic elements, which are located in **Ex**, are variables in the forward search, i.e., they are individually optimized. Intrinsic elements, which are located in **In**, are variables in the reverse search, i.e., they are synthesized from measurement data.

The general l_p-norm is used as the objective function, i. e.,

$$\left\| \vec{\varepsilon} \right\| = \left(\sum_{k=1}^{K} \left| \varepsilon_k \right|^p \right)^{1/p}, \tag{2.27}$$

with the error vector $\vec{\varepsilon}$. The error term ε_k is the weighted difference between the calculated and measured response in the form:

$$\varepsilon_k = w_k (F_k^c(\vec{p}) - F_k^m), \quad k = 1,2,...,K, \tag{2.28}$$

F_k^m is the measured response at frequency point *k*. F_k^c is the calculated response from the model with the vector $\vec{p} = [p_1, p_2, p_3, ..., p_n]^T$ (e.g. $[C_p, L_e, L_b, L_c, ...,]^T$). The complex weighting factor w_k considers generally two functions. Regarding an additional frequency dependency of w_k, it is possible to emphasize special ranges in accordance with the given reliability of measured data.

Different values of *p* are used in the internal and external reference planes of the data-fitting procedure. The objective function of l_2-norm (p=2) is applied to the internal reference plane because of the necessity of calculating the derivative differentiations. Conversely, the l_1-norm (p=1) is used in the external plane because of its known tolerance of large errors in microwave device modeling.

For the HBT device, the characterization is usually based on S-parameter measurements. We use a normalized l_1-norm in the external measurement reference plane with objective function

$$\left\|\vec{\varepsilon}\right\| = \frac{1}{4K}\sum_{i,j=1}^{2}\sum_{k=1}^{K}\frac{\left|\mathrm{Re}(\Delta S_{ij,k})\right| + \left|\mathrm{Im}(\Delta S_{ij,k})\right|}{m_{ij}}, \tag{2.29}$$

where

$$\Delta S_{ij,k} = S_{ij}^{m} - S_{ij}^{c}(\vec{p}, f_k),$$

$$m_{ij} = \max_{k}\{\left|S_{ij}^{m}(f_k)\right|\}, \ (i, j = 1,2),$$

$S_{i,j}^{m}(f_k)$ is the measured S-parameter at frequency f_k, $S_{i,j}^{c}(f_k)$ is the calculated corresponding S-parameter coefficient derived from extracted values of the model parameters, $\vec{p}$ is the vector of model parameters, K is the number of considered frequency points and m_{ij} is the largest magnitude for the measured S-parameter S_{ij}^{m}.

Two aspects of the defined objective function (2.29) should be mentioned: i) it is a normalized quantity which can be used to quantify the match degree of data-fitting; ii) the real and imaginary parts are calculated separately in contrast to the commonly used definitions because the convergence is faster. The searching space is reduced and the error function is larger and becomes more sensitive.

2.3.2 Parameter Extraction Technique

The analytical optimization concept described in the above was originally developed to overcome the well known consistency problem appearing in the experimental modeling of microwave MESFET's [32] and [33]. Due to the similarity of the HBT and MESFET small-signal equivalent circuits, the application of this general technique to the HBT device is expected to demonstrate its superior performance.

The small-signal HBT equivalent circuit model adopted here is shown in Figure 2.13. In Figure 2.13, the B-C junction splitting capacitance C_{bc} is simplified as a first

order approximation since its value can be easily determined from layout/process data or from the final optimization.

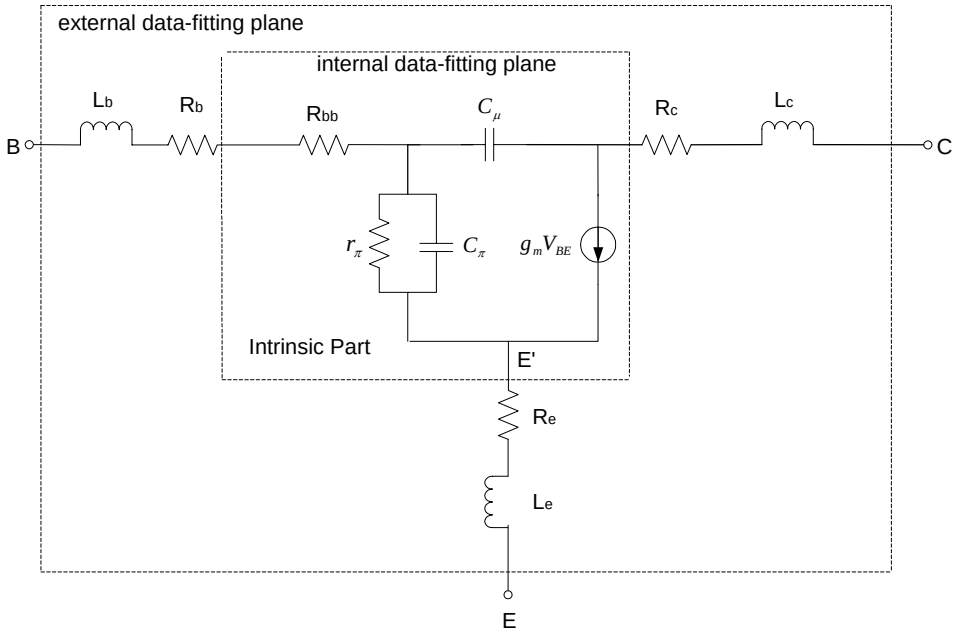

Figure 2.13 HBT model with two reference planes and intrinsic branch admittances.

It is well-known that there is no unique solution if all elements are assumed as variables and only measured extrinsic terminal S-parameters are to be matched. The results depend heavily on the starting condition and the optimizer used. If the data-fitting is performed by the proposed technique with respect to both the external and internal reference planes (Figure 2.13), this uncertainty can be eliminated.

In this work, only eight extrinsic parasitic elements are assigned as ordinary optimization variables in forward search. All intrinsic elements and variables are analytically calculated by incorporating the least squares data-fitting formulation. The measured terminal S-parameters are first de-embedded with respect to the extrinsic elements yielding the Y-parameters of the intrinsic HBT; branch admittances of the intrinsic π-structure are then obtained and fitted to each branch element by means of l_2 data-fitting with a reasonable frequency dependent weighting factor, in Figure 2.13.

A. Generating Initial Values for the Extrinsic Elements

The problem of the starting value vector can be easily eliminated with this technique. In this work, only the initial values for the extrinsic elements are required for the optimization procedure. They can be generated by using the measured data of HBT operating in a passive reverse-biased condition. In this case, the intrinsic HBT model can be simplified to a π-structure of only three capacitances, which can then be transformed into a *T*-structure as shown in Figure 2.14. Together with the base, emitter and collector parasitic resistive and inductive model elements, simple series R-L-C branches are established, which can be analytically calculated in terms of their branch impedance

$$R_l = Z_0 \frac{x_2}{x_1}, \tag{2.30}$$

$$L_l = \frac{Z_0}{2\pi f_0} \frac{x_3}{x_1}, \tag{2.31}$$

$$C_l = \frac{1}{2\pi f_0 Z_0} x_1, \ (l = e, b, c). \tag{2.32}$$

where x_1, x_2 and x_3 are the solutions of the following matrix equation:

$$\begin{bmatrix} \sum_k \tilde{f}_k^2 |z_k|^2 & -\sum_k \tilde{f}_k^2 \operatorname{Re}(z_k) & -\sum_k \tilde{f}_k^3 \operatorname{Im}(z_k) \\ -\sum_k \tilde{f}_k^2 \operatorname{Re}(z_k) & \sum_k \tilde{f}_k^2 & 0 \\ -\sum_k \tilde{f}_k^3 \operatorname{Im}(z_k) & 0 & \sum_k \tilde{f}_k^4 \end{bmatrix} \begin{bmatrix} x_1 \\ x_2 \\ x_3 \end{bmatrix}$$

$$= \begin{bmatrix} -\sum_k \tilde{f}_k^3 \operatorname{Im}(z_k) \\ 0 \\ \sum_k \tilde{f}_k^2 \end{bmatrix} \tag{2.33}$$

with

$$\tilde{f} = f_k / f_0 \ , \ z_k = Z^m_{l,k} / Z_0 \ , (l = e, b, c), \qquad (2.34)$$

and f_0 and Z_0 being the normalized frequency and impedance. In the reverse-biased condition, the defined internal reference plane (Figure 2.14) excludes the pad-capacitance C_p. The number of regular optimization variables is reduced to only two, showing no local minimum problem. Thus the optimization can be generally performed with zero starting values for pad-capacitances.

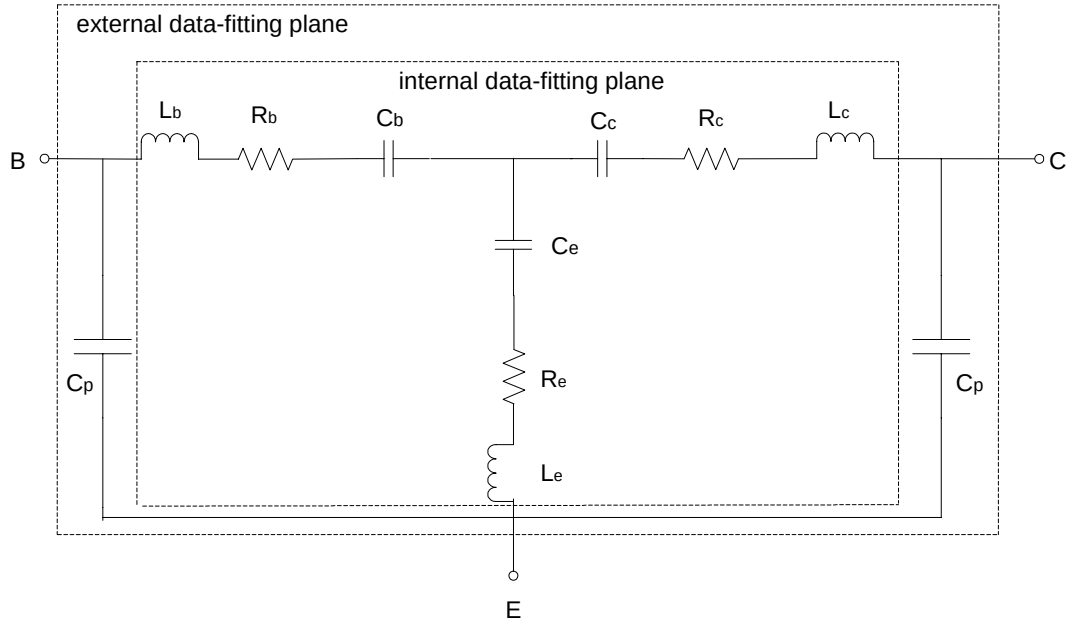

Figure 2.14 HBT model under reversed-biased condition used for generating starting values of extrinsic elements.

B. Extraction of Intrinsic Elements

The HBT intrinsic circuit, which is enclosed in the dashed line of Figure 2.13, includes six biased dependent elements: R_{bb}, C_μ, C_π, r_π, g_{m0}, τ. To determine the extrinsic and intrinsic elements in the equivalent circuit, the multi-dimensional optimization method is a possible solution. However, it is well-known that there is no unique solution if all the elements are assumed as variables and only the measured extrinsic terminal S-parameters are matched. Different element sets may result in a

comparable data-fitting quality. The result may depend heavily on the starting condition. The optimization process often runs into a local minimum and thus leads to some nonphysical/negative elements. Such an optimization technique is not appropriate to investigate bias dependent behavior of the series resistances, such as R_{bb}, which requires a physical explanation.

For the intrinsic circuit, the terminal impedance matrix [*Z*] and the intrinsic admittance matrix [*Y*] have the following relationship according to the equivalent circuit shown in Figure 2.13:

$$[Y] = ([Z] - [R])^{-1}, \tag{2.35}$$

where

$$Y = \begin{pmatrix} \frac{1}{r_\pi} + j\omega(C_\pi + C_\mu) & -j\omega C_\mu \\ g_{m0}e^{-j\omega\tau} - j\omega C_\mu & j\omega C_\mu \end{pmatrix}, \tag{2.36}$$

$$R = \begin{pmatrix} R_{bb} & 0 \\ 0 & 0 \end{pmatrix}, \tag{2.37}$$

and

$$Z = \begin{pmatrix} Z_{11} & Z_{12} \\ Z_{21} & Z_{22} \end{pmatrix}, \tag{2.38}$$

is the impedance matrix of the intrinsic circuit de-embedded from the measured S-parameters once the extrinsic parameters are known, e.g., from the data fitting at the external plane. Thus the internal data fitting can be carried out when the impedance matrix (2.38) is known.

Substituting equations (2.36) to (2.38) into equation (2.35), we have

$$Y_{11}Z_{11} - Y_{11}R_{bb} + Y_{21}Z_{12} - 1 = 0, \tag{2.39}$$

$$Y_{12}Z_{21} + Y_{22}Z_{22} - 1 = 0\,, \tag{2.40}$$

$$Y_{11}Z_{21} + Y_{21}Z_{22} = 0\,, \tag{2.41}$$

and
$$Y_{12}Z_{11} - Y_{12}R_{bb} + Y_{22}Z_{12} = 0\,. \tag{2.42}$$

Substituting the definitions of $[Y]$ and $[Z]$ into (2.40) and (2.42), we have

$$-j\omega C_{\mu}Z_{21} + j\omega C_{\mu}Z_{22} - 1 = 0\,, \tag{2.43}$$

$$-j\omega C_{\mu}Z_{11} + j\omega C_{\mu}R_{bb} + j\omega C_{\mu}Z_{12} = 0\,, \tag{2.44}$$

Introducing the dimensionless normalized variables,

$$\tilde{f}_k = f_k / f_0\,, \qquad f_0 = \max(f_k) \tag{2.45}$$

$$\omega = 2\pi f\,, \tag{2.46}$$

$$\omega_0 = 2\pi f_0\,, \tag{2.47}$$

$$\tilde{Z}_k = Z_k / Z_0 = \tilde{Z}_k^R + j\tilde{Z}_k^I\,, \tag{2.48}$$

where f_0 and Z_0 are normalized frequency and impedance (Z_0= 50 Ω), then the two equations become

$$-j\omega_0 \tilde{f}_k C_{\mu}Z_0\tilde{Z}_{21} + j\omega_0 \tilde{f}_k C_{\mu}Z_0\tilde{Z}_{22} - 1 = 0\,, \tag{2.49}$$

$$-j\omega_0 \tilde{f}_k C_{\mu}Z_0\tilde{Z}_{11} + j\omega_0 \tilde{f}_k C_{\mu}R_{bb} + j\omega_0 \tilde{f}_k C_{\mu}Z_0\tilde{Z}_{12} = 0\,. \tag{2.50}$$

Let us define the unknown scalars as

$$x_1 = \omega_0 C_{\mu}Z_0\,, \tag{2.51}$$

$$x_2 = \omega_0 C_{\mu}R_{bb}\,, \tag{2.52}$$

then we have:

$$\tilde{f}_k x_1\tilde{Z}_{21}^I - \tilde{f}_k x_1\tilde{Z}_{22}^I - 1 + j(-\tilde{f}_k x_1\tilde{Z}_{21}^R + \tilde{f}_k x_1\tilde{Z}_{22}^R) = 0\,, \tag{2.53}$$

$$\tilde{f}_k x_1\tilde{Z}_{11}^I - \tilde{f}_k x_1\tilde{Z}_{12}^I + j(-\tilde{f}_k x_1\tilde{Z}_{11}^R + \tilde{f}_k x_2 + \tilde{f}_k x_1\tilde{Z}_{12}^R) = 0\,, \tag{2.54}$$

where x_1 and x_2 can be solved by means of least square optimization method with the error being defined as:

$$\varepsilon_{k1} = \tilde{f}_k x_1 \tilde{Z}_{21}^I - \tilde{f}_k x_1 \tilde{Z}_{22}^I - 1 + j(-\tilde{f}_k x_1 \tilde{Z}_{21}^R + \tilde{f}_k x_1 \tilde{Z}_{22}^R), \tag{2.55}$$

$$\varepsilon_{k2} = \tilde{f}_k x_1 \tilde{Z}_{11}^I - \tilde{f}_k x_1 \tilde{Z}_{12}^I + j(-\tilde{f}_k x_1 \tilde{Z}_{11}^R + \tilde{f}_k x_2 + \tilde{f}_k x_1 \tilde{Z}_{12}^R). \tag{2.56}$$

The objective function is defined as

$$e = \sum_{i=1}^{2} \left\| \varepsilon_{ki} \right\|_p^2, \tag{2.57}$$

where $\left\| \varepsilon_{ki} \right\|_p^2 = \left[(\sum_{k=1}^{N} \left| \varepsilon_{ki} \right|^p)^{1/p} \right]^2$. Usually, we use l_2 ($p = 2$) norm so that we have

$$\begin{aligned} e &= \sum_{k=1}^{N} \left| \varepsilon_{k1} \right|^2 + \sum_{k=1}^{N} \left| \varepsilon_{k2} \right|^2 \\ &= \sum_{k=1}^{N} \left[(\tilde{f}_k x_1 \tilde{Z}_{21}^I - \tilde{f}_k x_1 \tilde{Z}_{22}^I - 1)^2 + (-\tilde{f}_k x_1 \tilde{Z}_{21}^R + \tilde{f}_k x_1 \tilde{Z}_{22}^R)^2 \right] \\ &+ \sum_{k=1}^{N} \left[(\tilde{f}_k x_1 \tilde{Z}_{11}^I - \tilde{f}_k x_1 \tilde{Z}_{12}^I)^2 + (-\tilde{f}_k x_1 \tilde{Z}_{11}^R + \tilde{f}_k x_2 + \tilde{f}_k x_1 \tilde{Z}_{12}^R)^2 \right] \end{aligned} \tag{2.58}$$

Consider x_i as unknown variables, the objective is to minimize the error functions with respect to x_i, i.e.,

$$\frac{\partial e}{\partial x_i} = 0, \ i = 1,2 \tag{2.59}$$

$$\begin{bmatrix} \sum_{k=1}^{N} \tilde{f}_k^2 \left[(\tilde{Z}_{21}^I - \tilde{Z}_{22}^I)^2 + (-\tilde{Z}_{21}^R + \tilde{Z}_{22}^R)^2 + (\tilde{Z}_{11}^I - \tilde{Z}_{12}^I)^2 + (-\tilde{Z}_{11}^R + \tilde{Z}_{12}^R)^2 \right] & \sum_{k=1}^{N} \tilde{f}_k^2 (-\tilde{Z}_{11}^R + \tilde{Z}_{12}^R) \\ \sum_{k=1}^{N} \tilde{f}_k^2 (-\tilde{Z}_{11}^R + \tilde{Z}_{12}^R) & \sum_{k=1}^{N} \tilde{f}_k^2 \end{bmatrix} \begin{bmatrix} x_1 \\ x_2 \end{bmatrix} = \begin{bmatrix} \sum_{k=1}^{N} \tilde{f}_k (\tilde{Z}_{21}^I - \tilde{Z}_{22}^I) \\ 0 \end{bmatrix}, \tag{2.60}$$

Once x_1 and x_2 have been found, we can obtain

$$C_\mu = \frac{x_1}{\omega_0 Z_0}, \tag{2.61}$$

$$R_{bb} = \frac{x_2}{x_1} Z_0 , \tag{2.62}$$

Similarly, substituting the definitions of $[Y]$ and $[Z]$ into equations (2.39) and (2.41), we have

$$\sum_{k=1}^{N} [\frac{1}{r_\pi} + j\omega(C_\pi + C_\mu)]Z_{11} - [\frac{1}{r_\pi} + j\omega(C_\pi + C_\mu)]R_{bb} + (g_{m0}e^{-j\omega\tau} - j\omega C_\mu)Z_{12} - 1 = 0 ,$$

(2.63)

$$\sum_{k=1}^{N} [\frac{1}{r_\pi} + j\omega(C_\pi + C_\mu)]Z_{21} + (g_{m0}e^{-j\omega\tau} - j\omega C_\mu)Z_{22} = 0 , \tag{2.64}$$

From $\omega = \omega_0 \tilde{f}_k$ and $Z_k = \tilde{Z}_k Z_0$, we have

$$\begin{aligned} &\sum_{k=1}^{N} [\frac{1}{r_\pi} + j\omega_0 \tilde{f}_k (C_\pi + C_\mu)]Z_0 \tilde{Z}_{11} - [\frac{1}{r_\pi} + j\omega_0 \tilde{f}_k (C_\pi + C_\mu)]R_{bb} \\ &+ (g_{m0}e^{-j\omega_0 \tilde{f}_k \tau} - j\omega_0 \tilde{f}_k C_\mu)Z_0 \tilde{Z}_{12} - 1 = 0 \end{aligned} \tag{2.65}$$

$$\sum_{k=1}^{N} [\frac{1}{r_\pi} + j\omega_0 \tilde{f}_k (C_\pi + C_\mu)]Z_0 \tilde{Z}_{21} + (g_{m0}e^{-j\omega_0 \tilde{f}_k \tau} - j\omega_0 \tilde{f}_k C_\mu)Z_0 \tilde{Z}_{22} = 0 , \tag{2.66}$$

Let us define four new unknown variables as

$$x_3 = \frac{Z_0}{r_\pi} , \tag{2.67}$$

$$x_4 = \omega_0 (C_\pi + C_\mu)Z_0 , \tag{2.68}$$

$$x_5 = \mathrm{Re}(g_{m0}e^{-j\omega_0 \tilde{f}_k \tau})Z_0 , \tag{2.69}$$

$$x_6 = \mathrm{Im}(g_{m0}e^{-j\omega_0 \tilde{f}_k \tau})Z_0 . \tag{2.70}$$

Then the above equations become

$$\begin{aligned} &\sum_{k=1}^{N} x_3 \tilde{Z}_{11}^R - \tilde{f}_k x_4 \tilde{Z}_{11}^I - x_3 \frac{x_2}{x_1} + x_5 \tilde{Z}_{12}^R - x_6 \tilde{Z}_{12}^I + \tilde{f}_k x_1 \tilde{Z}_{12}^I - 1 \\ &+ j(x_3 \tilde{Z}_{11}^I + \tilde{f}_k x_4 \tilde{Z}_{11}^R - \tilde{f}_k x_4 \frac{x_2}{x_1} + x_5 \tilde{Z}_{12}^I + x_6 \tilde{Z}_{12}^R - \tilde{f}_k x_1 \tilde{Z}_{12}^R) = 0 \end{aligned} , \tag{2.71}$$

$$\begin{aligned}&\sum_{k=1}^{N} x_3\tilde{Z}_{21}^{R} - \tilde{f}_k x_4\tilde{Z}_{21}^{I} + x_5\tilde{Z}_{22}^{R} - x_6\tilde{Z}_{22}^{I} + \tilde{f}_k x_1\tilde{Z}_{22}^{I} \\ &+ j(x_3\tilde{Z}_{21}^{I} + \tilde{f}_k x_4\tilde{Z}_{21}^{R} + x_5\tilde{Z}_{22}^{I} + x_6\tilde{Z}_{22}^{R} - \tilde{f}_k x_1\tilde{Z}_{22}^{R}) = 0\end{aligned}, \tag{2.72}$$

The real and imaginary parts of the equations are equal to zero. The solutions for x_i are given as follows

$$\sum_{k=1}^{N} x_3\tilde{Z}_{11}^{R} - \tilde{f}_k x_4\tilde{Z}_{11}^{I} - x_3\frac{x_2}{x_1} + x_5\tilde{Z}_{12}^{R} - x_6\tilde{Z}_{12}^{I} + \tilde{f}_k x_1\tilde{Z}_{12}^{I} - 1 = 0, \tag{2.73}$$

$$\sum_{k=1}^{N} x_3\tilde{Z}_{11}^{I} + \tilde{f}_k x_4\tilde{Z}_{11}^{R} - \tilde{f}_k x_4\frac{x_2}{x_1} + x_5\tilde{Z}_{12}^{I} + x_6\tilde{Z}_{12}^{R} - \tilde{f}_k x_1\tilde{Z}_{12}^{R} = 0, \tag{2.74}$$

$$\sum_{k=1}^{N} x_3\tilde{Z}_{21}^{R} - \tilde{f}_k x_4\tilde{Z}_{21}^{I} + x_5\tilde{Z}_{22}^{R} - x_6\tilde{Z}_{22}^{I} + \tilde{f}_k x_1\tilde{Z}_{22}^{I} = 0, \tag{2.75}$$

$$\sum_{k=1}^{N} x_3\tilde{Z}_{21}^{I} + \tilde{f}_k x_4\tilde{Z}_{21}^{R} + x_5\tilde{Z}_{22}^{I} + x_6\tilde{Z}_{22}^{R} - \tilde{f}_k x_1\tilde{Z}_{22}^{R} = 0, \tag{2.76}$$

i.e.

$$\begin{bmatrix} \sum_{k=1}^{N}\tilde{Z}_{11}^{R} - \frac{x_2}{x_1} & \sum_{k=1}^{N} -\tilde{f}_k\tilde{Z}_{11}^{I} & \sum_{k=1}^{N}\tilde{Z}_{12}^{R} & \sum_{k=1}^{N} -\tilde{Z}_{12}^{I} \\ \sum_{k=1}^{N}\tilde{Z}_{11}^{I} & \sum_{k=1}^{N}\tilde{f}_k(\tilde{Z}_{11}^{R} - \frac{x_2}{x_1}) & \sum_{k=1}^{N}\tilde{Z}_{12}^{I} & \sum_{k=1}^{N}\tilde{Z}_{12}^{R} \\ \sum_{k=1}^{N}\tilde{Z}_{21}^{R} & \sum_{k=1}^{N} -\tilde{f}_k\tilde{Z}_{21}^{I} & \sum_{k=1}^{N}\tilde{Z}_{22}^{R} & \sum_{k=1}^{N} -\tilde{Z}_{22}^{I} \\ \sum_{k=1}^{N}\tilde{Z}_{21}^{I} & \sum_{k=1}^{N}\tilde{f}_k\tilde{Z}_{21}^{R} & \sum_{k=1}^{N}\tilde{Z}_{22}^{I} & \sum_{k=1}^{N}\tilde{Z}_{22}^{R} \end{bmatrix} \begin{bmatrix} x_3 \\ x_4 \\ x_5 \\ x_6 \end{bmatrix} = \begin{bmatrix} \sum_{k=1}^{N} 1 - \tilde{f}_k x_1\tilde{Z}_{12}^{I} \\ \sum_{k=1}^{N}\tilde{f}_k x_1\tilde{Z}_{12}^{R} \\ \sum_{k=1}^{N} -\tilde{f}_k x_1\tilde{Z}_{22}^{I} \\ \sum_{k=1}^{N}\tilde{f}_k x_1\tilde{Z}_{22}^{R} \end{bmatrix}, \tag{2.77}$$

From the definitions of x_3, x_4, x_5 and x_6, we have

$$r_\pi = \frac{Z_0}{x_3}, \tag{2.78}$$

$$C_\pi = \frac{x_4 - x_1}{\omega_0 Z_0}, \tag{2.79}$$

$$\tau_d = \arctan(-\frac{x_6}{x_5})/(\omega_0\tilde{f}_s), \tag{2.80}$$

$$g_{m0} = \frac{\sqrt{x_5^2 + x_6^2}}{Z_0}. \tag{2.81}$$

The summations are carried out over all k supporting frequency points f_k.

2.4 Self-heating Effect on the HBT Series Resistance Extraction from Floating Terminal Measurement

The above approaches to extract the HBT small-signal model parameters are all based on the analysis of device S-parameters. However, due to the self-heating effect of the HBT device, some uncertainty is introduced when the device S-parameters are measured, thus affecting the accuracy of the model parameter extraction. For the modern HBT technologies, downscaling of emitter lateral dimensions increases the emitter resistance while decreases collector resistance. For example, most modern SiGe BiCMOS technology employs shallow or deep trench to achieve higher cut-off frequency and packing density. As a result, self-heating effect of HBT device becomes an important concern.

Besides the previously discussed methods to extract parasitic resistances from measured S-parameters, many methods also have been proposed to extract the series emitter resistance and collector resistance from DC measurements. For the extraction of emitter resistance, they can be categorized in two groups. Considerations involving the output characteristics in the normal active region [34] can be collected in one group while those which analyze the output characteristics in the saturated region [35] and [36] can be collected in another one. The Ning-Tang method [34], which is a representative of former group, is based on the observation of voltage drop at the base and emitter series resistance from the transistor forward Gummel plot. Although

emitter resistance can be extracted, the base resistance has to be known beforehand and the self-heating effect on the emitter resistance is neglected. Open collector measurement method is used to extract emitter resistance by analyzing the slope of input current versus output terminal voltage on the condition that the collector current is kept zero. In other words, the open collector condition refers to the collector input current is zero. To extract the emitter resistance from open-collector measurement setup the base current source is swept under the condition that the emitter pin grounded. By doing so, we get a voltage at the open collector that is proportional to the base current through this emitter resistor. If we derivate V_{CE} with respect to I_B, we get the equivalent R_E for each operating point as $R_E = \frac{\partial V_{CE}}{\partial I_B}$. The output voltage between base and collector is positive, thus the base-collector junction is forward biased at the open collector condition. Since the B-C junction is forward biased during the measurement, the device is conducting in saturated region. Except from the flyback measurement, the collector series resistance can be also extracted from dedicated R_C-active measurement by monitoring the substrate current of parasitic PNP transistor linked with the intrinsic NPN transistor [37] [38]. However, this method is not suitable for compound HBT devices, such as GaAs HBT, with no substrate PNP transistor presented.

In the conventional R_E-flyback measurement, the saturation voltage of a transistor including extrinsic emitter resistance is given by

$$V_{CE} = V_T In\left(\frac{1+\beta_r}{\beta_r}\right) + R_E I_B . \tag{2.82}$$

When we take the derivative of the collector voltage with respect to the base current, the emitter resistance is determined from the slope of the V_{CE}-I_B curve. In general, the R_E value will decrease as function of I_B. If it has reached a plateau, the value of R will

be the emitter resistance. Although it is a simple way to extract emitter resistance, it has the disadvantage such that it has to extract R_E for very high currents where the self-heating effect is pronounced. When the emitter resistance is current dependent, this might not be the value one would like to have. Both Incecik [39] and Park [40] proposed to use the corrected V_{CE}-I_B curve to extract the series resistance. However, Incecik's approach involves intensive numerical iteration while Park's method does not take into account the error induced due to high current self-heating effect.

As can be seen from the above discussion to extract the emitter and collector resistance accurately, the thermal resistance has to be determined first. At present, most junction temperature measurement methods rely on either optical IR thermometry or the pulse measurement equipment [41]. These equipments are costly and are not easily available to practicing engineers. Dawson *et al*. [42] proposed a method to extract the steady-state thermal resistance, which is based on the variation of the temperature-dependent β or V_{BE}. It requires the DC I-V measurements of at least two temperatures. Bovolon *et al*. [43] presented an alternate approach of determining the thermal resistance using various operating points. Other methods [44] need to control the substrate temperature using the thermal chuck. In [45], an elegant method is described to extract the thermal resistance requiring only the DC I-V curves at room temperature. However, it still needs to determine two DC model parameters beforehand.

In this section, we present a method to extract the series emitter and collector resistance based on the corrected DC output characteristics from floating terminal measurements. This method is simple and self-consistent; it can produce accurate emitter and collector resistance value without any numerical iteration. As a first condition to accurately determine the HBT series resistances, we first present a novel

approach to extract the thermal resistance using only the DC I-V characteristics measured at room temperature. For the reliable extraction of thermal resistance, only one model parameter has to be determined. This method is simple and robust, and it can produce accurate thermal resistance that is comparable to the conventional method [43]-[45]. The thermal resistance values calculated using our method are verified by extensive measurements on a variety of BJT/HBT devices.

2.4.1 New Extraction Method for Thermal Resistance

For the bipolar transistor, the increase in DC device temperature is solely determined by the thermal resistance and power dissipation. Mathematically, this is expressed as follows:

$$\Delta T = R_{th}\Delta P_{diss}, \tag{2.83}$$

where ΔT is temperature rise for the base-emitter junction, R_{th} is thermal resistance and ΔP_{diss} is the dissipation power. As a first order approximation, one can assume $\Delta P_{diss} = \Delta I_c V_{ce}$.

Based on the constant emitter current assumption, another useful formula, which relates the temperature rise with voltage change in the junction, is given in [42] and [46]:

$$\alpha = -\frac{\frac{nE_g}{q} - V_{junc}}{T}, \tag{2.84}$$

where $\alpha = \frac{\Delta V_{junc}}{\Delta T}$ is the emitter junction voltage temperature coefficient, ΔV_{junc} is the Base-Emitter (B-E) junction voltage change, V_{junc} is the Base-Emitter junction conduction voltage, n is the ideality factor for Base-Emitter forward current, and E_g

is the energy gap. For most bipolar transistors, *n* is always taken as $n = 1$, and E_g is given as 1.42 eV for GaAs at $T = 300$ K and 1.12 eV for Silicon at $T = 300$ K.

Substituting ΔT from (2.83) into (2.84) yields

$$R_{th} = -\frac{\Delta V_{junc} \cdot T}{\Delta P_{diss}\left(\frac{nE_g}{q} - V_{junc}\right)}. \tag{2.85}$$

At extreme temperatures, the emitter junction voltage temperature coefficient α deviates from a constant approximately over a large temperature range.

Based on the above assumptions, we can extract R_{th} using equation (2.85) from DC characteristics at a single temperature. After determining the ideality factor n from the forward Gummel plot, the DC I-V characteristics can be obtained using the constant base current bias. As the base current is increased, the self-heating effect becomes more significant than at lower base current level. Thus, the self-heating leads to the voltage change in the B-E junction. Our proposed method can be further illustrated as follows. Referring to Figure 2.15, this device is a homojunction silicon bipolar transistor with emitter dimensions 2um × 10um. From Figure 2.15(a) and 2.15(b), we have V_{BE}=0.894 V at V_{CE}=0.4 V, V_{BE}=0.8676 V at V_{CE}=4 V, I_C=12.31 mA at V_{CE}=0.4 V and I_C=17.73 mA at V_{CE}=4 V. With V_{junc} =810 mV and n =1, the gradient $\frac{\Delta V}{\Delta T}$ is observed to be $\frac{\Delta V}{\Delta T} = -1.033$ mV/^oC. The junction temperature rise, ΔT, can thus be calculated to be 25.55 ^oC from equation (2.84). Using equation (2.85), thermal resistance R_{th} is evaluated to be 610 ^oC/W.

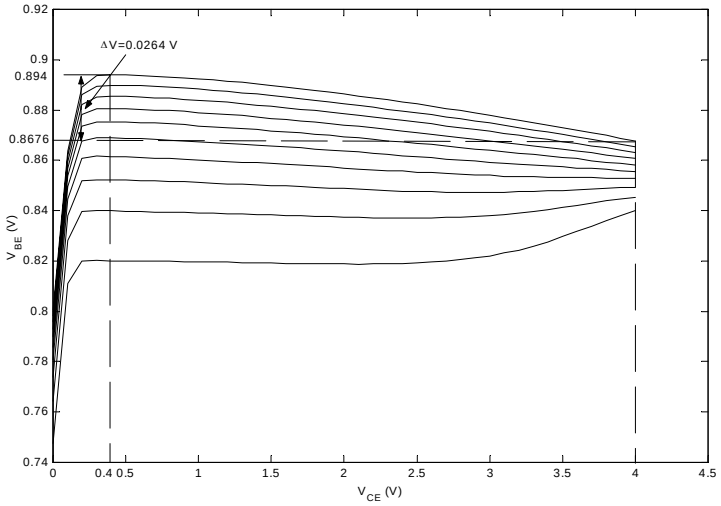

Figure 2.15(a) Device output characteristics (for different I_B input) showing self-heating effects of a homojunction silicon bipolar device from Philips Inc.

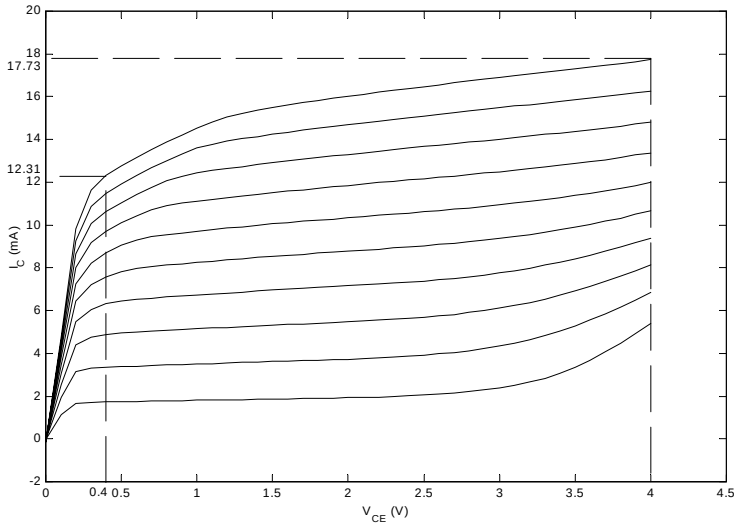

Figure 2.15(b)
Figure 2.15(b) Device I-V curves for different I_B input.

2.4.2 Experimental Verification on the Thermal Resistance Determination

Three types of BJT/HBT devices are selected for verification purposes. They include the GaAs HBT DC I-V characteristics data provided by reference [42], a pure silicon bipolar transistor from Philips Inc., and lastly, a SiGe HBT furnished by IBM. The IBM SiGe HBTs were fabricated using a self-aligned, epitaxial-base technology [47].

For each device, the thermal resistance is determined using equation (2.85). For the GaAs HBT device, using the proposed approach, the thermal resistance is extracted to be 106.88 ^{o}C/W. Compared with the results provided in [42], an error of less than 0.23% relative to the two-temperature method is achieved. Figure 2.16 shows the DC measurement data from reference [42] and, for the comparison purpose, Table 2.1 lists the extracted values of R_{th} using the proposed method and from the two-temperature method [42].

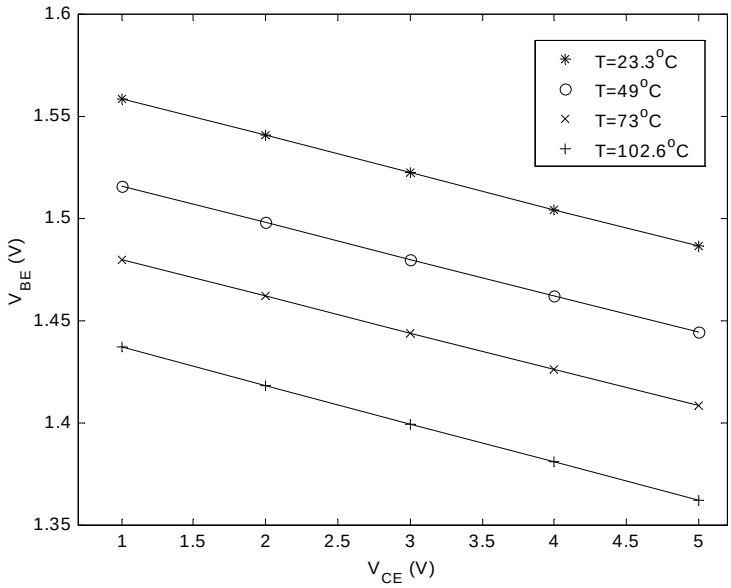

Figure 2.16(a) V_{BE} vs. V_{CE} for GaAs HBT device after [42]

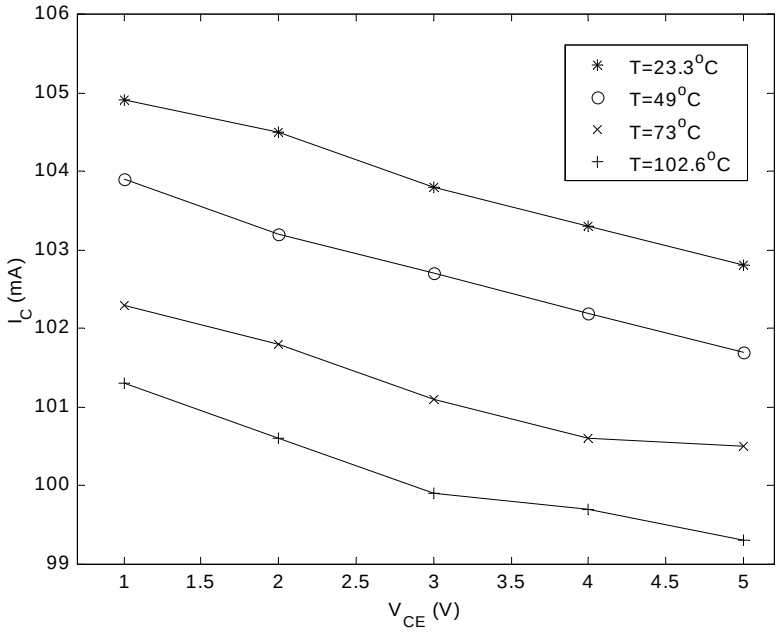

Figure 2.16(b) I_C vs. V_{CE} for GaAs HBT device after [42].

TABLE 2.1 Comparison of Extracted R_{th} Values

Temperature (^oC) / R_{th} Value	T=23.3	T=49	T=73	T=102.6
R_{th} from our method ($^oC/W$)	106.88	106.43	107.49	114.81
R_{th} from [42] ($^oC/W$)	106.63			

Figure 2.17 illustrates both the measured device output characteristics and simulation results of the SiGe HBTs. The extracted value of R_{th} using proposed method is 500.7 ^oC/W and the extracted value from the two-temperature method is about 500 ^oC/W. We also compare the results taken from pulsed *I-V* measurements with 1% duty circle of pulsed V_{BE}. Excellent agreement is still obtained. In Figure 2.18, the extracted values of R_{th} show good agreement compared to the results taken from the isothermal measurements [48]. The RMS error obtained is less than 0.35%.

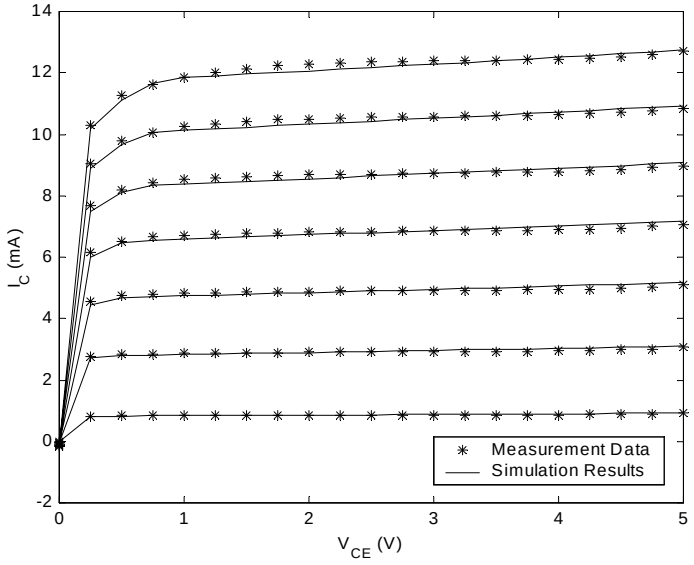

Figure 2.17(a) I-V curves of SiGe HBT device from IBM with emitter= $0.5\ \text{um} \times 40$ um

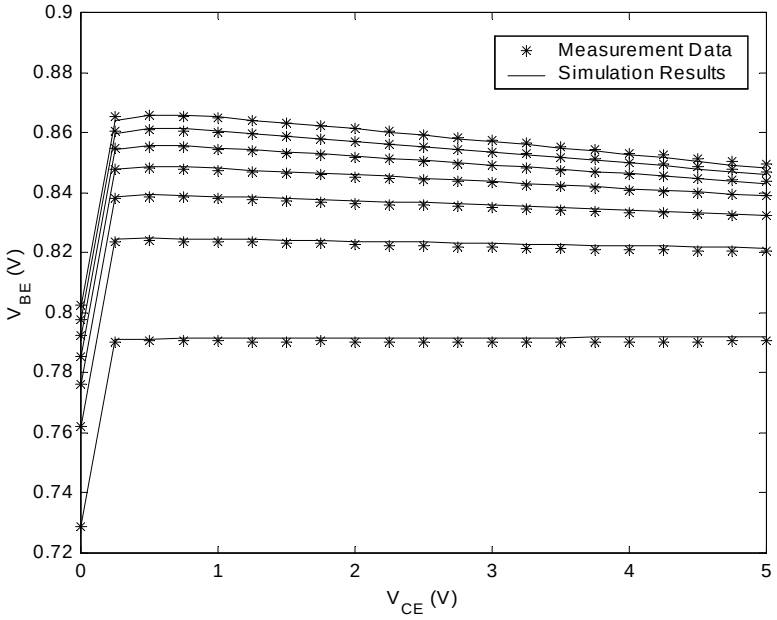

Figure 2.17(b) Both measured data and simulation results of device output characteristics showing self-heating effects.

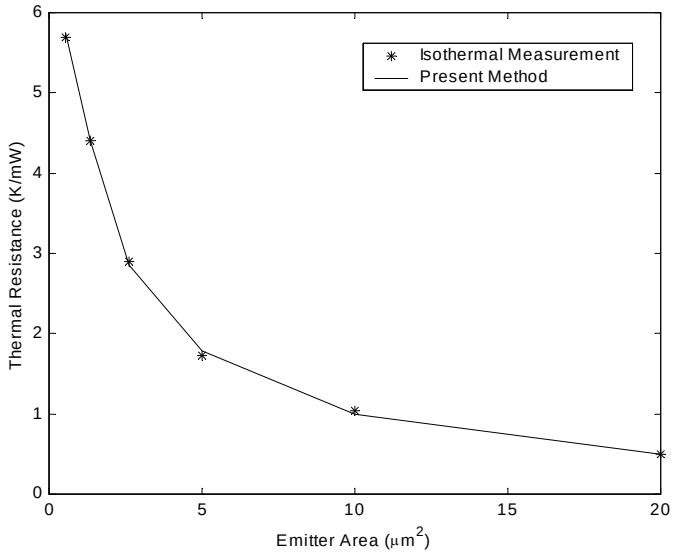

Figure 2.18: Thermal resistance versus emitter area for SiGe HBT device from IBM.

2.4.3 Self-heating Effect on the Extraction of Series Resistance from Flyback Measurement

During the flyback measurement, the HBT device is in the saturated region of operation, the base current I_B is given as follows:

$$I_B = I_S\left[\frac{1}{\beta_F}\left(\exp(qV_{BE}^{'}/n_F kT)-1\right)+\frac{1}{\beta_R}\left(\exp(qV_{BC}^{'}/n_R kT)-1\right)\right], \tag{2.86}$$

where the $V_{BE}^{'}$ and $V_{BC}^{'}$ are intrinsic voltages. Taking into account the voltage drop due to the series resistance, the intrinsic B-E junction voltage $V_{BE}^{'}$ is related to the terminal voltage V_{BE} by the following relation:

$$V_{BE}^{'} = V_{BE} - I_B R_B - (I_C + I_B)R_E\,. \tag{2.87}$$

In the flyback measurement, the collector current I_C is kept zero, thus the above relation is simplified as

$$V_{BE}^{'} = V_{BE} - I_B(R_B + R_E)\,. \tag{2.88}$$

Assuming constant junction temperature, the variation of base current with B-E voltage can be found by

$$dV_{BE}/dI_B = \frac{n_F kT}{q}\frac{\beta_F}{I_S + \beta_F I_B} + R_B + R_E . \tag{2.89}$$

However, when the self-heating effect is pronounced, the equation (2.89) does not hold, so we must take the derivative of B-E voltage with respect to the base current under temperature change condition

$$dV_{BE}/dI_B = \left(dV_{BE}/dI_B\right)_T + \left(dV_{BE}/dT\right)_{I_B}\frac{dT}{dI_B}, \tag{2.90}$$

where the first term of (2.90) is equation (2.89). The second term of (2.90) is derived as the following

$$\left(dV_{BE}/dT\right)_{I_B}\frac{dT}{dI_B} = \alpha R_{th} V_{BE} . \tag{2.91}$$

Since the α factor is with minus sign, the actual value of emitter resistance is expected to be higher than that extracted from conventional flyback measurement. The above derivation can also be applied to analyze the collector extraction from flyback measurement. It can be shown that the self-heating effect results in the increase of the collector resistance.

The above analysis shows the tendency of series emitter and collector resistance values against base current remain unchanged but shifted by an amount of $\alpha R_{th} V_{BE}$ and $\alpha R_{th} V_{CE}$, respectively.

2.4.4 Improved Extraction Method and Experimental Result

Since both emitter resistance and collector resistance have to be extracted at high current region, the thermal resistance R_{th} must be determined first. Once the R_{th}

is known, we may correct the V_{BE} value using equation (2.90) or (2.91). From the corrected V_{CE} against I_B curve, we are able to extract the R_E and R_C by eliminating the self-heating effect.

To verify the proposed method, a SiGe HBT device is used to extract the series emitter and collector resistances. The thermal resistance R_{th} is about 610K/W extracted from the method discussed in last section. Figure 2.19 shows the DC output characteristics of R_E flyback measurement. Figure 2.20 shows the extraction results obtained from the proposed method of equations (2.90) and (2.91) and the conventional method of equation (2.82).

As shown in Figure 2.19, the corrected V_{CE} voltage deviates from the measurement values gradually as the base current goes progressively higher, indicating the voltage drop due to the device self-heating. Consequently, as shown in Figure 2.30, the R_E value of 3.1 Ohms extracted from the corrected data is higher than the value of 2.4 Ohms extracted from the conventional method in equation (2.82). We can see that the self-heating effect leads to 29% error in the emitter resistance extraction. Figures 2.21 and 2.22 show the measurement data for collector resistance extraction and comparison with the conventional method. Similarly, the corrected V_{EC} is lower than the real measurement data, which in turn causes a lower R_C value of 3 Ohms, compared to the uncorrected value of 3.8 Ohms. The self-heating effect leads to 21% error in the collector resistance extraction. In conclusion, the conventional flyback method underestimates the emitter resistance and overestimates the collector resistance due to the device self-heating effect at high base current.

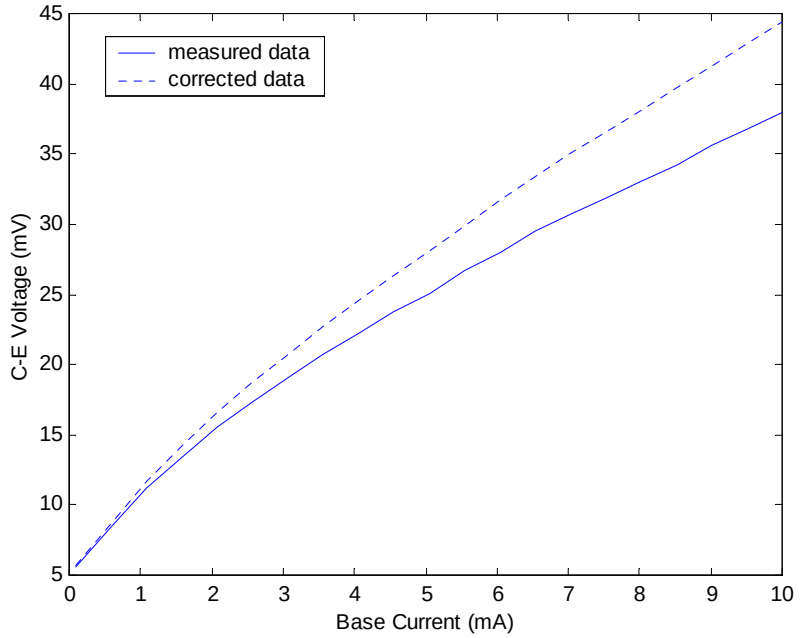

Figure 2.19. Typical measured V_{CE} versus I_B for I_C=0.

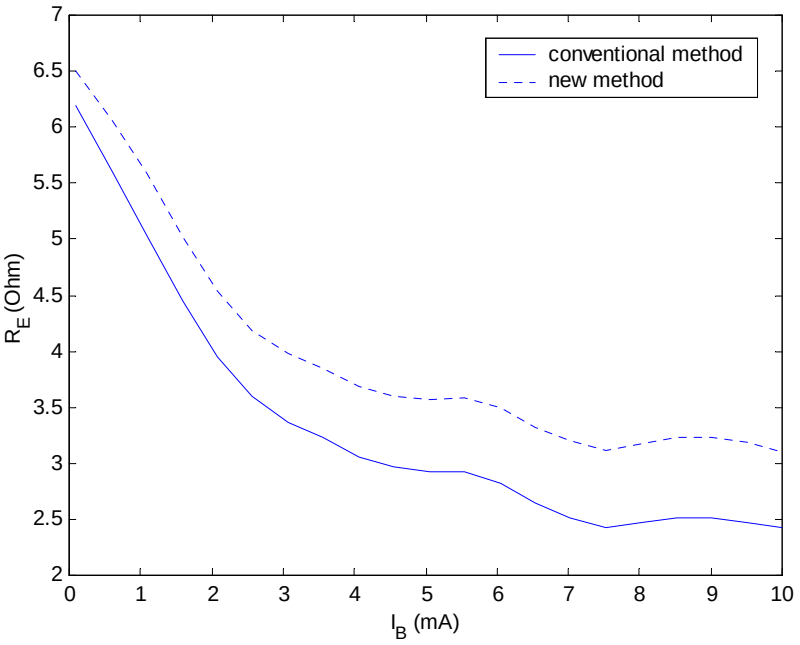

Figure 2.20. Comparison with conventional method of emitter resistance extraction.

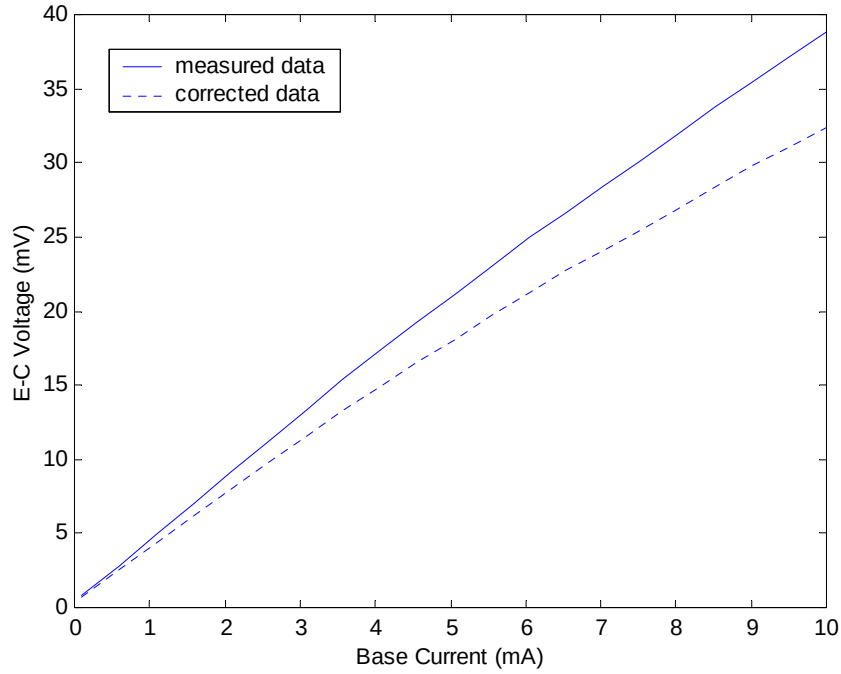

Figure 2.21: Comparison of measured characteristics with corrected characteristics.

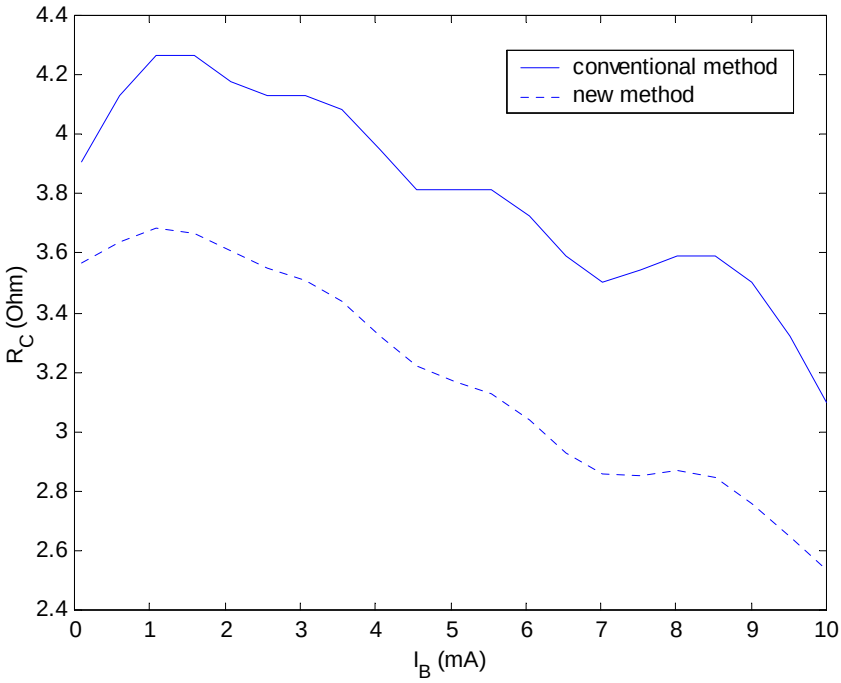

Figure 2.22. Comparison with conventional method of collector resistance extraction.

2.5 Experimental Verifications and Discussions

To verify the parameter extraction method presented in this chapter, one SiGe HBT device is used in this study. The device under test has emitter area of 0.5 × 40 μm^2. The cutoff frequency f_t and maximum oscillation f_{max} are 50 GHz and 47 GHz, respectively. For the studied HBT device, S-parameters have been calculated for different bias points which cover bias for normal operation. For better comparison, the simulation results are plotted in both the Smith Chart and linear plot. The calculated data agrees well with measured data as can be seen in the Figure 2.23.

Two approaches are used to calculate the HBT equivalent circuit elements. One is analytical approach in Section 2.2 and the other is optimization of fitting two reference planes in Section 2.3. As mentioned earlier, an objective function of l_2-norm is recommended for the internal plane due to the necessity to calculate derivatives. Tables 2.2 and 2.3 show the parameter values extracted at two different bias points using different methods. Figure 2.23 shows the comparison between measured and modeled S-parameters. Figures 2.24 and 2.25 show the magnitude and phase of S_{21} comparison.

As we can see from Figure 2.23, multi-plane data fitting approach gives excellent agreement between measured data and modeled results while the analytical approach show reasonable agreement to the measurement results. For the analytical approach, S_{21} of Figure 2.23 gives seemingly good agreement. However, when it is plotted directly versus frequency as shown in Figures 2.24 and 2.25, the derivation can be readily seen, especially at high frequency range.

From Tables 2.2 and 2.3, it can be seen that the emitter resistance value is not constant for different bias points. In addition, the R_E values extracted from the S-parameters and the proposed flyback method are listed for comparison. This clearly

shows the self-heating effect on the extraction of R_E.

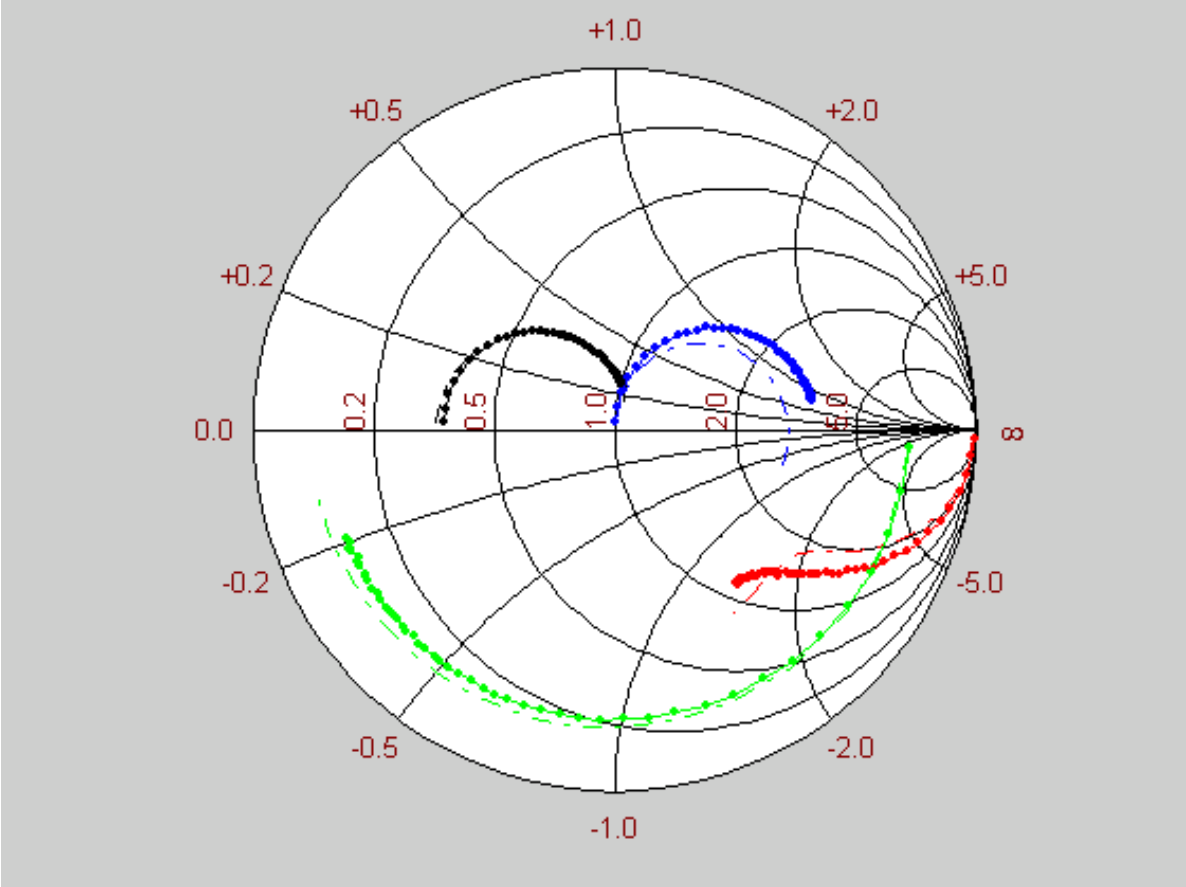

Figure 2.23 Comparison between modeled and measured S-parameters (I_b =60 μA, V_{CE}=3 V, frequency 0.05-10 GHz): dot line: measured data; solid line multi-plane fitting approach, dashed line analytical approach.

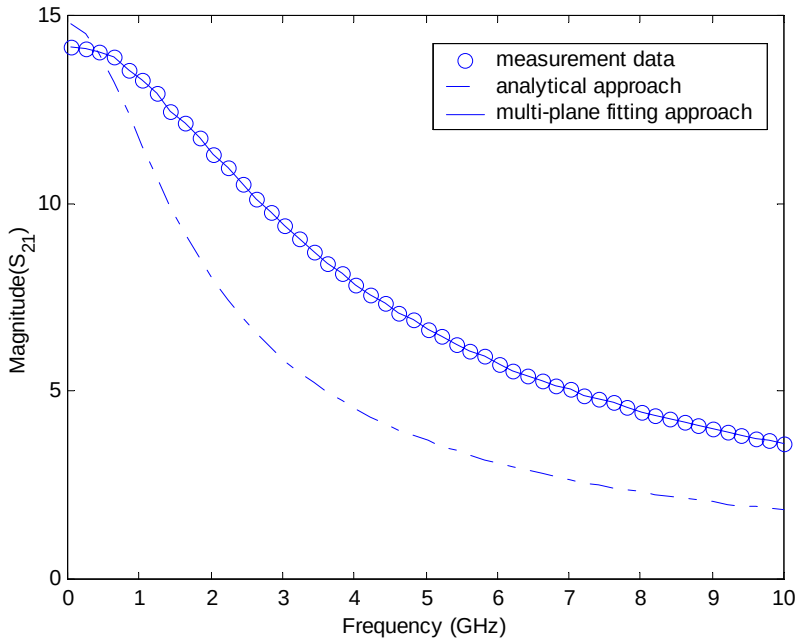

Figure 2.24 Comparison of magnitude of S_{21} between modeled and measured S-parameters (I_b =60 μA, V_{CE}=3 V, frequency 0.05-10 GHz).

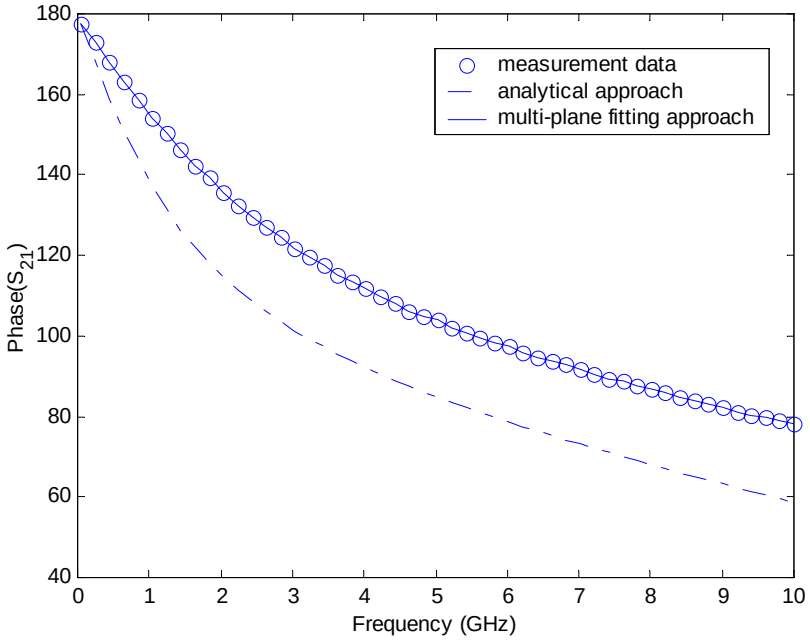

Figure 2.25 Comparison of phase of S_{21} between modeled and measured S-parameters (I_b =60 μA, V_{CE}=3 V, frequency 0.05-10 GHz).

TABLE 2.2 Comparison of Extracted HBT Small-Signal Parameter Values (I_b=60 μA, V_{CE}=3 V)

	Analytical Approach	Multi-plane Fitting Approach
L_c (pH)	25.55	23.2
L_b (pH)	21.37	19.7
L_e (pH)	5.28	6.32
C_p (fF)	64	71
R_c (Ohm)	2.396	2.702
R_b (Ohm)	1.413	0.789
R_e (Ohm)	1.512	1.78
R_{bb} (Ohm)	1.831	1.632
r_π (Ohm)	665	713
C_π (fF)	379	432

C_μ (fF)	107	113
C_{bc} (fF)	42	31
τ (ps)	2.483	2.118
g_{m0} (S)	0.132	0.157
R_e (Ohm) (from flyback method)	1.87	

TABLE 2.3 Comparison of Extracted HBT Small-Signal Parameter Values (I_b=110 μA, V_{CE}=3 V)

	Analytical Approach	Multi-plane Fitting Approach
L_c (pH)	25.55	23.2
L_b (pH)	21.37	19.7
L_e (pH)	5.28	6.32
C_p (fF)	64	71
R_c (Ohm)	2.04	2.012
R_b (Ohm)	1.413	1.203
R_e (Ohm)	1.14	1.741
R_{bb} (Ohm)	1.514	1.672
r_π (Ohm)	557	684
C_π (fF)	402	371
C_μ (fF)	123	102
C_{bc} (fF)	45	56
τ (ps)	1.903	1.724
g_{m0} (S)	0.41	0.38
R_e (Ohm) (from flyback method)	1.87	

Chapter 3

Modeling HBT Using the Contour-Integral and Multi-Connection Methods

3.1 Introduction

As discussed in the previous chapter, accurate determination of the HBT parasitic inductance and resistance is very important as the parasitic element values not only affect the extraction of intrinsic elements but also determine the input and output matching of the circuit. This eventually also affects the noise figure and maximum gain of the amplifier. Chapter 2 proposed a modified floating terminal method to extract the parasitic resistance by eliminating the thermal effect. To determine the parasitic inductance values, both the analytical approach and optimization approach discussed in Chapter 2 can be adopted. However, as we know, measurement-based methods all suffer from one drawback as S-parameter measurements always have some uncertainties [49] [50] due to the limitations of the measurement systems and human errors. The full-wave EM analysis can offer accurate S-parameters, but it is often time-consuming and possesses great difficulties in simulating the HBT intrinsic device. As such, the planar circuit approach to extract the parasitic inductance and model the HBT device is proposed. This chapter

discusses the analysis and modeling of the HBT devices by the planar circuit approach, e. g., the contour-integral method and the multi-connection method.

The concept of a planar circuit was introduced by Okoshi and Miyoshi [51] as an approach to analyze microwave integrated circuits. The planar circuit approach can be used to characterize a number of microwave integrated circuit components, basically in stripline [52] or microstrip configuration, which typically has one dimension, normally the substrate thickness is much smaller than the operating wavelength.

The planar circuit approach was originally derived based on the stripline configuration. However, for the HBT device, the emitter strip can only be treated as a microstrip configuration with no upper dielectric material present. With reference to the microstrip component, it should be observed that it can be approximately considered as a planar circuit, as the electromagnetic field is not entirely confined to the substrate region but, particularly near the edges of the metallization, extends into air outside the dielectric substrate. In other words, the presence of stray fields makes the planar-circuit concept not rigorously applicable to microstrip components. Nonetheless, as discussed in this part of the work, provided suitable modifications in terms of effective parameters are made, planar circuit models provide accurate enough characterizations of microstrip circuits.

Due to the advantages of the planar circuit approach, several new components have been designed, such as 3-dB hybrid circuits [53], circulators [54] and Ferrite resonators [55]. Circular polarization in microstrip antennas was also obtained by exciting two degenerate orthogonal modes in a planar structure [56].

As will be shown in Section 3.2, for those components with regular shapes (i.e., the HBT device with one emitter finger falls into this group.), the Green's function approach offers an accurate and fast calculation of the impedance. However, for

components with arbitrary shape (i.e., the HBT device with multi-finger falls into this group.), the equivalent circuit parameters can be derived from the contour-integral and/or the segmentation method [57]-[59]. In the contour-integral method, the wave equation is first converted to an integral equation along the circuit periphery. Thus, the required computation time is reduced appreciably, as compared with other methods in which the field must be solved over the entire area of the circuit [60].

3.2 Modeling One-Finger HBT Device by Resonant-Mode Technique

To apply the planar circuit approach to extract the HBT parasitic inductance, the emitter of one-finger HBT device may be treated as a rectangular microstrip resonator with dimensions $a \times b$, where a and b being the emitter width and length, respectively. Therefore, the ortho-normalized eigenfunction satisfying the boundary conditions can be obtained by the resonant-mode expansion technique [61] as follows

$$\Phi_{mn}(x,y) = \frac{\varepsilon_m \varepsilon_n}{\sqrt{ab}} \cos(k_{xm}x)\cos(k_{ym}),$$

$$k_{xm} = m\pi/a \ , \ k_{yn} = n\pi/b, \tag{3.1}$$

$$\varepsilon_m = \begin{cases} 1 & (\text{for m} = 0) \\ \sqrt{2} & (\text{for m} \neq 0) \end{cases} \qquad \varepsilon_n = \begin{cases} 1 & (\text{for n} = 0) \\ \sqrt{2} & (\text{for n} \neq 0) \end{cases},$$

where ε_m and ε_n are coefficients to make ϕ_{mn} satisfy the normalizing condition. The above equation leads directly to a Green's function [62]

$$G(x,y \mid x_0,y_0) = \frac{j\omega\mu d}{ab} \sum_{m=0}^{\infty} \sum_{n=0}^{\infty} \frac{\cos(k_{xm}x_0)\cos(k_{yn}y_0)}{k_{xm}^2 + k_{yn}^2 - k^2} \times \cos(k_{xm}x)\cos(k_{yn}y) \tag{3.2}$$

From the planar circuit principle [51], the input impedance Z_{in} of the one-port rectangular circuit, as shown in Figure 3.1, can be written as

$$Z_{in} = \sum_{m=0}^{\infty} \sum_{n=0}^{\infty} \frac{j\omega\mu d\varepsilon_m^2 \varepsilon_n^2}{ab(k_{xm}^2 + k_{yn}^2 - k^2)} (\cos k_{xm} T)^2 \left(\frac{\sin k_{xm} W/2}{k_{xm} W/2} \right)^2 \tag{3.3}$$

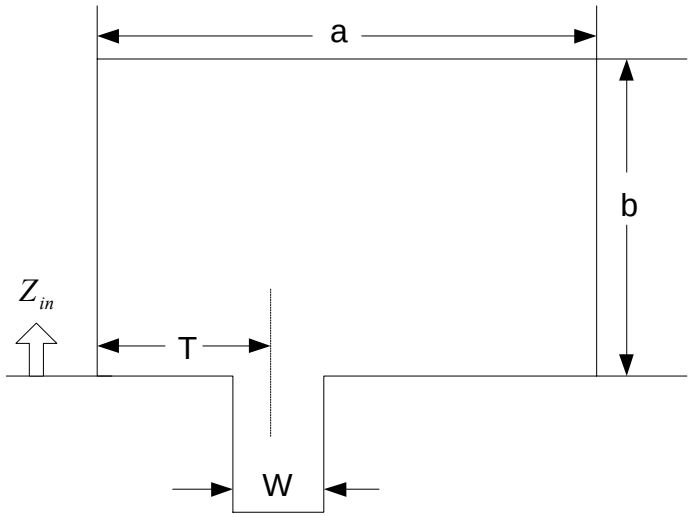

(a)

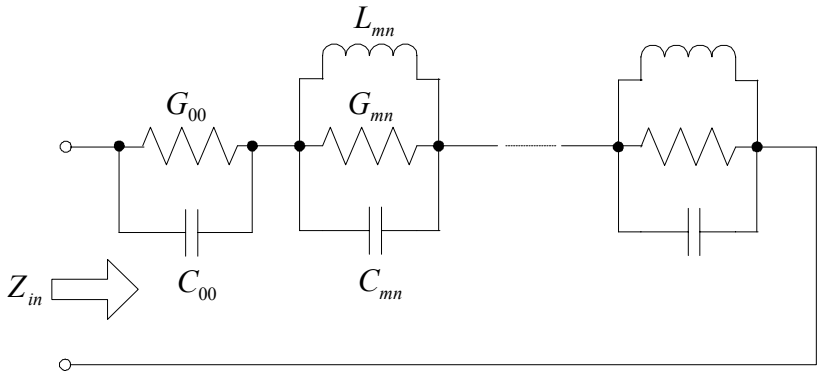

(b)

Figure 3.1 One-port planar resonator and its equivalent circuit: (a) one-port rectangular resonator, (b) equivalent circuit of one-port planar resonator.

If the circuit loss is taken into account, equation (3.3) can be re-written as

$$Z_{in} = \sum_{m=1}^{\infty} \sum_{n=1}^{\infty} \frac{1}{j\omega C_{mn} - j(1/\omega L_{mn}) + G_{mn}} + \frac{1}{j\omega C_{00} + G_{00}} \tag{3.4}$$

In the above expression, the second term $(j\omega C_{00} + G_{00})^{-1}$ stems from the mode with m=n=0. This mode corresponds to the charging and discharging of the static

capacitance of the circuit. Parameters C_{00} and G_{00} express the static capacitance and the associated dielectric loss, and are given below

$$C_{00} = \varepsilon ab / d \,, \tag{3.5}$$

$$G_{00} = C_{00}(\tan\delta + r/d) \,, \tag{3.6}$$

where r is the skin depth of the conductor.

Equation (3.4) shows that the equivalent circuit representing the input impedance is given, as shown in Figure 3.1(b), by a series connection of a number of parallel resonant circuits corresponding to each mode including the zero-frequency resonance (m=n=0). Parameters C_{mn}, L_{mn} and G_{mn} in equation (3.4) directly give the equivalent circuit parameters in each resonance circuit. These parameters can be computed in terms of geometrical parameters by using equation (3.4) as follows

$$f_{mn} = \frac{\sqrt{(m/a)^2 + (n/b)^2}}{2\sqrt{\varepsilon\mu}} \,, \tag{3.7}$$

$$C_{mn} = \frac{\varepsilon ab}{\varepsilon_m^2 \varepsilon_n^2} \cdot \frac{1}{\cos^2(k_{xm}T)} \cdot \frac{1}{F} \,, \tag{3.8}$$

$$L_{mn} = \frac{\varepsilon_m^2 \varepsilon_n^2 \mu d \cos^2(k_{xm}T)}{2ab[(m\pi/a)^2 + (n\pi/b)^2]} F \,, \tag{3.9}$$

$$G_{mn} = 2\pi f_{mn} C_{mn} / Q_0 \,, \tag{3.10}$$

$$F = \left(\frac{\sin(k_{xm}W/2)}{k_{xm}W/2} \right)^2 \,, \tag{3.11}$$

$$Q_0^{-1} = Q_d^{-1} + Q_c^{-1} \,, \tag{3.12a}$$

$$Q_d = 1/\tan\delta \,, \tag{3.12b}$$

$$Q_c = d/r \,. \tag{3.12c}$$

The equivalent circuit of a planar resonator in Figure 3.1(b) suggests that when the resonance frequencies are widely separated and the Q factor of the resonance is relatively high, the circuit characteristics in the vicinity of a resonant frequency can be expressed approximately in terms of a set of L, C and G.

However, for microstrip-type circuit, it has been shown [63]-[64] that the dynamic properties of the microstrip (including higher order modes) can be approximated by a planar waveguide model. This is a waveguide with lateral magnetic walls, having the same height d as the substrate thickness. The width w_e and the permittivity ε_e of the filling dielectric are determined by the conditions that both the phase velocity and the characteristic impedance have to be the same as for the microstrip line. As the dominant mode of the planar waveguide is a TEM mode, the equality of the phase velocities imposes that the filling dielectric has the same effective permittivity ε_e of the quasi-TEM mode of the microstrip line. Therefore, it is reasonable to extend the planar circuit model to the case of two-dimensional microstrip circuits with effective dimensions and an effective permittivity [65]. The effective permittivity is used to account for the electric-field lines being more or less confined to the substrate material and therefore, it depends on the electric-field distribution along the edge of the planar element. Considering the EM field as the superposition of the resonant modes of the structure, it is evident that a different effective permittivity should be ascribed to resonant modes having a different field distribution along the periphery of the circuit. Wolff and Knoppik have developed a theory [66] for computing the resonant frequencies of circular and rectangular microstrip resonators using a planar model. This model is characterized by effective dimensions and effective permittivities which depend on the resonance mode; it can

be used in conjunction with the resonant-mode technique to determine the parameters of the equivalent circuit.

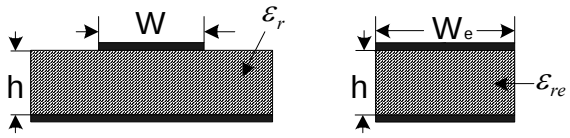

Figure 3.2 Planar waveguide model for a microstrip line.

Therefore, to calculate the capacitance value, the effective width and effective length, given by Wheeler [67], must be used. For the microstrip resonator with narrow strip geometry, the fringing capacitance must also be taken into account. Therefore, the equation (3.8) can be replaced with the following expression [65]

$$C_{0,dyn} = \frac{C_{0,stat}}{\xi\zeta} \tag{3.13}$$

where

$$\xi = \begin{cases} 1, \text{ for m} = 0 \\ 2, \text{ for m} \neq 0 \end{cases}$$

and

$$\zeta = \begin{cases} 1, \text{ for n} = 0 \\ 2, \text{ for n} \neq 0 \end{cases}.$$

In practical applications, only a finite number of resonance circuits are to be included in the equivalent circuit; such a number depends on the frequency range of interest and on the approximation required. In a low-frequency approximation [68], only the first two resonant modes can be taken into account, i.e., the static mode resonating at zero frequency and the first higher mode. For the HBT device studied, the peak f_t is at 50 GHz thus only two cells can give satisfied result. However, as the

scaling down of the HBT device, more cells are needed to be included to improve the accuracy.

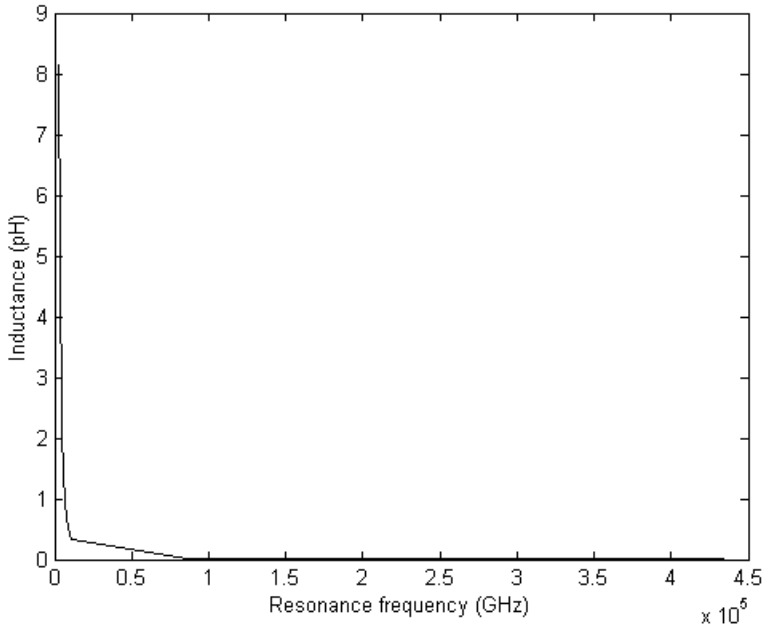

Figure 3.3 Extracted inductance versus resonance frequency.

A single emitter SiGe HBT device is selected to verify the above analysis. The emitter is of dimension of 0.5 x 40 μm^2. The substrate thickness is 0.8 μm. The inductance value is calculated using equations (3.7)-(3.13) and shown in Figure 3.3.

As shown in Figure 3.3, the inductance value is 8.17 pH at the lowest resonance frequency 2173 GHz. The inductance value drops sharply after the first resonance. The inductance at the lowest resonance frequency dominates the total inductance value, thus justifies the above statement. Compared the inductance value 6.32 pH calculated and optimized from measured S-parameters shown in Table 2.2, the inductance value extracted from the resonance-mode technique is a very good initial value for the overall optimization of the S-parameters.

The above analysis and calculation demonstrate that an accurate characterization of a two-dimensional microstrip circuit and extraction of equivalent circuit element

can be achieved through an effective planar circuit model in conjunction with the resonant-mode technique, provided a suitable effective permittivity and effective dimensions account for the reactive energy associated with fringing field of the corresponding mode.

3.3 Contour-Integral Approach to the Modeling Multi-Finger HBT Device.

The method in the above section is only valid for simple emitter geometry, e.g. rectangular, as the Green's function is available. For the multi-finger HBT device, however, the contour-integral method must be employed to calculate the impedance matrix of the equivalent circuit.

The contour integral method is a method that solves the unknown field quantities in the contour integral equation that describes the fields or potential function in the boundary of a defined volume in space. The contour integral method is applied to electromagnetic scattering problems, where the solutions usually are formulated using the integral equation on the surface of the scatters and solved by the method of moments. The boundary element method comes in as a numerical procedure that is used to discretize an integral equation and this method plays the role of the method of moments in the contour integral method in this section.

As a result of the discretization by the boundary element method, a set of matrix equations is formed, for which the unknown potentials on the boundary can be solved by various matrix solvers. The major advantages of the boundary element approach is that

it reduces the formulation of the problem to one dimension, as compared to most formulations in the method of moments and the finite element method.

The accuracy of the boundary element method in solving two-dimensional electromagnetic problems depends on two important factors: the integral equation that describes the field along the periphery of the two-dimensional circuits and the order of the boundary elements used in the discretization process. The first factor is essential in obtaining a rigorous formulation of the problem, while the other factor is to improve the accuracy of the potential description of each boundary element. In this section, only the constant boundary element will be considered as that the formulation can be simplified considerably.

The contour integral method of two-dimensional planar circuits usually employs the scalar Green's function for homogenous problems. However, the microstrip circuit is actually an inhomogeneous two-dimensional problem with an air-dielectric interface. As such, there is a need to replace the constitutive parameters in the air and dielectric regions of the original problem, by a set of effective constitutive parameters that fille the entire space in the equivalent problem. Moreover, the physical dimensions of the microstrip lines in the original problem must be replaced by the corresponding equivalent dimensions to account for the fringing effect at the edges. Since the dielectric permeability does not exhibit magnetic properties, the effective permeability is assumed to be that of air. Hence only the effective permittivity and effective dimension are considered in the equivalent problem. With this equivalent concept, the Green's function for two-dimensional homogenous problems is used and is expressed in terms of the Hankel function of the second kind.

Okoshi [51] used the contour integral equation with scalar Green's function in solving stripline planar circuits. He formulated with equivalent voltages and currents on the contour of the planar circuit, discretized using the boundary element method and obtained the impedance Z matrix for the planar circuit.

3.3.1 Derivation of Contour-integral Equation for the Circuit in the Same Plane

Before proceeding to the theoretical development, the assumptions used in the formulation shall be stated. The arbitrary shaped planar circuit is considered as a two-dimensional problem with the following assumptions:

a. The substrate thickness is electrically thin in the x-direction, as shown in Figure 3.4.
b. The conductor on the top surface and ground plane is a perfect electric conductor and the conductor is infinitely thin.
c. The interior of the closed surface is filled by material with an effective permittivity.
d. The perimeter of the planar circuit is bounded by a perfect magnetic wall, except on the segments where coupling ports exist.

The first assumptions are valid in most practical cases for microwave frequencies. Assumptions (c) and (d) are consequences of the fact that the homogeneous Green's function is used.

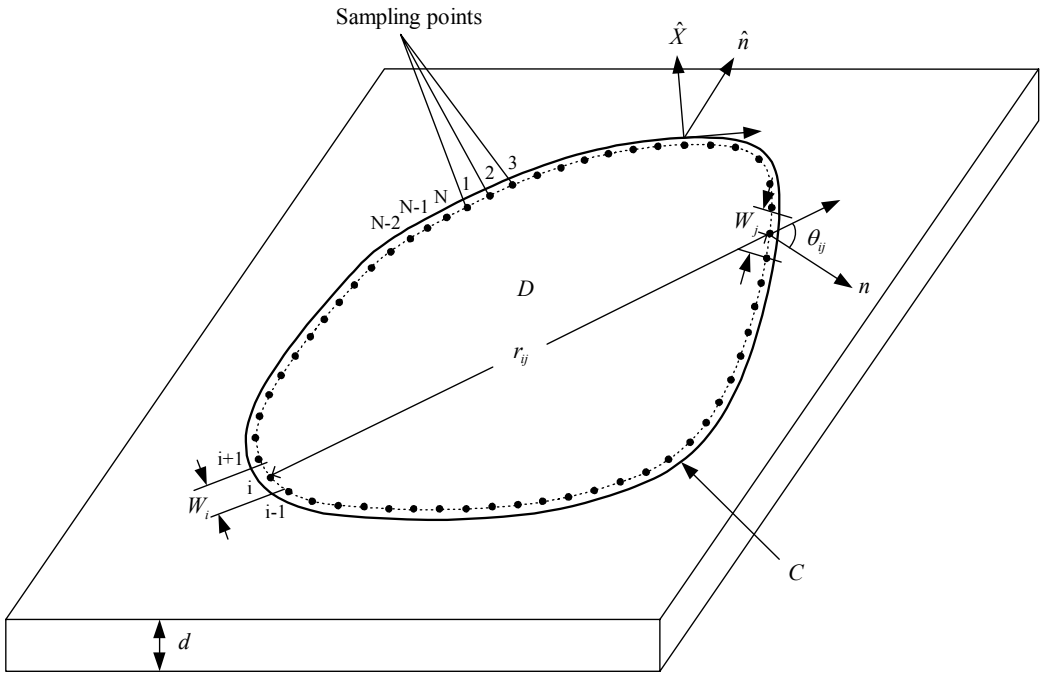

Figure 3.4 Symbols used in the integral equation representation of the wave equation.

In the contour integral method, the wave equation is first converted to an integral equation along the circuit periphery as follows

$$(\nabla_T^2 + k^2)V = 0 \quad (\text{in } D), \tag{3.14}$$

$$\frac{\partial V}{\partial n} = 0 \quad (\text{on } C), \tag{3.15}$$

where C and D denotes the periphery and the region and inside the periphery, as shown in Figure 3.4. In general, RF voltage V is a complex quantity and is analytic in the domain D and on the boundary C. This implies that its derivatives are continuous in the domain and on the boundary.

For two-dimensional problem, a solution of Helmholtz equation (3.14) is given by Green's function for a delta source function

$$(\nabla_T^2 + k^2)G(\bar{r} - \bar{r}') = -\delta(\bar{r} - \bar{r}'), \tag{3.16}$$

where $\delta(\bar{r}-\bar{r}')$ is the Dirac function (delta function), *r* and *r'* are the observation and source points, respectively. Mathematically, the solution of the Green's function is given by

$$G(\bar{r},\bar{r}') = \frac{j}{4}H_0^2(k\,|\,\bar{r}-\bar{r}'\,|), \tag{3.17}$$

where H_0^2 is the Hankel function of the second kind of zero order.

From vector calculus, the Green's formula for two-dimensional problems is given by

$$\int_D (\varphi\nabla_T^2\phi - \phi\nabla_T^2\varphi)dS = \oint_C (\varphi\nabla_T\phi - \phi\nabla_T\varphi)\cdot\hat{n}\,ds, \tag{3.18}$$

where φ and ψ are scalar quantities, *D* and *C* are the surface and boundary of the planar circuit, respectively.

Let $\psi=V$ and $\phi = G(\bar{r},\bar{r}')$ in equation (3.18), and using equations (3.16) and (3.17), it can be shown that

$$V(\bar{r}') = \frac{1}{2j}\oint_c \left[k\cos\theta H_1^{(2)}(k\,|\,\bar{r}-\bar{r}'\,|\,V(\bar{r}) + H_0^{(2)}(k\,|\,\bar{r}-\bar{r}'\,|)\frac{\partial}{\partial n}V(\bar{r})\right]ds, \tag{3.19}$$

and the line current density J_j, flowing into the segment at the coupling port is given by

$$J_j = \frac{1}{j\omega\mu d}\frac{\partial V}{\partial n}. \tag{3.20}$$

To solve equation (3.19) numerically, we divide the circuit periphery into *N* incremental sections numbered as *1*, *2*, …, *N*, having width W_1, W_2, W_3, … W_N, respectively, as illustrated in Figure 3.4. *N* sampling points are set to be at the center of each section. For accurate calculations, the section width is usually taken to be much smaller than $\lambda_g/20$. Therefore, the coupling port occupies two or more sections.

When the magnetic and electric field intensities are assumed constant over each width of these sections, the above integral equation (3.19) can be replaced by the summation over N sections. The resulting expression is given by

$$V_i = \sum_{i=j}^{N} (h_{ij} I_j + u_{ij} V_j), \tag{3.21}$$

where V_i is the voltage over the ith section and I_j $(=J_j W_j)$ is the total current flowing into the jth section.

The matrix elements u_{ij} and h_{ij} for matrices U and H, are given as

$$u_{ij} = \delta_{ij} - \frac{k}{2j} \int_{W_j} \cos\theta H_1^{(2)}(k \mid \bar{r} - \bar{r}' \mid) ds, \tag{3.22a}$$

$$h_{ij} = \frac{\omega \mu d}{2} \int_{W_j} H_0^2(k \mid \bar{r} - \bar{r}' \mid) ds. \tag{3.22b}$$

Solving equation (3.21), the voltage on each sampling point is given as

$$V = U^{-1} H I. \tag{3.23}$$

Therefore the impedance matrix of the equivalent N-port circuit is obtained as

$$Z = U^{-1} H. \tag{3.24}$$

In practice, the coupling ports are connected to only a few of the N sections. Thus, rows and columns corresponding to the sections that are open-circuited can be deleted from the Z-matrix to obtain the impedance matrix.

To calculate the impedance matrix, the equation (3.21) must be numerically evaluated. The Hankel function exhibits a logarithmic singular behavior as the argument of the function goes to zero. This occurs when k equals zero or when source point coincides with the observation point on the boundary. Therefore, the integrals in equations (3.22) must be taken care of when performing the numerical integration.

To solve the case when the source point i coincides with the observation point j, the derivation of u_{ij} and h_{ij} should be treated separately.

a) Evaluation of u_{ij}

From equation (3.22), as the source point approaches the observation point along the element, i. e. $i=j$, the integral involving the Hankel function of the second kind of first order, goes to zero. This can be seen from Figure 3.5. The observation point is located at the center of the element, where the unit normal vector $\hat{n}$ is orthogonal to the element direction. As i approaches to the j along the element, the tangential unit vector $\hat{r}_{ij}$ is always parallel to the element length. As such, the angle θ between $\hat{n}$ and $\hat{r}_{ij}$ is always 90°, which implies that $\cos\theta$ is always zero. Hence, the integrand of the integral for u_{ij} is zero throughout the interval of integration, except at the point $i=j$. However, it is known that the integral of a function that is defined only at one point in the interval of integration is equal to zero. Therefore, it is proven that for $i=j$, $u_{ij}=1$.

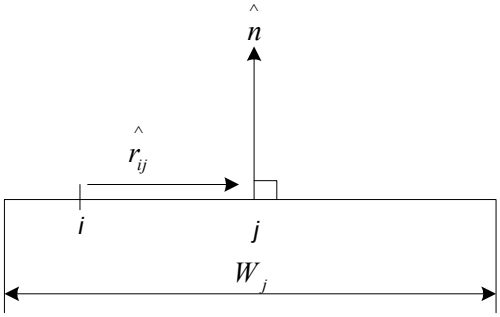

Figure 3.5 Element consideration for u_{ij} at $i=j$.

b) Evaluation of h_{ij}

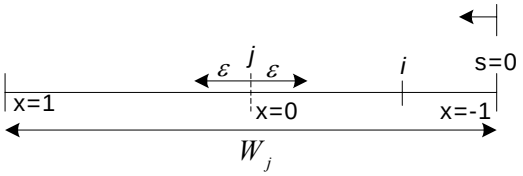

Figure 3.6 Element consideration for h_{ij} at $i=j$.

The element considered here is a straight line as shown in Figure 3.6. This is true for most cases since the contour is appropriately subdivided in segments that are sufficiently small for the assumption of the constant electric field or voltage across that element. Note that the relationship between *s* and *x* is given by

$$s = \frac{W_j}{2}(1+x). \tag{3.25}$$

From equation (3.25), the distance of any point along element *j* with respect to point *i* can be deduced as

$$R = \left|\bar{r} - \bar{r}'\right| = \left|\frac{W_j}{2} - 1\right| = \left|\frac{W_j}{2}x\right|. \tag{3.26}$$

Substitute equation (3.25) and (3.26) into equation (3.22b), we have

$$h_{ij} = \frac{\omega\mu d}{2}\int_{W_j} H_0^{(2)}(k\left|\bar{r} - \bar{r}'\right|)ds = \frac{\omega\mu d}{4}W_j\int_{-1}^{1} H_0^{(2)}(kx\frac{W_j}{2})dx. \tag{3.27}$$

Next, the interval in the vicinity of point *j* is introduced. This integral is required to examine the behavior of the integral as *i* approaches *j*. Hence equation (3.27) can be rewritten as

$$h_{ij} = \frac{\omega\mu d}{2}W_j \lim_{\varepsilon\to 0}\int_{\varepsilon}^{1} H_0^{(2)}(kx\frac{W_j}{2})dx. \tag{3.28}$$

To evaluate the integral in equation (3.28), the following mathematical formulas for Hankel functions and Bessel functions are used:

$$H_0^{(2)}(kx\frac{W_j}{2}) = J_0(kx\frac{W_j}{2}) - jY_0(kx\frac{W_j}{2}), \tag{3.29}$$

where

$$J_0(kx\frac{W_j}{2}) = \sum_{n=0}^{\infty}(-1)^n\frac{1}{(n!)^2}(kx\frac{W_j}{4})^{2n},$$

$$Y_0(kx\frac{W_j}{2}) = \frac{2}{\pi}[\gamma + In(kx\frac{W_j}{2})]J_0(kx\frac{W_j}{2}) + \frac{2}{\pi}\sum_{n=1}^{\infty}(-1)^{n+1}\frac{1}{(n!)^2}(kx\frac{W_j}{4})^{2n}\sum_{r=1}^{n}\frac{1}{r},$$

and γ=0.5772 is the Euler's constant.

Using equation (3.29) into the integral in equation (3.28)

$$\lim_{\varepsilon\to 0}\int_{\varepsilon}^{1} H_0^{(2)}(kx\frac{W_j}{2})dx =$$

$$\sum_{n=0}^{\infty}(-1)^n \frac{1}{(n!)^2 2^{2n}}\lim_{\varepsilon\to 0}\int_{\varepsilon}^{1}(kx\frac{W_j}{2})^{2n}[1-j\frac{2}{\pi}(\gamma+In(kx\frac{W_j}{4})]dx$$

$$+ j\frac{2}{\pi}\sum_{n=1}^{\infty}(-1)^n \frac{1}{(n!)^2 2^{2n}}\sum_{r=1}^{n}\frac{1}{r}\lim_{\varepsilon\to 0}\int_{\varepsilon}^{1}(kx\frac{W_j}{2})^{2n}dx. \qquad (3.30)$$

Equation (3.30) can be evaluated analytically and simplified to the following

$$\lim_{\varepsilon\to 0}\int_{\varepsilon}^{1} H_0^{(2)}(kx\frac{W_j}{2})dx =$$

$$[1-j\frac{2}{\pi}(\gamma+In(kx\frac{W_j}{4})-1)]$$

$$+\sum_{n=1}^{\infty}(-1)^n \frac{1}{(n!)^2 2^{2n}}\frac{1}{2n+1}(kx\frac{W_j}{2})^{2n}\left\{1-j\frac{2}{\pi}[\gamma+In(kx\frac{W_j}{4})-\frac{1}{2n+1}-\sum_{r=1}^{n}\frac{1}{r}]\right\}. \qquad (3.31)$$

It is found through numerical calculations that the contributions to the integral from the terms in the summation series are negligible compared to the first term on the right hand side of equation (3.31). Hence, h_{ij} at $i=j$ is evaluated to be

$$h_{ij} = \frac{\omega\mu d}{2}W_j[1-\frac{2j}{\pi}(In\frac{kW_j}{4}-1+\gamma)]. \qquad (3.32)$$

Summarize the integrals in equation (3.22):

$$u_{ij} = \begin{cases} 1, & \mathrm{i=j} \\ \dfrac{k}{2j}\displaystyle\int_{W_j}\cos\theta H_1^{(2)}(kr)ds, & \mathrm{i\neq j} \end{cases}. \qquad (3.33a)$$

$$h_{ij} = \begin{cases} \dfrac{\omega\mu d}{2}\dfrac{1}{W_j}\displaystyle\int_{W_j} H_0^{(2)}(kr)ds, & \mathrm{i\neq j} \\ \dfrac{\omega\mu d}{2}[1-\dfrac{2j}{\pi}(In\dfrac{kW_i}{4}-1+\gamma)], & \mathrm{i=j} \end{cases}. \qquad (3.33b)$$

The numerical integration of u_{ij} and h_{ij} involves the following integrals:

$$\int_0^{W_j(W_i)} k\cos\theta H_1^{(2)}(k\,|\,\bar{r}-\bar{r}'\,|)dl\,,$$

$$\int_0^{W_j(W_i)} H_0^{(2)}(k\,|\,\bar{r}-\bar{r}'\,|)dl\,.$$

Note that in the above integrals, the integration is carried our along the element length. In this section, the equations for the angle θ and the distance R between the source and the observation points are expressed in terms of the local coordinates of each element.

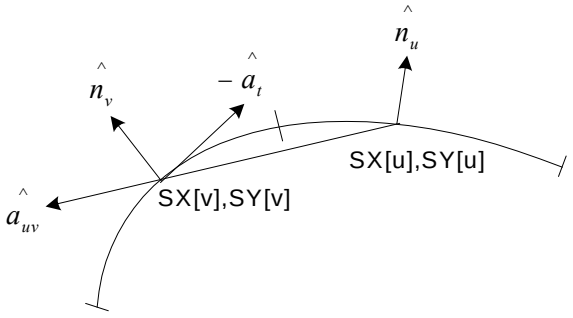

Figure 3.7 Element considerations for integration of u_{ij} and h_{ij}.

Referring to Figure 3.7, the center of the elements, *i* and *j*, are denoted by SX[i] and SX[j], respectively:

$$\text{SX[i]=0.5(X[i+1]-X[i])}$$

$$\text{SY[i]=0.5(Y[i+1]-Y[i]).} \qquad (3.34)$$

For i=*u* or *v*, X[·] and Y[·] are the coordinates at the two ends of each element.

By simple geometrical manipulations, the unit tangential vector of the element *v* can be obtained as

$$\hat{a}_t = \frac{1}{W_v}\{(X[v+1]-X[v])\,\hat{a}_x + (Y[v+1]-Y[v]\,\hat{a}_y\} \qquad (3.35)$$

The unit normal vector to the element is obtained from equation (3.35).

Through a transformation matrix as follows:

$$\hat{a}_n = \begin{pmatrix} 0 & 1 \\ -1 & 0 \end{pmatrix} \hat{a}_t ,$$

$$\hat{a}_n = \frac{1}{W_v}\{X[v+1]-X[v])\,\hat{a}_x - (Y[v+1]-Y[v]\hat{a}_y\}. \tag{3.36}$$

The distance R_{uv} between the middle points of element u and v is given by

$$R_{uv}\,\hat{a}_{uv} = (SX[v]-SX[u])\,\hat{a}_x + (SY[v]-SY[u])\,\hat{a}_y . \tag{3.37}$$

Using equations (3.35) and (3.37), the distance R_{uv} from the middle point of element u to any other point on the element v is

$$\bar{R} = R_x\,\hat{a}_x + R_y\,\hat{a}_y = R_o\,\hat{a}_R + l\,\hat{a}_t \tag{3.38}$$

where R_o is the distance from the middle point of the element u to the starting point of element v. The solutions for R_x and R_y in equation (3.38) are as follows:

$$R_x = (X[v]-SX[u]) + \frac{1}{W_v}(X[v+1]-X[v]),$$

$$R_y = (Y[v]-SY[u]) + \frac{1}{W_v}(Y[v+1]-Y[v]),$$

$$\text{for } 0 \le l \le W_v \tag{3.39}$$

Therefore, the argument R in the Hankel function is given by

$$R = \sqrt{R_x^2 + R_y^2} \tag{3.40}$$

To calculate the angle θ, we make use of the unit vector along the R-direction as follows:

$$\cos\theta = \hat{a}_R \cdot \hat{a}_n$$

$$= \frac{1}{RW_v}\{R_x(Y[v+1]-Y[v]) - R_y(X[v+1]-X[v])\}, \tag{3.41}$$

Equations (3.39)-(3.41) are used in the numerical integration of the Hankel functions for the computation of h_{ij} and u_{ij} using Simpson's rule.

3.3.2 Derivation of Contour-integral Equation for the Circuit in Different Height

Equations (3.19) and (3.41) are only valid for the circuit within the same plane. However, for compound semiconductor process, the HBT fingers are of different height resulting from etching process. Thus equations (3.19) and (3.41) must be modified to account for the RF voltage variations on the periphery due to the different substrate height.

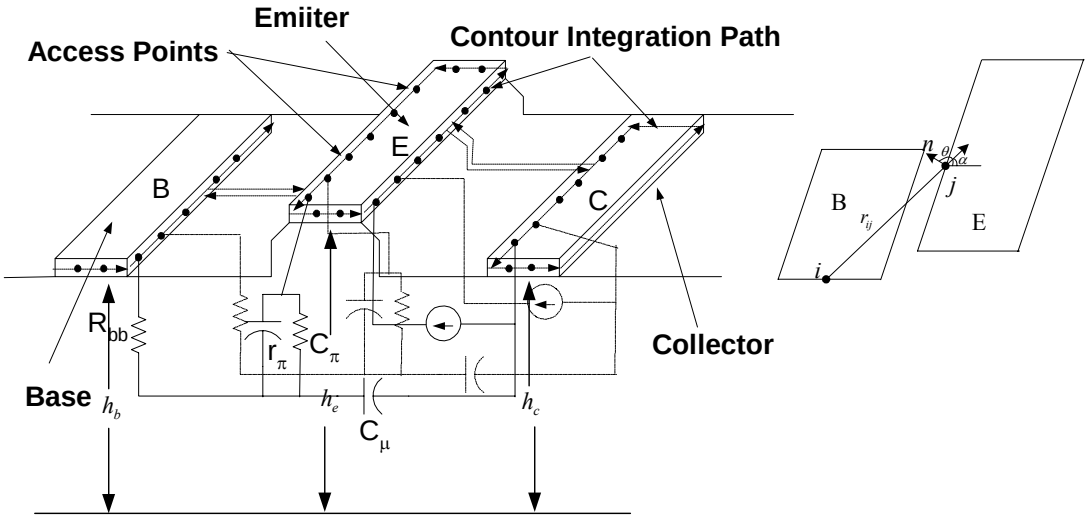

Figure 3.8 HBT device with base, emitter and collector in different height.

For the configuration shown in Figure 3.8, the RF voltage on a point on the periphery can be rewritten as

$$V(\bar{r}') = \frac{1}{2j}\oint_{c1}\left[k\cos\alpha\cos\theta H_1^{(2)}(k|\bar{r}-\bar{r}'|V(\bar{r}) + j\omega h_b H_0^{(2)}(k|\bar{r}-\bar{r}'|)i(\bar{r}))\right]ds$$

$$+\frac{1}{2j}\oint_{c2}\left[k\cos\alpha\cos\theta H_1^{(2)}(k|\bar{r}-\bar{r}'|V(\bar{r}) + j\omega h_e H_0^{(2)}(k|\bar{r}-\bar{r}'|)i(\bar{r}))\right]ds$$

$$+\frac{1}{2j}\oint_{c3}\left[k\cos\alpha\cos\theta H_1^{(2)}(k|\bar{r}-\bar{r}'|V(\bar{r}) + j\omega h_c H_0^{(2)}(k|\bar{r}-\bar{r}'|)i(\bar{r}))\right]ds \quad (3.42)$$

where h_b, h_e and h_c are the substrate height for base, emitter and collector strips, respectively.

Therefore, by applying the contour-integral formulation to base, emitter and collector strips, respectively, the following equations hold:

$$u_{ij} = \begin{cases} 1, & \text{i} = \text{j} \\ \dfrac{k}{2j}\displaystyle\int_{W_j} \cos\alpha \cos\theta H_1^{(2)}(kr)ds, & \text{i} \neq \text{j} \end{cases} \tag{3.43a}$$

$$h_{ij} = \begin{cases} \dfrac{\omega\mu h_b}{2}\dfrac{1}{W_j}\displaystyle\int_{W_j} H_0^{(2)}(kr)ds, & \text{i} \neq \text{j} \\ \dfrac{\omega\mu h_b}{2}[1-\dfrac{2j}{\pi}(In\dfrac{kW_i}{4}-1+\gamma)], & \text{i} = \text{j} \end{cases} \tag{3.43b}$$

for base;

$$u_{ij} = \begin{cases} 1, & \text{i} = \text{j} \\ \dfrac{k}{2j}\displaystyle\int_{W_j} \cos\alpha \cos\theta H_1^{(2)}(kr)ds, & \text{i} \neq \text{j} \end{cases} \tag{3.44a}$$

$$h_{ij} = \begin{cases} \dfrac{\omega\mu h_e}{2}\dfrac{1}{W_j}\displaystyle\int_{W_j} H_0^{(2)}(kr)ds, & \text{i} \neq \text{j} \\ \dfrac{\omega\mu h_e}{2}[1-\dfrac{2j}{\pi}(In\dfrac{kW_i}{4}-1+\gamma)], & \text{i} = \text{j} \end{cases} \tag{3.44b}$$

for emitter and

$$u_{ij} = \begin{cases} 1, & \text{i} = \text{j} \\ \dfrac{k}{2j}\displaystyle\int_{W_j} \cos\alpha \cos\theta H_1^{(2)}(kr)ds, & \text{i} \neq \text{j} \end{cases} \tag{3.45a}$$

$$h_{ij} = \begin{cases} \dfrac{\omega\mu h_c}{2}\dfrac{1}{W_j}\displaystyle\int_{W_j} H_0^{(2)}(kr)ds, & \text{i} \neq \text{j} \\ \dfrac{\omega\mu h_c}{2}[1-\dfrac{2j}{\pi}(In\dfrac{kW_i}{4}-1+\gamma)], & \text{i} = \text{j} \end{cases} \tag{3.45b}$$

for collector.

Considering that all the *N* sections on each contour are coupling ports and that the planar circuit is represented by and *N*-port equivalent circuit. The elements of impedance matrix can be written as follows

$$u_{ij} = \begin{cases} 1, & \text{i = j} \\ \dfrac{3k}{2j}\int_{W_j} \cos\alpha \cos\theta H_1^{(2)}(kr)ds, & \text{i} \neq \text{j} \end{cases} \tag{3.46a}$$

$$h_{ij} = \begin{cases} \dfrac{\omega\mu(h_b + h_e + h_c)}{2}\dfrac{1}{W_j}\int_{W_j} H_0^{(2)}(kr)ds, & \text{i} \neq \text{j} \\ \dfrac{\omega\mu(h_b + h_e + h_c)}{2}[1 - \dfrac{2j}{\pi}(In\dfrac{kW_i}{4} - 1 + \gamma)], & \text{i = j} \end{cases} \tag{3.46b}$$

Thus the impedance matrix can be calculated from equation (3.46). The argument r_{ij} in Hankel is determined by the Cartesan coordinates in the rectangular space:

$$r_{ij} = \sqrt{[SX(i) - SX(j)]^2 + [SY(i) - SY(j)]^2 + [SZ(i) - SZ(j)]^2}\ .$$

3.4 Hybrid Modeling Approach to HBT Device

The contour-integral method discussed in the above section can only calculate the impedance of the HBT parasitic elements. However, to model the HBT device with active intrinsic part must be taken into account, the HBT device can be treated as an embedded multi-port network [69]: an equivalent circuit of the intrinsic device and an equivalent circuit of the extrinsic chip. The equivalent circuit of a HBT intrinsic device contains a controlled current source responsible for device amplification, while the equivalent circuit of the extrinsic chip contains parasitic elements such as stray capacitances and lead inductances and resistances. The effect of additional elements on the scattering matrix of the entire device can be calculated using the embedding formulations. Figure 3.9(a) presents two subnetworks connected by internal ports.

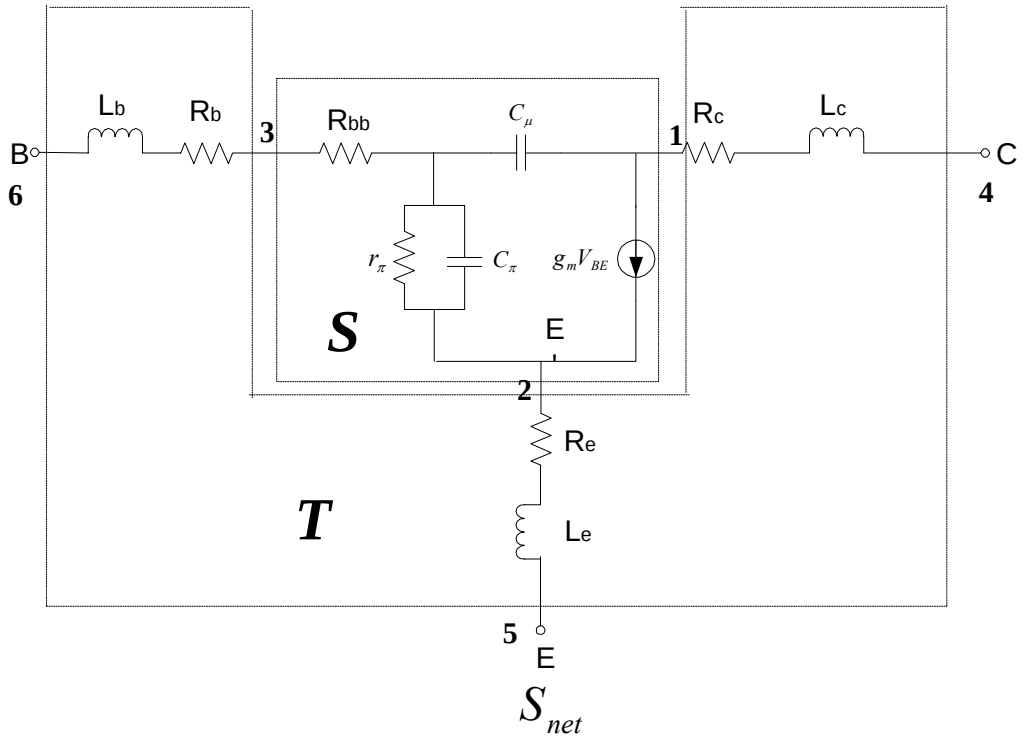

(a)

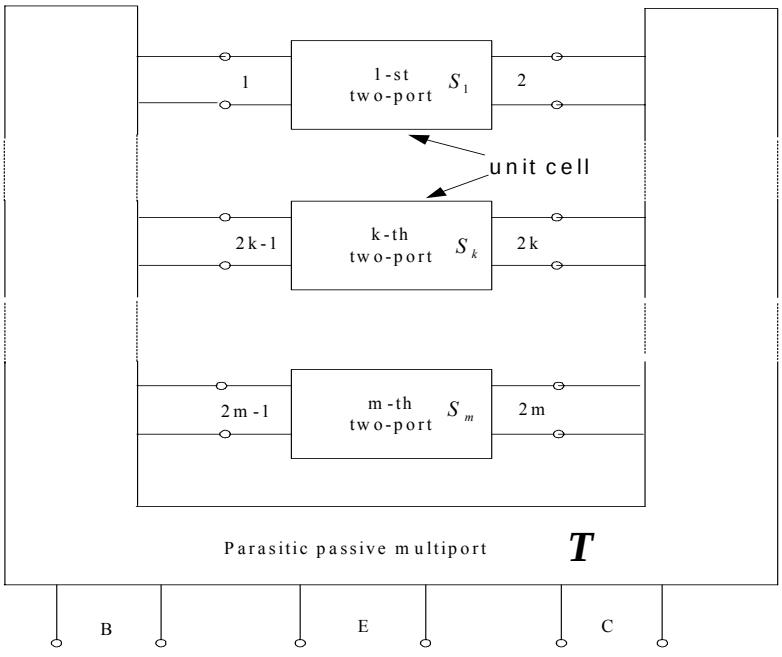

(b)

Figure 3.9 (a) Multiport network illustration of HBT unit cell. S_{net} is the scattering matrix of the entire network referred to external ports.
(b) HBT device decomposed into m active two-ports and a parasitic passive multiport with n=3 external ports.

Referring to Figure 3.9(a), **T** is the scattering matrix for the HBT parasitic passive multiport consisting of lead inductances, stray capacitances and resistance for emitter, base and collector. The scattering matrix **T** for the HBT parasitic passive network can be found by partitioning the embedding network's scattering matrix **T** into submatrices

$$\begin{bmatrix} b_e \\ b_i \end{bmatrix} = \begin{bmatrix} T_{ee} & T_{ei} \\ T_{ie} & T_{ii} \end{bmatrix} \begin{bmatrix} a_e \\ a_i \end{bmatrix}, \tag{3.47}$$

where a_e, b_e and a_i, b_i are vectors of incoming and outgoing waves, respectively, in the external and internal ports of the network.

Similarly, the HBT intrinsic circuit, can be described by the system of equations

$$b_s = Sa_s \tag{3.48}$$

where **S** is the scattering matrix for the HBT intrinsic circuit consisting of current source, dynamic capacitance and bias-dependent resistance. The connections of pairs of internal ports of **S** and **T** subnetworks impose restrictions on vectors of internal incoming and outgoing waves of the forms

$$a_i = b_s \tag{3.49}$$

$$b_i = a_s \tag{3.50}$$

From equations (3.47)-(3.50), by first eliminating b_i, we obtain

$$a_i = (S^{-1} - T_{ii})^{-1} T_{ie} a_e \tag{3.51}$$

and, after eliminating a_i from the first equation of (3.47)

$$b_e = [T_{ee} + T_{ei}(S^{-1} - T_{ii})^{-1} T_{ie}] a_e \tag{3.52}$$

The coefficient matrix in this equation

$$S_{net} = T_{ee} + T_{ei}(S^{-1} - T_{ii})^{-1} T_{ie} \tag{3.53}$$

is the scattering matrix of the whole network referred to the external ports.

For the HBT device expressed in the multiport scheme shown in Figure 3.9 (a), the multiport matrix is as follows:

$$\begin{pmatrix} b_6 \\ b_5 \\ b_4 \\ b_3 \\ b_2 \\ b_1 \end{pmatrix} = \begin{pmatrix} S_{66} & S_{65} & S_{64} & S_{63} & 0 & 0 \\ S_{56} & S_{55} & S_{54} & 0 & S_{52} & 0 \\ S_{46} & S_{45} & S_{44} & 0 & 0 & S_{41} \\ S_{36} & 0 & 0 & S_{33} & S_{32} & S_{31} \\ 0 & S_{25} & 0 & S_{23} & S_{22} & S_{21} \\ 0 & 0 & S_{14} & S_{13} & S_{12} & S_{11} \end{pmatrix} \begin{pmatrix} a_6 \\ a_5 \\ a_4 \\ a_3 \\ a_2 \\ a_1 \end{pmatrix} \tag{3.54}$$

referring to equation (3.47), $a_e = \begin{pmatrix} a_6 \\ a_5 \\ a_4 \end{pmatrix}$, $b_e = \begin{pmatrix} b_6 \\ b_5 \\ b_4 \end{pmatrix}$ and $a_i = \begin{pmatrix} a_3 \\ a_2 \\ a_1 \end{pmatrix}$, $b_i = \begin{pmatrix} b_3 \\ b_2 \\ b_1 \end{pmatrix}$ are vectors of incoming and outgoing waves, respectively, in the external and internal ports of the network. $T_{ee} = \begin{pmatrix} S_{66} & S_{65} & S_{64} \\ S_{56} & S_{55} & S_{54} \\ S_{46} & S_{45} & S_{44} \end{pmatrix}$ is the scattering matrix for HBT extrinsic equivalent circuit calculated by contour-integral method, $T_{ii} = S = \begin{pmatrix} S_{33} & S_{32} & S_{31} \\ S_{23} & S_{22} & S_{21} \\ S_{13} & S_{12} & S_{11} \end{pmatrix}$ is the scattering matrix for the HBT intrinsic part, $T_{ei} = \begin{pmatrix} S_{63} & 0 & 0 \\ 0 & S_{52} & 0 \\ 0 & 0 & S_{41} \end{pmatrix}$ and $T_{ie} = \begin{pmatrix} S_{36} & 0 & 0 \\ 0 & S_{25} & 0 \\ 0 & 0 & S_{14} \end{pmatrix}$ are connection matrix related to connections of external ports.

The overall scattering matrix for HBT two-port network can be converted from three-port scattering matrix calculated from equation (3.53):

$$b_1' = \left[S_{net66} - \frac{S_{net65} S_{net46}}{1 + S_{net55}} \right] a_1' + \left[S_{net64} - \frac{S_{net65} S_{net54}}{1 + S_{net55}} \right] a_2' \tag{3.55}$$

$$b_2' = \left[S_{net46} - \frac{S_{net45} S_{net56}}{1 + S_{net55}} \right] a_1' + \left[S_{net44} - \frac{S_{net45} S_{net54}}{1 + S_{net55}} \right] a_2' \tag{3.56}$$

Therefore the final two-port scattering parameters can be further written as the following as:

$$S_{11}^{'} = S_{net66} - \frac{S_{net65}S_{net46}}{1+S_{net55}}, \tag{3.57a}$$

$$S_{12}^{'} = S_{net64} - \frac{S_{net65}S_{net54}}{1+S_{net55}}, \tag{3.57b}$$

$$S_{21}^{'} = S_{net46} - \frac{S_{net45}S_{net56}}{1+S_{net55}}, \tag{3.57c}$$

$$S_{22}^{'} = S_{net44} - \frac{S_{net45}S_{net54}}{1+S_{net55}}. \tag{3.57d}$$

3.5 Results and Discussions

A typical GaAs HBT device is selected to verify the above analysis. The selected HBT transistor has a multi-finger $2\times20\times4$ configuration and h_c=2.5 μm, h_b=2.59 μm and h_e=2.82 μm. The multi-finger HBT device is divided as shown in Figure 3.8, where the dot indicates the coupling ports to be evaluated. The contour-integral analysis is subsequently applied and the scattering matrix parameters for each unit cell parasitic subnetwork are calculated using equations (3.42)-(3.46). In the contour-integral calculation, the width of each coupling port W_i is 0.4 μm along the device strips. Equation (3.46) is applied to calculate the impedance matrix for the HBT parasitic passive multiport. The intrinsic device is connected to the strip periphery as the equivalent circuit parameters are determined by the field distribution along the periphery. The impedance matrix of HBT intrinsic device is calculated by the well-known chain matrix formulation. The intrinsic element values are calculated by the analytical approach discussed in Chapter 2 and are listed in Table 3.1. The overall scattering matrix of the HBT device is obtained by merging the two matrices together

using equation (3.53). The final two-port scattering matrix is computed by the transformation of equation (3.57).

Table 3.1 HBT Small-signal intrinsic parameter values for the extracted bias points

	I_b=100 uA, I_c=9.4 mA, V_{CE}=4 V.	I_b=200 uA, I_c=19.2 mA, V_{CE}=3 V.	I_b=290 uA, I_c=26.3 mA, V_{CE}=4.5 V.
R_{bb} (Ohm)	8.3	8.9	9.4
C_u (fF)	23	27	28
r_π (Ohm)	3679	2538	742
C_π (pF)	2.7	1.2	0.9
τ (ps)	2.7	2.1	1.7
G_m (Sie)	0.19	0.42	0.59
C_{bc} (fF)	42	13	17

Figure 3.10 shows the comparison of measured S-parameters versus calculated S-parameters by both the analytical approach discussed in Chapter 2 and the hybrid approach discussed in Section 3.4. Reasonable agreement between the measured and analytical calculated S-parameters is noted. However, the simulation results calculated by the analytical approach deviate from the measured data as the frequency increases. While the S-parameters simulation by the hybrid approach show better agreement to the measurement data. This is expected as the contour-integral calculation takes into account the coupling among the multi-fingers. As the operating frequency increases, the equivalent circuit approach for the HBT extrinsic part is not accurate enough. For example, the parasitic inductance should be replaced by the

resonator equivalent circuit. Although the analytical approach can adopt a more comprehensive but complex equivalent circuit the unique determination of the model parameter is difficult.

The calculated residual error is tabulated in Table 3.2. As noted from Table 3.2, for all three biasing points, the hybrid approach shows lower residual errors compared to the analytical approach, indicating a better agreement throughout the entire frequency range.

Table 3.2 Residual error for the extracted bias points

Residual error	I_b=100 uA, I_c=9.4 mA, VCE=4 V.	I_b=200 uA, I_c=19.2 mA, VCE=3 V.	I_b=290 uA, I_c=26.3 mA, VCE=4.5 V.
Analytical Approach	4.2%	4.7%	5.1%
Hybrid Approach	1.8%	2.1%	1.9%

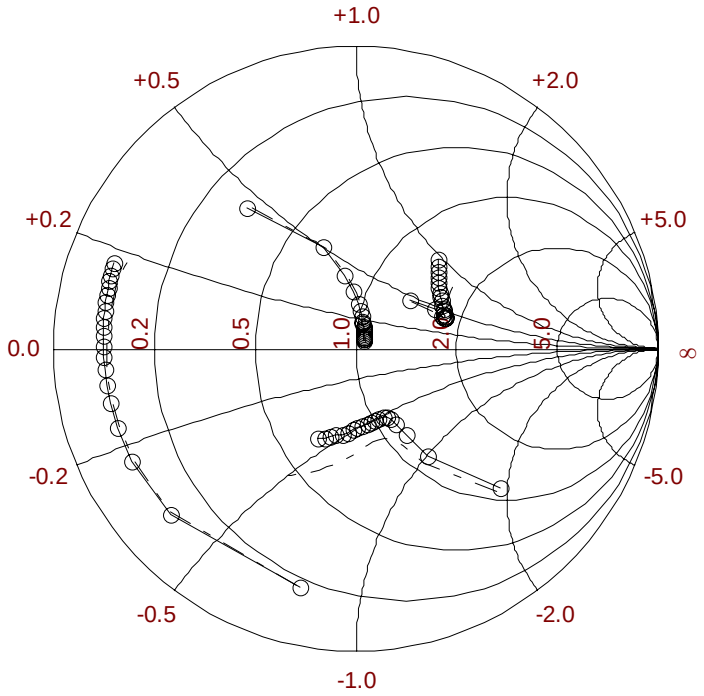

Figure 3.10(a) Measured and simulated S-parameters for GaAs HBT. (solid line: hybrid approach; circle line: measurement data; dashed line: analytical approach; I_b=100 μA, V_{CE}=4V, I_C=9.4 mA, frequency: 1-20 GHz; S12*5, S21/20).

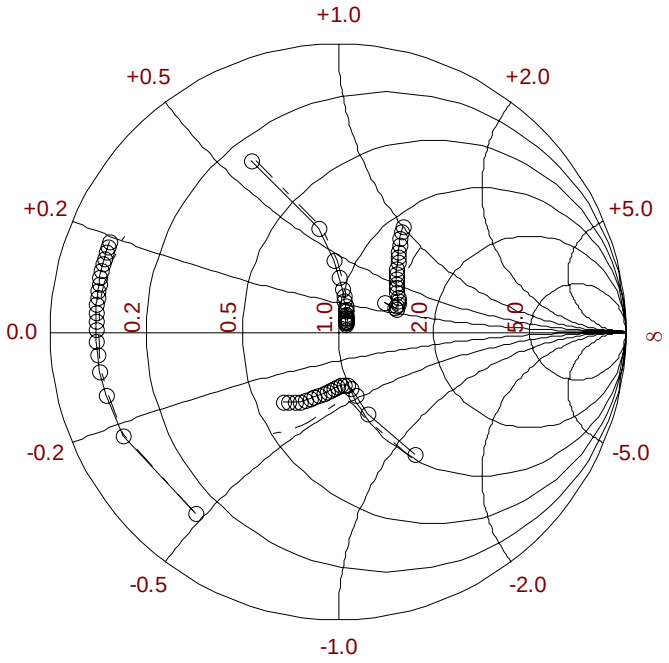

Figure 3.10(b) Measured and simulated S-parameters for GaAs HBT. (solid line: hybrid approach; circle line: measurement data; dashed line: analytical approach; I_b=200 μA, V_{CE}=3V, I_C=19.2 mA, frequency: 1-20 GHz; S12*5, S21/20).

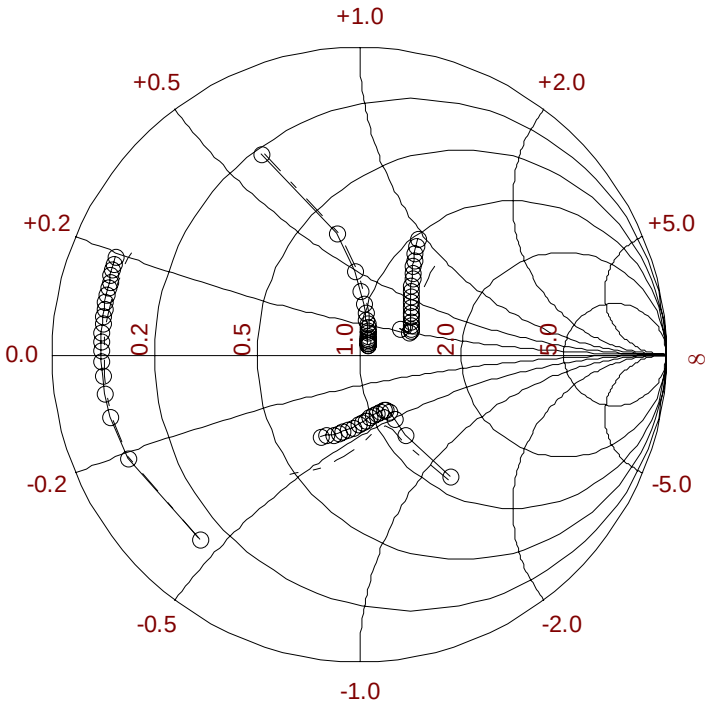

Figure 3.10(c) Measured and simulated S-parameters for GaAs HBT. (solid line: hybrid approach; circle line: measurement data; dashed line: analytical approach; I_b=290 μA, V_{CE}=4.5V, I_C=26.3 mA, frequency: 1-20 GHz; S12*5, S21/20).

Chapter 4

Modeling the RF Noise of HBT by the Wave Approach

4.1 Introduction

In the technology development and device design for low-noise applications [70], various analytical equations are used. These equations give the minimum noise figure NF_{min}, the optimal source reflection coefficient $\Gamma_{G,opt}$ and equivalent noise resistance R_n of a bipolar transistor as a function of bias conditions and small-signal transistor parameters. In the past noise models [71]-[78] were often developed using a small-signal equivalent circuit combined with a model for physical noise sources including the shot noise and thermal noise. The most often used model equation to calculate noise performance of bipolar transistors has been those in [71], e.g. employed in [72], or those of van der Ziel [73], e.g. used in [74]. They are both based on the pioneering analysis of noise sources in bipolar transistors by van der Ziel and Becking [79]. These are put on a more profound theoretical basis by van Vliet [80] to determine the noise performance of the transistor as a function of the bias conditions and transistor parameters, like series resistors, junction capacitances and transit time.

Herzel, Heinemann [81], [82] and Voinigescu *et al*. [77], have published different equations to calculate the four noise parameters of bipolar transistors. Both of them give the minimum noise figure in terms of the small-signal parameters of the transistors. This is attractive both in predicting noise behavior from device simulation and as substitute for noise measurements since they give the minimum noise figure readily as a function of the small-signal admittance parameters of the device. Herzel and Heinemann's approach, which is also referred to be the thermodynamic model, makes use of the well-known fluctuation-dissipation theorem to describe device noise. In contrast to most SPICE noise models [71]-[78], the expression for the high-frequency spectrum of thermal current noise in bipolar devices was derived from quantum mechanical linear response theory instead of relying on an equivalent circuit.

This chapter addresses the issue on the RF noise analysis of HBT device. It will describe one of the most promising features that the new proposed method can offer, i.e., the noise properties can be evaluated concurrently without any domain transformation with the determination of the S-parameters. In the past, multiple conversions were needed before gain and noise properties could be solved. Apparently, in this approach, the computational time for both gain and noise evaluation is shortened since they can be computed together without any conversion.

In this part of the work, some computer-aided noise analysis methods for linear two-port networks with general internal topology are proposed. Without imposing the constraint of $\overline{a_n b_n^*} = 0$ [83], a few general expressions for the computation of the four noise parameters of the basic two-port network in terms of the equivalent temperatures T_a and T_b are derived. Based on this fundamental concept, two alternative approaches, which lead to faster computation of the four noise parameters of a two-port with any arbitrary internal topology in microwave circuits, are

discussed. By means of wave representation for noise [84], the need to adopt any sparse matrix techniques for the evaluation of the N×N inverse as required in the conventional analysis [85] is removed. The second proposed method can be easily incorporated into existing CAD tools. Moreover, it provides the unification of the Gupta's multi-connection method for signal analysis with the noise analysis.

Following the evaluation of the SPICE noise model and thermodynamic noise model in Section 4.2, noise analysis, based on the T-wave and S-wave approaches are carried out. In Section 4.3, the various definitions of the noise representations will be discussed in relation to the noise wave concept. These basic noise representations are subsequently extended to any arbitrary internal topology two-port network. Some conventional noise analyses for two-port networks with any internal topology are also reviewed in this section. Following this, the derivation of some new expressions for the four noise parameters in terms of the equivalent noise temperatures are illustrated in Section 4.4. Next, two alternative approaches, T-wave and S-wave, are discussed in Section 4.5. Finally, Section 4.6 proposes a new method to extract the equivalent noise temperatures.

4.2 Evaluation of the SPICE Noise Model and Thermodynamic Model

In most SPICE-like simulators, e.g. SpectreRF, and harmonic balance simulators, e.g. Advanced Design System, the nonlinear noise model for bipolar transistor is described by two shot noise current generators flowing from the base and collector to the emitter and two thermal noise voltage generators at the base and emitter, as shown in Figure 4.1(a). An analytical equation of the minimum noise

factor F_{min} was derived as follows in terms of the *Y*-parameters, the series base resistance R_B and series resistance R_E [77].

$$F_{\min} = 1 + \frac{qI_C}{kT|Y_{21}|^2}\left(\mathrm{Re}(Y_{11}) + A\right), \tag{4.1}$$

$$A = \sqrt{\left(1 + \frac{2kT|Y_{21}|^2(R_B + R_E)}{qI_C}\right)\left(|Y_{11}|^2 + \frac{I_B|Y_{21}|^2}{I_C}\right) - \left(\mathrm{Im}(Y_{11})\right)^2}\,, \tag{4.2}$$

where I_C and I_B are collector and base current, respectively. The optimum generator admittance at which F_{min} occurs for a given bias point and frequency is given:

$$Y_{G,opt} = G_{G,opt} + jB_{G,opt}\,, \tag{4.3}$$

where

$$G_{G,opt} = \sqrt{\frac{I_B|Y_{21}|^2 + I_C|Y_{11}|^2}{\frac{2kT}{q}|Y_{21}|^2(R_B + R_E) + I_C} - \left(\frac{I_C\,\mathrm{Im}(Y_{11})}{\frac{2kT}{q}|Y_{21}|^2(R_B + R_E) + I_C}\right)^2}\,, \tag{4.4}$$

$$B_{G,opt} = \frac{-\mathrm{Im}(Y_{11})}{\frac{2kT}{q}|Y_{21}|^2\frac{R_B + R_E}{I_C} + 1}, \tag{4.5}$$

The noise resistance R_n, which relates to the input-referred noise voltage, is given as the following:

$$R_n = \frac{I_C}{\frac{2kT}{q}|Y_{21}|^2} + (R_B + R_E)\,. \tag{4.6}$$

It can be seen that the first term of R_n comes from the collector shot noise $2qI_C$, and the second term comes from the base and emitter resistances.

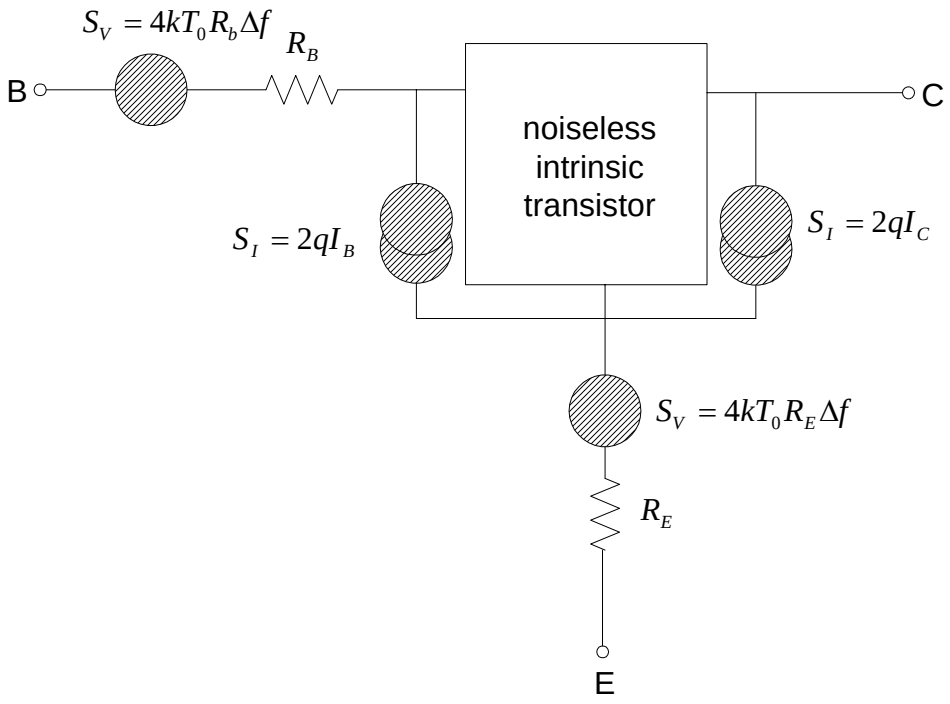

Figure 4.1(a) Schematic of the SPICE noise model.

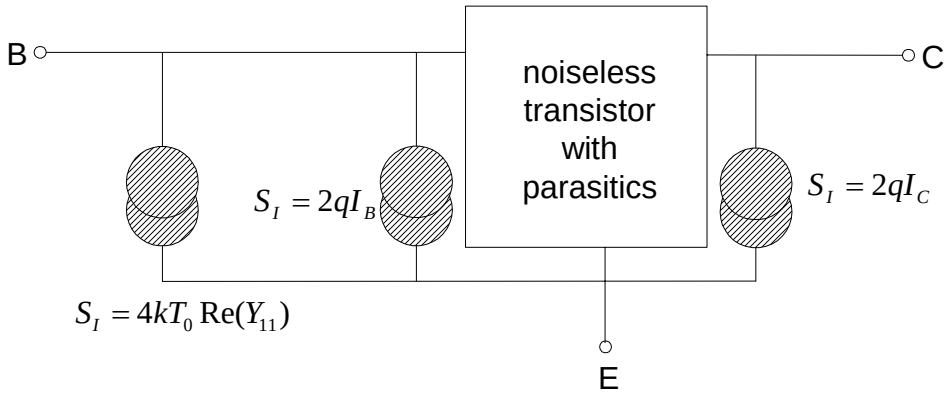

Figure 4.1(b) Schematic of the thermodynamic noise model.

The other description of transistor is the so-called thermodynamic approach [81] [82]. The shot noise generators are the same as those in the SPICE models, however, the thermal noise is represented by an input noise current generator $S_I = 4kTRe(Y_{11})$, which was derived from the fluctuation-dissipation theorem or generalized Nyquist expression for two poles near equilibrium, as shown in Figure

4.1(b). The thermal noise current generator operates on the whole transistor including parasitic base and emitter resistances and directly relates to the small-signal input admittance *Y*-parameters. Consequently, the four noise parameters are calculated directly from *Y*-parameters without extracting parasitic base and emitter resistances, thus providing significant time saving for the optimization of noise figure at a particular frequency. The minimum noise factor equation for the thermodynamic model is [81], [82]

$$F_{\min} = 1 + \frac{I_B + \frac{2kT}{q}\mathrm{Re}(Y_{11}) + I_C\left(\frac{\mathrm{Re}(Y_{11}) + G_{G,opt}}{|Y_{21}|}\right)^2}{\frac{2G_{G,opt}kT}{q}}, \tag{4.7}$$

where $G_{G,opt}$ is the real part of the generator admittance (or source conductance) at the minimum noise factor:

$$G_{G,opt} = \sqrt{(\mathrm{Re}(Y_{11}))^2 + |Y_{21}|^2 \frac{2I_B + \frac{4kT\,\mathrm{Re}(Y_{11})}{q}}{2I_C}}. \tag{4.8}$$

The imaginary part of the generator admittance at the minimum noise figure is equal to the conjugate of the imaginary part of the input admittance of the transistor

$$B_{G,opt} = -\mathrm{Im}(Y_{11}). \tag{4.9}$$

Equation (4.9) is different from (4.5). This is due to the different formulations of the input noise current source and input-referred noise voltage source, which will be discussed below. The noise resistance R_n relating to the input-referred noise voltage is given by the following

$$R_n = \frac{I_C}{\frac{2kT}{q}|Y_{21}|^2}. \tag{4.10}$$

The second term in the right hand side of equation (4.6) does not exist in equation (4.10) because in the thermodynamic model the thermal noise is taken into account through an input current source and the input-referred noise voltage is obtained by short-circuiting the input and calculating the input voltage which generates the equal output noise. Thus, the thermal noise, when described by an input current noise source, does not contribute to the input-referred noise voltage, and hence it does not contribute to the noise resistance R_n.

The four noise parameters based on the SPICE noise model and thermodynamic model have been calculated from 2 GHz to 18 GHz at I_C=2.584 mA. The IBM SiGe HBT device with an emitter size of 0.5 um (emitter width) × 20 um (emitter length) × 2 (number of emitter strips) is used for the verification.

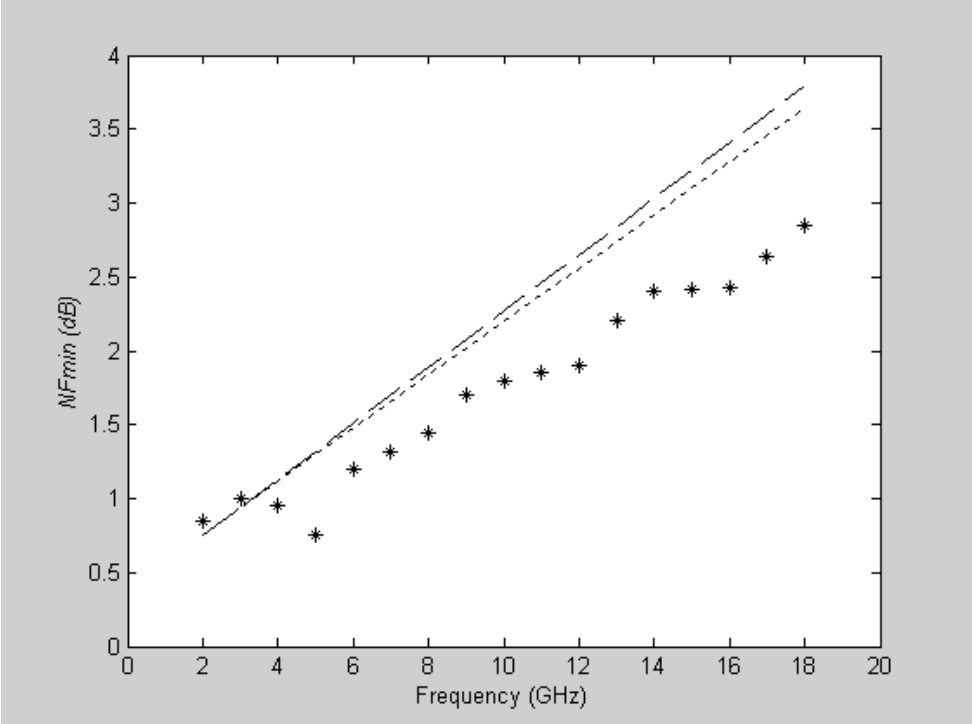

Figure 4.2 (a) Comparison of modeled and measured NF_{min} versus frequency at Ic=2.584 mA
(*: measured data; dotted line: thermodynamic model; dashed line: SPICE model.).

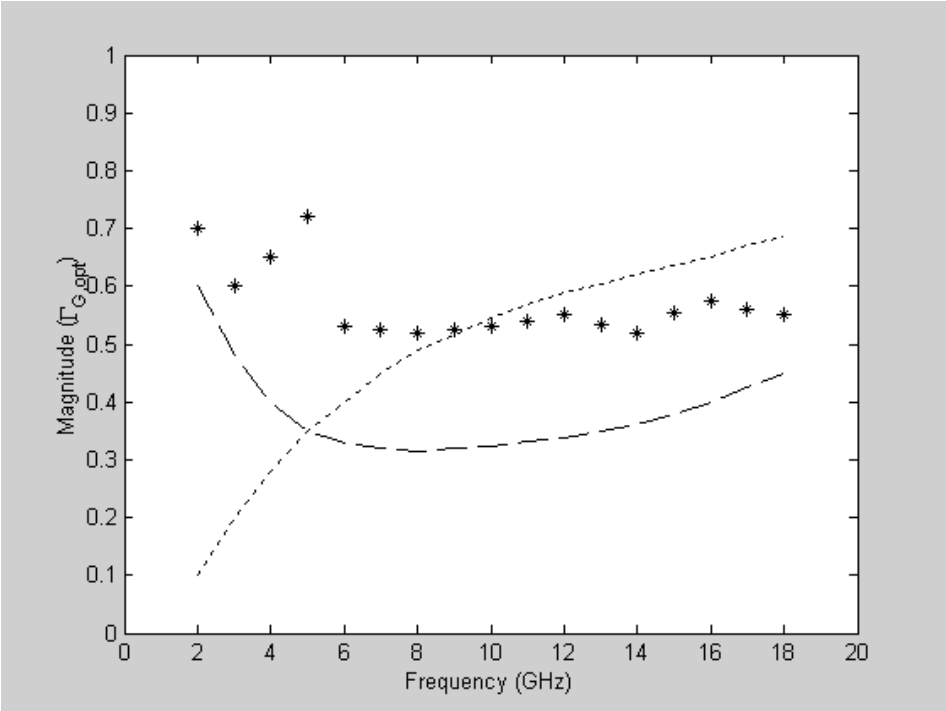

Figure 4.2 (b) Comparison of modeled and measured magnitude of $\Gamma_{G,opt}$ versus frequency at Ic=2.584 mA
(*: measured data; dotted line: thermodynamic model; dashed line: SPICE model.).

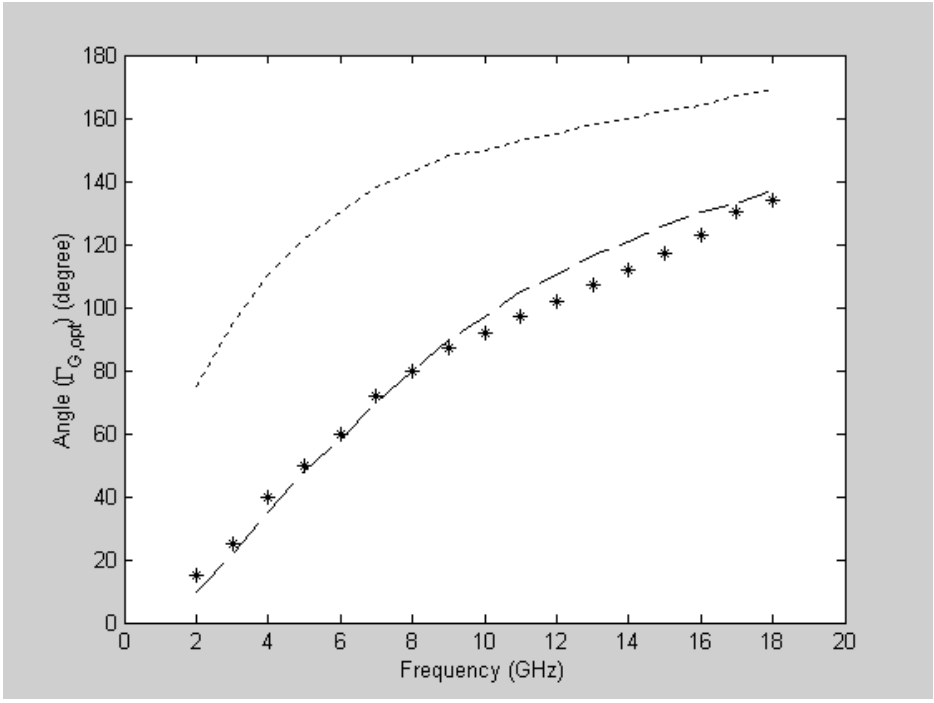

Figure 4.2(c) Comparison of modeled and measured angle of $\Gamma_{G,opt}$ versus frequency at Ic=2.584 mA
(*: measured data; dotted line: thermodynamic model; dashed line: SPICE model.).

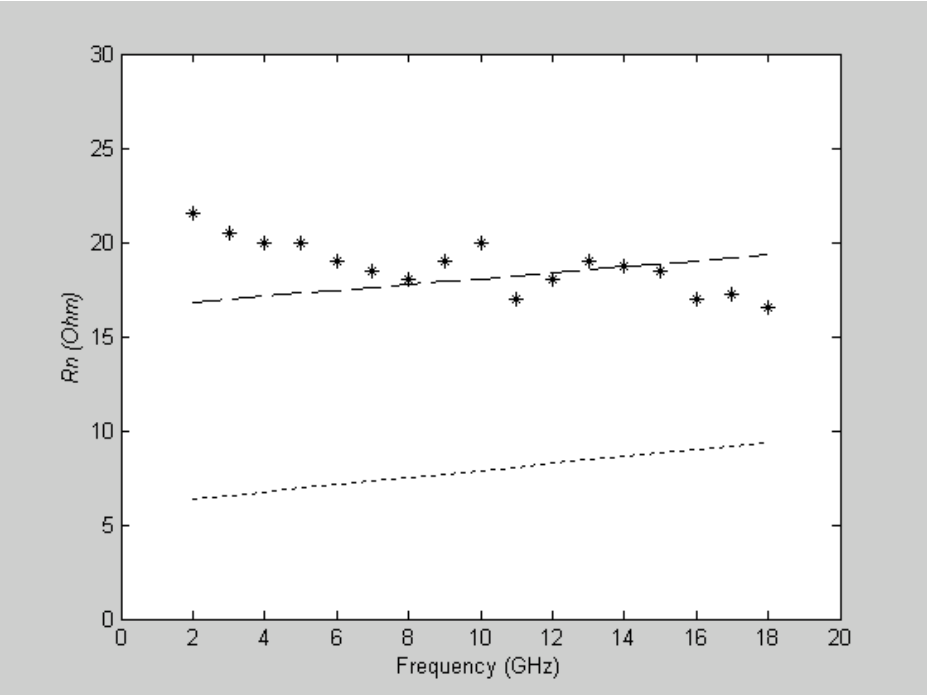

Figure 4.2 (d) Comparison of modeled and measured equivalent noise resistance R_n versus frequency at Ic=2.584 mA
(*: measured data; dotted line: thermodynamic model; dashed line: SPICE model.).

From Figure 4.2(a), it can be seen that the SPICE noise model and the thermodynamic noise model lead to nearly identical minimum noise figure and optimum noise matching admittance for the device under test despite of different consideration of the thermal noise. The noise resistance, however, differs by the amount of base and emitter resistance between the two models. The essential differences between the two models are two-fold: on one hand, the thermal noise source in the SPICE model is determined by the series resistance, while the thermal noise source in the thermodynamic model is determined by the real part of the input *Y*-parameter Y_{11}; on the other hand, the thermal noise in the SPICE model is represented by a voltage source in series with input voltage, while the thermal noise in the thermodynamic model is represented by a current source in parallel with the input current. These differences can be used to explain the agreement and discrepancies.

As we know that any noise network can be replaced by a chain noise equivalent circuit, which consists of the original two-port (assumed to be noiseless), the correlated input-referred current noise source $\left\langle i_n^2 \right\rangle$, and the correlated input-referred voltage noise source $\left\langle v_n^2 \right\rangle$. Independent of the physical sources of noises inside the device, the four noise parameters can be expressed as a function of $\left\langle i_n^2 \right\rangle$, $\left\langle v_n^2 \right\rangle$, and the cross correlation $\left\langle v_n i_n^* \right\rangle$ [86], [87]

$$F_{\min} = 1 + 2\left(C_r + \sqrt{R_n G_n - C_i^2}\right), \tag{4.11}$$

$$G_{G,opt} = \sqrt{\frac{G_n}{R_n} - \left(\frac{C_i}{R_n}\right)^2}, \tag{4.12}$$

$$B_{G,opt} = \frac{C_i}{R_n}, \tag{4.13}$$

$$R_n = \frac{\left\langle v_n^2 \right\rangle}{4kT\Delta f}, \tag{4.14}$$

where

$$G_n = \frac{\left\langle i_n^2 \right\rangle}{4kT\Delta f}, \tag{4.15}$$

$$C_r = \frac{\mathrm{Re}\left(\left\langle v_n i_n^* \right\rangle\right)}{4kT\Delta f}, \tag{4.16}$$

$$C_i = \frac{\mathrm{Im}\left(\left\langle v_n i_n^* \right\rangle\right)}{4kT\Delta f}. \tag{4.17}$$

By transforming the two noisy two-ports in Figure 4.1(a) and Figure 4.1(b) to their chain noisy two-ports, $\left\langle i_n^2 \right\rangle$ is obtained by open circuiting the input and dividing the output noise current by $|H_{21}|^2$; $\left\langle v_n^2 \right\rangle$ is obtained by short circuiting the input and

dividing the output noise current by $|Y_{21}|^2$ and the cross correlation $\langle v_n i_n^* \rangle$ is then calculated using the internal noise sources common to both i_n and v_n, which is the collector shot noise $2qI_C$ in both models. For SPICE noise model:

$$\langle i_n^2 \rangle = 2qI_B + \frac{2qI_C|Y_{11}|^2}{|Y_{21}|^2}, \tag{4.18}$$

$$\langle v_n^2 \rangle = 4kT(R_B + R_E) + \frac{2qI_C}{|Y_{21}|^2}, \tag{4.19}$$

$$\langle v_n i_n^2 \rangle = \frac{2qI_C Y_{11}^*}{|Y_{21}|^2}, \tag{4.20}$$

and for thermodynamic model:

$$\langle i_n^2 \rangle = 4kT\,\mathrm{Re}(Y_{11}) + 2qI_B + \frac{2qI_C|Y_{11}|^2}{|Y_{21}|^2}, \tag{4.21}$$

$$\langle v_n^2 \rangle = \frac{2qI_C}{|Y_{21}|^2}, \tag{4.22}$$

$$\langle v_n i_n^* \rangle = \frac{2qI_C Y_{11}^*}{|Y_{21}|^2}. \tag{4.23}$$

Thus the following relations between the two models can be found.

1) The cross correlation $\langle v_n i_n^* \rangle$ and hence C_r and C_i are the same for both models.
2) $\langle i_n^2 \rangle$ is the same for both models except for an extra term $4kTRe(Y_{11})$ in the thermodynamic model.
3) $\langle v_n^2 \rangle$ is the same for both models except for an extra term $4kT(R_B+R_E)$ in the SPICE model.
4) The product of $\langle i_n^2 \rangle$ and $\langle v_n^2 \rangle$, which determines the G_nR_n product, shares two common terms.

Consequently, the difference in R_n, $G_{G,opt}$ and $B_{G,opt}$ between the two models can be readily understood from the difference in $\left\langle v_n^2 \right\rangle$ and $\left\langle i_n^2 \right\rangle$. The minimum noise figure is expected to differ only by the G_nR_n product, as can be seen from equation (4.11). Although G_n and R_n are very different for the two models, their product G_nR_n, which shares two common terms, could be similar. In that case, similar NF_{min} values are obtained using both models despite the difference in $Y_{G,opt}$ and R_n. The two models give a similar G_nR_n product, which is responsible for the agreement in NF_{min} shown in Figure 4.2(a).

4.3 Noise in Linear Two-Port Networks

When a two-port network is dispersive, the output waveform may differ from the input, because of its failure to transmit all spectral components with equal gain (or attention) and delay. By careful design of the two-port, or band-limit the bandwidth of the input waveform, such distortions can largely be avoided. However, noise generated within the two-port can still change the waveform of the output signal. This noise can arise from losses in the two-port which may or may not contain any active devices.

Using the spectral representation of noise sources, noisy two-port network may be described by small-signal equations, e.g. the transistor equivalent circuit as shown in chapter 2. The circuit theory of linear noisy networks shows that any noisy two-port can be replaced by its equivalent circuit, which consists of the original two-port (now assumed as noiseless) and two additional noise sources. There are many equivalent representations for noisy two-ports. Some of these are illustrated in Figure 4.3.

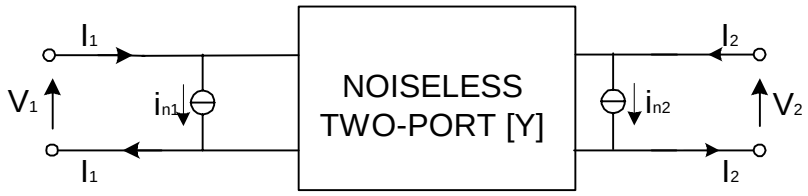

Figure 4.3 (a) Admittance representation of a noisy two-port.

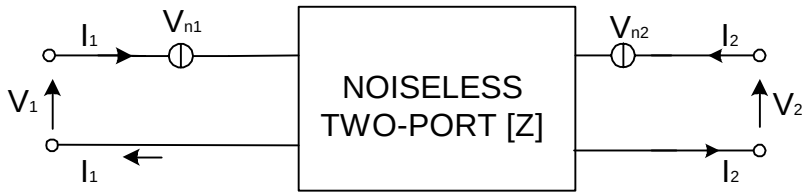

Figure 4.3 (b) Impedance representation of a nosy two-port.

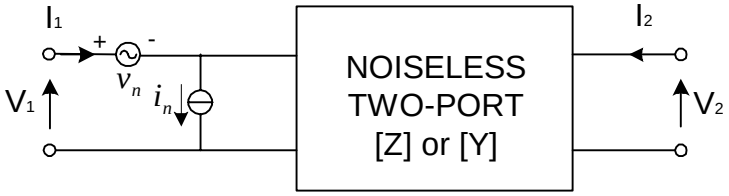

Figure 4.3 (c) Equivalent representation with two noise sources at the input of a nosy two-port.

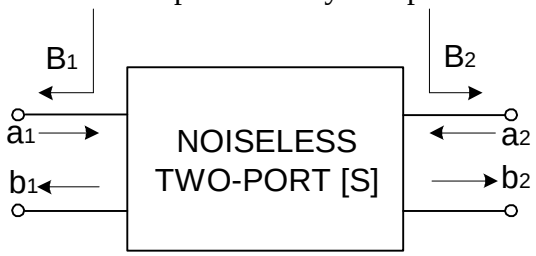

Figure 4.3 (d) Wave representation of noisy two-port with input and output noise wave sources.

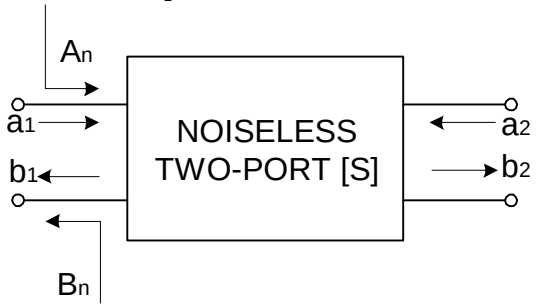

Figure 4.3 (e) Wave representation of a noisy two-port with two input noise sources.

The respective spectral representations of the noisy two-port as indicated in Figure 4.3 are tabulated in Table 4.1. The noise parameters corresponding to each type of the representations are also presented in the table. In general, the noise sources as depicted in Figure 4.3 do not exist in the positions marked in these figures; they are merely concentrated equivalent representations of the effect of all the noise currents and noise voltages or equivalently all the noise waves inside the two-port network.

These primary noise sources are not statistically independent. Generally, the noise behavior of a linear noisy two-port network can be characterized by four parameters, namely, by two power spectral densities, and the real and imaginary parts of the corresponding cross spectral density. The power spectral density is defined as the Fourier transform of the well-known auto-correlation function; the cross spectral density is defined as the Fourier transform of the cross-correlation function. The average power of a noise source $\overline{e}^2(t)$ can be calculated by using Parseval's theorem. The average power is assumed to be stationary, i.e.

$$\overline{e}^2(t) = \int_0^\infty w(f)df \tag{4.24}$$

where w(f) is the one-sided density.

Table 4.1 A collection of some types of equivalent two-port noise representation.

Equivalent Forms	Spectral Representations	Noise Parameters
Admittance representation with input and output current noise sources. See Figure 4.3(a)	$\begin{bmatrix} I_1 \\ I_2 \end{bmatrix} = \begin{bmatrix} Y_{11} & Y_{12} \\ Y_{21} & Y_{22} \end{bmatrix} \begin{bmatrix} V_1 \\ V_2 \end{bmatrix} + \begin{bmatrix} I_{n1} \\ I_{n2} \end{bmatrix}$	$G_1 = \dfrac{\overline{\lvert I_{n1} \rvert^2}}{4kT_0 df}$, $G_2 = \dfrac{\overline{\lvert I_{n2} \rvert}}{4kT_0 df}$, $\rho_c = \lvert \rho_c \rvert e^{\phi_c} = \dfrac{\overline{I_{n1}^* I_{n2}}}{\sqrt{\lvert I_{n1} \rvert^2 \lvert I_{n2} \rvert^2}}$
Impedance representation with input and output voltage noise sources. See Figure 4.3(b)	$\begin{bmatrix} V_1 \\ V_2 \end{bmatrix} = \begin{bmatrix} Z_{11} & Z_{12} \\ Z_{21} & Z_{22} \end{bmatrix} \begin{bmatrix} I_1 \\ I_2 \end{bmatrix} + \begin{bmatrix} V_{n1} \\ V_{n2} \end{bmatrix}$	$R_1 = \dfrac{\overline{\lvert V_{n1} \rvert^2}}{4kT_0 df}$, $R_2 = \dfrac{\overline{\lvert V_{n2} \rvert^2}}{4kT_0 df}$, $\rho_v = \lvert \rho_v \rvert e^{\phi_v} = \dfrac{\overline{V_{n1}^* V_{n2}}}{\sqrt{\lvert V_{n1} \rvert^2 \lvert V_{n2} \rvert^2}}$
Chain representation with input current and voltage noise sources. See Figure 4.3(c)	$\begin{bmatrix} V_1 \\ I_1 \end{bmatrix} = \begin{bmatrix} A & B \\ C & C \end{bmatrix} \begin{bmatrix} V_2 \\ -I_2 \end{bmatrix} + \begin{bmatrix} V_n \\ I_n \end{bmatrix}$	$R_N = \dfrac{\overline{\lvert V_n \rvert^2}}{4kT_0 df}$, $g_N = \dfrac{\overline{\lvert I_n \rvert^2}}{4kT_0 df}$, $\rho = \lvert \rho \rvert e^{\phi} = \dfrac{\overline{V_n^* I_n}}{\sqrt{\lvert V_n \rvert^2 \lvert I_n \rvert^2}}$
S-wave representation with input and output port noise wave sources. See Figure 4.3(d)	$\begin{bmatrix} b_1 \\ b_2 \end{bmatrix} = \begin{bmatrix} S_{11} & S_{12} \\ S_{21} & S_{22} \end{bmatrix} \begin{bmatrix} a_1 \\ a_2 \end{bmatrix} + \begin{bmatrix} B_1 \\ B_2 \end{bmatrix}$	$T_{B1} = \dfrac{\overline{\lvert B_1 \rvert^2}}{kdf}$, $T_{B2} = \dfrac{\overline{\lvert B_2 \rvert^2}}{kdf}$, $\rho_B = \lvert \rho_B \rvert e^{\phi_B} = \dfrac{\overline{B_1^* B_2}}{\sqrt{\lvert B_1 \rvert^2 \lvert B_2 \rvert^2}}$
T-wave representation with input port noise wave sources. See Figure 4.3(e)	$\begin{bmatrix} a_1 \\ b_1 \end{bmatrix} = \begin{bmatrix} T_{11} & T_{12} \\ T_{21} & T_{22} \end{bmatrix} \begin{bmatrix} b_2 \\ a_2 \end{bmatrix} + \begin{bmatrix} A_n \\ -B_n \end{bmatrix}$	$T_A = \dfrac{\overline{\lvert A_n \rvert^2}}{kdf}$, $T_B = \dfrac{\overline{\lvert A_B \rvert^2}}{kdf}$, $\rho_{AB} = \lvert \rho_{AB} \rvert e^{\phi_{AB}} = \dfrac{\overline{A_n^* B_n}}{\sqrt{\lvert A_n \rvert^2 \lvert B_n \rvert^2}}$

By the convention in noise analysis [88], the spectral density w(f) is defined in terms of positive frequency only. The mean square value $\overline{e^2}(t)$ is often expressed by (4.25) as a function of the noise frequency bandwidth Δf

$$\overline{e^2}(t) = w(f_n)\Delta f \tag{4.25}$$

The bandwidth Δf used in all noise calculations is the bandwidth of an ideal band-pass circuit that has a rectangular response of the same area and peak value as the sources [83] and [89]. In Table 4.1, ρ_c, ρ_v, ρ, ρ_b and ρ_{ab} are the correlation coefficients of the respective spectral representations. From Table 4.1, it is noted that any one of the noise representations can be transformed into any other forms by means of some simple algebraic manipulations. A detailed description of the manipulations can be found in [90].

From the earlier discussions, it was noted that the above concept can be extended to a more general multiport case. This can easily be done if all the noisy networks of the multiport are represented by their respective noiseless equivalent of the original subcircuit with noise current sources connected across each port. Thus, by applying the Kirchhoff's current law for the whole network, the admittance representation [91]-[93] is thus represented as

$$\overline{I} = \overline{YV} + \overline{I_n}\,, \tag{4.26}$$

where $\overline{Y}$ is the admittance matrix of the multiport, $\overline{V} = [\mathrm{V}_1\ \mathrm{V}_2\ \ldots\ \mathrm{V}_n]^{\mathrm{T}}$ is a column vector of port voltages, $\overline{I} = [\mathrm{I}_1\ \mathrm{I}_2\ \ldots\ \mathrm{I}_n]^{\mathrm{T}}$ is a column vector of port currents, and $\overline{I_n} = [\mathrm{I}_{n1}\ \mathrm{I}_{n2}\ \ldots\ \mathrm{I}_{nn}]^{\mathrm{T}}$ is a column vector of noise current sources. Alternatively, the noise wave representation of a linear multiport can also be adopted, and is expressed as:

$$\overline{B} = \overline{SA} + \overline{B_n}\,, \tag{4.27}$$

where $\overline{S}$ is the scattering matrix of the multiport, $\overline{A}=[A_1\ A_2\ \ldots\ A_n]^T$ is a column vector of the port incoming noise waves, $\overline{B}=[B_1\ B_2\ \ldots\ B_n]^T$ is a column vector of the port outgoing noise waves, and $\overline{B_n}=[B_{n1}\ B_{n2}\ \ldots\ B_{nn}]^T$ is a column vector of the port equivalent noise wave sources.

Since the noise behavior is characterized by their self-power and cross-power spectral densities, hence, by arranging these spectral densities in matrix form, a so-called correlation matrix is obtained. The various forms of normalized noise correlation matrix for the different noise representations are tabulated in Table 4.2. In Table 4.2, the overbar denotes statistical average, *k* is the Boltzmann's constant, T_0 is the reference absolute temperature, i.e., 290K, df is the noise bandwidth and finally, the plus sign denotes the conjugate transpose.

Table 4.2 Normalized correlation matrices for admittance, impedance, ABCD, S-wave and T-wave representations.

Type of Normalized Noise Correlation Matrix	Expression
Admittance Representation	$C_Y = \frac{1}{4kT_0 df}\overline{\begin{bmatrix} I_{n1} \\ I_{n2} \end{bmatrix}\begin{bmatrix} I_{n1} \\ I_{n2} \end{bmatrix}^+}$
Impedance Representation	$C_Z = \frac{1}{4kT_0 df}\overline{\begin{bmatrix} V_{n1} \\ V_{n2} \end{bmatrix}\begin{bmatrix} V_{n1} \\ V_{n2} \end{bmatrix}^+}$
ABCD Representation	$C_A = \frac{1}{4kT_0 df}\overline{\begin{bmatrix} V_n \\ I_n \end{bmatrix}\begin{bmatrix} V_n \\ I_n \end{bmatrix}^+}$
S-wave Representation	$C_S = \frac{1}{4kT_0 df}\overline{\begin{bmatrix} B_{n1} \\ B_{n2} \end{bmatrix}\begin{bmatrix} B_{n1} \\ B_{n2} \end{bmatrix}^+}$
T-wave Representation	$C_T = \frac{1}{4kT_0 df}\overline{\begin{bmatrix} -A_n \\ B_n \end{bmatrix}\begin{bmatrix} -A_n \\ B_n \end{bmatrix}^+}$

Generally, the noise correlation matrices are Hermitian matrices because

$$\mathrm{Im}(c_{11})=\mathrm{Im}(c_{22})=0;\ c_{12}=c_{21}^{*}, \tag{4.28}$$

where the c_{ij} with indices i,j=1,2 is the element of the correlation matrix. This in turn implies that the noise properties of noisy linear two-ports can be fully described by four real numbers, namely c_{11}, c_{22}, the real term of c_{12} and the imaginary term of c_{12}. In addition, these matrices as illustrated in Table 4.2 are positive semi-definite [87].

After the boundary conditions of the two-port network with arbitrary internal topology are imposed in equations (4.26) and (4.27), it is noticed that the resultant correlation matrices are N×N in size. These boundary conditions may includes may include expression like $\overline{B}=\overline{\Gamma A}$ with $\overline{A}$ and $\overline{B}$ being the vectors of incoming and outgoing waves at their ports respectively and $\overline{\Gamma}$ is the connection matrix. As an example, if we eliminate vector $\overline{B}$ from equation (4.27) using the imposed boundary, we obtain

$$\overline{A}=(\overline{\Gamma}-\overline{S})^{-1}\overline{B_n}=\overline{W}^{-1}\overline{B_n}\ . \tag{4.29}$$

Hence, it follows that a correlation matrix of the incident noise waves in all circuit ports is expressed as:

$$\overline{\overline{AA^{+}}}=\overline{W}^{-1}\left(\overline{\overline{B_nB_n^{+}}}\right)\left(\overline{W}^{-1}\right)^{+}, \tag{4.30}$$

where, for clarity, the double overbar denotes statistical average and the single overbar represents a matrix. The middle term on the right-hand side of equation (4.30), which is enclosed in the bracket, is the correlation matrix of the noise wave sources representing noise generated in all circuit elements. Similar to the noise wave approach, the admittance representation has been derived by Niclas [92] [93] and Dobrowolski [91]. There also exists a (N×N) inverse, which is reproduced here as $-Y_{ed}[Y_{dd}+y]^{-1}$, when the admittance representation is adopted.

At this point of time, it can be realized that there is a necessity to solve $(\Gamma\text{-}S)^{-1}$ (see equation 4.30) or $-Y_{ed}[Y_{dd}+y]^{-1}$, which are both N×N matrix, by using the sparse matrix techniques. This is truly not efficient as the computation time will be long if N is large. A review of Table 4.1 shows that except for the Scattering (S) or Transfer (T) representation, a physical insight into the reflection coefficient, coupling, VSWR and other noise associated properties of the network cannot be obtained directly from these representations without some conversions.

Besides the above, in 1962, Penfield [84] had based on his noise analysis on the constraint that the normalization impedance Z_0 used was the optimum source impedance, and obtained $\overline{a_n b_n^*} = 0$. However, such an analysis is often not practical as the optimum source impedance is one of the four unknowns that one is looking for. Implicitly, References [85] and [91] have not imposed such a constraint. Nevertheless, no attempt has been made to derive more general expressions for the four noise parameters in terms of the equivalent noise temperatures T_a and T_b, since these are the parameters that are of most engineering interest and are most convenient to work with.

The motivation behind this part of the work arises from the need to integrate the noise wave representation into efficient algorithms that alleviate the above the problems. Without imposing the constraint $\overline{a_n b_n^*} = 0$, some general expressions for the four noise parameters in terms of the equivalent noise temperatures T_a and T_b are also presented. The derivation of these general expressions will be explained in detail in section 4.4. Based on the Scattering and Transfer representations, two alternative methods that can result in faster and more efficient computation of the four noise parameters as compared to the conventional methods are proposed in section 4.5.

4.4 New Expressions for Noise Parameters

The basic concept of noise analysis, which has been discussed earlier, consists of replacing the two-port noisy network with a noise-free network and two noise sources, see Figure 4.3 (d). The wave representation differs from the impedance or admittance representation in that the noise sources are the noise-wave generators A_n and B_n at the input of the two-port network as shown in Figure 4.3(e), or the noise wave generators B_{n1} and B_{n2} at each end of the network as given in Figure 4.3(d). These noise wave sources represent the noise generated in the two-port network. The noise-wave generators A_n and B_n at the input of the two-port network, in terms of the parameters of the Rothe-Dahlke model [83] are respectively given as:

$$A_n = -\frac{V_n + Z_0 I_n}{2\sqrt{\mathrm{Re}(Z_0)}} = -a_n, \tag{4.31}$$

and

$$B_n = \frac{V_n - Z_0^* I_n}{2\sqrt{\mathrm{Re}(Z_0)}} = b_n, \tag{4.32}$$

where Z_0 is a normalization impedance. a_n and b_n are introduced so as to account for the sign conversion. Thus, if the scattering matrix of the two-port is **S**, we obtain

$$\begin{bmatrix} b_1 \\ b_2 \end{bmatrix} = \begin{bmatrix} S_{11} & S_{12} \\ S_{21} & S_{22} \end{bmatrix} \begin{bmatrix} a_1 \\ a_2 \end{bmatrix} + \begin{bmatrix} S_{11} & 1 \\ S_{21} & 0 \end{bmatrix} \begin{bmatrix} A_n \\ B_n \end{bmatrix}, \tag{4.33}$$

The equivalent noise temperatures T_a and T_b, and the correlation coefficient $\rho_{ab} = |\rho| e^{\phi}$, in terms of these noise sources, are respectively defined as

$$T_a = \frac{\overline{|A_n|^2}}{kB}, \tag{4.34}$$

$$T_b = \frac{\overline{|B_n|^2}}{kB}, \tag{4.35}$$

and

$$\rho_{ab} = \frac{\overline{a_n b_n^*}}{\sqrt{\overline{|a_n|^2}\,\overline{|b_n|^2}}}, \tag{4.36}$$

where k is the Boltzmann's constant and B is the frequency bandwidth. Using these fundamental definitions and the noise parameters equations as found in [93], the four noise parameters are thus derived as

$$R_n = \frac{|Z_0|^2 (T_a + T_b) + 2\sqrt{T_a T_b}\,\mathrm{Re}\left((Z_0^*)^2 \rho_{ab}\right)}{4T_0\,\mathrm{Re}(Z_0)}, \tag{4.37}$$

$$(F-1)_{\min} = \frac{1}{2T_0\,\mathrm{Re}(Z_0)}$$

$$\left(\sqrt{\left((T_a + T_b)|Z_V|^2 - 2\,\mathrm{Re}\left((Z_0^*)^2 \rho_{ab}\right)\right)\left(T_a + T_b - 2\,\mathrm{Re}(\rho_{ab})\sqrt{T_a T_b}\right) - 4T_a T_b\,\mathrm{Im}(Z_0^* \rho_{ab})^2}\right.$$

$$\left. + Z_0 T_a - T_b Z_0^*\right), \tag{4.38}$$

$$R_{opt} = \frac{\sqrt{\left((T_a + T_b)|Z_V|^2 - 2\,\mathrm{Re}\left((Z_0^*)^2 \rho_{ab}\right)\sqrt{T_a T_b}\right)\left(T_a + T_b - 2\,\mathrm{Re}(\rho_{ab})\sqrt{T_a T_b}\right) - 4T_a T_b\,\mathrm{Im}(Z_0^* \rho_{ab})^2}}{T_a + T_b - 2\sqrt{T_a T_b}\,\mathrm{Re}(\rho_{ab})} \tag{4.39}$$

and

$$X_{opt} = \frac{2\,\mathrm{Im}(Z_0^* \rho_{ab})\sqrt{T_a T_b}}{T_a + T_b - 2\,\mathrm{Re}(\rho_{ab})\sqrt{T_a T_b}}, \tag{4.40}$$

where T_0=290 K is the reference absolute temperature. The equivalent temperatures T_a and T_b are adopted mainly because the magnitudes of the self- and cross-power spectral densities are too small to be handled by the computer. This small magnitude in the self- and cross-power spectral densities can result in large propagation error and run-off error. The equivalent noise temperatures T_a and T_b, and the coefficient ρ_{ab}, which are of manageable quantities, can easily be obtained from the correlation matrix of the noise sources. This correlation matrix is given as follows:

$$C_T = \begin{bmatrix} \overline{|A_n|^2} & \overline{-A_n B_n^*} \\ -A_n^* B_n & |B_n|^2 \end{bmatrix}. \tag{4.41}$$

The noise figure of the whole network can finally be computed from

$$F = F_{\min} + \frac{R_n}{R_s}\left|\frac{Z_s}{Z_{opt}} - 1\right|^2. \tag{4.42}$$

4.5 The T-wave and S-wave Approaches

4.5.1 The T-wave Approach

From Figure 4.3(e), it can be deduced that the matrix transformation of the wave representation is given as

$$\begin{bmatrix} a_1 \\ b_1 \end{bmatrix} = \begin{bmatrix} T_{11} & T_{12} \\ T_{21} & T_{22} \end{bmatrix} \begin{bmatrix} b_2 \\ a_2 \end{bmatrix} + \begin{bmatrix} A_n \\ B_n \end{bmatrix}, \tag{4.43}$$

where T_{ij}, i,j=1,2 are the transfer scattering parameters of the two port. By extending this analysis to circuits containing multiports, it is assumed that each linear noisy network may be represented as the interconnection of lossy passive multiports which introduce only thermal noise, and noisy active two-ports. Each linear element in the circuit may be represented by its noiseless equivalent having the same transfer matrix T as the original network. As shown in Figure 4.4, noisy generated in each element is represented by its mutually correlated noise wave sources at the input of the network. The correlation matrix of an interconnection of two noisy n-ports is a linear transformation of their individual correlation matrices. The formula that relates the resulting correlation matrix to the correlation matrices of the n-ports according to their connection is expressed as

$$C_T = C_T^{(1)} + \sum_{i=1}^{M-1}\left(\prod_{k=1}^{i} T^{(k)}\right) C_T^{(i+1)} \left[\prod_{k=1}^{i} T^{(k)}\right]^+ \tag{4.44}$$

where M is the total number of two-port networks, the superscript refers to the connected n-ports, the plus sign denotes the Hermitian complex conjugate and C_T is the correlation (N×N) matrix.

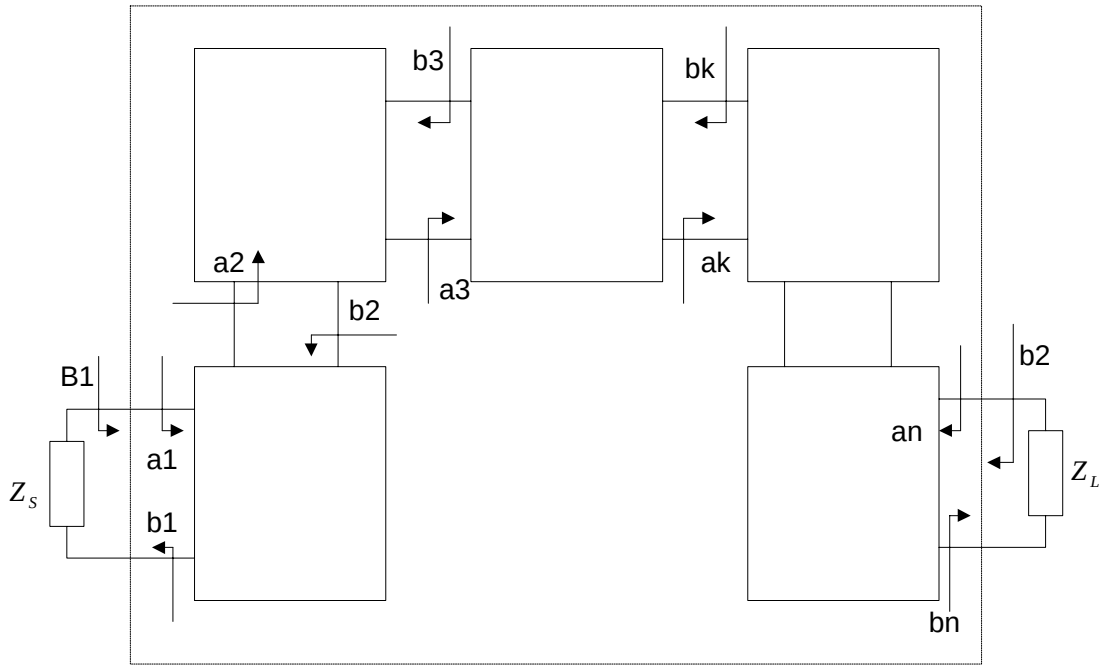

Figure 4.4 Equivalent circuit of a noisy multiport network with noiseless elements and noise wave sources at the input port.

The correlation matrix of lossy passive multiports can be evaluated from equation (4.45) which is expressed as

$$C_T = kTB\left(\begin{bmatrix} -I & 0 \\ 0 & I \end{bmatrix} + T\begin{bmatrix} I & 0 \\ 0 & -I \end{bmatrix}T^{+}\right), \tag{4.45}$$

where T is the transfer matrix of the original network, I is the identity matrix of size (N/2 x N/2) and the plus sign denotes the Hermitian complex conjugate. The quantity in the bracket of equation (4.45) is called the noise distribution matrix because it describes how the thermal noise power generated in the multiport is distributed over its ports. The correlation matrix of active HBT device is obtained by

$$C_T = kTB\begin{bmatrix} C_1 & C_2 \\ C_2^{*} & C_3 \end{bmatrix}, \tag{4.46}$$

where

$$C_1 = \xi_{11} + 2\,\mathrm{Re}[\xi_{12}(T_{11} - T_{12})] + \left|T_{11} - T_{12}\right|^2 \xi_{22}, \tag{4.47}$$

$$C_2 = -\xi_{11} + (T_{21}^* - T_{22}^*)[\xi_{12} + (T_{11} - T_{12})\xi_{22}] - \xi_{12}(T_{11} - T_{12}), \tag{4.48}$$

$$C_3 = \xi_{11} + 2\,\mathrm{Re}[(T_{22} - T_{21})\xi_{12}^*] + \left|T_{21} - T_{22}\right|^2 \xi_{22}, \tag{4.49}$$

$$\xi_{11} = G_{opt}(F_{\min} - 1) - \frac{(F_{\min} - 1)^2}{4R_n} + R_n \left| \frac{T_{11} + T_{22} - T_{12} - T_{21}}{Z_0(T_{21} - T_{22} + T_{11} - T_{12})} + Y_{opt} - \frac{(F_{\min} - 1)^2}{2R_n} \right| \tag{4.50}$$

$$\xi_{12} = \frac{-2R_n}{Z_0(T_{21} - T_{22} + T_{11} - T_{12})} \left(\frac{T_{11} + T_{22} - T_{12} - T_{21}}{Z_0(T_{21} - T_{22} + T_{11} - T_{12})} + Y_{opt} - \frac{(F_{\min} - 1)}{2R_n} \right) \tag{4.51}$$

$$\xi_{22} = \frac{4R_n}{\left|Z_0(T_{21} - T_{22} + T_{11} - T_{12})\right|^2} \tag{4.52}$$

and T_{ij}, i,j=1,2, are the transfer parameters of the HBT device.

4.5.2 The S-wave Approach

From [94], we can see Gupta's multi-connection method can be applied to noise analysis as well as in signal analysis. Through this multi-connection method, we can partition the multi-port into external and internal ports. Hence, the matrix transformation of the wave representation of Figure 4.3(d) can be re-written as

$$\begin{bmatrix} b_p \\ b_c \end{bmatrix} = \begin{bmatrix} S_{pp} & S_{pc} \\ S_{cp} & S_{cc} \end{bmatrix} \begin{bmatrix} a_p \\ a_c \end{bmatrix} + \begin{bmatrix} N_{pp} & N_{pc} \\ N_{cp} & N_{pp} \end{bmatrix} \begin{bmatrix} B_p \\ B_c \end{bmatrix}, \tag{4.53}$$

where a_p, b_p and a_c, b_c are vectors of incoming and outgoing waves, respectively, in the external and internal ports of the circuit, and B_p and B_c are noise sources at the external and internal ports of the circuit, respectively. The connections of pairs of internal ports impose on the vectors of incoming and outgoing waves in the form:

$$b_c = \Gamma_c a_c \tag{4.54}$$

From equation (4.53) and (4.54), by first eliminating b_c, we obtain

$$a_c = (\Gamma_c - S_{cc})^{-1} S_{cp} a_p + (\Gamma_c - S_{cc})^{-1} (N_{cp} B_p + N_{cc} B_c), \tag{4.55}$$

and, after next eliminating a_c, we have in the overall S-parameters as

$$b_p = [S_{pp} + S_{pc}(\Gamma_c - S_{cc})^{-1} S_{cp}] a_p + S_{pc}(\Gamma_c - S_{cc})^{-1} (N_{cp} B_p + N_{cc} B_c) + N_{pp} B_p + N_{pc} B_c \tag{4.56}$$

The correlation matrix is evaluated as

$$C_T = \left[S_{pc}(\Gamma_c - S_{cc})^{-1} N_{cp} + N_{pp} \quad S_{pc}(\Gamma_c - S_{cc})^{-1} N_{cc} \right] \overline{\begin{bmatrix} B_p \\ B_c \end{bmatrix}^+ \begin{bmatrix} B_p \\ B_c \end{bmatrix}} \begin{bmatrix} S_{pc}(\Gamma_c - S_{cc})^{-1} N_{cp} + N_{pp} \\ S_{pc}(\Gamma_c - S_{cc})^{-1} N_{cc} + N_{pc} \end{bmatrix}^*, \tag{4.57}$$

where + sign denotes the Hermitian complex conjugate and * sign is the complex conjugate.

Similar to the near optimal ordering of the connection sequence proposed by Monato and P. Tiberio [95], we call for, at each step, the connection of the two components whose resulting multiport has the fewest ports. Equation (4.56) and (4.57) are then used repeatedly for combining two components connected together at each step of the analysis. The computational efficiency of the method can be improved by proper ordering and numbering of the internal ports of the two multiports being interconnected.

4.5.3 Calculation of Noise Wave Correlation Matrices of Embedded Multiport by Contour-Integral Method and Multi-Connect Method

Realistic noise modeling of microwave HBT transistor requires the consideration of parasitic elements embedding an intrinsic chip of the device. The embedding circuit composed of parasitic stray capacitances, lead resistances, and inductances is

typically passive. It produces only thermal noise. Since the mechanism of noise generation of the intrinsic device is of a more complicated nature, it is very convenient to consider and model it separately. The effects of a parasitic element circuit on the correlation matrix of the entire device may be computed by appropriate embedding formulation.

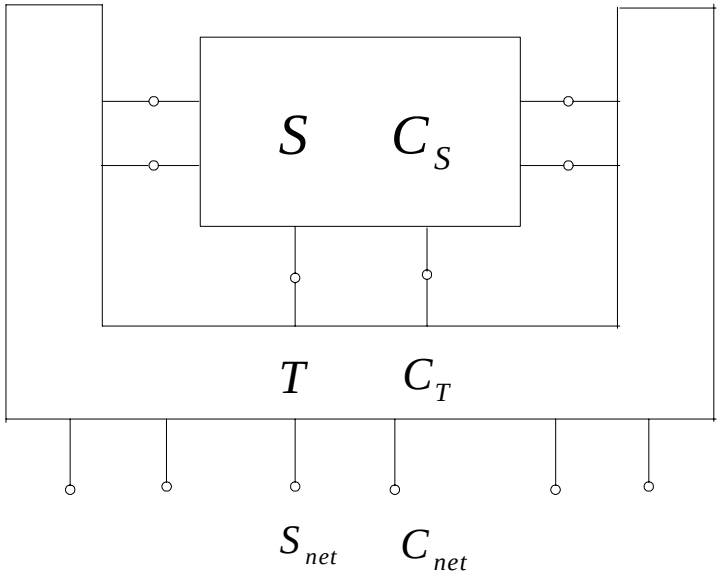

Figure 4.5 Two subnetworks with scattering matrices **S** and **T** described by their noise wave correlation matrices $\mathbf{C_S}$ and $\mathbf{C_T}$ and connected by internal ports. The resultant scattering and noise wave correlation matrices are $\mathbf{S_{net}}$ and $\mathbf{C_{net}}$.

Figure 4.5 presents a noisy multiport subnetwork with scattering matrix **S** embedded in a noisy subnetwork with scattering matrix **T**. It is assumed that noise properties of both subnetworks are described by noise wave correlation matrices $\mathbf{C_S}$ and $\mathbf{C_T}$, respectively. The noise wave correlation matrix of the resultant network is computed by partitioning ports of the embedding subnetwork into two categories: external and internal ports. Accordingly, the system of equations

$$\mathbf{b} = \mathbf{T}\,\mathbf{a} + \mathbf{c} \tag{4.58}$$

can be written as

$$\begin{bmatrix} b_e \\ b_i \end{bmatrix} = \begin{bmatrix} T_{ee} & T_{ei} \\ T_{ie} & T_{ii} \end{bmatrix} \begin{bmatrix} a_e \\ a_i \end{bmatrix} + \begin{bmatrix} c_e \\ c_i \end{bmatrix} \tag{4.59}$$

where a_e, b_e, c_e and a_i, b_i, c_i are vectors of noise waves, respectively, at the external and internal ports of the subnetwork **T**.

The embedded subnetwork is described by the system of equations

$$b_S = Sa_S + c_S \tag{4.60}$$

which, for HBT device, is the intrinsic part of the equivalent circuit.

The connection of internal ports of the embedding subnetwork **T** with appropriate ports of the subnetwork **S** impose restrictions on the vectors of incoming and outgoing noise waves in the forms

$$a_i = b_S \tag{4.61}$$

$$b_i = a_S \tag{4.62}$$

From (4.60), (4.61), (4.62), and the second equation of (4.59), by first eliminating $\mathbf{b_i}$, we obtain

$$a_i = [S^{-1} - T_{ii}]^{-1} T_{ie} a_e + [I - ST_{ii}]^{-1} c_S + [S^{-1} - T_{ii}]^{-1} c_i \tag{4.63}$$

and, after eliminating $\mathbf{a_i}$ from the first equation of (4.59)

$$\begin{aligned} b_e = {} & \{T_{ee} + T_{ei}[S^{-1} - T_{ii}]^{-1} T_{ie}\} a_e \\ & + T_{ei}[I - ST_{ii}]^{-1} c_S + T_{ei}[I - ST_{ii}]^{-1} S c_i + c_e \end{aligned} \tag{4.64}$$

In (4.64),

$$c_{out} = T_{ei}[I - ST_{ii}]^{-1} c_S + T_{ei}[I - ST_{ii}]^{-1} S c_i + c_e \tag{4.65}$$

is a vector of resultant noise waves of the whole network referred to the external ports.

Using equation (4.65), the resultant noise wave correlation matrix of the network can be found as

$$C_{net} = \Lambda C_S \Lambda^+ + [I \mid \Lambda S] C_T [I \mid \Lambda S]^+ \tag{4.66}$$

where $\mathbf{C_T}$ is the noise wave correlation matrix of network **T**

$$\mathbf{C_T} = kT\,(\mathbf{I} + \mathbf{S}\,\mathbf{S}^+) \tag{4.67}$$

where **S** is the scattering matrix of HBT parasitic passive multiport, which is calculated by equation (3.58) of contour-integral method, and Λ is the matrix given as

$$\Lambda = T_{ei}[I - ST_{ii}]^{-1}. \tag{4.68}$$

The final two-port noise wave correlation matrix can be obtained from three-port noise wave correlation matrix by the following transformation:

$$C = K' C_T K'^{+} \tag{4.69}$$

where

$$K = \begin{bmatrix} 1 & 0 & -\dfrac{S_{net13}}{1+S_{net33}} \\ 1 & 0 & -\dfrac{S_{net13}}{1+S_{net33}} \end{bmatrix}. \tag{4.70}$$

To take into account the device distributed nature, the HBT device can be assumed to be a noisy *n*-port consisting of a lossy passive network embedding a number (*m*) of noisy two-port devices, specifically HBT intrinsic unit cells. We can also assume that each unit cell of the HBT intrinsic equivalent circuit can be described by its scattering matrix and its noise correlation matrix. As shown in Figure 4.6, the circuit to be analyzed can be treated as the interconnection of a passive noisy multiport and *m* noisy two-ports. The passive noisy multiport generates only thermal noise. Using the results in Table 4.1, it is obvious that the circuit in Figure 4.6(a) can be represented by its noiseless equivalent with noise wave sources. Figure 4.6(b) presents this equivalent.

Considering all *m* unit cells of the circuit, we have a set of linear equations whose matrix form is

$$\mathbf{b} = \mathbf{S}\,\mathbf{a} + \mathbf{c} \tag{4.71}$$

where

$$a = \begin{bmatrix} a^{(1)} \\ a^{(2)} \\ \vdots \\ a^{(k)} \\ \vdots \\ a^{(m)} \end{bmatrix} \qquad b = \begin{bmatrix} b^{(1)} \\ b^{(2)} \\ \vdots \\ b^{(k)} \\ \vdots \\ b^{(m)} \end{bmatrix} \qquad c = \begin{bmatrix} c^{(1)} \\ c^{(2)} \\ \vdots \\ c^{(k)} \\ \vdots \\ c^{(m)} \end{bmatrix} \tag{4.72}$$

and

$$S = \begin{bmatrix} S^{(1)} & 0 & \cdots & 0 & \cdots & 0 \\ 0 & S^{(2)} & & & & 0 \\ \vdots & & \ddots & & & \vdots \\ 0 & & & S^{(k)} & & 0 \\ \vdots & & & & \ddots & 0 \\ 0 & \cdots & \cdots & 0 & 0 & S^{(m)} \end{bmatrix} \tag{4.73}$$

The connections between the m unit cells impose constraints on the vectors **a** and **b**, which can be represented as a matrix equation

$$\mathbf{b} = \mathbf{\Gamma}\,\mathbf{a} \tag{4.74}$$

where $\mathbf{\Gamma}$ is the connection matrix.

After elimination of the vector **b** from (4.71) and (4.74), we obtain

$$\mathbf{W}\,\mathbf{a} = \mathbf{c} \tag{4.75}$$

where

$$\mathbf{W} = \mathbf{\Gamma} - \mathbf{S} \tag{4.76}$$

is the connection scattering matrix of the analyzed network.

Using (4.75) we are able to get a correlation matrix of the incident noise waves at all circuit ports. Because

$$\mathbf{a} = \mathbf{W}^{-1}\,\mathbf{c} \tag{4.77}$$

it follows that

$$\overline{aa^+} = W^{-1}\overline{cc^+}(W^{-1})^+ = W^{-1}C(W^{-1})^+ \tag{4.78}$$

where the daggers indicates the Hermitian complex conjugate of vectors and matrices. In (4.78),

$$\mathbf{C} = \overline{\mathbf{cc}^+} \tag{4.79}$$

is the correlation matrix of the noise wave sources representing noise generated in the circuit elements.

Because the noise wave sources $\mathbf{c}^{(k)}$ of the *k*th unit cell are uncorrelated with those of any other circuit element, the correlation matrix **C** is a block diagonal matrix of the form

$$\boldsymbol{C} = \overline{\boldsymbol{cc}^+} = \begin{bmatrix} \boldsymbol{C}_s^{(1)} & \mathbf{0} & \cdots & \mathbf{0} & \cdots & \mathbf{0} \\ \mathbf{0} & \boldsymbol{C}_s^{(2)} & & & & \vdots \\ \vdots & & \ddots & & & \vdots \\ \mathbf{0} & & & \boldsymbol{C}_s^{(k)} & & \mathbf{0} \\ \vdots & & & & \ddots & \vdots \\ \mathbf{0} & \cdots & \cdots & \mathbf{0} & \cdots & \boldsymbol{C}_s^{(m)} \end{bmatrix} \tag{4.80}$$

in which $\boldsymbol{C}_s^{(1)}$, $\boldsymbol{C}_s^{(2)}$, ……, $\boldsymbol{C}_s^{(m)}$ are correlation matrices of the noise wave sources of individual network elements and the **0s** represent null matrices.

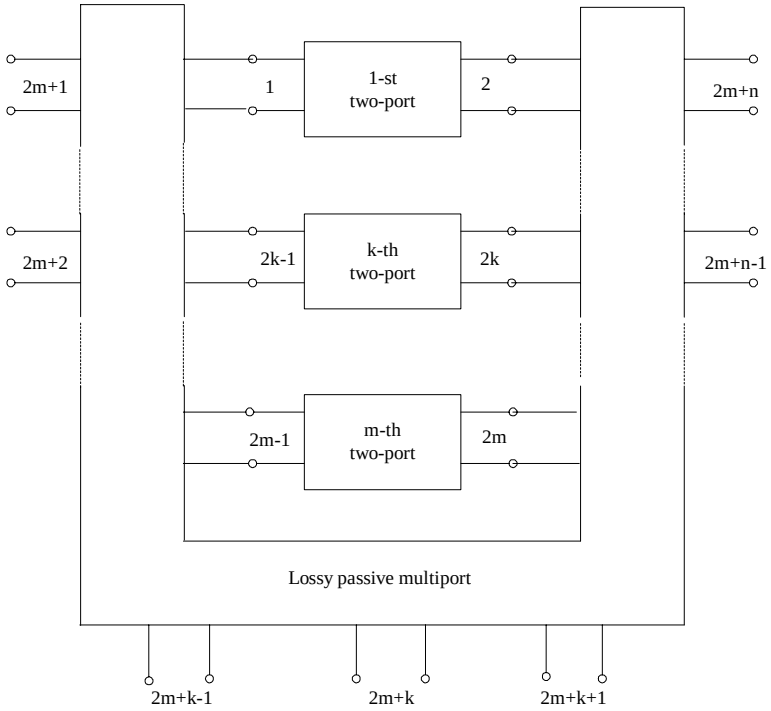

Figure 4.6(a) Noisy circuit decomposed into m noisy active two-ports and a noisy passive multiport with n external ports.

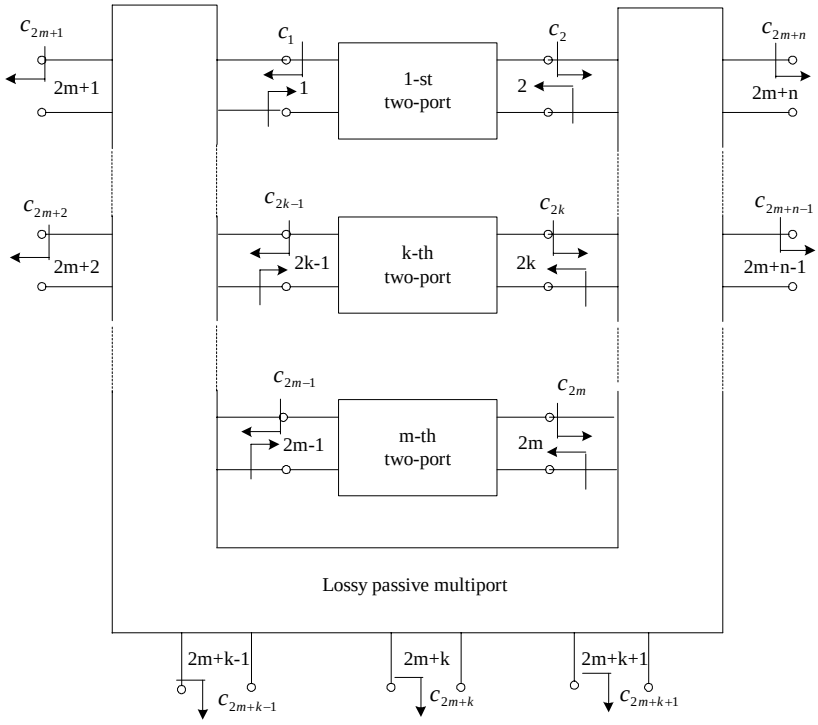

Figure 4.6(b) Noiseless equivalent of the noisy linear circuit presented in Figure 4.6(a).

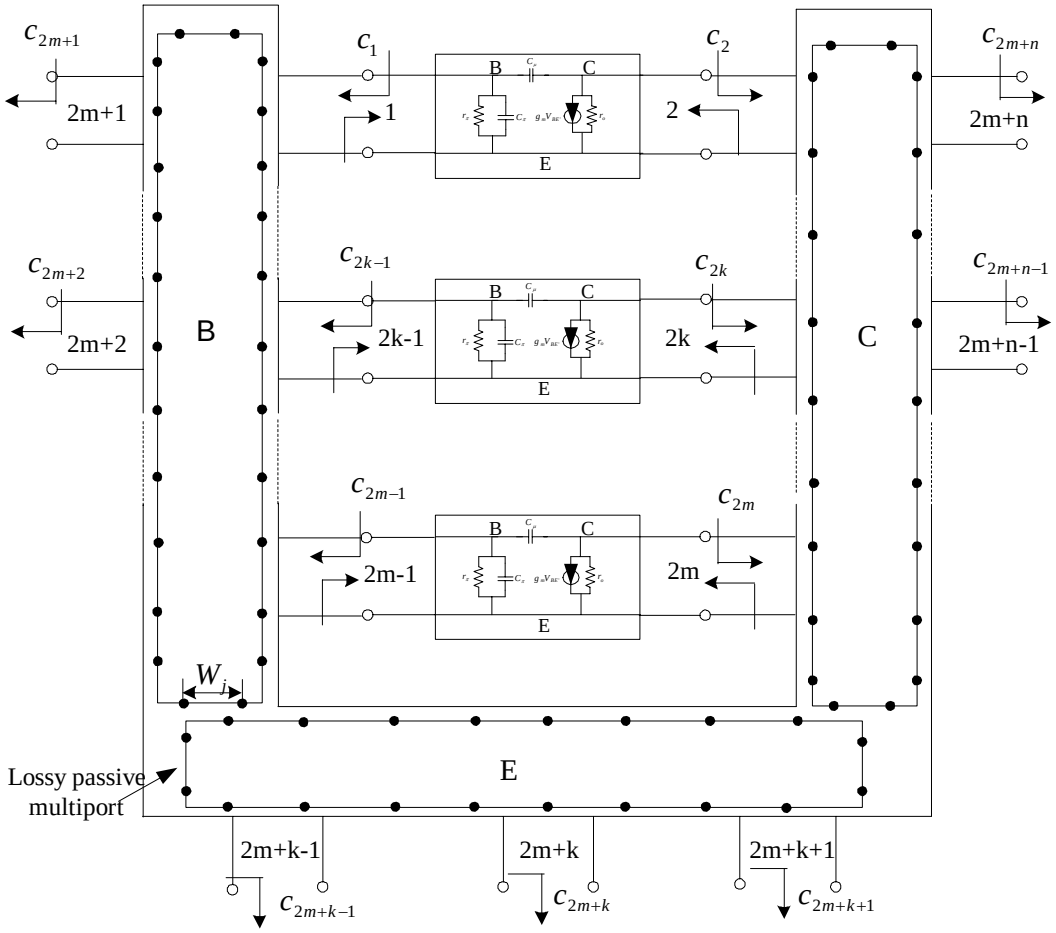

Figure 4.6(c) Noiseless equivalent of HBT noisy circuit separated into m unit cells and the coupling ports in parasitic periphery.

4.6 Determination of Equivalent Noise Temperatures

To evaluate the noise performance of the HBT device using S-wave and T-wave approaches, the equivalent noise temperatures must be known. The noise model parameters, T_b and T_c can be determined by assigning T_b to ambient temperature 290K, and calculating T_c analytically. The analytical derivation of extracting T_c is based on the nodal analysis of HBT small-signal equivalent circuit and noise figure definition.

The noise figure quantitatively describes the performance of a noisy microwave device. The noise figure is defined as the ratio of the total available noise power at the output of the device to the available noise power at the output due to thermal noise from the input termination R, where R is at the standard temperature 290 K. Let G_A represent the available power gain. Let N_{int} be the noise generated inside the two-port referred to the output, and let N_{inj} represent the noise injected at the input referred to the output. The noise figure may be expressed as [96]

$$F = \frac{P_{Si}/P_{Ni}}{P_{So}/P_{No}} = \frac{P_{Si}}{P_{Ni}} \frac{N_{\text{int}} + N_{inj} G_A}{P_{Si} G_A} = 1 + \frac{N_{\text{int}}}{N_{inj}}, \tag{4.81}$$

where $G_A = \frac{P_{So}}{P_{Si}}$, P_{Si} is the available signal power at the input, $P_{Ni} = kT_0\Delta f$ is the available noise power due to R at $T = T_0 = 290K$ in 1 Hz bandwidth, P_{So} is the available signal power at the output and P_{No} is total noise power at the output. In the above HBT temperature noise model, the device noise is modeled by the noisy resistor. The thermal noise in the frequency band Δf, generated by the noisy resistor *R*, which is held at uniform temperature T, is modeled with a parallel current generator. This current has the mean-square value

$$\left\langle i_0^2 \right\rangle = \frac{4kT\Delta f}{R}, \tag{4.82}$$

Assume we have an arbitrary linear small-signal equivalent circuit with N resistors. Let n' and n" represent the input and output node numbers, respectively. From the circuit nodal analysis, the output voltage generated by the resistor R can be expressed as:

$$V_{out} = (Z_{out,n'} - Z_{out,n''}) \cdot i_n \tag{4.83}$$

where **Z** is the impedance matrix of the circuit. According to Nyquist's theorem, the thermal noise generated by this resistor can be represented by a current generator i_n. This generator lies in parallel with a noiseless resistor, as shown in Figure 4.7(a).

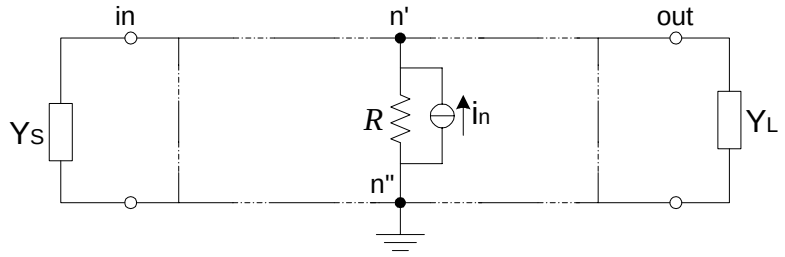

Figure 4.7(a) Arbitrary linear small-signal equivalent circuit.

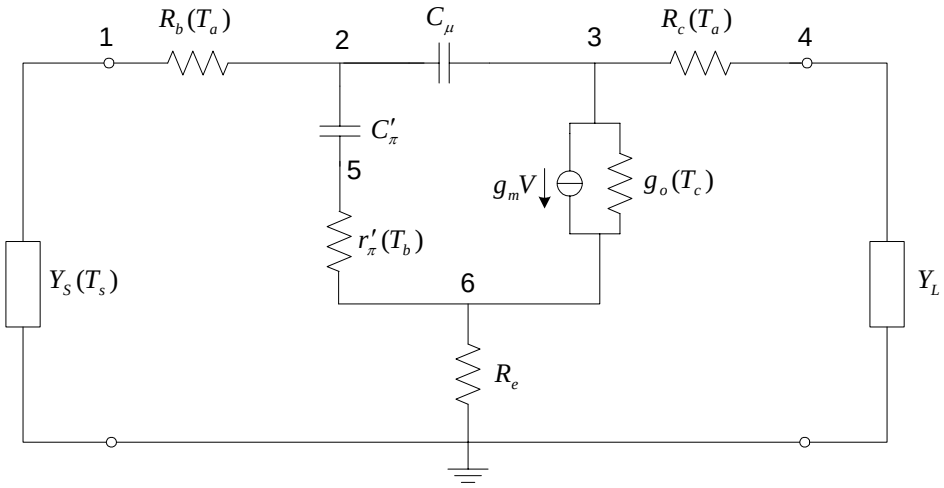

Figure 4.7(b) Noise model equivalent circuit of HBT device with nodal number with the external source and load admittances.

Thus the mean-square value of the output noise voltage is obtained as

$$\left\langle V_{out}^2 \right\rangle = \left| Z_{out,n'} - Z_{out,n''} \right|^2 \frac{4kT_n \Delta f}{R}, \tag{4.84}$$

where T_n is the resistor noise temperature.

Therefore the total output noise power N_{int} delivered to the load Y_L by all N resistors is

$$N_{\text{int}} = 2k\Delta f \ \text{Re}(Y_L) \sum_{n=1}^{N} \frac{T_n}{R} \left| Z_{out,n'} - Z_{out,n''} \right|^2 . \tag{4.85}$$

Similarly,

$$N_{inj} = 2\left|Z_{out,in}\right|^2 T_S \Delta f \ \mathrm{Re}(Y_L)\mathrm{Re}(Y_S), \tag{4.86}$$

where Y_S and T_S are the source admittance and temperature, respectively.

The noise figure of the circuit, *F*, is obtained by combining (4.81), (4.85) and (4.86)

$$F = 1 + \frac{\sum_{k=1}^{N} \frac{T_k}{R_k}\left|Z_{out,n'} - Z_{out,n''}\right|^2}{T_S \ \mathrm{Re}(Y_S)\left|Z_{out,in}\right|^2}. \tag{4.87}$$

By solving the (4.87), the noise temperature of any resistor is

$$T_m = R_m \frac{(F-1)T_S \ \mathrm{Re}(Y_S)\left|Z_{out,in}\right|^2 - \sum_{\substack{k=1 \\ k\neq m}}^{N} \frac{T_k}{R_k}\left|Z_{out,n'} - Z_{out,n''}\right|^2}{\left|Z_{out,m'} - Z_{out,m''}\right|^2}. \tag{4.88}$$

This expression enables the direct analytical calculation of an associated noise temperature [97]-[99].

To apply the above principle, the circuit topology and the number of noise resistors must be specified. Now we apply (4.88) to the HBT temperature noise model as shown in Figure 4.7(b). Figure 4.7(b) shows the HBT temperature noise model, together with the external source and load admittances. Setting an collector noise temperature T_c to the output conductance r_0 while keeping all other resistances at the ambient temperature T_a, the device noise performance can be modeled as in Section 4.5.

The value of T_c can be extracted from the noise figure F by the use of (4.88). Referring to the node number given in Figure 4.7(b)

$$T_c = r_0 \frac{(F-1)\cdot T_S \cdot \mathrm{Re}(Y_S)\cdot\left|Z_{4,1}\right|^2 - T_a \cdot \Phi}{\left|Z_{4,3} - Z_{4,6}\right|^2}, \tag{4.89}$$

where

$$\Phi = \frac{\left|Z_{4,1} - Z_{4,2}\right|^2}{R_b} - \frac{\left|Z_{4,5} - Z_{4,6}\right|^2}{r_\pi^{'}} - \frac{\left|Z_{4,6} - Z_{4,0}\right|^2}{R_e} - \frac{\left|Z_{4,3} - Z_{4,4}\right|^2}{R_c},$$

where the inverse admittance elements of matrix **Z** are given by

$$Y_{11} = Y_S + \frac{1}{R_b},$$

$$Y_{12} = Y_{21} = -\frac{1}{R_b},$$

$$Y_{22} = \frac{1}{R_b} + j\omega(c_\pi^{'} + c_u),$$

$$Y_{23} = Y_{32} = -j\omega c_u,$$

$$Y_{25} = Y_{52} = -j\omega c_\pi^{'},$$

$$Y_{33} = j\omega c_u + g_0 + \frac{1}{R_c},$$

$$Y_{34} = Y_{43} = -\frac{1}{R_c},$$

$$Y_{35} = Y_{62} = -g_m e^{-j\omega\tau},$$

$$Y_{36} = Y_{63} = -g_0,$$

$$Y_{44} = \frac{1}{R_c},$$

$$Y_{55} = j\omega c_\pi^{'} r_\pi^{'},$$

$$Y_{56} = -\frac{1}{r_\pi^{'}},$$

$$Y_{65} = -\frac{1}{r_\pi^{'}} + g_m e^{-j\omega\tau},$$

$$Y_{66} = g_0 + \frac{1}{r_\pi^{'}}.$$

where $r_\pi^{'} = \dfrac{r_\pi}{1+\omega^2 r_\pi^2 c_\pi^2}$ and $c_\pi^{'} = \dfrac{1+\omega^2 r_\pi^2 c_\pi^2}{\omega^2 r_\pi^2 c_\pi}$.

As noted in Figure 4.8, T_c is significantly higher than the ambient temperature value and is obtained to be a function of collector current.

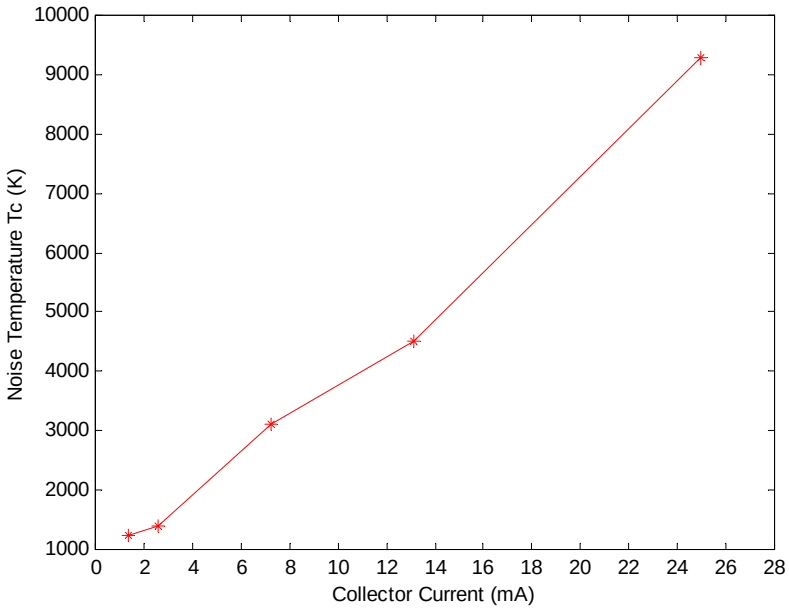

Figure 4.8 Extracted collector noise temperature T_c versus collector current for the GaAs HBT device at Vcb=1V.

4.7 Experiments, Results and Discussions

Based on the discussions above and the equivalent noise temperature extracted from the HBT small-signal equivalent circuit, the S-wave approach has been applied to predict the noise behavior of GaAs HBT at I_C=2.37 mA. A MATLAB program for the noise calculation by wave approach is written to demonstrate the feasibility of the proposed method. The noise performance of the GaAs HBT device is measured for verification purpose. The simulated results using both the SPICE noise model and the wave approach are compared with measured results as shown in Figures 4.9-4.12.

The selected HBT transistor has a multi-finger $2\times20\times2$ configuration and h_c=2.5 μm, h_b=2.59 μm and h_e=2.82 μm. As shown in Figure 3.9 (b), to take into account the distributed nature of the HBT device, the multi-finger HBT device is divided into m=10 unit cells with each unit cell has a finger $1\times2\times4$ μm^2. For each HBT unit cell, the contour-integral analysis has been applied and the scattering matrix parameters for each HBT unit cell parasitic subnetwork are calculated using equations (3.42)-(3.46). In the contour-integral calculation, the width of each coupling port W_i is 0.4 μm along the device strips. The equation (3.46) is applied to calculate the impedance matrix for the parasitic passive multiport. The intrinsic device is connected to the strip periphery as the equivalent circuit parameters are determined by the field distribution along the periphery. The impedance matrix of HBT intrinsic device is calculated by the well-known chain matrix formulation. The intrinsic element values are calculated by the analysis method discussed in Chapter 2. The overall scattering matrix of the HBT device is obtained by merging the two matrices together using equation (3.53). The final two-port scattering matrix is computed by the transformation in equation (3.57).

The results of the four noise parameters, both measured and simulated by wave approach and the SPICE model, are depicted in Figures 4.9-4.12. As noted from Figure 4.9 to Figure 4.12, the results calculated by the wave approach agree better with the measured results, compared with calculated results by the SPICE model, especially as the frequency is progressively increased. The SPICE model agrees with the measured results reasonably at lower frequency range and deviates at higher frequencies. This is expected as the HBT equivalent circuit is approximated by simple lumped elements in the SPICE model while the contour-integral method takes into account the distributed nature of the parasitic strips. Therefore, the S-parameters calculated by contour-integral method are more accurate than those obtained from the

SPICE model. In terms of the computational effort, the SPICE model has advantage over the wave approach as the SPICE model does not require the calculation of the inverse of large matrix. From the earlier discussions on the wave approach, it can be seen that an easy manipulation would result if the number of input ports of all the connected ports is equal to the number of output ports. However, if the number of input is smaller than the number of output ports or when there are more input ports than output ports, an extended matrix transformation has to be used. Such an analysis would prevent it from being used as a generalized technique for noise analysis. The S-wave approach, on the other hand, does not have such a problem and can easily be implemented by the existing CAD tools.

In addition to the above considerations, the S-wave approach is noticed to be more prone to rounding-off errors as there is a need for matrix conversions from impedance parameters to the scattering parameters. This existing problem would be aggravated if the internal topologies are complex and long. For this work, the computation time between the conventional admittance representation, which is adopted in commercial software, and the S-wave approach is not compared. Moreover, the computation time is dependent on the complexity of the internal topology of the two-port network.

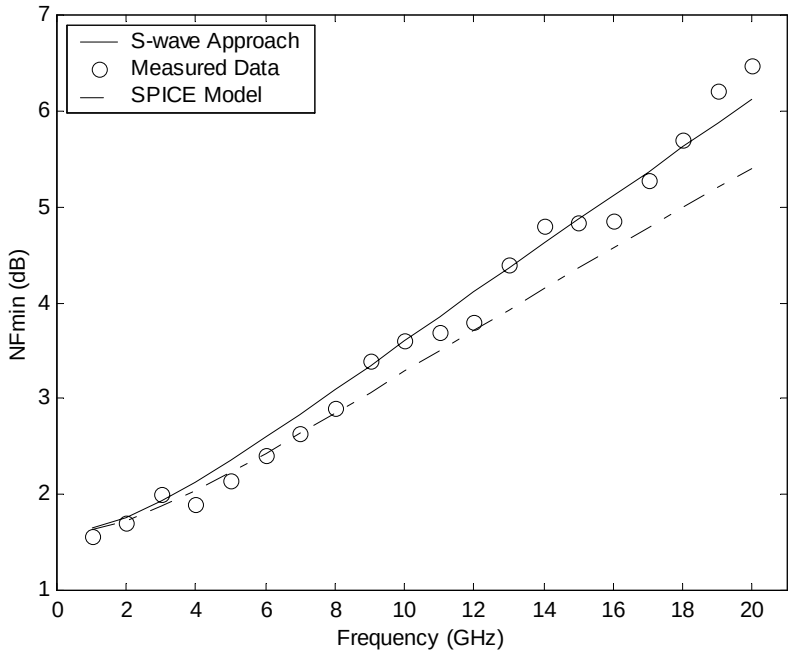

Figure 4.9 Comparison of different approaches to the prediction of NF_{min} versus frequency at Ic=2.37 mA.

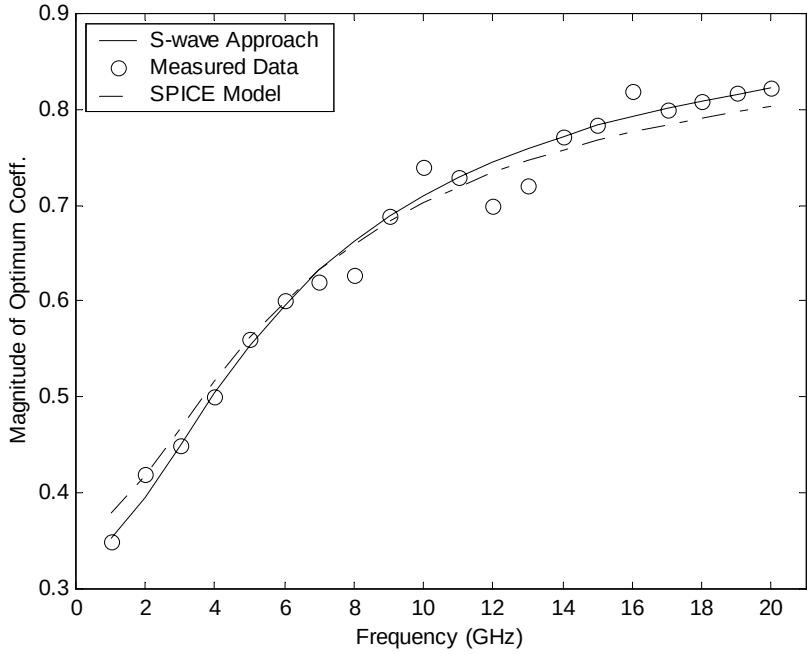

Figure 4.10 Comparison of different approaches to the prediction of the magnitude of $\Gamma_{G,opt}$ versus frequency at Ic=2.37 mA.

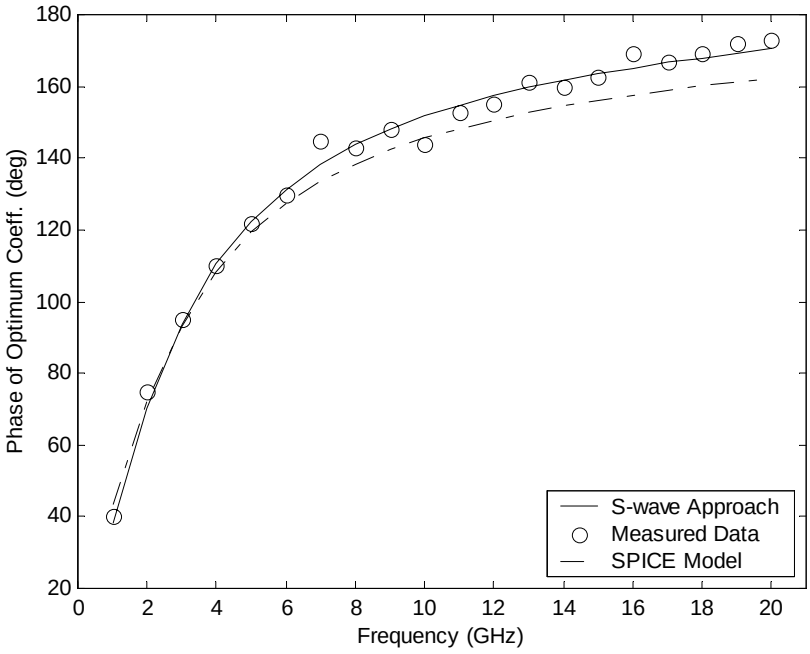

Figure 4.11 Comparison of different approaches to the prediction of the phase of $\Gamma_{G,opt}$ versus frequency at Ic=2.37 mA.

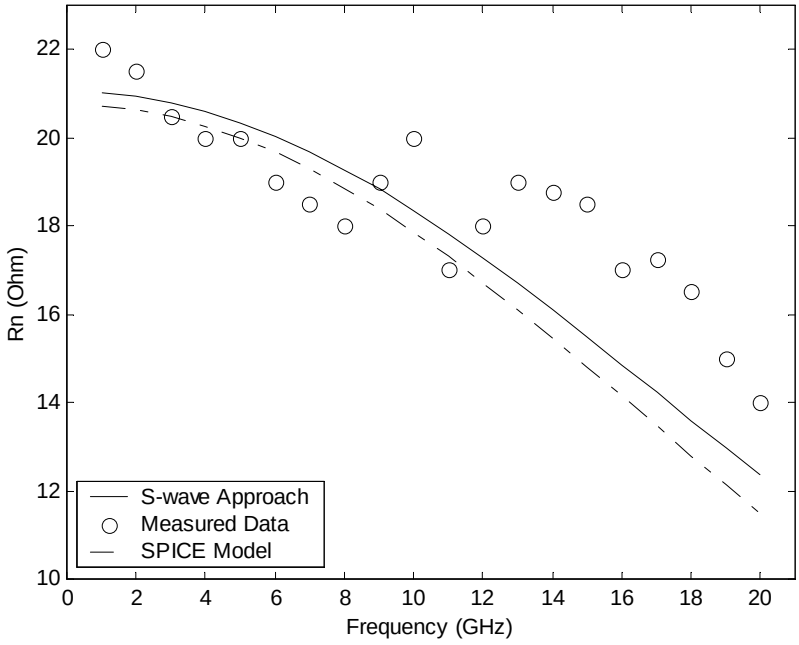

Figure 4.12 Comparison of different approaches to the prediction of the R_n versus frequency at Ic=2.37 mA.

Chapter 5

Large-Signal HBT Models and Modification of VBIC Avalanche Model

5.1 Introduction

Having discussed the small-signal model and parameter extraction, this chapter is devoted to the analysis of HBT large signal models. The BJT/HBT large signal model is probably the first nonlinear transistor model following the invention of the first point-contact bipolar transistor. In 1954, Ebers and Moll proposed a large signal model (EM) for the bipolar transistor. This model is still the background of today's bipolar transistor models [100]. It describes the fundamentals of the DC behavior of the bipolar transistor. However, low and high current effects, as well as parasitic resistors and dynamic behavior are not yet covered in this model. Based on the EM model, an alternative, yet mathematically identical formulated, Gummel-Poon model, has been introduced [101]. The EM model covers all essential effects, which are then included in the Gummel-Poon model, published in 1970. The important advantage of modeling the bipolar transistor with Gummel-Poon model is the clear and standardized descriptions of many effects by introducing the "integral charge control relation" [102]. Therefore, over the years, the Gummel-Poon model has become a standard for the modeling of bipolar transistors.

For modern transistors with the continuous trend to smaller geometries, second order effects become more and more important. Due to the higher integration and the necessity to improve the design yield, the need for more precise simulation results and thus to better models has intensified. Many companies have therefore developed in-house models, and in some cases publish them in public domain. Such a model is the Philips MEXTRAM (Most EXquisite TRAnsistor Model) model. It was developed in 1986 by de Graaff, Klostermann and Jansen [103].

Later, in 1995, a US industry consortium has proposed a new bipolar model, called VBIC95 (Vertical Bipolar Inter-Company). Its goal was to become an accepted standard for today's bipolar transistors [104]. Besides an improved model, which includes the parasitic PNP transistor of integrated NPN transistors, the VBIC 95 is aimed to be as much as possible similar to the standard GP model. Today, it has changed its name to VBIC.

HICUM (HIgh CUrrent Model) model development started around the 1980's with the derivation of the first set of the equations for an improved one-dimensional model [105] [106]. The name HICUM was derived from *high-current model*, indicating that HICUM initially was developed with special emphasis on modeling the operating region at high current densities which is important for certain high-speed applications. In contrast to the Gummel-Poon model, HICUM is based on an extended and "generalized integral charge control relation" [107] [108].

Due to the structural similarities of homojunction bipolar transistors and SiGe heterojunction bipolar transistors, the model used for the design of the HBT circuit is the same as those for the silicon homojunction bipolar transistors. In this chapter, the BJT/HBT large signal models are discussed and encapsulated. Simulation results using the GP model and the VBIC model are also compared. Following this, a

modified avalanche breakdown model is proposed, which can be used to simulate the breakdown behavior well up to high current densities.

5.2 Gummel-Poon Model

Classical theory of drift transistors gives for the forward components of the transfer current, which equals the collector current I_C in the DC case. However, the equations as well as the corresponding relations for the charges are based on several simplifying assumptions, such as the one-dimensional transistor structure. However, in view of today's advanced transistors, the most critical ones are highlighted as follows:

(a) The solutions are restricted only to the neutral base region. Especially, the asymptotic case of very high injection is of no practical interest;
(b) The drift field in the neutral base is calculated purely from an ideal exponential doping profile, neglecting the influence of bandgap variations due to the high doping; and
(c) The equations are derived only for the quasi-static case.

Furthermore, the range of medium and high current densities, which is of practical interest, especially for high-speed applications, cannot be described by asymptotic solutions of basic device physics equations of classical transistor theory in continuous form as it is required for compact models. This disadvantage is avoided by the "integral charge control relation" which was developed by Gummel and is given by the following generalized relations. The transfer current reads as

$$i_T = \frac{I_S}{Q_p / Q_{p0}} \left[\exp\left(\frac{v_{be}}{V_T} \right) - \exp\left(\frac{v_{bc}}{V_T} \right) \right], \tag{5.1}$$

with the saturation current I_S. Q_p is the total hole charge of the one-dimensional transistor, with its zero-bias value Q_{p0}, and reads in normalized form

$$Q_p / Q_{p0} = 1 + Q_{jc} / Q_{p0} + Q_{je} / Q_{p0} + Q_f / Q_{p0} . \tag{5.2}$$

In this expression

$$Q_{je} = \int_0^{v_{be}} C_{je}(v) dv , \tag{5.3a}$$

$$Q_{jc} = \int_0^{v_{bc}} C_{jc}(v) dv , \tag{5.3b}$$

are the charges stored in the base-emitter (BE) and base-collector (BC) junction and

$$Q_f = \int_0^{i_1} \tau_f(i) di = \int_0^{v_{be}} C_{de}(v) dv \tag{5.4}$$

is the minority charges stored in the total transistor. The junction capacitances C_{je} and C_{jc} as well as the forward bias transit time τ_f can be determined experimentally via small-signal S-parameter measurements. Using adequate analytical relations for these small-signal quantities, the charges can be calculated as a function of bias, e.g., the junction capacitances are described in most compact models by a more or less expensive modification of the classical formula in order to avoid the pole at the diffusion voltage.

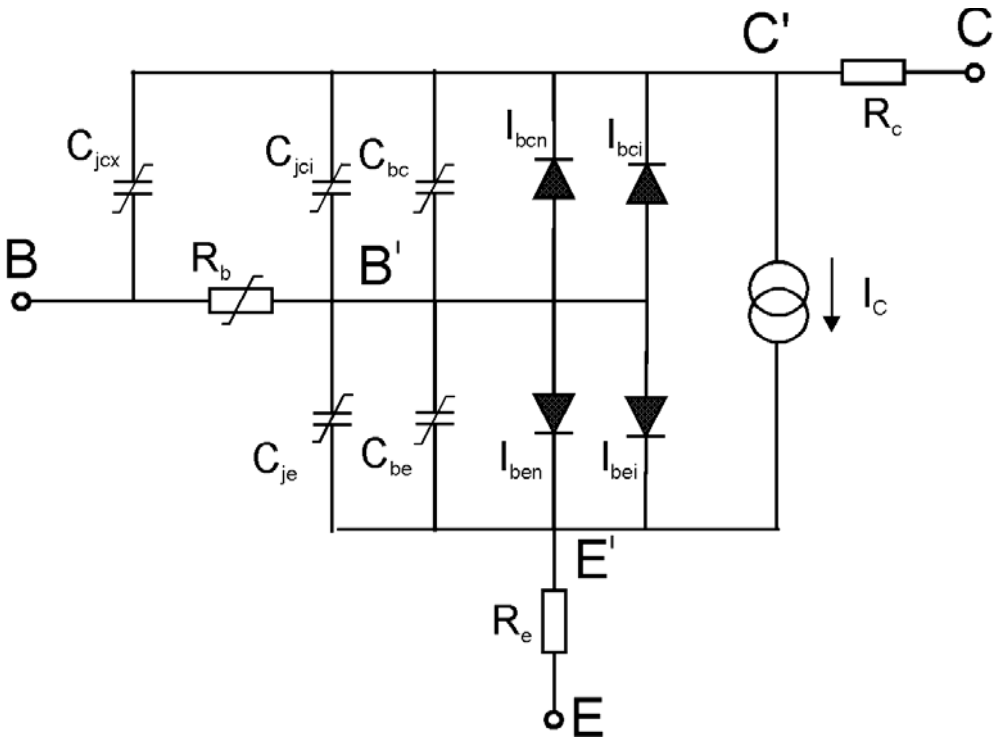

Figure 5.1 Equivalent circuit of the Gummel-Poon model.

Figure 5.1 depicts the equivalent schematic of the Gummel-Poon large signal model. In contrast to the EM model, Gummel-Poon model has nearly identical equivalent schematic and a representation of many important second-order effects present in actual devices. The two most important effects are those of low current and high-level injection. The low-current effects result from additional base current due to the recombination that degrades the current gain. The effects of high-level injection also reduce current gain. The effects of high-level injection also reduce the current gain and in addition cause an increase in τ_f and τ_R. In the Gummel-Poon model, an essential detail considered for the calculation of the DC as well as the AC performance is the majority carrier base charge normalized to its value without bias:

$$q_B = \frac{Q_B}{Q_{B0}}, \tag{5.5}$$

where q_B can also be calculated as

$$q_B = \frac{q_1}{2} + \sqrt{\left(\frac{q_1}{2}\right)^2 + q_2}\,, \tag{5.6}$$

with

$$q_1 = 1 + \frac{1}{Q_{B0}}\int_0^{V_{BE}} C_{jE}(V)dV + \frac{1}{Q_{B0}}\int_0^{V_{BC}} C_{jC}(V)dV\,, \tag{5.7}$$

covering the Early effect (Base width modulation) and

$$q_2 = \frac{1}{I_{KF}} I_S\left(e^{\frac{V_{BE}}{NF\cdot V_T}} - 1\right) + \frac{1}{I_{KR}} I_S\left(e^{\frac{V_{BC}}{NR\cdot V_T}} - 1\right), \tag{5.8}$$

covering the Webster effect (high current behavior). In practice, the following simplifications are applied to all common implementations of the GP model. Equation (5.6) is approximated by

$$q_B \approx \frac{q_1}{2}(1 + \sqrt{1 + 4q_2})\,, \tag{5.9}$$

and charge q_1 is approximated by

$$q_1 \approx 1 + \frac{V_{bc}}{V_{AF}} + \frac{V_{be}}{V_{AR}} \approx \frac{1}{1 - \frac{V_{bc}}{V_{AF}} - \frac{V_{be}}{V_{AR}}}\,. \tag{5.10}$$

In the Gummel-Poon model, a current independent value τ_{f0} for the transit time is assumed, i.e., $Q_f = \tau_{f0} i_T$ in equation (5.2). As a consequence, equation (5.1) gives a simple quadratic equation (5.9) for i_T, which can be solved directly and is numerically

efficient by introducing the "knee current" $I_{KF} = Q_{p0}\tau_{f0}$ as a model parameter. The strong increase of τ_f due to high-current effects was taken into account only for dynamic operation by using the so-called Kirk-factor [109] which describes the current dependence of w_B in the high current range.

The best-known variant of the Gummel-Poon model is the SPICE Gummel-Poon model (SGPM) that is available in the widely used circuit simulator SPICE. Due to a lot of simplifications, the SGPM is no more based on the integral charge control relation, i.e., the relation between the DC transfer current and the AC quantities C_{je}, τ_f, etc. is lost. In addition to Q_f/Q_{p0}, the ratios Q_{ie}/Q_{p0} in equation (5.2) are now replaced by simple voltage ratios v_{be}/V_{AR} and v_{bc}/V_{AF} in equation (5.10). This may be often justified for the base-collector term, if the v_{be} range is not too large, giving a nearly constant forward Early voltage V_{AF}. But for a normal transistor operation, a fairly constant value for the reverse Early voltage V_{AR} can not be found. As a consequence, large errors in the transfer characteristic and the transconductance are observed already at low current densities. This problem can be circumvented by introducing an additional parameter, the "emission coefficient", n_F (>1), so that v_{be}/V_T is replaced by $v_{be}/n_F V_T$ in equation (5.1) and V_{AR} is set to infinite. Further weaknesses are the rough approximations for the junction capacitances at forward bias as well as for τ_F used in AC and transient analysis. NQS effects are taken into account only for the transfer current at low current densities, but not for the minority charge.

In microwave and high-speed circuits, transistor operation at medium and high current densities is often required. At low current densities, the cutoff frequency f_T is determined by the junction capacitances and increases with current density. Since the junction capacitance can be extracted accurately as can be seen from Chapter 2, usually the agreement between the measured data and the SGP modeled data is usually good for low current densities while it deviates when the current densities become progressively higher, see Figure 5.2. Additionally, both the cutoff frequency and the current gain usually take their maximum values at medium current densities. A further increase in the current densities leads to a decrease in the cutoff frequency and the current gain which is the strongest above a certain critical current density, as shown in Figure 5.2.

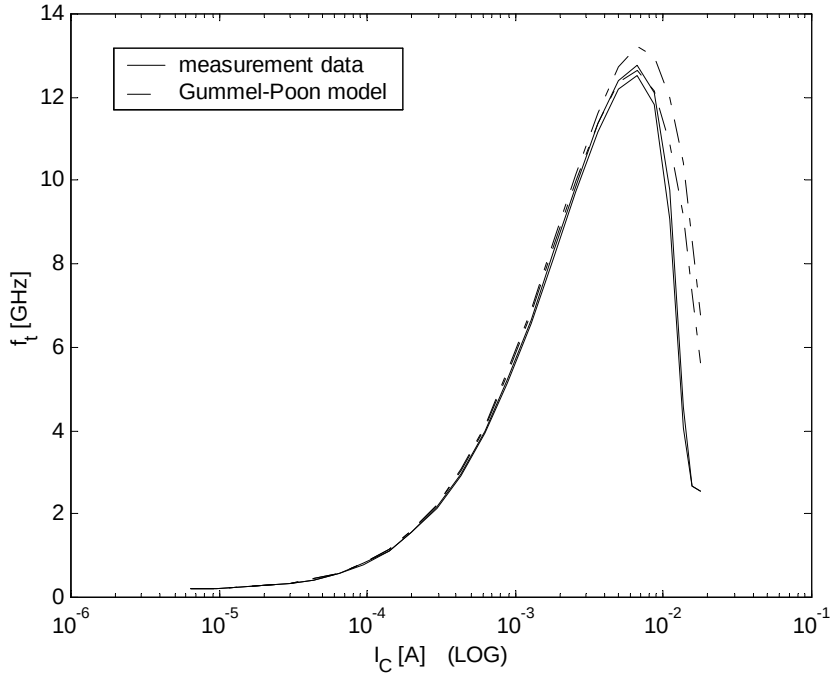

Figure 5.2 (cutoff frequency) f_t vs. I_C simulated by Gummel-Poon model.

Because the Gummel-Poon model does not take into account the avalanche effect, it is not able to simulate the breakdown behavior, as can be seen from Figure

5.3. In addition to the lack of breakdown model, SGP also has the shortcoming of poor modeling of the so-called “knee-region”. For the modern HBTs, when a device with a lightly doped collector region is operated at high injection level in the collector region, the DC current gain falls sharply from its maximum value, as the unity gain frequency f_t. Such an operating regime is generally referred to as quasi-saturation. Quasi-saturation is defined as the region where the internal base-collector metallurgical junction is forward biased, while the external base-collector terminal remains reverse biased. In this mode of operation, minority carriers are injected into the epitaxial region, widening the electrical base of the device and thus reducing the current gain and storing the excess charges in the epitaxial region. In Figure 5.3, a plot of I_C versus V_{CE} for various fixed base currents is shown. At a low level of base input current, the model fits the measured results reasonably, which is mainly determined by the parasitic collector resistance. As the base current increases, the simulation results begins to deviate from the measurement results, indicating the onset of the base push-out effect.

As discussed earlier, despite of the computational efficiency of Gummel-Poon model, another shortcoming is that self-heating effect is not included in the model. This drawback severely limits the usage and simulation accuracy for high power HBT device, such as the GaAs HBT for power amplifier amplifications. As shown in Figure 5.4, the device self-heating effect causes the change in base-emitter junction at high power dissipation, which in turn leads to the decrease of the base current through a thermal feedback loop.

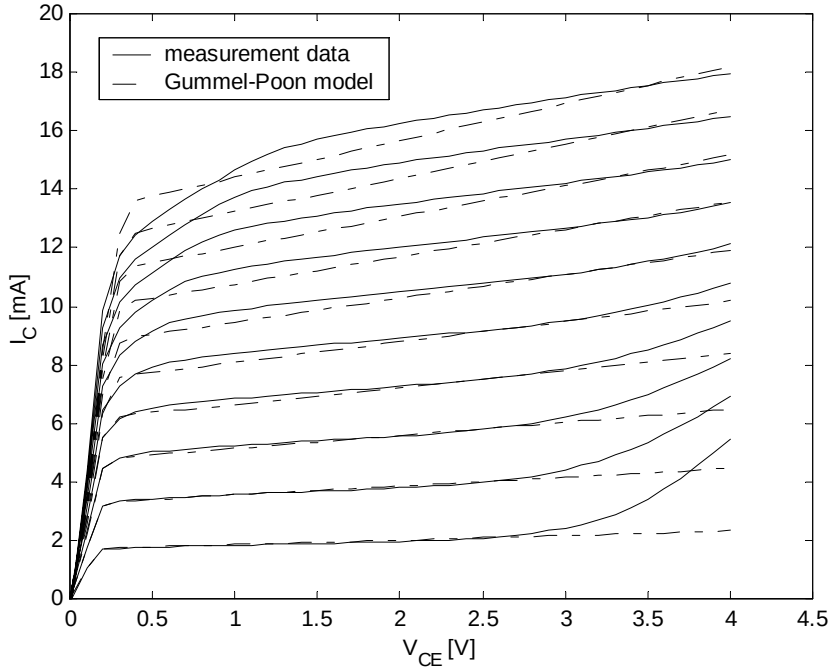

Figure 5.3 *Ic* vs. V_{CE} simulated by Gummel-Poon model.

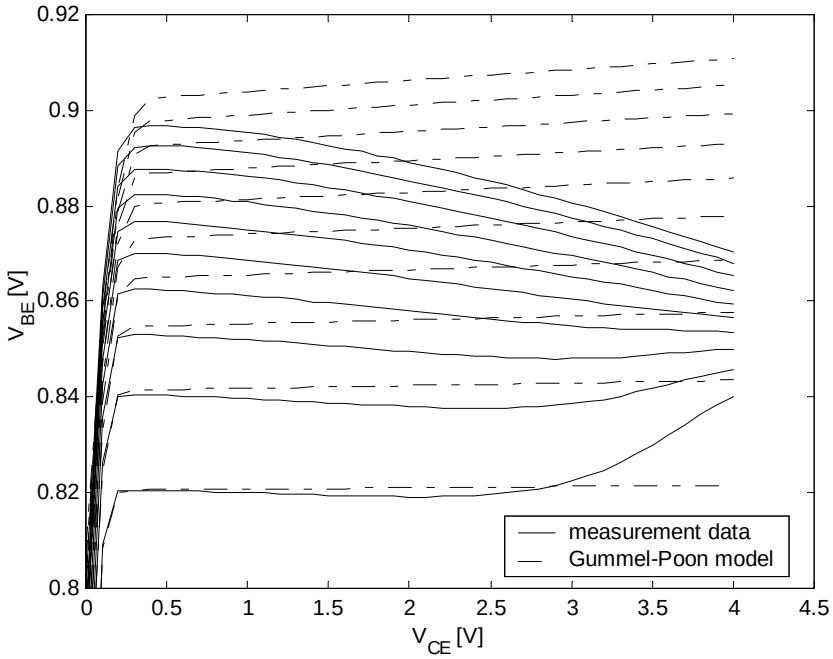

Figure 5.4 V_{BE} vs. V_{CE} simulated by Gummel-Poon model.

5.3 Vertical Bipolar Inter-Company Model

5.3.1 VBIC Equivalent Network

The VBIC model includes an intrinsic transistor (NPN/PNP) based on the Gummel-Poon model, and a parasitic substrate transistor (PNP/NPN) modeled with a partial Gummel-Poon model which takes into account the high level injection. Figure 5.5 shows the VBIC model equivalent circuit with the excess phase and self-heating subcircuits.

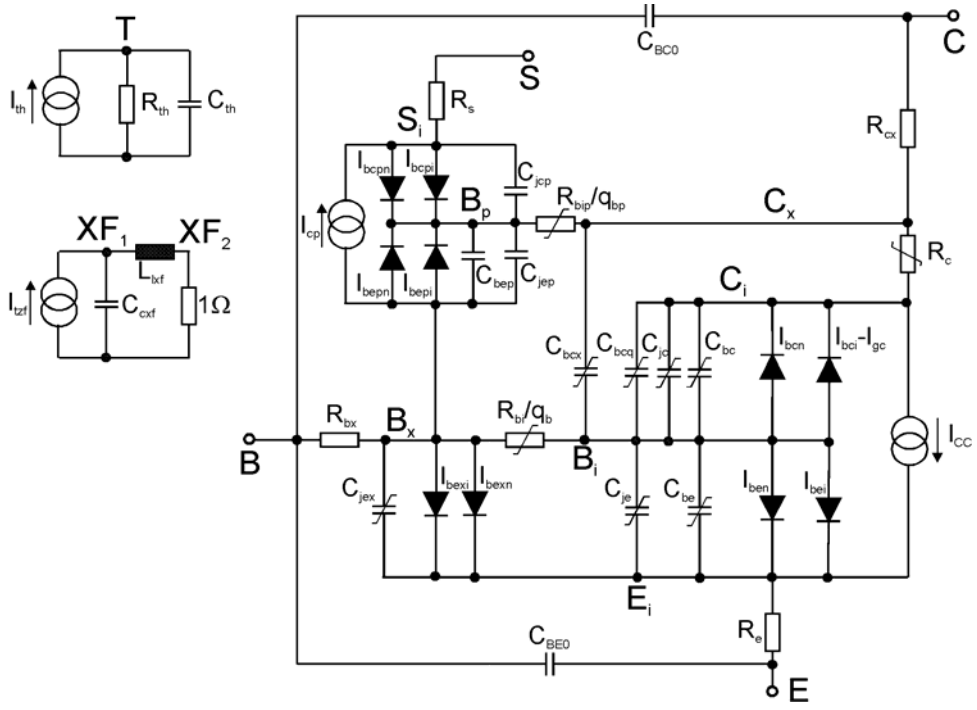

Figure 5.5 Equivalent circuit of VBIC model with excess phase and self-heating subcircuits.

The forward transport current I_{CC} takes into account the forward high injection, the reverse high injection and the Early effect into consideration [110] [111].

$$I_{CC} = I_S\left(\exp(^{qV_{bei}}\!/_{kT}) - \exp(^{qV_{bci}}\!/_{kT})\right)/\, q_b\,. \tag{5.11}$$

The normalized base charge q_b in equation (5.11) is modeled using depletion and diffusion charge components, and not with the approximate linearized depletion charges used in the GP model, so

$$q_b = q_1 + \frac{q_2}{q_b}, \tag{5.12}$$

$$q_1 = 1 + \frac{q_{je}}{V_{ER}} + \frac{q_{jc}}{V_{EF}}, \tag{5.13}$$

$$q_2 = \frac{I_{tf}}{I_{KF}} + \frac{I_{tr}}{I_{KR}}, \tag{5.14}$$

where the B-E and B-C depletion charges are

$$q_{je} = q_j(V_{bei}, P_E, M_E),$$

$$q_{jc} = q_j(V_{bci}, P_C, M_C).$$

Here, V_{EF} and V_{ER} are forward and reverse Early voltages, I_{KF} and I_{KR} are forward and reverse knee currents, and P_E, P_C and M_E, M_C are the built-in potentials and grading coefficients of the B-E and B-C junctions. Equation (5.13) is different from Gummel-Poon model in equation (5.10). Here, q_{je} and q_{jc} are the normalized charges of the space charge capacitors C_{je} and C_{jc}. This implies that the space charge capacitors have to be modeled before the Early voltages are extracted.

The base current I_b is divided into the base-emitter current I_{be} and the base-collector current I_{bc}. The total base-emitter current is partitioned into I_{bei} and I_{bex} to model the distributed nature of the base. The base-collector current includes the ideal and non-ideal components and also a weak avalanche current component, I_{gc} [112] [113]. The intrinsic collector current I_{epi} is modeled with the enhanced Kull's quasi-saturation model [114] with the elements of the intrinsic collector resistance R_{CI} and epitaxial change Q_{C0}.

5.3.2 Modeling the SiGe HBT Using VBIC Model

As a first step, the junction capacitances are measured with a calibrated network analyzer for the highest measurement accuracy. Accurate capacitance measurements are extremely difficult at high frequencies. Therefore the capacitance values are derived directly from the S-parameters measured at the collector and emitter of the device, with a CW frequency signal applied to the base. The frequency used is 500 MHz to eliminate the effects of the test set roll-off at low frequencies, and low enough to eliminate bonding inductance and other parasitic inductance considerations. The depletion capacitances is extracted using the "cold-modeling" technique discussed in Chapter 2 with the following expressions

$$C_{jc} = \frac{-imag(Y_{21})}{\omega}, \tag{5.15}$$

$$C_{je} = \frac{imag(Y_{11} + Y_{21})}{\omega}. \tag{5.16}$$

From the $C_{je}(V_{be})$ data, C_{je}, P_E and M_E are extracted while C_{jc}, P_C and M_C were determined from the $C_{jc}(V_{bc})$ data using the nonlinear optimization [115] as shown in Figure 5.6 and Figure 5.7. Strictly speaking, the B-C capacitance up to low forward bias of V_{BC} generally consists of a bias dependent capacitance and a bias independent isolation capacitance C_{COX}. Since it is quite difficult to separate these two components, C_{COX} is included in the optimization.

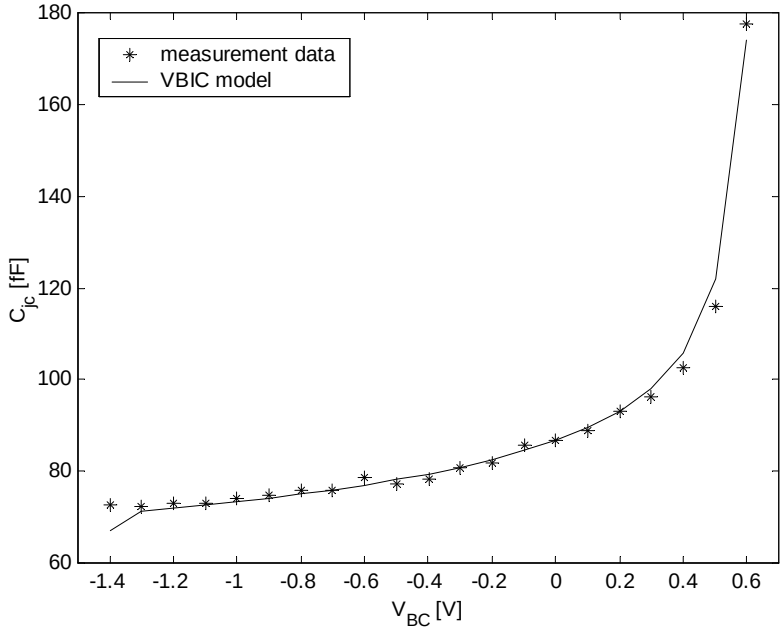

Figure 5.6 B-C junction capacitance C_{jc} vs. biasing voltage V_{BC}.

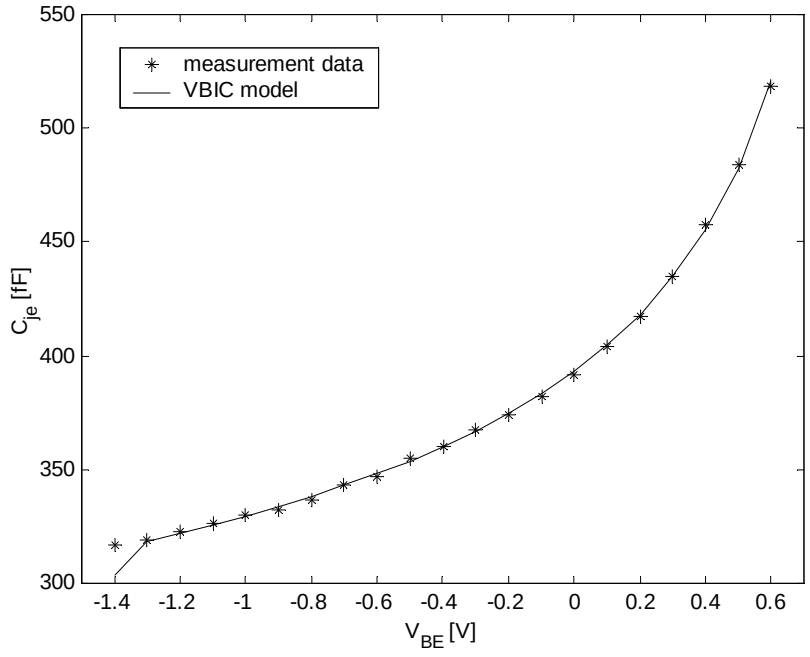

Figure 5.7 B-E junction capacitance C_{je} vs. biasing voltage V_{BE}.

Next the forward and reverse Gummel measurements are taken. The base-emitter voltage was varied from 0.3 to 1 V. The reverse junction voltage used is 0 V to avoid the generation of avalanche/tunneling currents and self-heating. From the

forward Gummel data (in the linear part of the InI_C against V_{BE} curve), estimates for I_S and N_F are made while N_R is determined from the slope of InI_E against V_{BC} curve of the reverse Gummel plot. The base-emitter ideal $I_{BEI/NEI}$ and non-ideal $I_{BEN/NEN}$ portions in the InI_B against V_{BE} curve of the forward Gummel plot, respectively, as shown in Figure 5.8. Similarly, the base-collector ideal $I_{BCI/NCI}$ and nonideal $I_{BCN/NCN}$ parameters were extracted from InI_B against V_{BC} curve of the reverse Gummel plot.

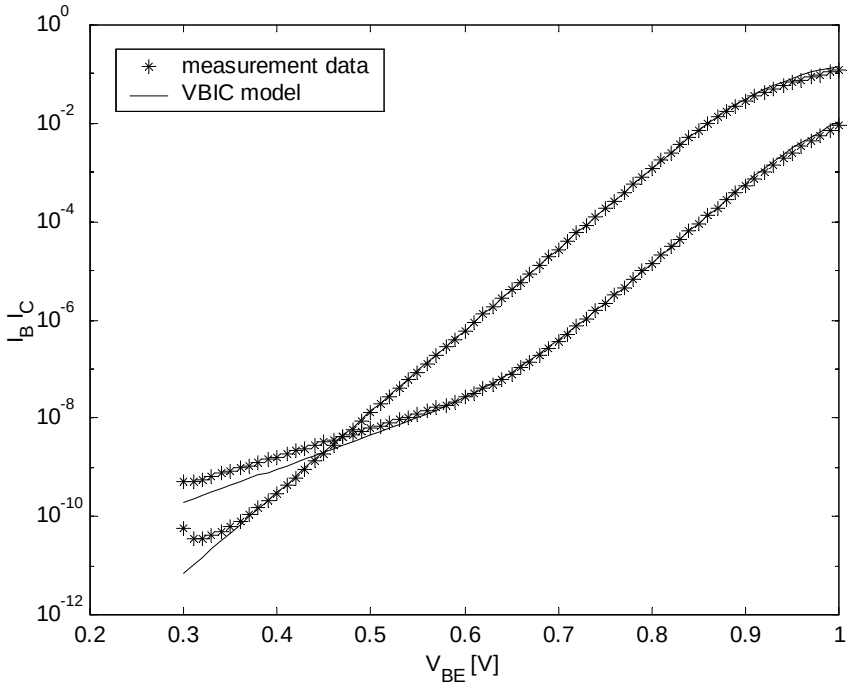

Figure 5.8 Forward Gummel plot.

The knee currents are the high injection currents at which the current gain β starts to decrease from its peak value. From the forward β against V_{BE} or I_C, as shown in Figure 5.9, and reverse β against I_E curves, estimates can be made for I_{KF} and I_{KR}, respectively.

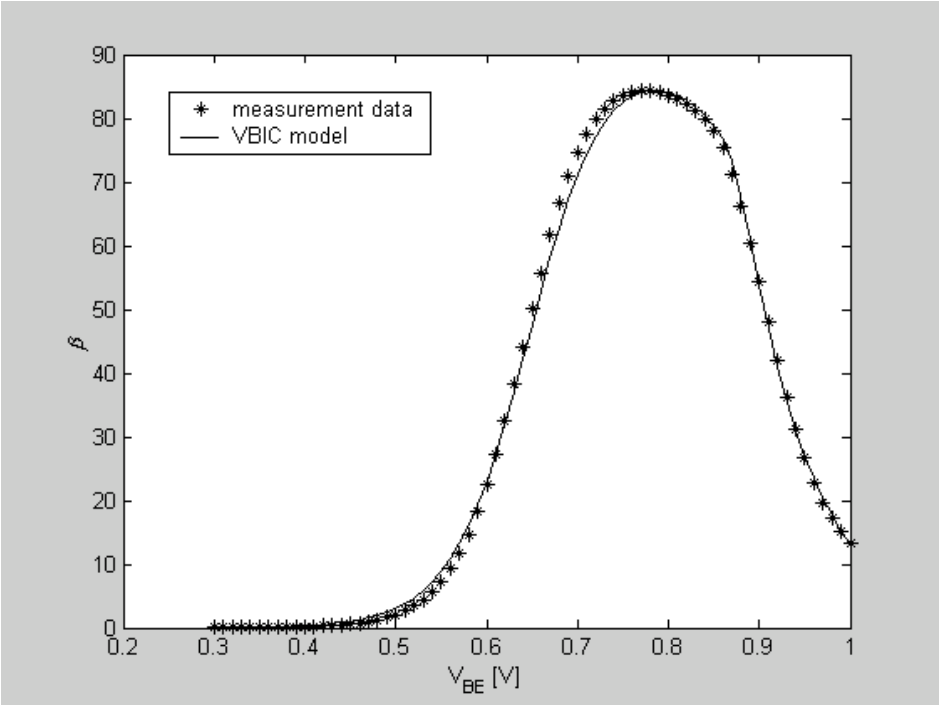

Figure 5.9 Forward current gain I_C/I_B.

The parasitic PNP transistor parameters are determined from the substrate current in the reverse Gummel plot because the base-collector junction is forward biased and the parasitic resistor is conducting. Sine the SiGe HBT device used in this work does not have a substrate terminal, a PN diode is used to model the parasitic substrate effect associated with the extrinsic base instead of a PNP transistor. This technique gives rise to a reasonable estimate when direct measurements are not possible for extracting the parameters.

The output DC IV characteristics of the SiGe HBT are measured under either forced voltage (V_{BE} = constant) or a forced current (I_B = constant) condition. Early voltage measured at using forced V_{BE} at a high injection level is expected to degrade rapidly due to the self-heating effect as I_C increases dramatically even with a small increase in V_{CB}.

Physically the Early voltage accounts for the amount of base-width modulation due to the change in the collector-base reverse voltage. Forward Early voltage V_{EF} and reverse Early voltage V_{ER} are obtained using the following equations:

$$\left(Q_{j,bc}^{f} - \frac{C_{j,bc}^{f} I_{C}^{f}}{g_{0}^{f}}\right) \Big/ V_{EF} + Q_{j,be}^{f} \Big/ V_{ER} = -1, \tag{5.17}$$

$$\left(Q_{j,be}^{r} - \frac{C_{j,be}^{r} I_{E}^{r}}{g_{0}^{r}}\right) \Big/ V_{ER} + Q_{j,bc}^{r} \Big/ V_{EF} = -1. \tag{5.18}$$

Here the superscripts *f* and *r* denote forward and reverse modes respectively and g_0 is the output conductance which is determined from the forward and reverse output characteristics at fixed low bias V_{BE} and V_{BC}. This Early model was developed under the low injection condition. As the Early voltage approximation in the Gummel-Poon model is known to have inaccuracies in Early effect modeling, junction depletion charge is used in the VBIC model. In equations (5.17) and (5.18), Q_j is the junction charge and C_j is the junction capacitance which is calculated from the S-parameter measurement discussed above.

The output characteristics of a transistor normally exhibit the quasi-saturation and/or a high injection effects which are used to extract the epi-layer parameters. The output characteristics were measured at seven different base currents and epi-layer parameters (*Vo*, $R_{CI,}$ H_{RCF} and *GAMMA*) were extracted by optimization in quasi-saturation region. The modeling of the current in the intrinsic collector region is based on the analysis of [114]. Since Kull's quasi-saturation model can predict the negative g_0 at a high value of V_{BE}, the original formula has been modified to be as follows

$$I_{epi0} = \left\{ \frac{V_{rci} + V_{tv}\left[K_{bci} - K_{bcx} - \log_{e}\left(\frac{K_{bci}+1}{K_{bcx}+1}\right)\right]}{R_{CI}} \right\}, \tag{5.19}$$

$$K_{bci} = \left[1 + \gamma \exp\left(\frac{V_{bci}}{V_{tv}}\right)\right]^{1/2},$$

$$K_{bcx} = \left[1 + \gamma \exp\left(\frac{V_{bcx}}{V_{tv}}\right)\right]^{1/2},$$

where $V_{rci} = V_{bci} - V_{bcx}$. In Kull's queai-saturation model, this is coupled with a velocity saturation model $\mu = \mu_0 / \left(1 + \mu_0 |\nabla \phi_e| v_{sat}\right)$ where v_{sat} is the electron saturation speed. This modified the denominator above to become $R_{CI}(1+|V_{rci}|/V_O)$ where $V_O = w_{epi} v_{sat} / \mu_0$. This velocity model is undesirable because it causes discontinuities in the high order derivatives and because it gives a negative g_0. By using an alternative model $\mu = \frac{\mu_0}{\left[1 + \left(\mu_0 \nabla \phi_e / v_{sat}\right)^2\right]^{1/2}}$, and by using $I_{epi0} R_{CI}$ instead of V_{rci}, both of the abovementioned problems are overcome. Furthermore, V_O is empirically changed to V_{rci} through the high R_C parameter H_{RCF} to account for the increase in the collector current with increases of V_{rci} at a high V_{bci}. The final model for the current in R_{CI} is

$$I_{rci} = \left(\frac{I_{epi0}}{\left\{ 1 + \frac{I_{epi0} R_{CI}}{V_O \left[1 + \frac{0.5\left(V_{rci}^2 + 0.01\right)^{1/2}}{V_O H_{RCF}} \right]} \right\}^2} \right)^{1/2}, \qquad (5.20)$$

where a smooth approximation to $|V_{rci}|$ is used to avoid numerical problems and preserve high order continuity. Figure 5.10 shows a fit of VBIC to forward output

data that includes significant quasi-saturation effects. Figure 5.11 shows VBIC correctly predicts g_0 over a wide range.

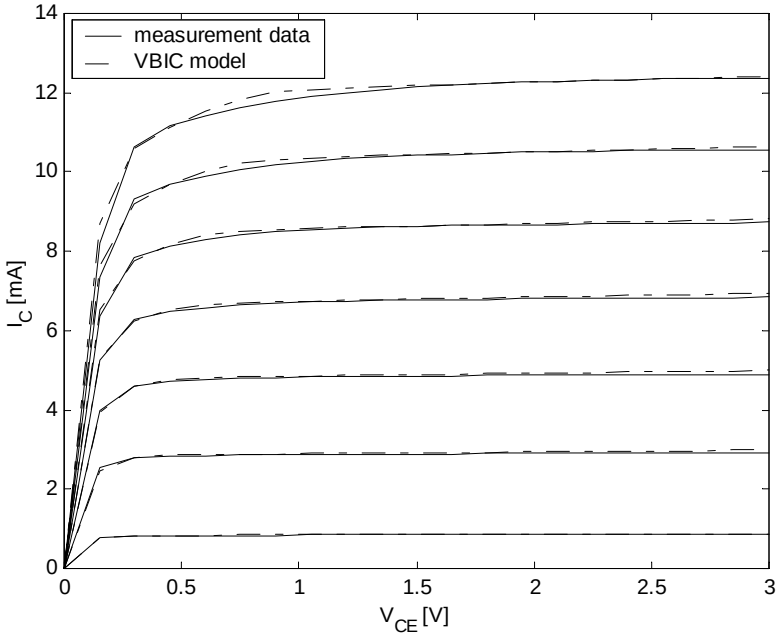

Figure 5.10 Forward output data with quasi-saturation effects.

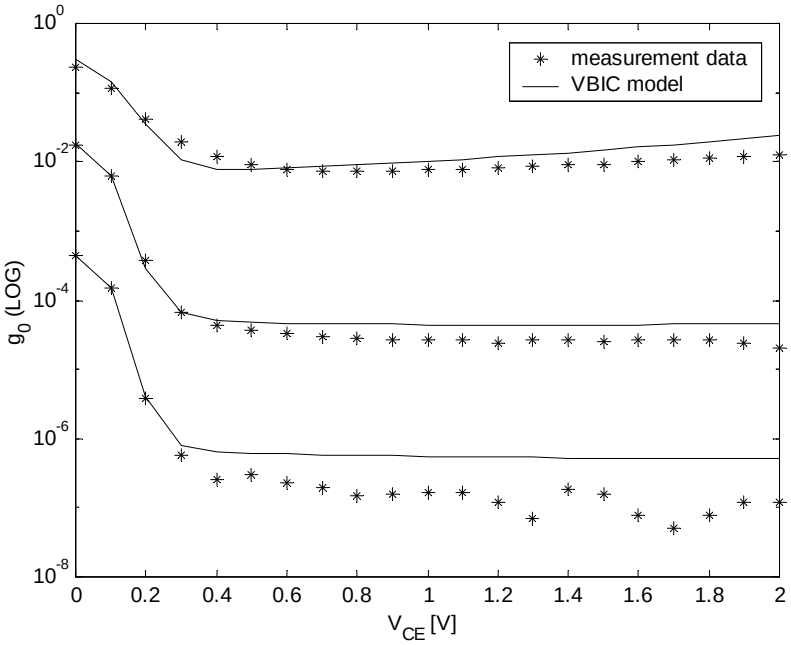

Figure 5.11 Output conductance affected by quasi-saturation.

The next step is the inclusion of the finite base, collector and emitter resistance in the VBIC model. As discussed in Chapter 2, the emitter resistance can be

determined by stimulating the base with a current in strong saturation and measuring the collector-emitter voltage. The collector current is kept small and the applied base current is swept to high value. The inverse of the gradient in the characteristics together with the thermal resistance can then be used to obtain the emitter resistance. The measurement of the collector resistance is similar to the emitter resistance. Here, current is applied to the base and collector, and the collector-emitter voltage is measured. The distributed nature of the base resistance makes it difficult be modeled. Nonlinear effect of the base resistance with the base current has been incorporated in the Gummel-Poon model in a rather simple manner. In the VBIC model, the base resistance of the intrinsic and parasitic transistors is bias dependent and the resistances are modulated by the normalized base charges. To extract the inner base resistance, the input impedance-circle method is used. Extrapolating these measurements to high frequencies where the transistor capacitances essentially act as short, the input impedance of the transistor is then basically the emitter resistance plus the base resistance. Since the base resistance, and also the parameter W_{BE} which determines the split of the base-emitter modeling, are fine-tuned by optimization after the extraction of the transit time parameters, this approximation is a good initial value for the later optimization. However, as there are some uncertainties in extracting resistances from only the DC data or AC data, extracted resistances are refined by the simultaneous optimization of the DC and AC data in this work.

In a bipolar transistor, avalanche currents are generated in the base-collector depletion region when the transistor is operated in the forward model nearly at the breakdown voltage. In the VBIC model, the weak avalanche is modeled with the collector depletion capacitance parameters P_C and M_E for predicting the avalanche current I_{gc} and is given by [112] [113]

$$I_{gc} = (I_{cc} - I_{bc})AVC1(P_C - V_{bci}) \cdot \exp[-AVC2(P_C - V_{bci})^{M_E - 1}], \quad (5.21)$$

where I_{cc}-I_{bc} is the collector current without avalanche, V_{bci} is the internal base-collector voltage, and *AVC1* and *AVC2* are the model parameters. The weak avalanche breakdown parameters are extracted from the decrease in the base current at a high value of the collector voltage, as shown in Figure 5.13. In this measurement, the base-emitter voltage is kept constant and V_{CB} is increased until the base current has significantly decreased due to avalanche. To avoid high current effects and internal heating the base-emitter voltage is set to a low value of 0.6 V. The difference between I_B at low and at high V_{CB} is the generated avalanche current. The avalanche parameters *AVC1* and *AVC2* are extracted using the least-square fit. The parameters P_C and M_E in equation (5.21) are obtained from the base-collector depletion capacitance measurement. However, the VBIC avalanche model is limited to predict the breakdown behavior in a low current density. A modified VBIC avalanche model is proposed in the next section, which extends the original VBIC model up to high current density regions.

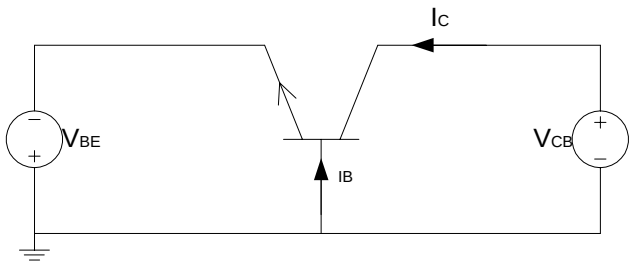

Figure 5.12 Measurement setup to characterize HBT's avalanche multiplication.

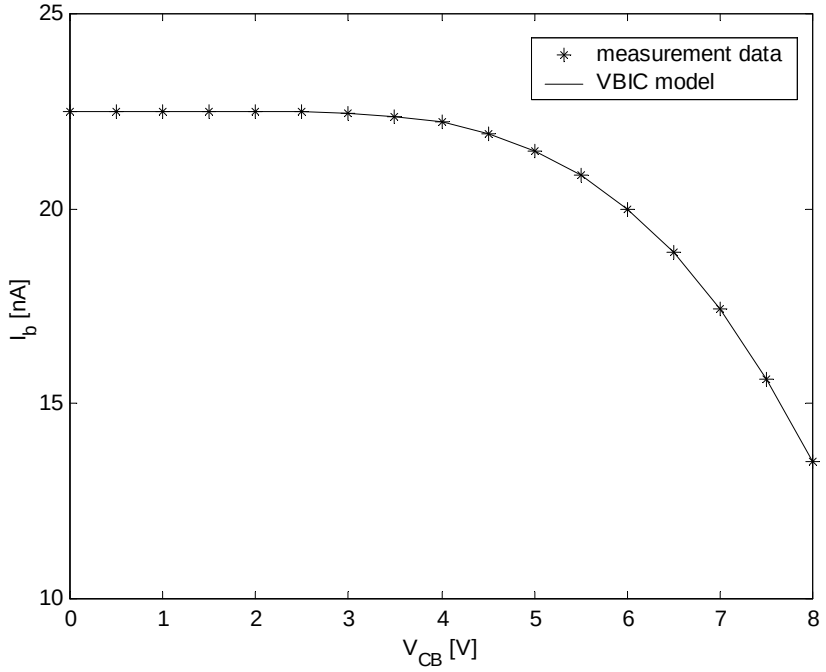

Figure 5.13 Decrease of base current due to avalanche.

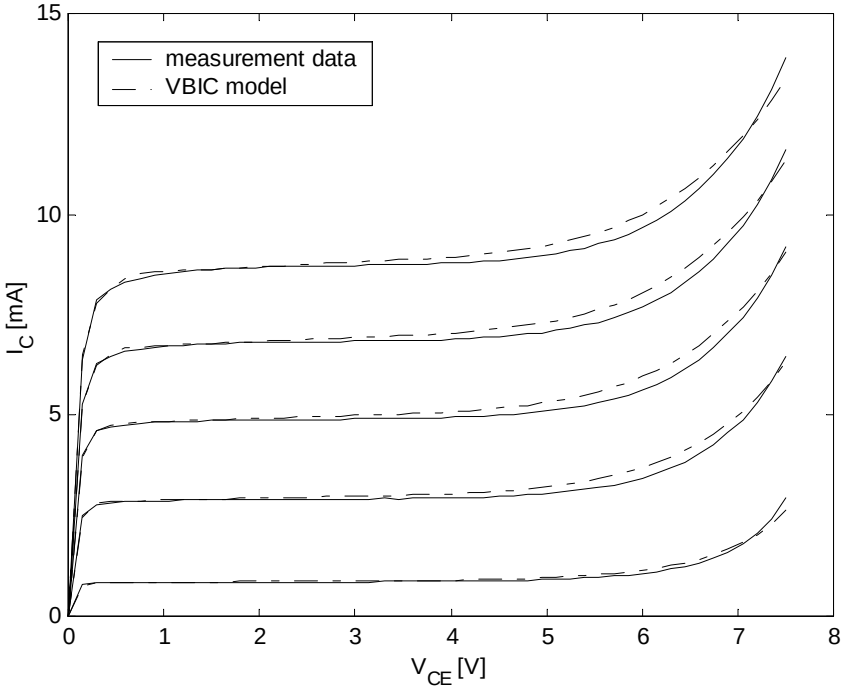

Figure 5.14 Measured and modeled forward output characteristics with avalanche multiplication and self-heating effects.

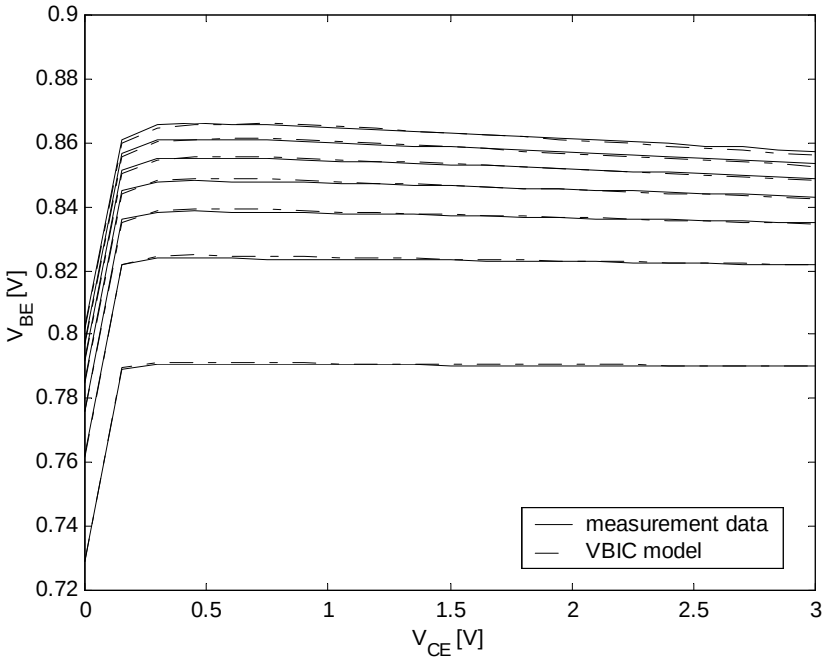

Figure 5.15 Measured and modeled V_{BE} change due to self-heating effect, with the thermal resistance extracted by the method discussed in chapter 2.

The final parameters are the transit parameters. Transit time τ_F is commonly determined from the cutoff frequency f_T measurements. The cutoff frequency was determined using S-parameter measurements in the common-emitter configuration by extrapolating $|h_{21}|$. The modeling equation for the remaining parameters is the following

$$TFF = TF \cdot (1 + QTF \cdot q_1) \cdot \left[1 + XTF \cdot \left(\frac{I_F}{I_F + ITF} \right)^2 \cdot \exp\left(\frac{V_{bci}}{1.44 \cdot VTF} \right) \right]. \qquad (5.22)$$

As can be seen from the above equation that except for *QTF*, we can also apply the known Gummel-Poon extraction methods also to the VBIC model. Some procedures split the modeling into two steps. Firstly, using V_{BC}=0, the above equation is simplified and the parameters *TF*, *XTF* and *ITF* are extracted; secondly, with a varying V_{CE}, the last parameter *VTF* is calculated. However, it must be assured that

the transistor is biased outside the quasi-saturation region. For small values of the forward transport current, equation (5.22) simplifies to

$$TFF = TF \cdot (1 + QTF \cdot q_1) . \tag{5.23}$$

This allows to model *TF* and *QTF*. However, the effects are difficult to separate. Therefore, we might start with *QTF*=0, and obtain its final value from fine-tuning optimization.

The S-parameter measurements were carried out using a HP 8510C vector network analyzer at room temperature. The parasitic components associated with the resistance, inductance and capacitance of the probes, pads and interconnects were carefully de-embedded [116] [117]. The input and output RF connections from the transistor fixture were made through SMA connectors. Regulated DC power supplies HP 4142 were connected though a bias-T network for biasing the transistor. As a small increase in V_{BE} can cause a large base-emitter current swing, precautions should be taken to avoid the damage to the transistor. After all the connections was made, V_{BE} was set to 0.75 V and V_{CE} was then slowly increased. This would help protect the transistor base-emitter junction by limiting current flow. f_T was measured at two V_{CE} values as a function of the collector current. The forward transit parameters were obtained from the intercept of the $1/2\pi f_T$ against $1/I_C$ curve. The voltage- and current-dependent parameters (*VTF* and *ITF*) of the transit time were further estimated by optimization as discussed above.

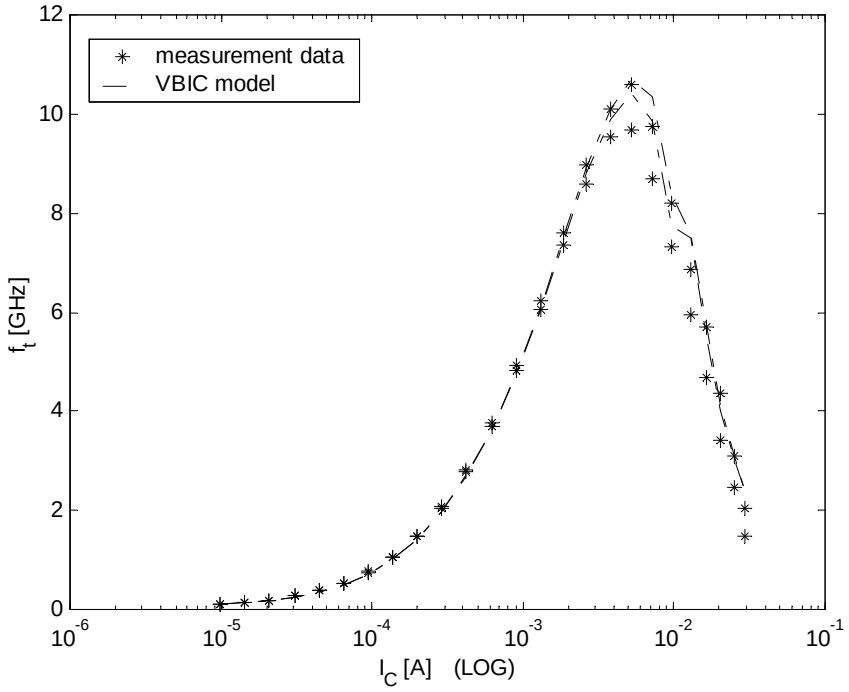

Figure 5.16 f_t (cutoff frequency) vs. I_C simulated by VBIC model.

The above developed extraction procedure is successfully applied to extract the SiGe HBT from IBM. The device under test has an emitter dimension of $0.5\times 20\times 2 \quad \mu m^2$. The extraction method maximally decoupled the interaction of model parameters. Figure 5.17 shows the extraction flow chart and Table 5.1 lists the VBIC model parameters for the studied SiGe HBT device.

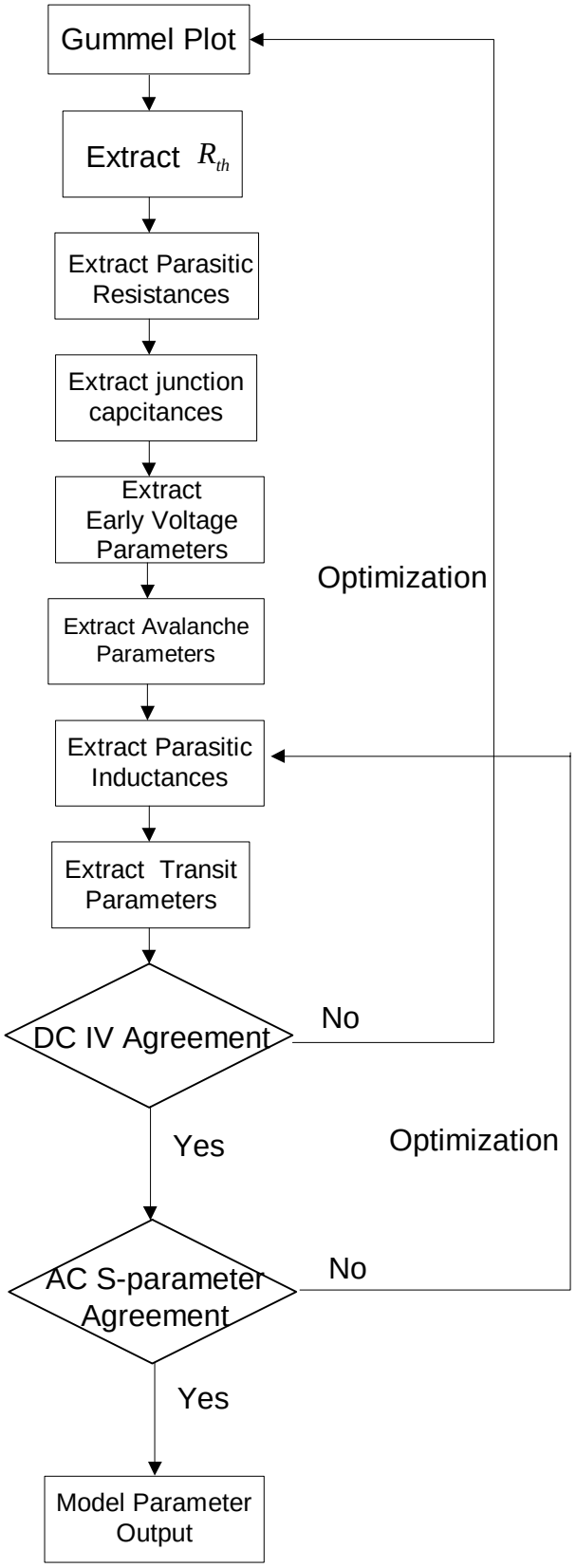

Figure 5.17 VBIC model parameter extraction flow chart.

TABLE 5.1 Extracted VBIC model parameters of the SiGe HBT at room temperature

Model Parameter	Value	Model Parameter	Value
IS (aA)	43.2	RE (Ohm)	0.5
NF	1	RCI (Ohm)	60.12
NR	1	LB (pH)	21.37
IBEI (aA)	26.9	LE (pH)	5.28
NEI	1	LC (pH)	25.55
IBEN (pA)	1.493	AVC1	0.1083
NEN	2.5	AVC2	23.85
IBCI (aA)	2.748	RTH (C/W)	330
NCI	1	CJE (fF)	304.3
IBCN (fA)	42.07	PE	0.894
NCN	2	ME	0.31
IKF (mA)	93.76	CJC (fF)	85.04
IKR (mA)	14.39	PC	0.584
VEF (V)	28.5	MC	0.167
VER (V)	1.248	TF (pS)	2.483
RBX (Ohm)	0.413	XTF	1.928
RBI (Ohm)	1.811	ITF	0.348

5.4 Characterization and Modeling of Avalanche Multiplication in SiGe HBT by Improved VBIC Avalanche Model

In the SiGe HBT device, the peak cutoff frequency f_T, breakdown voltage BV_{CEO} and Early voltage V_A, are three parameters that are closely linked. There is a reciprocal relationship between f_T and both BV_{CEO} and V_A. From a transistor design perspective, the base and emitter profile are assumed constant and the f_T may be increased either by increasing the collector doping concentration or making the collector shorter (e.g., by decreasing the collector epi-layer thickness). Both methods delay the onset of the Kirk effect. Increasing the collector doping decreases the Early voltage because of the increased base-width modulation; it also increases impact ionization, which lowers BV_{CEO}. The reduction in collector epi-layer thickness also increases the impact ionization due to the higher field from the same voltage supported over a shorter distance. This tradeoff between f_T and BV_{CEO} is referred to as the “Johnson Limit” [118] [119]. In power amplifier applications, device breakdown voltage is one of the critical specifications. Therefore, the avalanche multiplication in both III-V HBTs [120] [121] and SiGe HBTs [122] [123] has received intensive research worldwide. Chen *et al*. [124] analyzed the breakdown mechanism of GaAs/AlGaAs HBT devices using a simple punch-through breakdown model. Niu *et al*. [122] [125] measured the avalanche multiplication factor in SiGe HBT’s by a technique which could separate the avalanche multiplication and Early effect contributions to the increase of collector current with collector-base bias. This allows safe measurements at practical current densities. It was found that a lower multiplication factor in SiGe HBT’s resulted in high V_{CB} due to the population of high energy holes at the base side of the collector-base space charge region where the Ge content peaks. This can be confirmed by a 2-D energy balance simulation. It is

concluded that the avalanche multiplication factor changes with current density in modern SiGe HBTs. However, present compact models for circuit simulation have not reflected those new findings in modern bandgap-engineering of SiGe HBTs.

As discussed in Section 5.2, in the standard SPICE Gummel-Pool model (SGP), there is no avalanche breakdown model included to account for avalanche breakdown. In the more advanced bipolar models such as VBIC and MEXTRAM, the avalanche model is based on the well-known Chynoweth's empirical law and local electric field derivation. In HICUM model, the avalanche model is derived similar to that of MEXTARM on the basis that breakdown is caused by the maximum local electric field, but more is dependent on the device geometric parameter [126]. One basic common assumption for all the above is that the weak avalanche, i.e. the generated avalanche current should be much smaller than that of the collector current density. This assumption may not hold for highly doped base HBT when the generated avalanche current density is high.

In this section, based on various device electrical characteristics that are categorized into three groups, a modified VBIC avalanche multiplication model is proposed. By simply replacing one constant avalanche model parameter with a linearly dependent one, the new avalanche model predicts the breakdown behavior from weak avalanche well up to very high current densities.

5.4.1 Classification of Avalanche Multiplication Behavior

From the DC characteristics of the SiGe HBT device, three groups of avalanche breakdown characterization is noted (Figure 5.18):

(A) Nearly constant breakdown voltage BV_{CEO} with the increase of the collector current, as shown in Figure 5.18(a);

(B) BV_{CEO} increases with the increase of the collect current density, as shown in Figure 5.18(b); and

(C) BV_{CEO} decreases with the increase of the collect current density, as shown in Figure 5.18(c).

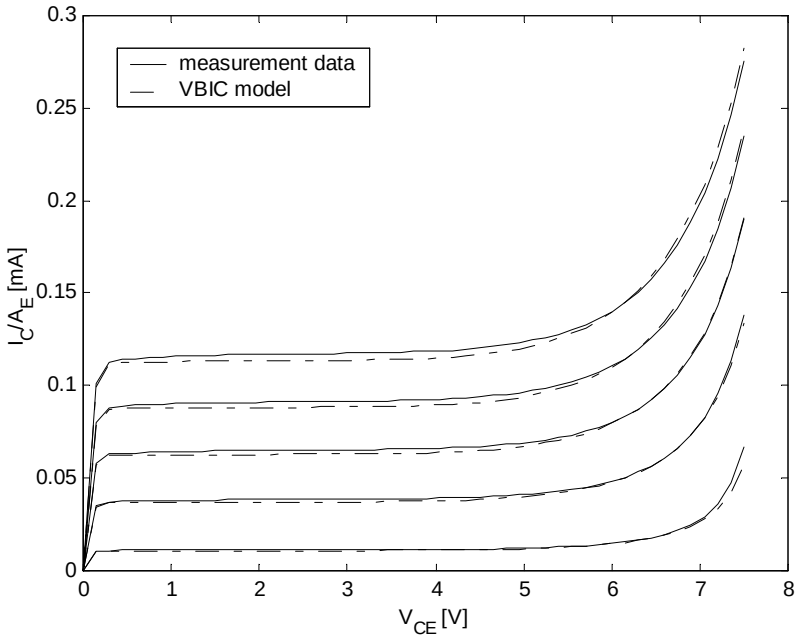

(a) Constant breakdown voltage BV_{CEO} with collector current density increase

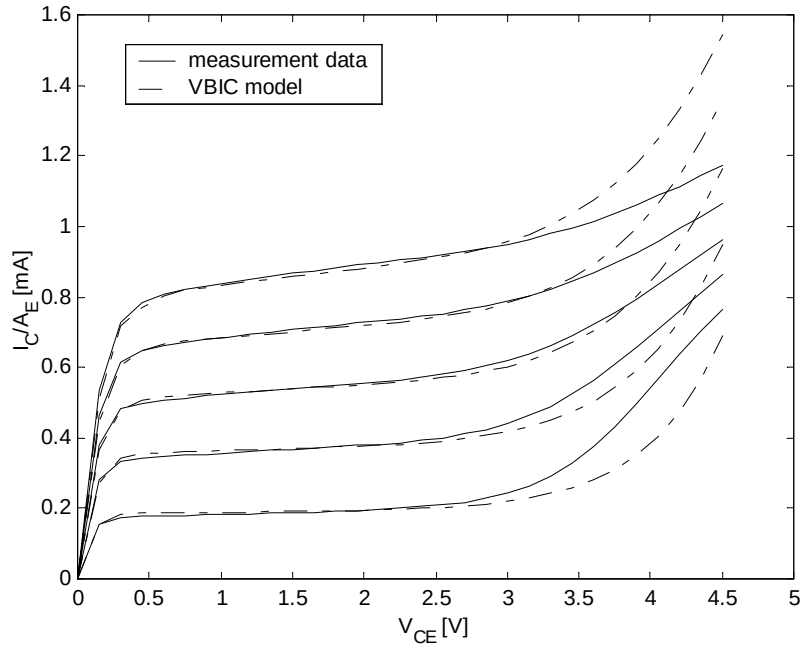

(b) BV_{CEO} increases with collector current density

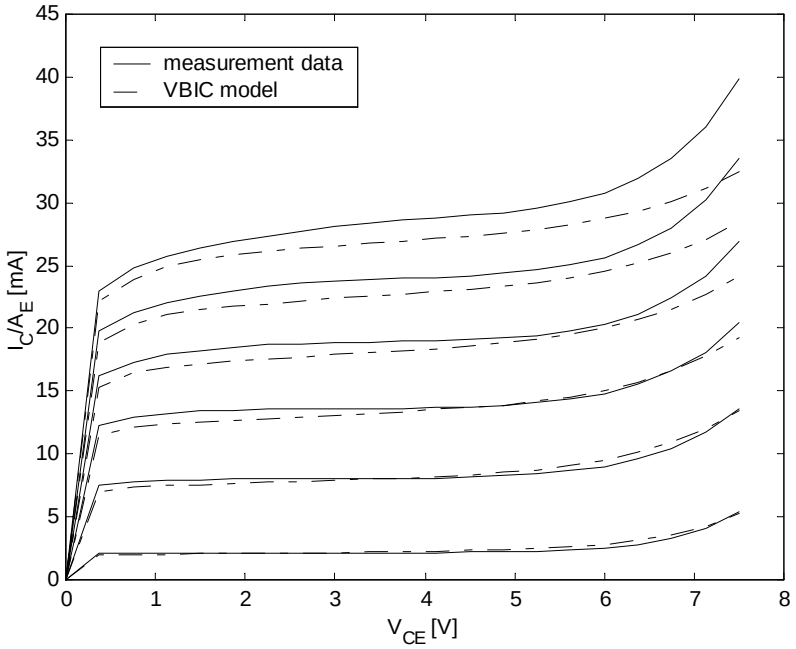

(c) BV_{CEO} decreases with collector current density.

Figure 5.18 Three kinds of avalanche breakdown behavior in HBT device.

In Figure 5.18, the collector current density is normalized to the emitter area, A_E. The device presented in Figure 5.18(b) has a highly doped collector with SIC, while the device in Figure 5.18(c) has a lightly doped collector. It is of interest to note that the collector current density J_C and the ratio of avalanche current to collector current, *Avc*, for the above three groups have the following observations:

(i) Group A, see Figure 5.18(a), has the lowest current density *Jc* (<0.15mA/μm^2) and Avc1 (<0.2);

(ii) Group C, see Figure 5.18(c), has the highest *Jc* (>2.5mA/μm^2) and Avc1 (>0.5);

(iii) Group B, see Figure 5.18(b), has J_C around 1mA/μm^2, which Avc1 lies between Group A and C.

It can be seen from Figure 5.18 that the VBIC model fits well only for Group A device, which is the basic assumption for the weak avalanche breakdown model. In close inspection, BV_{CEO} of group B increases when the collector current increases while that of Group C shows the reverse trend. It is well-known that the BC junction

avalanche multiplication has strong dependence in the collector current density. In the presence of high-level injection, the BC junction space-charge modulation and the Ohmic voltage drop in bulk collector are two dominant factors for reducing the junction field.

In modern advanced high-speed SiGe heterojunction bipolar transistor technologies, base push-out at high current density can be avoided by using a higher collector doping concentration since the Kirk “knee” current densities is proportional to the collector doping. While epitaxial technology should in theory allow an arbitrary definition of the collector profile, conventional ion-implant collectors have been preferred in order to confine the collector implant to the intrinsic device region and minimize base-collector capacitance. Selectively collector implantation (SIC) is used to locally increase the collector doping (pedestal-collector bipolar transistor) for preventing base push-out for the high current operation.

In the situation of high collector current densities, the collector current can decrease the maximum electric field due to space-charge modulation, since the compensation of charges in the BC space charge region (SCR) by free carriers reduces the effective doping and electric field, thus decreasing the avalanche multiplication factor at a high current density level.

Besides space-charge modulation, a voltage drop in the epi-layer and internal transistor heating may also result in a lowering of the avalanche current. In the case of generation current, the maximum electric field may reside at the base-collector junction or at the buried layer, the avalanche current is only a function of the electrical field at the internal base-collector junction. Therefore, the validity of VBIC avalanche model is restricted to the low current densities. For high current densities, current spreading in the collector region changes the electric-field distribution and decreases

the maximum electric field. The DC IV characteristics of Group B in Figure 5.18(b) clearly illustrate the increase of BV_{CEO} while increasing the collector current densities.

For the high voltage SiGe HBT without SIC, shown in Figure 5.18(c), the collector is lightly doped to achieve a high BV_{CEO}, avalanche multiplication factor dramatically decreases at lower collector doping due to its smaller BC junction field. The fact that there is no avalanche multiplication at low V_{CB} in the lightly doped collector device strongly suggests that the kinetic energy of electrons never reaches the threshold for avalanche multiplication, despite the large total potential drop. Consequently, in addition to the sufficiently high collector voltage drop, the occurrence of impact ionization requires the peak field to exceed a certain critical value, below which the kinetic energy of the electrons is always lost before reaching the threshold to create an electron-hole pair, Figure 5.18(c). Consequently, the strong field also needs to expand in the BC-SCR for a certain distance so that “lucky” electrons can gain enough energy to create an electron-hole pair. Both Monte-Carlo and hydrodynamic modeling of the multiplication predict a “dead space” closed to the base where, despite the large electric field, no impact ionization takes place.

The breakdown behavior of high current densities also involves much more effects such as self-heating or temperature dependence and dead space effect [127]. Some works [128] investigated the details of dead space effect using numerical simulation. However, in compact modeling for circuit simulation, a closed-form formula is desired. In [122], the avalanche model is derived with the assumptions that collector current does not affect the electric field distribution in the depletion layer and the avalanche behavior of high current is due to the temperature dependence of avalanche parameter. Therefore, one more avalanche model parameter is necessary. This can be extracted by the thermal resistance measurement. In addition, as noted in

[122], avalanche multiplication factor changes with current density in modern SiGe HBTs. It is concluded that there is a need for model, which is as a function of current density, to accurately predict distortions in circuit simulation. Currently there is no model in any commercial EDA tool which can predict these characteristics as a whole.

5.4.2 Avalanche Modeling Enhancement

Based on the above analysis in the above, the proposed model modification may proceed from the VBIC model, keeping the resultant model as simple and consistent as that of VBIC model as possible. As can be seen from the equivalent circuit, VBIC includes a weak avalanche current source for the base-collector junction I_{gc} to account for the onset of avalanche current. It is essentially based on the MEXTRAM avalanche model and derived from the well-known Chynoweth's empirical law as well as on the assumption that the breakdown behavior is caused by the local maximum electric field. In contrast to the original MEXTRAM avalanche model, the effect of base-collector current on avalanche current is more explicitly included in the VBIC avalanche model:

$$I_{gc} = (I_{cc} - I_{bc}) A_{VC1} (P_C - V_{bci}) \cdot \exp\left[- A_{VC2} (P_C - V_{bci})^{MC-1} \right],$$

where A_{VC1}, A_{VC2} are constant avalanche model parameters, P_C and M_C are the built-in potential and grading coefficient of the base-collector space charge capacitance, respectively. V_{bci} is the internal nodal voltage across base-collector junction. A_{VC1} is an empirical parameter of value related to the ratio of avalanche current to collector current source while A_{VC2} is an parameter reflecting the maximum electric field in the base-collector depletion for the charge capacitance. In the VBIC model, A_{VC2} is further considered temperature linear dependent through temperature mapping:

$$A_{VC2}(Temp) = A_{VC2}(Tnom) \cdot \left[1 + T_{AVC} \cdot (Temp - Tnom)\right]. \quad (5.24)$$

The overall behavior of DC IV is very sensitive to avalanche parameters (A_{VC1} and A_{VC2}). Therefore they should be extracted by the data-fitting procedure from DC characterization. For safe operation, the base-emitter voltage should be kept constant and low enough. At the same time, the base-collector voltage is increased slowly until the base current has significantly decreased due to avalanche effect. Following this, the base-emitter voltage or base current can be varied.

From Figure 5.18, the discrepancies of VBIC avalanche model to the measured results can be seen. The agreement leaves much to be desired, especially in the high collect current region. This is due to the fact that in the cause of generation current, the maximum electric-field may reside at the base-collector junction or at the buried layer, the avalanche current is only a function of the electrical field at the internal base-collector junction. Therefore, the validity of this model is restricted to the low current densities. For high current densities, current spreading in the collector region changes the electric-field distribution and decreases the maximum electric field. The generation of avalanche current is very sensitive to the maximum electric field. At higher current densities, the base push-out occurs. Self-heating effect also could be pronounced. In view of all these, it is difficult to make accurate and simple model for the high collector current. As discussed in the previous section, above avalanche modeling in VBIC can only fit well in Group A which is having a lower collector current density or weak avalanche, i.e., the avalanche current is much smaller than the collector current source. However, with small modification to the existing VBIC model, both Group B and C can be better modeled. From a data-fitting process, it can be realized that different values of A_{VC1} or A_{VC2} is varied, different curves in Figure 5.18(b) and Figure 5.18(c) can be fitted well. Further by analyzing the resulting

parameter values for the dependence of bias current density, the VBIC constant avalanche model parameter is a linear function of the bias current density:

$$A_{VC2} = A_{VC2}^{'} - A_{VC3}(I_{cc} - I_{bc}), \tag{5.25}$$

where A_{VC3} is a new model parameter and A_{VC2}' is the same parameter as that in the original avalanche model but its value is different in the modified avalanche model. In practice, I_{cc}, the collector current source, is the main portion of the collector current and is much larger than I_{bc} due to the high current gain in SiGe HBTs. Therefore, the parameter can be extracted by the following method:

- Set A_{VC3} = 0, the model degenerates to the original VBIC form.
- Extracting A_{VC2} using the least square method to fit the lowest and highest current curve characterization.
- Put the resulting values into above equation, the new model parameters $A_{VC2}^{'}$ and A_{VC3} can be solved.

If parameter A_{VC1} is modified to a current dependent one, similar results can be obtained. Similar to the modified parameter in Eq. (5.25), the A_{VC1} can be re-written as a linear function of the bias current density:

$$A_{VC1} = A_{VC1}^{'} - A_{VC4}(I_{cc} - I_{bc}) \tag{5.26}$$

where A_{VC4} is a new model parameter and A_{VC1}' is the same parameter as that in the original avalanche model but its value is different in the modified avalanche model.

However, to maintain the physical meaning of compact model, extending parameter A_{VC2} is preferred. The results are presented in Figures 5.19 and 5.20. To verify the modified avalanche model, the modified VBIC avalanche model has been implemented in commercial IC-CAP software package and compared with standard VBIC avalanche model and measured data. Parameter extraction and simulation are

implemented using IC-CAP Parameter Extraction Language and the build-in optimizer.

Figures 5.19 and 5.20 show simulation results of modeling enhancement for device group B and C. Solid lines are the measurement data and the dashed lines are simulation results with modified VBIC avalanche models. Figure 5.19(a) and Figure 5.20(a) are simulated results with enhancement for parameter A_{VC1} for Group B and Group C devices, respectively. Figure 5.19(b) and Figure 5.20(b) are the better enhancement by implementing parameter A_{VC2} into the current dependent one for group B and group C devices, respectively.

For Group B device with current density around 1mA/μm^2, the simulation results with the original VBIC avalanche model in Figure 5.18(b) are compared with the modified avalanche VBIC model simulation in Figure 5.19. It can be seen that better agreement simulation results for high current density simulation results can be obtained. For the Group C device with even higher current density, the better agreement still can be seen, especially in the high current density region of Figure 5.20. However, because of much higher current density, compared with Group A and Group B devices with weak and medium high current densities, respectively, the fitting improvement is not so good as Group B. This might be due to the fact that at very high current density several other effects, such as device self-heating and dead space effect, become pronounced, which further complicate the avalanche generation. The more complex avalanche generation mechanism at very high collector current density may make the assumption, i.e., the avalanche model parameter is linearly proportional to the increase of collector current density, become invalid.

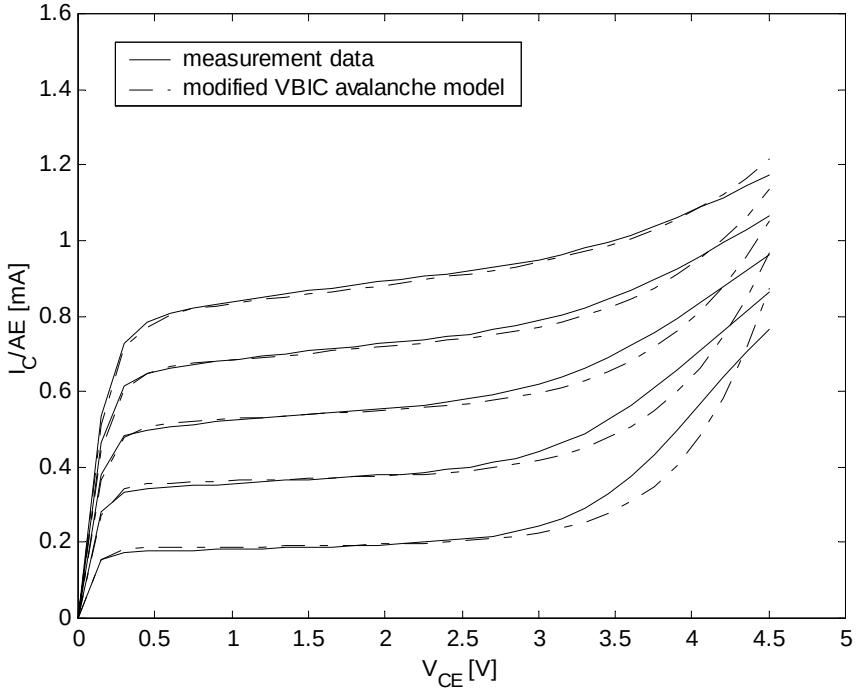

Figure 5.19 Comparison with measured data with modified VBIC avalanche model for device B with SIC.

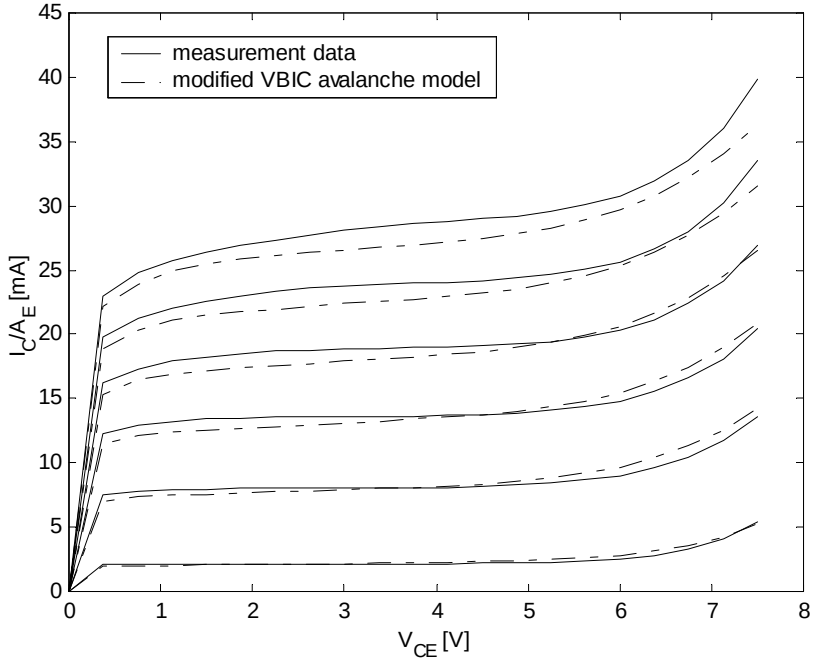

Figure 5.20 Comparison with measured data with modified VBIC avalanche model for device C without SIC.

In the original VBIC model, both weak avalanche model parameters A_{vc1} and A_{vc2} in the VBIC model are constant. In this section, an empirical enhancement for VBIC avalanche multiplication model has been developed, parameter A_{vc1} is replaced by linear current dependent function and parameter A_{vc2} is replaced by current linear dependent function. By simply replacing a constant avalanche model parameter with linear current dependent parameter, the new model can predict all the observed avalanche behaviors accurately. It extends the validity of the original model from the low current density region or weak avalanche into the high current density region that is more interesting in today's HBT power applications. One of the advantages of this enhancement is its simplicity which requires no extra measurement compared with the other approaches [129]. The simplicity of this modification makes it is readily implemented into the commercial modeling tools and the newly added model parameter can be easily extracted.

Chapter 6

Analysis and Design of Active Slot Antenna with EBG Feed

6.1 Introduction

This chapter addresses the issue of antenna analysis and design. The planar antenna is typically integrated with the active microwave circuit to form the active integrated antenna. Among various types of planar antennas, the CPW slot antenna is most favorable because it can be easily integrated with active devices without vias. However, the use of the planar antenna has been limited by its narrow bandwidth. In this chapter, a technique based on the electromagnetic bandgap (EBG) structure is proposed to increase the impedance bandwidth. Both simulation and measurement results demonstrate that this technique can effectively enhance the impedance bandwidth without degrading the antenna radiation pattern.

On the basis of various approaches to model and extract the HBT model parameters discussed from Chapters 2-5, a HBT power amplifier has also been designed and integrated with an EBG-fed slot antenna. The fabricated active integrated antenna has been measured and verified with the analysis provided. The measured results show the validity of the approaches employed throughout this thesis.

6.2 Review of Previous Works on Electromagnetic/Photonic Bandgap

One- and two-dimensional periodic structures for electromagnetic wave have been studied since the early days of microwave radar and have been developed over the years [130]. Recently, there is a new terminology called electromagnetic/photonic bandgap (EBG/PBG), which is originated from optics [131] have been applied in the microwave region. The application includes the suppression of surface waves, the construction of Perfect Magnetic Conducting (PMC) planes and antenna gain enhancement [132]-[134].

Electromagnetic bandgap structures are artificial electromagnetic crystals having a spatially periodic constant with a lattice parameter comparable to the wavelength of the electromagnetic wave. When suitably designed, an electromagnetic bandgap structure is capable of suppressing the propagation of electromagnetic wave along certain directions over a band of frequencies. The first experimental demonstration of a three-dimensional photonic bandgap was by Yablonovitch *et al.* [135]. Since that tim,e several other photonic bandgap structures, especially those compatible with coplanar waveguide configuration, have been investigated [136] [137], and applications, such as high-impedance ground plane structures for antenna have been demonstrated [136].

A conductor-backed coplanar waveguide (CBCPW) can support, besides the dominant CPW mode, two other parasitic modes, namely the parallel plate mode and the microstrip mode, respectively. These parasitic modes, when excited, coupled power from the dominant coplanar waveguide mode to a leaky mode. When compared to a conventional coplanar waveguide, the loss of power through leakage is responsible for the higher transmission loss in a CBCPW.

Yang, *et al*., proposed a nonleaky conductor backed coplanar waveguide [138]. In this transmission line the top ground plane on either side of the center strip conductor are replaced by two-dimensional photonic-bandgap lattice. The lattice consists of a periodic array of square metal pads with recess and interconnected by narrow lines. Over a predetermined frequency band, the photonic-bandgap lattice behaves as a perfect magnetic conductor (PMC), and has a band-stop-type characteristic.

The unit cell is modeled along the *x*-direction as a transmission line of length equal to the substrate thickness *h* [139]. The propagation constant on this line is denoted as β. Furthermore to take into account the presence of a lower ground plane, the line is terminated at the bottom by a perfect electric conductor (PEC). In the lattice, the gaps between adjacent pads and the interconnecting lines between the pads give rise to a capacitance *C* and an inductance *L*. Hence, the transmission line is terminated at the top by a parallel equivalent circuit consisting of a capacitor *C* and an inductor *L*. The equivalent circuit model is shown in Figure 6.1.

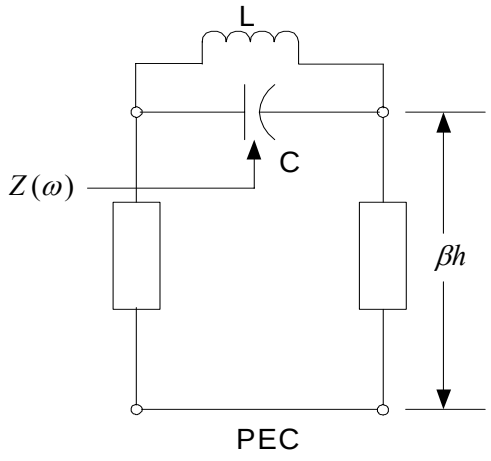

Figure 6.1 Equivalent circuit model for the unit cell.

Based on this model, the surface of a photonic-bandgap lattice is assigned a sheet impedance that is equal to the impedance of the parallel equivalent circuit, and is expressed as

$$Z = \frac{j\omega L}{1-\omega^2 LC}. \tag{6.1}$$

This equation suggests that the surface impedance is very high at the resonant frequency ω_0 given by

$$\omega_0 = \frac{1}{\sqrt{LC}}. \tag{6.2}$$

Consequently at ω_0 the surface behaves as a perfect magnetic conductor (PMC). This type of impedance characteristic makes the photonic-bandgap structure reject a predetermined band of frequencies. Over this high-impedance surface or ground plane, the tangential electric and magnetic fields have an antinode and a node, respectively. Furthermore, from equation (6.1), the surface impedance below and above ω_0 is inductive and capacitive, respectively.

The perfect magnetic conductor (PMC) behavior of the photonic bandgap structure can be verified by illuminating the surface with a uniform plane wave and observing the phase of the reflected wave [139]. When the frequency of the incident wave is far below and above ω_0, the surface according to equation (6.1) has either an inductive or capacitive impedance. Consequently, the phase of the reflected wave from this surface, depending on frequency being greater than or less than ω_0, is either π or $-\pi$. At ω_0 the surface has a very high impedance, and therefore the phase of the reflected wave is zero. The phase falls within $+\pi/2$ and $-\pi/2$ when the magnitude of the surface impedance exceeds the impedance of free space.

The first investigation of microstrip patch antenna with an EBG structure was reported by Vaughan *et al.* [140]. In his work, 2D EBG structure with square lattice,

periodically distributed conical holes, was utilized as substrate for a microstrip antenna. It is found that the ripples in the radiation pattern can be effectively removed by using this structure. Following this find, several similar microstrip antenna with EBG substrates of circular holes were proposed to improve the radiation pattern by suppressing surface waves [141] [142].

A new version of 2D EBG structure for microstrip antenna by Qian *et al.* [143], in which, a patch antenna is surrounded by a periodic 2D pattern consists of a square lattice of small metal pad with grounding vias in the center. 1.6 dB higher gain and 3 times bandwidth improvement also have been obtained by this structure.

All the aforementioned microstrip patch antennas have EBG structure in their substrate. This EBG structure requires drilling of a periodic pattern through the substrate. This process is not compatible with monolithic circuit technology. Therefore, in [144], Radisic *et al.* demonstrated experimentally that an EBG structure in the ground plane could be used to replace the EBG structure in the substrate. This structure is fabricated by partial etching of the ground plane. The measurement results suggest that this structure performs better than the conventional EBG substrate structure. Horii and Tatsumi [145] constructed a microstrip patch antenna with this EBG structure in the ground plane and it is found that this structure has not only improved the radiation patterns, it suppresses higher harmonics effectively with the proper choice of lattice structure and the ratio of lattice period and hole size.

6.3 EBG Lattice Design Considerations

From the transmission line theory, the propagation constant and phase velocity of a lossless transmission line are given, respectively, as

$$\beta = \omega\sqrt{LC}\,, \tag{6.3}$$

and

$$v_p = 1/\sqrt{LC}, \tag{6.4}$$

where L and C are the inductance and capacitance per unit length along the transmission line. Thus, slow-wave propagation can be accomplished by effectively increasing the L and C values. One way to do this is by introducing periodic variations along the direction of propagation, such as drilling holes in the substrate or by etching patterns in the microstrip ground plane [146]. Because the fields in a microstrip line are concentrated in the electric substrate region, these periodic variations strongly perturb the nature of the microstrip field distributions. In contrast, the fields in CPW are localized in the two slots, so that perforation of the two ground planes will have little effect on CPW guided-wave propagation. Therefore, in order to increase the effective capacitance and inductance along the CPW line, several periodic structures have been investigated, as depicted in Figure 6.2 – Figure 6.4.

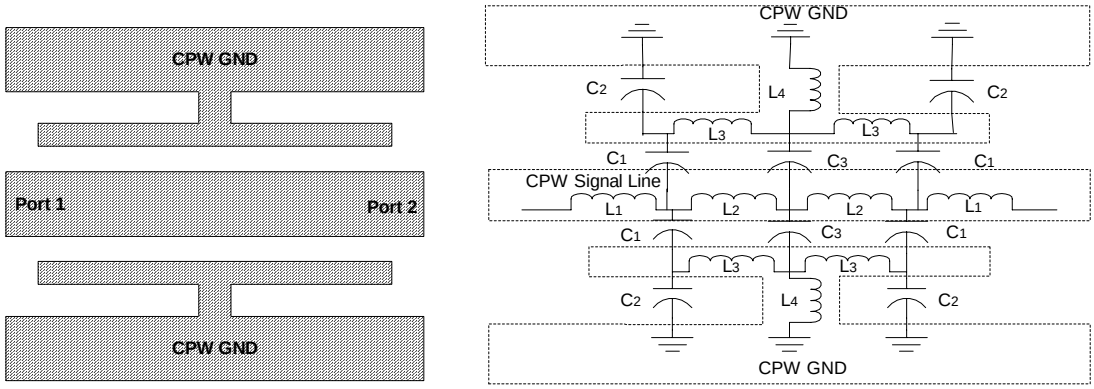

(a) (b)

Figure 6.2 (a) Unit cell of PBG structure A. (b) Corresponding equivalent circuit.

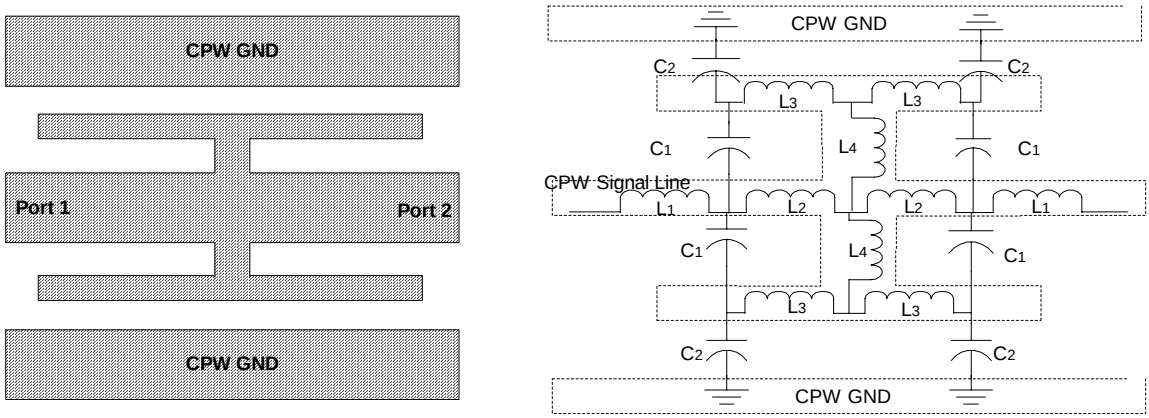

(a) (b)

Figure 6.3 (a) Unit cell of PBG structure B. (b) Corresponding equivalent circuit.

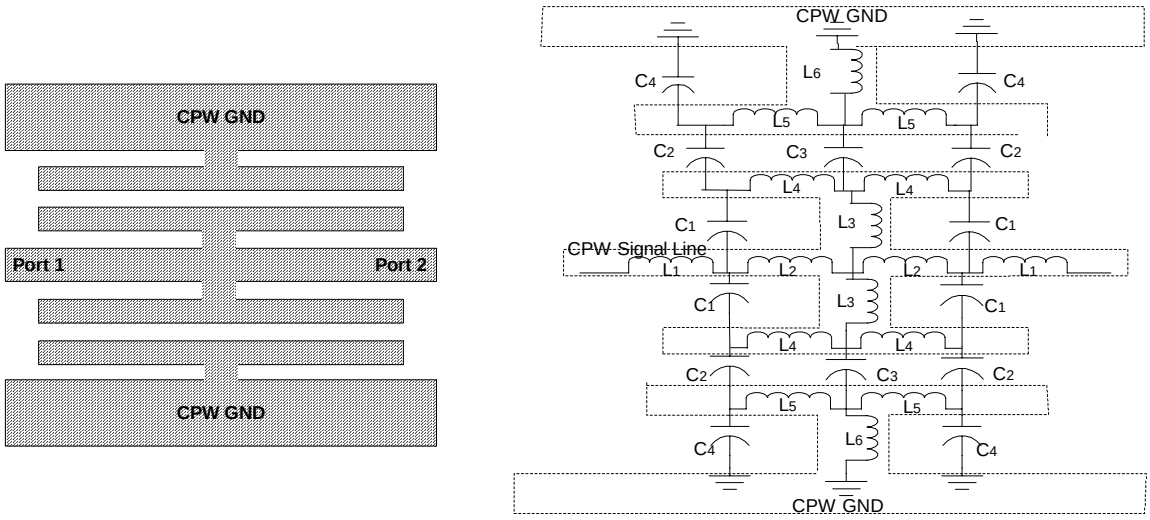

(a) (b)

Figure 6.4 (a) Unit cell of PBG structure C. (b) Corresponding equivalent circuit.

In each of above schemes, the width of the CPW center conductor is narrowed, enhancing the inductance per unit length. To increase the capacitance to ground, the two ground planes of the CPW line are brought closer in proximity to the center

conductor. This can be accomplished by branching out the two ground planes, as in Figure 6.2 (a), by branching out the center conductor, as in Figure 6.3 (a), or by combining the two effects, as in Figure 6.4 (a).

These unit cells offer several advantages. First, the overall footprints of the periodic structures remain the same when compared to a standard 50-Ω CPW transmission line. Although performing the edges of the two ground planes can potentially enhance the capacitive and inductive effects, doing so reduces the transmission line's compatibility with active devices and increases the overall footprint of the periodic structure. Second, the completely uniplanar geometries of the structures eliminate any uncertainty in positioning the signal line in reference to the ground plane. This differs from some microstrip periodic structures, where the insertion loss and return loss vary depending upon where the top conductor is placed in reference to the periodically etched ground plane [147]. Finally, the above structures offer very simple fabrication that can be implemented on one side of dielectric substrate using standard etching techniques. No additional procedures in the form of ion-implanting or cross-tie overlays are required, and the smallest dimensions of the unit cells are still large enough, such that no photoreduction or photolithographic processes are required.

Full-wave analysis is required for accurate analysis of each unit cell, since the inductive and capacitive values of any periodic structure are not entirely independent owing to coupling effects [148]. Figure 6.2 (b), Figure 6.3 (b) and Figure 6.4(b) corresponds to equivalent models, respectively. In the corresponding equivalent circuit models, each narrow conducting line in the unit cell can be modeled as an inductance while any pair of parallel conducting edges is represented by some capacitance value.

The required unit cell length for cutoff frequency f_c can be estimated [149] as

$$f_{C_i} = \frac{c}{2\sqrt{\varepsilon_{eff}}L_i}, \qquad i=x \text{ or } y \tag{6.5}$$

where c is the speed of the light, L_i is the given period and ε_{eff} is the effective permittivity of substrates. In reality, ε_{eff} increases along the frequency and will depend on the number of unit cells in the periodic structures. That is, an ideal periodic structure, infinite in extent, will experience a higher effective dielectric constant than for periodic structures with a finite number of cells owing to the coupling interaction between cells. The effective dielectric constant can be calculated [150]-[152] from two-port S-parameters as follows:

$$e^{-\gamma l} = \left(\frac{1 - S_{11}^2 + S_{21}^2}{2S_{21}} + K \right)^{-1}, \tag{6.6}$$

where

$$K = \left\{ \frac{(S_{11}^2 - S_{21}^2 + 1)^2 - (2S_{11})^2}{(2S_{21})^2} \right\}^{1/2}, \tag{6.7}$$

then, from propagation constant $\gamma = \alpha + j\beta$,

$$\varepsilon_{eff} = \left\{ \frac{c}{\varpi l} In\left(\frac{1 - S_{11}^2 + S_{21}^2}{2S_{21}} + K \right) \right\}^2. \tag{6.8}$$

Although the full-wave analysis offers the accuracy of the simulation, a common disadvantage of this approach — as with all numerical methods — is that it does not provide any clear analytic review of the effect of geometrical dimensions of the EBG structure. Using simple electrostatic and conformal mapping approximation, the following intends to provide a design guide that links the geometrical dimensions with the response of the EBG structure.

Let us focus on two commonly used EBG unit cells which are illustrated in Figure 6.5(a) and Figure 6.5(b). The corresponding lossless equivalent circuits are also superimposed in Figure 6.5(a) and Figure 6.5(b). From the transmission-line theory, the propagation constant and phase velocity of a lossless transmission line are given, respectively, as $\beta = \omega\sqrt{LC}$ and $v_p = 1/\sqrt{LC}$, where L and C are the inductance and capacitance per unit length along the transmission line. Thus, further slow-wave propagation can be accomplished by effectively changing the C and L values along the transmission feed line.

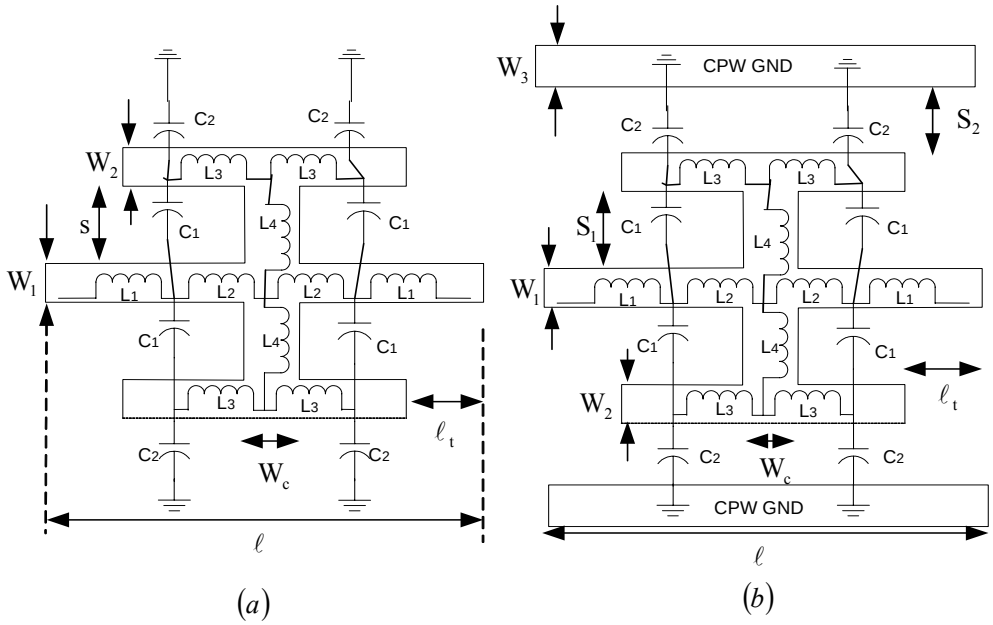

(a) (b)

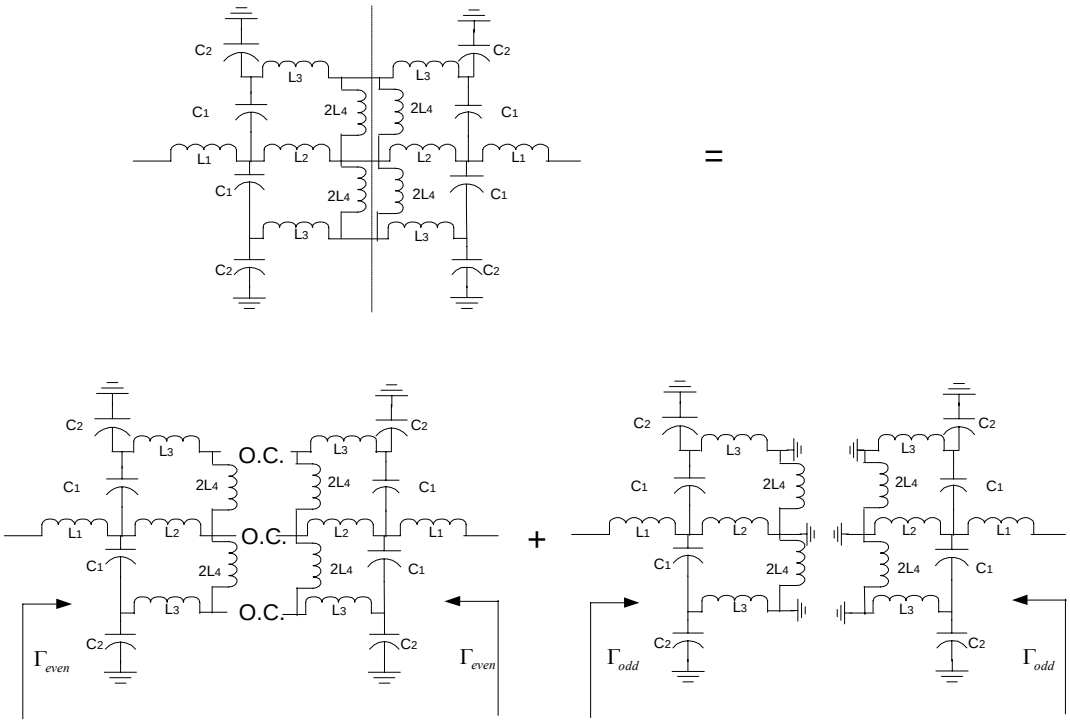
C2
L3
C1
2L4
L1
L2
O.C.
Γeven
Γodd
=
+

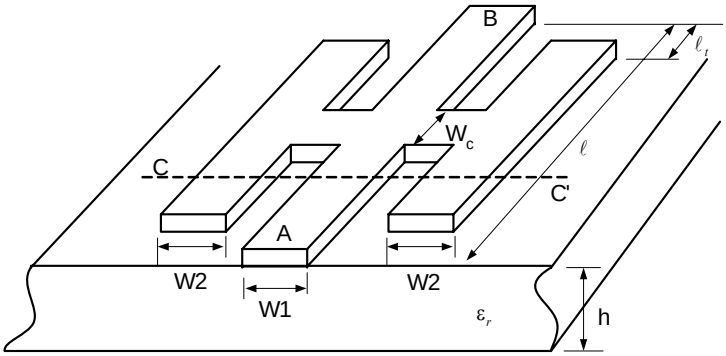
B
C
C'
A
Wc
W2
W1
ℓ
ℓt
h
εr

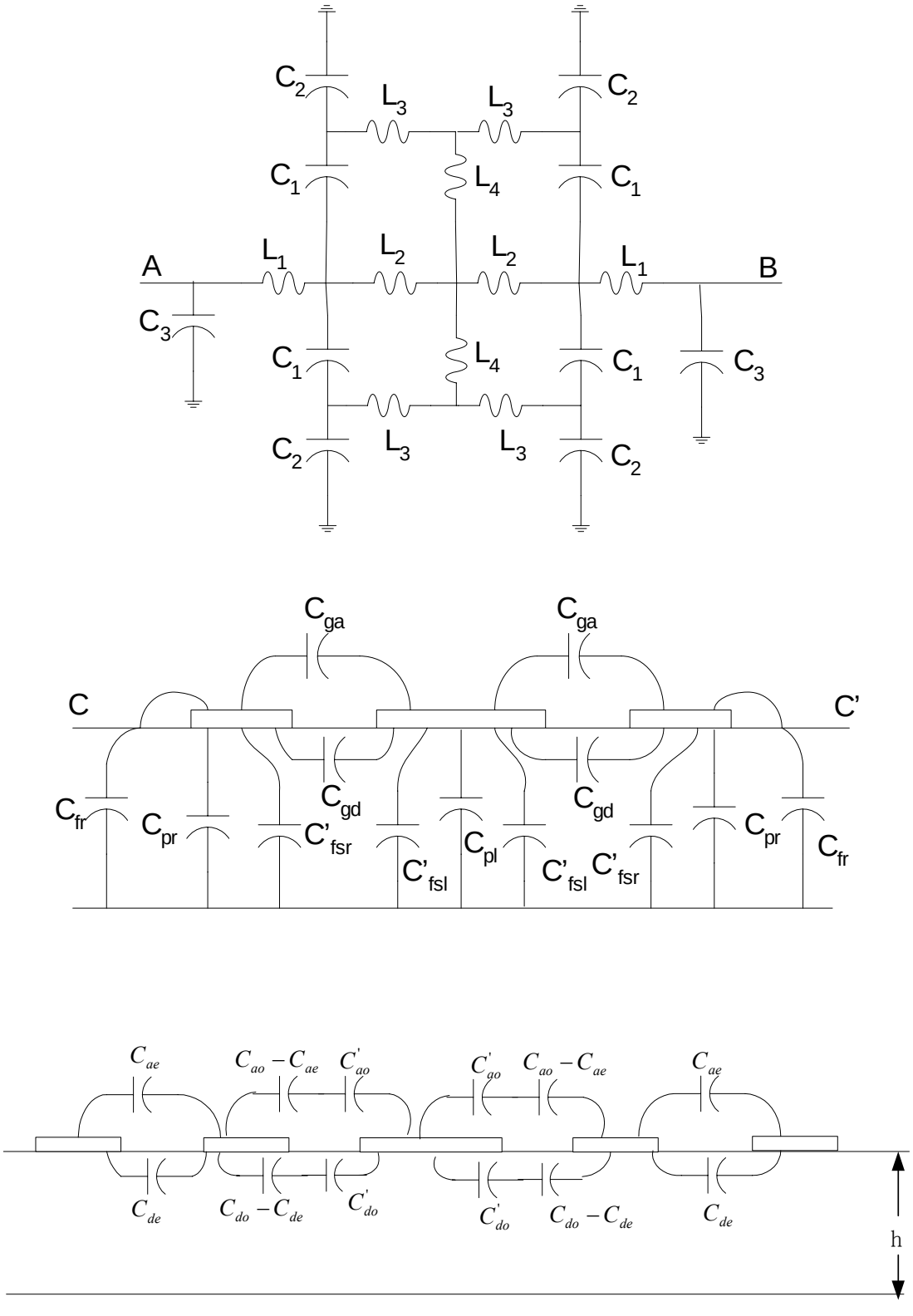

(c)

Figure 6.5 Typical EBG unit cell for microstrip (a) and coplanar (b) structures, and their corresponding lossless equivalent circuits (c) separation of equivalent circuit of for the derivation of equivalent capacitance.

The unit cell S-parameters of the equivalent circuit shown in Figure 6.5(a) and (b) are expressed as follows:

$$S_{11} = S_{22} = \frac{1}{2}\left(\Gamma_{odd} + \Gamma_{even}\right), \tag{6.9}$$

$$S_{12} = S_{21} = \frac{1}{2}\left(\Gamma_{even} - \Gamma_{odd}\right), \tag{6.10}$$

where

$$\Gamma_o = \frac{2\omega^2 L_2 C_1\left[1-\omega^2 L_3 C_2\right]\left[j\omega L_1 - 50\right] + \left[1-\omega^2 L_3\left(C_1+C_2\right)\right]\left[1-\omega^2 L_2 C_3\right]\left[j\omega L_1 - 50\right] - j\omega L_2}{2\omega^2 L_2 C_1\left[1-\omega^2 L_3 C_2\right]\left[j\omega L_1 + 50\right] + \left[1-\omega^2 L_3\left(C_1+C_2\right)\right]\left[1-\omega^2 L_2 C_3\right]\left[j\omega L_1 + 50\right] - j\omega L_2} \tag{6.11}$$

$$\Gamma_e = \frac{1 + j\omega\left[j\omega L_1 - 50\right]\left[2C_2 + C_3\right] - \omega^2\left[L_3 + 2\left(L_4 + L_2\right)\right]\left[C_1 + C_2 + j\omega\left(j\omega L_1 - 50\right)\left(2C_1C_2 + C_3\left(C_1 + C_2\right)\right)\right]}{1 + j\omega\left[j\omega L_1 + 50\right]\left[2C_2 + C_3\right] - \omega^2\left[L_3 + 2\left(L_4 + L_2\right)\right]\left[C_1 + C_2 + j\omega\left(j\omega L_1 + 50\right)\left(2C_1C_2 + C_3\left(C_1 + C_2\right)\right)\right]} \tag{6.12}$$

Hence, the effective permittivity can easily be obtained as

$$\varepsilon_{eff} = \mathrm{Imag}\left(\frac{\left[\ln\left(\left(1 - S_{11}^2 + S_{21}^2 \pm \sqrt{\left(S_{11}^2 - S_{21}^2 + 1\right)^2 - \left(2S_{11}\right)^2}\right) \Big/ \left(2S_{21}\right)\right)\right]^2}{\omega^2 \mu_0 \varepsilon_0 \ell^2}\right), \tag{6.13}$$

where ℓ is the total horizontal length of the unit EBG cell and the operator Imag(.) implies taking the imaginary term enclosed in the bracket. The characteristic impedance of the EBG unit cell is given as

$$Z_o = 50\sqrt{\frac{\left(1 + S_{11}\right)^2 - S_{21}^2}{\left(1 - S_{11}\right)^2 - S_{21}^2}}. \tag{6.14}$$

Hence, the effective per unit length inductance and per unit length capacitance are respectively computed from

$$L_{eff} = \mathrm{imag}\left(\frac{Z_o\sqrt{\varepsilon_{eff}}}{\ell c_o}\right), \tag{6.15}$$

$$C_{eff} = \text{imag}\left(\frac{\sqrt{\varepsilon_{eff}}}{\ell Z_o c_o}\right), \tag{6.16}$$

where c_o is the speed of light. The capacitance C_1 for the microstrip EBG unit cell is approximated by

$$C_1 = \frac{(\ell - 2\ell_t - W_c)(C_{ga} + C_{gd})}{2}, \tag{6.17}$$

$$C_2 = \frac{(\ell - 2\ell_t - W_c)(C_{fr} + C_{pr} + C'_{fsr})}{2}, \tag{6.18}$$

$$C_3 = \frac{(\ell - 2\ell_t - W_c)(2C'_{fsl} + C_{pl})}{2}, \tag{6.19}$$

$$C_{ga} = \frac{1}{2}(\varepsilon_r + 1)\varepsilon_o \frac{K(k'_0)}{K(k_o)} - \Delta C_f \ , \tag{6.20}$$

where

$$k_o = \sqrt{\frac{\frac{S}{h}\left(\frac{S}{h} + \frac{W_1}{2h} + \frac{W_2}{h}\right)}{\left(\frac{S}{h} + \frac{W_1}{2h}\right)\left(\frac{S}{h} + \frac{W_2}{h}\right)}},$$

$$k'_o = \sqrt{1 - k_o^2}$$

$$\Delta C_f = \frac{1}{2}\left[\frac{\varepsilon_r + 1}{2c_o Z_m(W_2, h, \varepsilon_r = 1)} - \frac{1}{c_o 60\pi}\frac{K(k_1)}{K(k'_1)}\right],$$

$$k_1 = \textbf{tanh}\left(\frac{\pi W_2}{4h}\right),$$

$$k'_1 = \sqrt{1 - k_1^2} \ ,$$

$$Z_m(W_y, h, \varepsilon_r) = \begin{cases} 60\,\textbf{ln}\left(\frac{8h}{W_y} + \frac{W_y}{4h}\right), & \frac{W_y}{h} \le 1, \\ \frac{120\pi}{\left[\frac{W_y}{h} + 1.393 + 0.677\,\textbf{ln}\left(\frac{W_y}{h} + 1.444\right)\right]}, & \frac{W_y}{h} \ge 1, \end{cases}$$

and

$$C_{gd} = \frac{1}{2}\sqrt{(C_{osl} - C_{esl})(C_{osr} - C_{esr})}, \tag{6.21}$$

where

$$C_{osy} = \frac{1}{60\pi c_o}\frac{K(k_2)}{K(k'_2)},$$

$$k_2 = \frac{\tanh\left(\frac{\pi W_y}{4h}\right)}{\tanh\left(\frac{(S+W_y)\pi}{4h}\right)},$$

$$k_2' = \sqrt{1-k_2^2},$$

c_o is the speed of light.

$$C_{esy} = \frac{1}{60\pi c_o}\frac{K(k_3)}{K(k_3')},$$

$$k_3 = \tanh\left(\frac{\pi W_y}{4h}\right)\tanh\left(\frac{\pi(S+W_y)}{4h}\right),$$

$$k_3' = \sqrt{1-k_3^2},$$

$$W_y = \begin{cases} \frac{W_1}{2}, & y = l, \\ W_2, & y = r, \end{cases},$$

$$C_{fr} = \frac{1}{2}\left[\frac{\varepsilon_{re}(W_2,h,\varepsilon_r)}{c_o Z_m(W_2,h,\varepsilon_r=1)} - \frac{\varepsilon_o\varepsilon_r W_2}{h}\right],$$

$$\varepsilon_{re}(W_y,h,\varepsilon_r) = \begin{cases} \frac{1}{2}\left[\varepsilon_r + 1 + (\varepsilon_r - 1)\left[\frac{1}{\sqrt{1+\frac{12h}{W_y}}} + 0.04\left(1-\frac{W_y}{h}\right)^2\right]\right], & \frac{W_y}{h} \le 1, \\ \frac{1}{2}\left[\varepsilon_r + 1 + \frac{\varepsilon_r - 1}{\sqrt{1+\frac{12h}{W_y}}}\right], & \frac{W_y}{h} \ge 1, \end{cases},$$

$$C'_{fsy} = C_{esy} - C_{py} - C_{fsy},$$

$$C_{py} = \frac{\varepsilon_o\varepsilon_r W_y}{h},$$

$$C_{fsy} = \frac{1}{2}\left(\frac{1}{60\pi c_o}\frac{K(k_4)}{K(k_4')} - C_{py}\right),$$

$$k_4 = \tanh\left(\frac{\pi W_y}{4h}\right),$$

$$k_4' = \sqrt{1-k_4^2},$$

$$L_i = \frac{Z_m(W_i,h,\varepsilon_r)}{2\pi f}\sin\left(\frac{2\pi\ell_i\sqrt{\varepsilon_{re,i}}}{\lambda}\right), i = 1,2,3,4 \ , \qquad (6.22)$$

where h is the height of the substrate, s is the separation distance between the fingers, and the ratio of the elliptic functions is given approximately as

$$\frac{\mathrm{K}(\mathrm{k}')}{\mathrm{K}(\mathrm{k})}=\begin{cases}\dfrac{1}{\pi}\ln\left(2\dfrac{1+\sqrt{\mathrm{k}'}}{1-\sqrt{\mathrm{k}'}}\right), & 0\le \mathrm{k}^2\le 0.5,\\ \dfrac{\pi}{\ln\left(2\dfrac{1+\sqrt{\mathrm{k}}}{1-\sqrt{\mathrm{k}}}\right)}, & 0.5\le \mathrm{k}^2\le 1.\end{cases} \tag{6.23}$$

Similarly, referring to Figure 6.5, for the coplanar EBG unit cell, the corresponding capacitance can be approximated by

$$C_1=(C_{ao}-C_{ae}+C_{do}-C_{de})//(C_{ao}^{'}+C_{do}^{'}), \tag{6.24}$$

$$C_2=C_{ae}+C_{de}, \tag{6.25}$$

where

$$C_{ae}=\varepsilon_0\frac{K(k_1)}{K(k_2)}, \tag{6.26}$$

$$k_1=\sqrt{\frac{(z_4^2-z_3^2)(z_2^2-z_1^2)}{(z_4^2-z_2^2)(z_3^2-z_1^2)}},$$

$$k_2=\sqrt{\frac{(z_3^2-z_2^2)(z_4^2-z_1^2)}{(z_4^2-z_2^2)(z_3^2-z_1^2)}},$$

$$z_1=\frac{2s_1w_2}{2w_2+w_1},$$

$$z_2=w_2+\frac{2s_1w_2}{2w_2+w_1},$$

$$z_3=w_2+\frac{2s_1w_2}{2w_2+w_1}+s_2,$$

$$z_4=w_2+\frac{2s_1w_2}{2w_2+w_1}+w_3+s_2,$$

$$C_{ao}=\varepsilon_0\frac{K(k_5)}{K(k_6)}, \tag{6.27}$$

$$k_5 = \sqrt{\frac{1-(\frac{z_1}{z_2})^2\sqrt{\frac{z_4^2-z_2^2}{z_4^2-z_1^2}}}{1-(\frac{z_1}{z_3})^2\sqrt{\frac{z_4^2-z_3^2}{z_4^2-z_1^2}}}},$$

$$k_6 = \sqrt{\frac{(\frac{z_3}{z_2})^2\sqrt{\frac{z_4^2-z_1^2}{z_4^2-z_3^2}}-1}{(\frac{z_3}{z_1})^2\sqrt{\frac{z_4^2-z_1^2}{z_4^2-z_3^2}}-1}},$$

$$C_{de} = \varepsilon_0\varepsilon_r\frac{K(k_3)}{K(k_4)}, \tag{6.28}$$

$$k_4 = \sqrt{\frac{(\sinh^2(\frac{\pi z_3}{2h})-\sinh^2(\frac{\pi z_2}{2h}))(\sinh^2(\frac{\pi z_4}{2h})-\sinh^2(\frac{\pi z_1}{2h}))}{(\sinh^2(\frac{\pi z_3}{2h})-\sinh(\frac{\pi z_1}{2h}))(\sinh^2(\frac{\pi z_4}{2h})-\sinh^2(\frac{\pi z_2}{2h}))}},$$

$$C_{do} = \varepsilon_0\varepsilon_r\frac{K(k_7)}{K(k_8)}, \tag{6.29}$$

$$k_7 = \sqrt{\frac{(t_1-t_2)(t_5-t_3)}{(t_5-t_2)(t_1-t_3)}},$$

$$k_8 = \sqrt{\frac{(t_5-t_1)(t_2-t_3)}{(t_5-t_2)(t_1-t_3)}},$$

where

$$t_i = -\frac{\tanh^2\frac{\pi z_i}{2h}}{\tanh^2\frac{\pi z_2}{2h}}\sqrt{\frac{\tanh^2\frac{\pi z_4}{2h}-\tanh^2\frac{\pi z_2}{2h}}{\tanh^2\frac{\pi z_4}{2h}-\tanh^2\frac{\pi z_i}{2h}}}, \qquad i=1,2,3$$

$$t_5 = 0,$$

$$C_{ao}^{'} = \varepsilon_0 \frac{K(k_9^{'})}{K(k_9)}, \tag{6.30}$$

$$k_9 = \frac{2s_1}{2s_1 + w_1 + 2w_2},$$

$$k_9^{'} = \sqrt{1 - k_g^2},$$

and

$$C_{do}^{'} = \varepsilon_0 \varepsilon_r \frac{K(k_{10})}{K(k_{11})}, \tag{6.31}$$

$$k_{10} = \sqrt{\frac{(t_1 - t_2)(t_3 - t_4)}{(t_1 - t_3)(t_2 - t_4)}},$$

$$k_{11} = \sqrt{\frac{(t_2 - t_3)(t_1 - t_4)}{(t_1 - t_3)(t_2 - t_4)}},$$

where

$$t_1 = -\sinh^2 \frac{\pi}{2h}\left(\frac{s_1 w_1}{2w_2 + w_1} + \frac{w_1}{2}\right),$$

$$t_2 = -\sinh^2 \frac{\pi}{2h}\left(\frac{s_1 w_1}{2w_2 + w_1}\right),$$

$$t_3 = 0,$$

$$t_4 = 1.$$

All the inductances in the microstrip and coplanar EBG unit cell can be approximated from

$$\mathrm{L_i} = \frac{\mathrm{Z_{o,i}}}{\omega} \sin\left(\frac{\omega \ell_{\mathrm{i}} \sqrt{\varepsilon_{\mathrm{eff,i}}}}{\mathrm{c_o}}\right), \forall \mathrm{i} = 1,2,3,4, \tag{6.32}$$

where $\varepsilon_{\mathrm{eff,i}}$ is the effective permittivity of the i^{th} transmission line, ℓ_{i} is the length of the i^{th} transmission line and $\mathrm{Z_{oi}}$ is the characteristic impedance of the i^{th} transmission line. A typical result of the computed effective permittivity is shown in Figure 6.6. As

shown in the figure, by cascading more EBG unit cells, the effective permittivity becomes fatter and lower in value. In addition, the variation of the effective permittivity within the frequency bands of interest for the cascaded EBG unit cells becomes less sharp. This in turn can greatly help to improve the matching of the antennas at the multi-band frequencies.

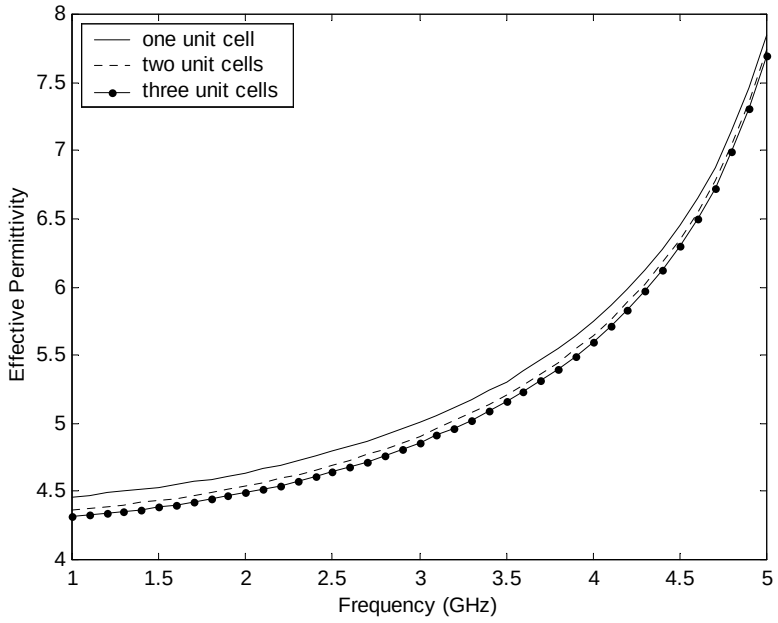

Figure 6.6 Calculated effective permittivity of periodic structure shown in Figure 6.5 (b).

Several EBG structures have been designed based on the above discussion. The cutoff frequency is determined to be 3.8 GHz, from equation (6.5), the unit length is found to be about 12 mm. Figure 6.7 shows the geometric dimensions and substrate parameters of EBG structure B.

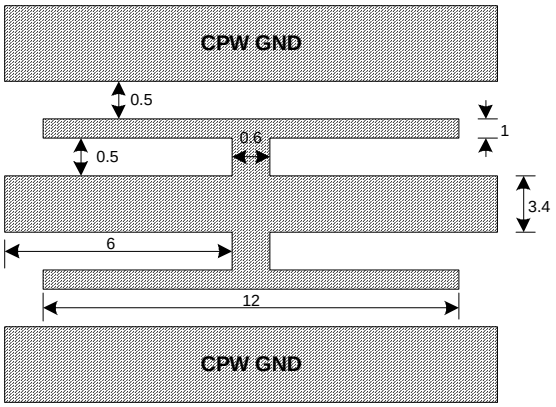

Figure 6.7 Geometric dimensions of designed EBG structure B (units in millimeters, substrate thickness h=1.6 mm; $\varepsilon_r = 4.4$).

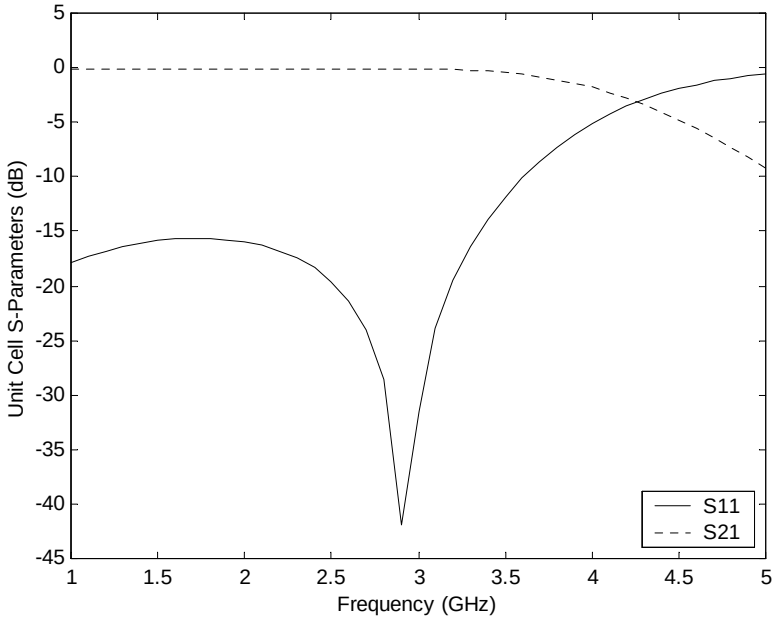

Figure 6.8 Simulated response of unit cell in Figure 6.3 (a)

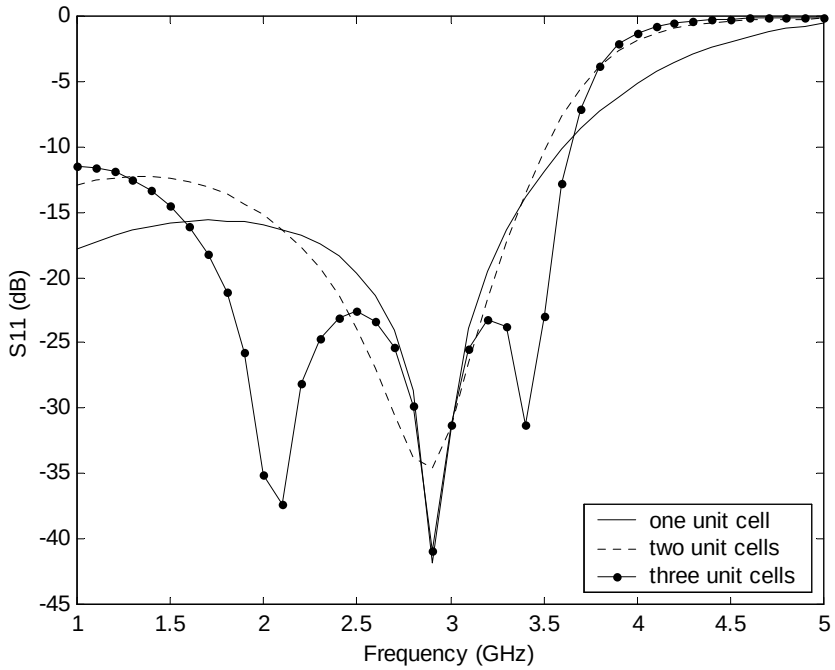

Figure 6.9 Simulated response of one unit cell, two unit cells and three unit cells in Figure 6.3(a).

It can be seen from Figure 6.9 as the number of unit cell increases, the S11 has a shaper attenuation at cutoff frequency. This can be explained by *m*-derived filter theory [153]. For the *T*-network, the propagation constant is given as

$$e^{\gamma} = 1 + \frac{Z_1^{'}}{2Z_2^{'}} + \sqrt{\frac{Z_1^{'}}{Z_2^{'}}\left(1 + \frac{Z_1^{'}}{4Z_2^{'}}\right)}\ , \tag{6.33}$$

where $Z_1^{'}$ and $Z_2^{'}$ are the *m*-derived components as

$$Z_1^{'} = j\omega Lm\,, \tag{6.34a}$$

$$Z_2^{'} = \frac{1}{j\omega Cm} + \frac{(1-m^2)}{4m} j\omega L\,, \tag{6.34b}$$

which results in the circuit in Figure 6.10.

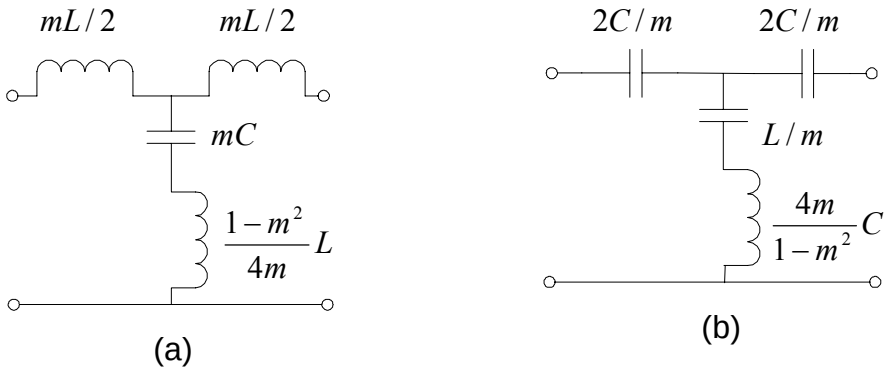

Figure 6.10 *m*-derived filter sections. (a) Low-pass *T*-section. (b) High-pass *T*-section.

For the low-pass m-derived filter,

$$\frac{Z_1'}{Z_2'} = \frac{-(2\omega m/\omega_c)^2}{1-(1-m^2)(\omega/\omega_c)^2}, \tag{6.35}$$

where $\omega_c = 2/\sqrt{LC}$. Then,

$$1+\frac{Z_1'}{4Z_2'} = \frac{1-(\omega/\omega_c)^2}{1-(1-m^2)(\omega/\omega_c)^2}. \tag{6.36}$$

If we restrict 0<*m*<1, then these results show that e^{γ} is real and $|e^{\gamma}| > 1$ for $\omega > \omega_c$. Thus the stopband begins at $\omega = \omega_c$. However, when $\omega = \omega_\infty$, where

$$\omega_\infty = \frac{\omega_c}{\sqrt{1-m^2}}, \tag{6.37}$$

the denominators vanish and e^{γ} becomes infinite, implying infinite attention. Physically, this pole in the attention characteristic is caused by the resonance of the series *LC* resonator in the shunt arm of the *T*; this is easily verified by showing that the resonance frequency of this *LC* resonator is ω_∞. Equation (6.37) indicates that $\omega_\infty > \omega_c$, so infinite attention occurs after the cutoff frequency, ω_c. The position of the pole at ω_∞ can be controlled with the value of *m*.

6.4 Design of Multi-band Antenna with EBG Feed

From the transmission line model [154] [155] the input impedance of the microstrip antenna can be written as

$$Z_{antenna} = \frac{1}{Y_{slot}} + jX_{feed} \tag{6.38}$$

where X_{feed} is determined by the feedline.

From the discussions in the previous section, it can be seen that the EBG lattice offers more flexibility to design the transmission line. The inductance and capacitance values of EBG can be adjusted by varying the dimensions of EBG lattice geometries, thus can effectively cancel the reactive part of the antenna impedance. If the spacing between CPW center conductor and ground is maintained, the optimization variables can be further reduced.

Two basic but different types of multi-band antennas have been adopted for this study. These include the tri-band coplanar EBG slot antenna and the tri-band microstrip dipole antenna. They are selected mainly because of its simplicity and ease in implementing multi-band frequency operations. The selection of these antennas is to show that the use of EBG feeding network is not limited to any particular technologies.

To verify the above analysis, a triple-band rectangular-ring slot antenna with PBG feed has been designed, fabricated and tested. For the comparison purpose, a reference antenna has also been fabricated and tested [156]. The slot antenna consists of three concentric rectangular-ring slots and is printed on a substrate of thickness h and relative permittivity ε_r. The conventional CPW and EBG lattice feedlines are designed to have 50 Ω characteristic impedance in order to match the measurement system. The CPW's signal strip has a width of W_c and the gap spacing between the

signal strip and the coplanar ground is S_c. The CPW feedline also has a tuning stub of length t, at a distance d away from the conducting strip in the center of the slot antenna. The distance d is fixed to be 0.3 mm for both EBG-fed antenna and reference antenna. The resonance frequencies of the reference antenna approximately correspond to the perimeters of the slot, being about 0.83 λ_s – 0.92 λ_s. It is also noted that the wavelength in the slot, λ_s, is determined to be about 0.78 free-space wavelength by considering the presence of different dielectric substrate on the two sides of the slot. For the EBG-fed slot antenna, the PBG feedline is designed with a cutoff frequency of 3.8 GHz and with three cascaded unit cells. The geometric parameters of the EBG feedline are given in Figure 6.7. For the convenience of comparison, all the geometric parameters, except feedline, are the same for EBG-fed antenna and reference antenna. The layouts and photos of EBG antenna and reference antenna are shown in Figures 6.11 and 6.12, respectively. Table 6.1 gives the geometric parameters for two antennas.

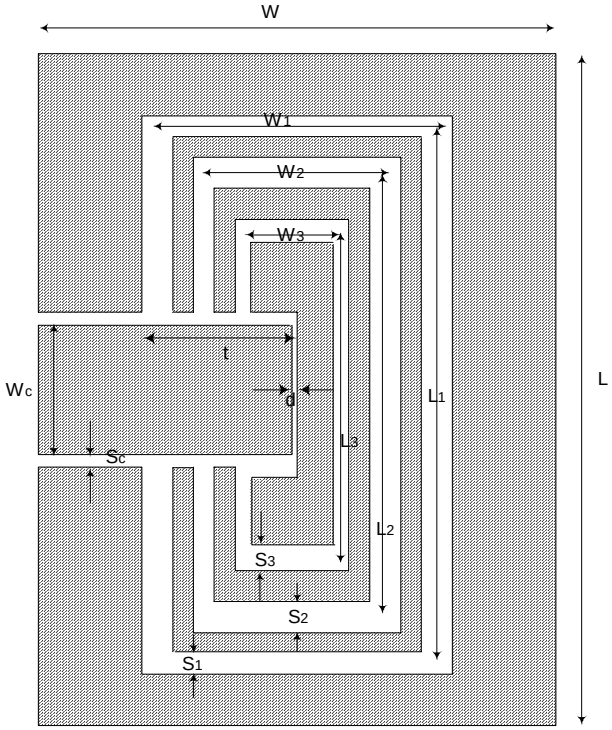

(a)

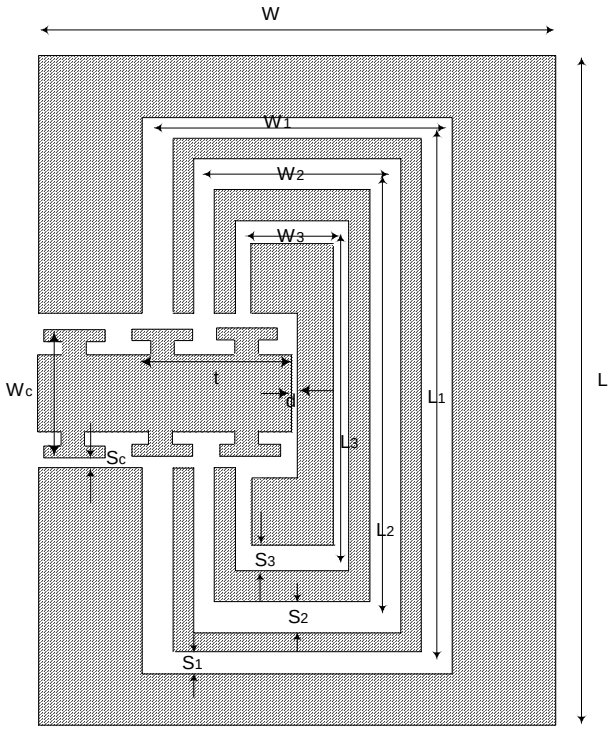

(b)

Figure 6.11 Geometric dimensions of multi-band slot antenna (a) slot antenna with conventional CPW feed (b) slot antenna with EBG feed.

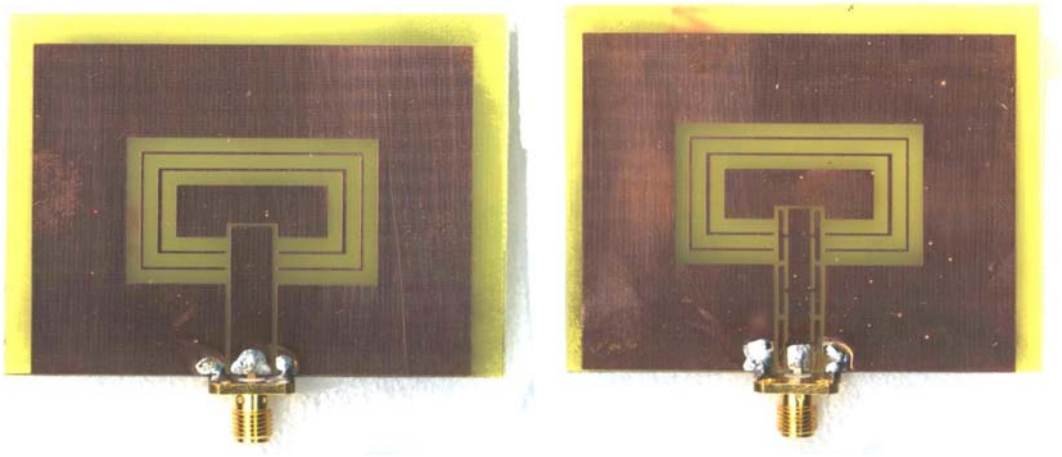

(a) (b)

Figure 6.12 Fabricated slot antenna (a) slot antenna with conventional CPW feed (b) slot antenna with EBG feed.

Table 6.1 Geometric parameters for reference antenna and EBG-fed antenna.

L	W	L_1	W_1	P_1	L_2	W_2	P_2	L_3
65 mm	50 mm	35 mm	20 mm	0.88 λ_s	30 mm	15 mm	0.88 λ_s	24.5mm
W_3	P_3	S_1	S_2	S_3	t	D	W_c	S_c
10 mm	0.92 λ_s	2 mm	2 mm	2 mm	8.8mm	0.3mm	6.4mm	0.5 mm

Similarly, the basic structure of a typical tri-band microstrip dipole antenna with conventional feed-line is illustrated in Figure 6.13(a) whereas the tri-band microstrip dipole antenna with EBG feed is given in Figure 6.13(b). The physical dimensions of the microstrip dipole antennas are also listed in Figures 6.13(a) and (b). Both the conventional-fed and EBG-fed tri-band microstrip dipole antennas are designed respectively at resonant frequencies of 0.9GHz, 1.8GHz and 2.4GHz. In order to reduce the antenna coupling between the different elements, the microstrip dipole antenna corresponding to a resonant frequency of 0.9GHz is separated as far away from the dipole antenna corresponding to a resonant frequency of 1.8GHz. Based on a

detailed parametric variation, the optimum separation distances between the microstrip dipole antennas and the feed line are also given in Figure 6.13(a) and (b). In order to re-use the same fixture, the length L_f is purposely maintained the same as the conventional feed line even though it is noted that there is a reduction in the physical length for EBG-fed tri-band antenna. To improve the matching at 0.9GHz, the corresponding EBG dipole antenna is tapered towards the feed-end. Both the microstrip dipole and coplanar slot antennas are fabricated on FR4 dielectric materials of 1.57mm thick substrate.

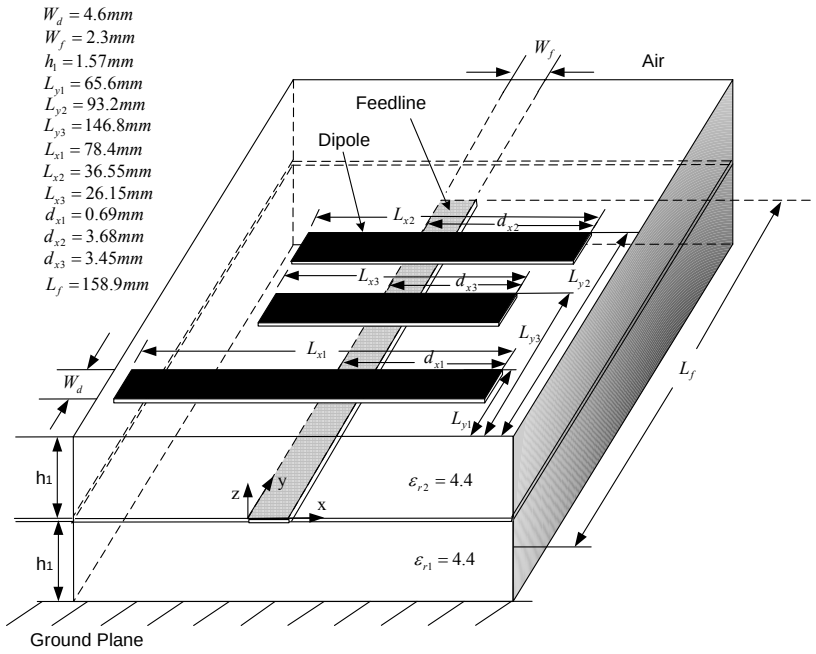

(a)

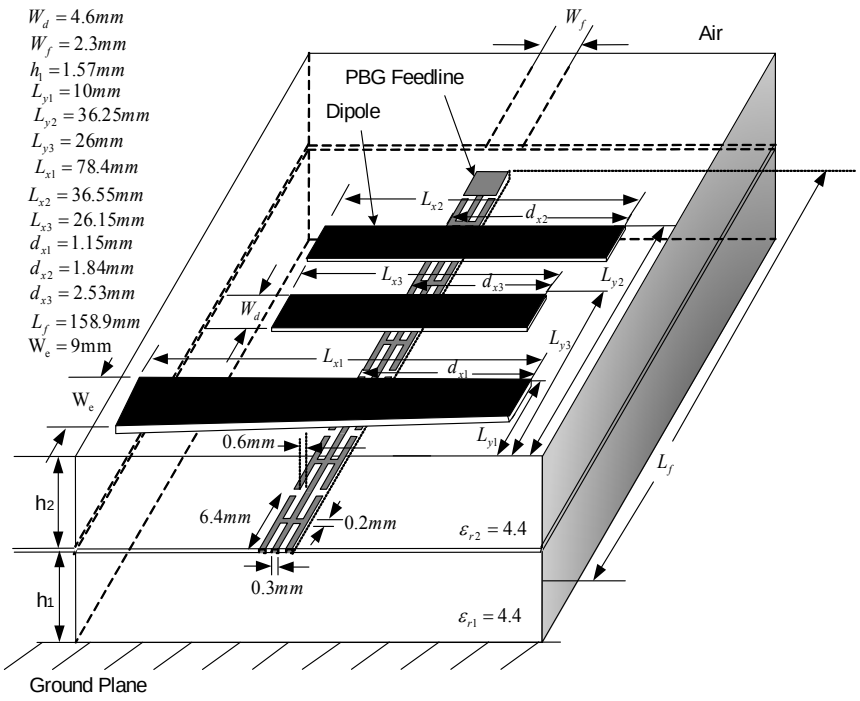

(b)

Figure 6.13 The tri-band microstrip dipole antenna. (a) conventional-fed dipole antenna. (b) EBG-fed microstrip dipole antenna.

Using equations (6.9)-(6.44) and Method of Moments, the four antennas are designed and fabricated. Figure 6.14 (a) shows the simulated return loss for reference antenna and EBG-fed slot antenna. As can be seen, the EBG feedline effectively increase the impedance bandwidth for all the resonance frequencies. The EBG-fed slot antenna experience slightly higher resonance frequency compared with the reference antenna. This can be attributed to the increase of the effective permittivity along the frequency, as shown in Figure 6.6. Hence the resonance frequency is shifted up. In addition, the measurement results of both antennas show higher resonance frequency and wider bandwidth compared to the corresponding simulation results. This may be due to the additional inductive effect introduced by the antenna feeding SMA connectors.

Table 6.2 Performance Comparison for reference antenna and PBG-fed antenna.

	CPW-fed antenna	PBG-fed antenna
f_1	1.86 GHz	1.88GHz
BW_1	7 %	10 %
$Gain_1$	4.1 dBi	4.3 dBi
f_2	2.4GHz	2.45GHz
BW_2	8 %	16 %
$Gain_2$	4.6 dBi	4.6 dBi
f_3	3.25 GHz	3.5 GHz
BW_3	8.3 %	20.8 %
$Gain_3$	5.1 dBi	5.5 dBi

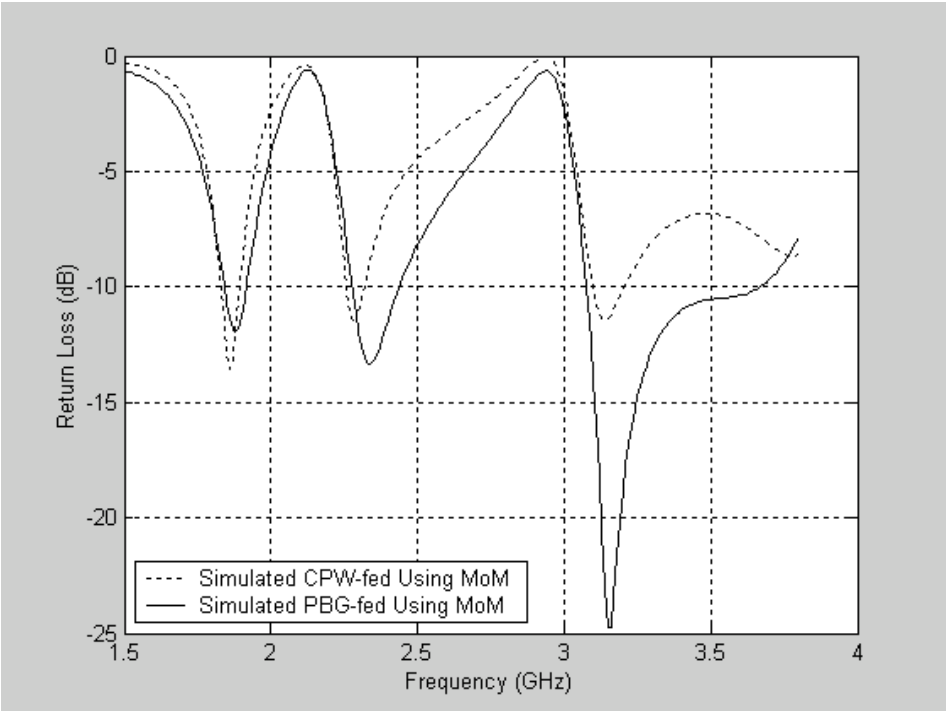

Figure 6.14 (a) Simulated return loss for the PBG-fed slot antenna and reference antenna.

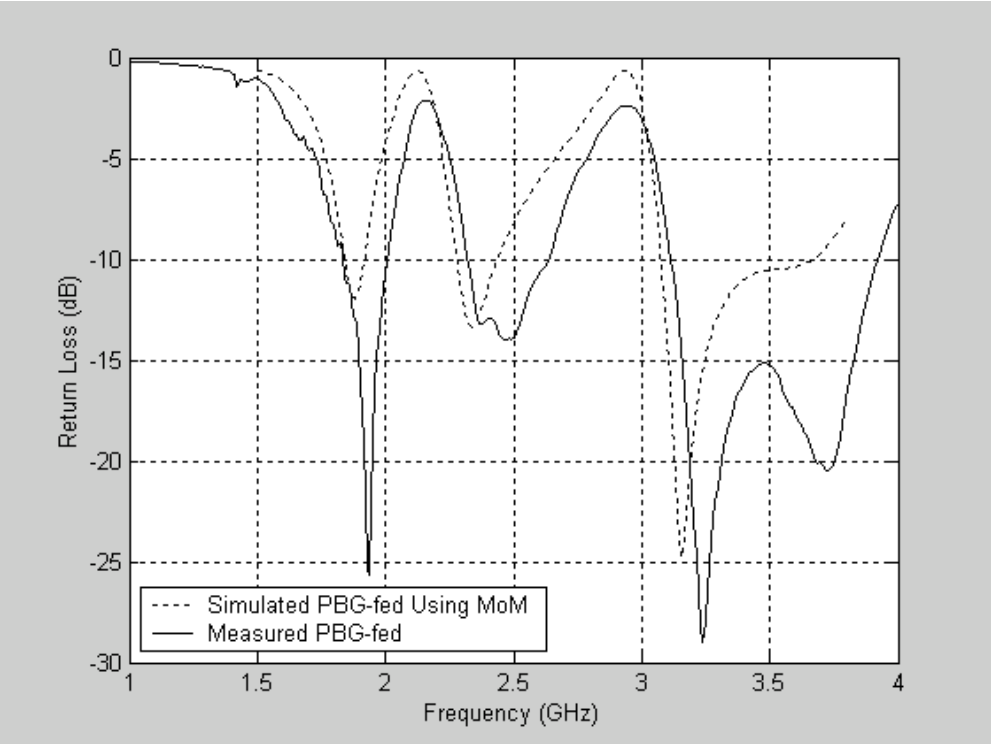

Figure 6.14 (b) Simulated and measured return loss for PBG-fed slot antenna.

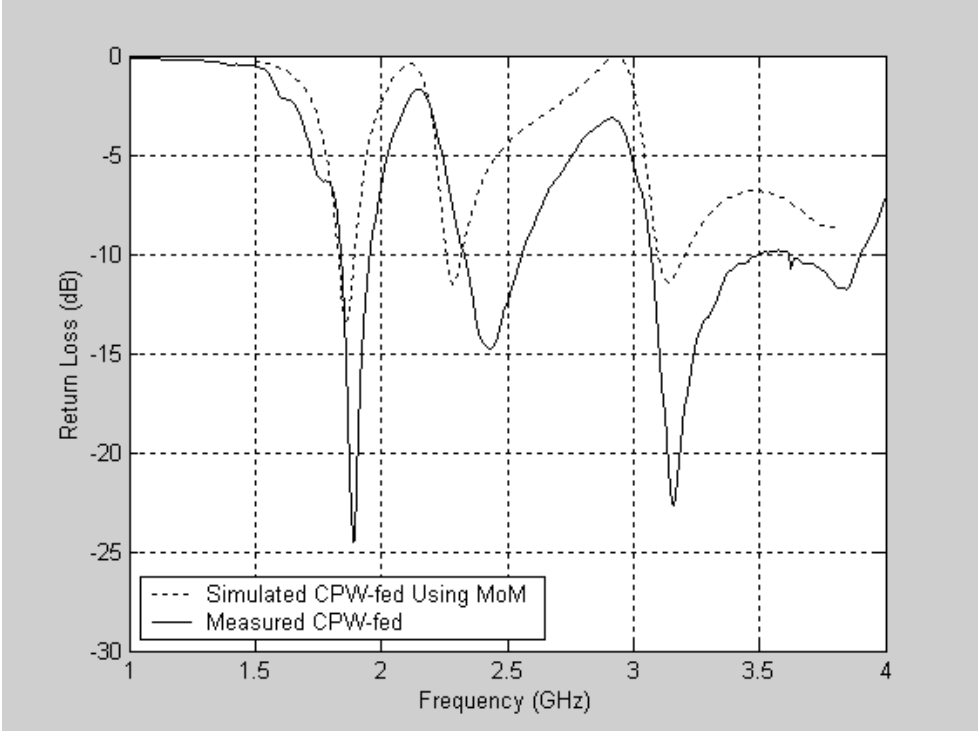

Figure 6.14 (c) Simulated and measured return loss for reference antenna.

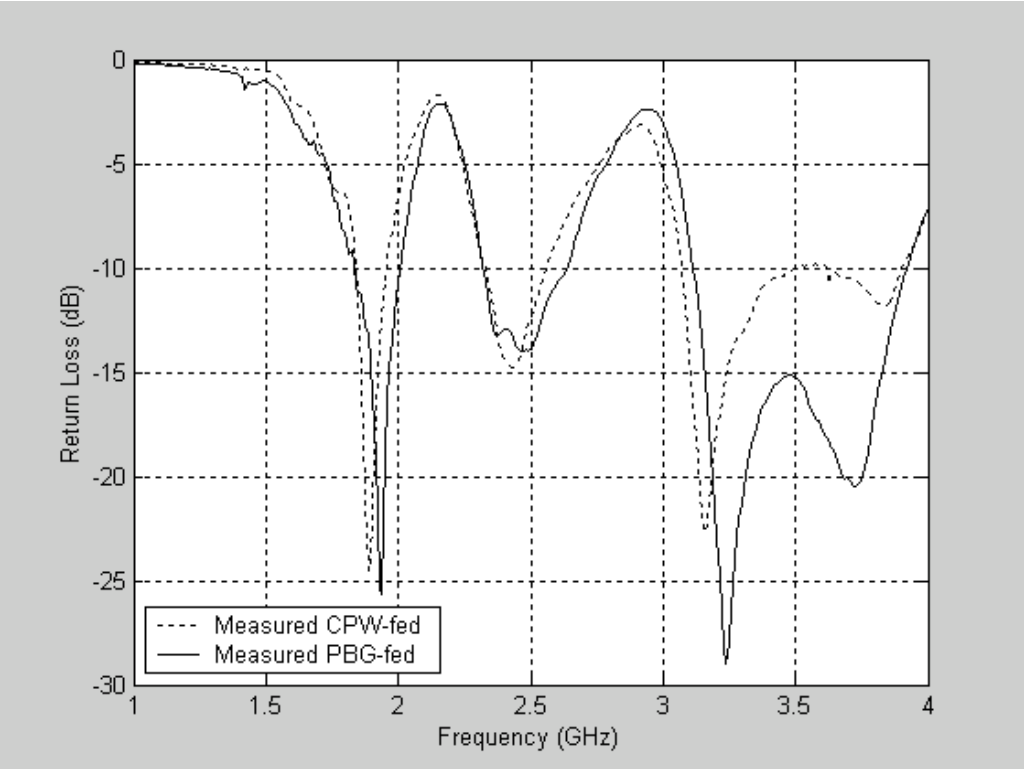

Figure 6.14 (d) Measured return loss for PBG-fed slot antenna and reference antenna.

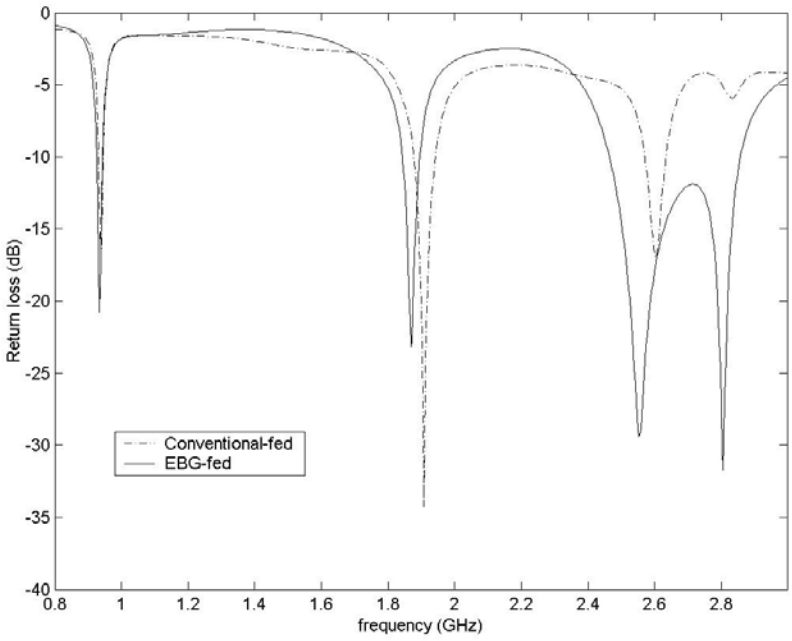

Figure 6.15 Measured return loss comparison between the conventional-fed and the EBG-fed tri-band microstrip antennas.

As evident from Figures 6.14(a) to (d), the EBG feed-line concept effectively increases the impedance bandwidth for all the measured resonance frequencies. As noted from Figure 6.14(d), the bandwidths for all the resonance frequencies increase from 7% to 10% at 1.88 GHz; from 8% to 16% at 2.45 GHz and from 8.3% to 20.8% at 3.5 GHz, respectively. Similarly, for Figure 6.15, the impedance bandwidths for all the available resonance frequencies increase from 0.334% to 1.08% at 0.9GHz, from 1.1% to 1.43% at 1.8GHz, and from 2.17% to 3% at 2.4GHz.

Table 6.2 shows the antenna performance comparison of the conventional-fed and the EBG-fed coplanar slot antennas. As noted from the table, the measured gains at all the available bands for both types of antennas remain relatively the same. With the EBG/PBG integration, it can be concluded that there is a mark improvement in the impedance bandwidth for all the bands for both the microstrip and coplanar technologies. In fact, the EBG feed-line concept is seen to be most appropriate for coplanar technologies as the improvement of the bandwidth is much larger.

Figures 6.16 to 6.18 show the measured E-plane and H-plane co-polarization and cross-polarization radiation patterns of the conventional-fed and EBG-fed coplanar slot antenna at 1.9GHz, 2.4GHz and 3.3GHz. Figures 6.19(a) and (b) show the measured E-plane and H-plane co-polarization radiation patterns of both the conventional-fed and EBG-fed tri-band microstrip antennas at 1.8GHz and 2.4GHz. Due to the upward shift of the resonant frequencies, the antenna with EBG feed is electrically larger. The slight improvement in the PBG-fed antenna gain might be due to the increased antenna size or due to the suppression of higher-order harmonics by the EBG structure. As noted from all the figures, there is no significant change in the radiation patterns for both technologies.

In conclusion, a novel concept of using EBG feed-line for antenna has been proposed to enhance the impedance bandwidth. Two novel types of antennas, namely a tri-band microstrip EBG-fed antenna and the coplanar slot EBG-fed antenna, have been designed and fabricated. As noted from the experimentation, the use of the EBG matching concept can indeed help to improve the impedance bandwidth for all the multi-band frequencies and with no significant degradation in the radiation patterns and antenna gain.

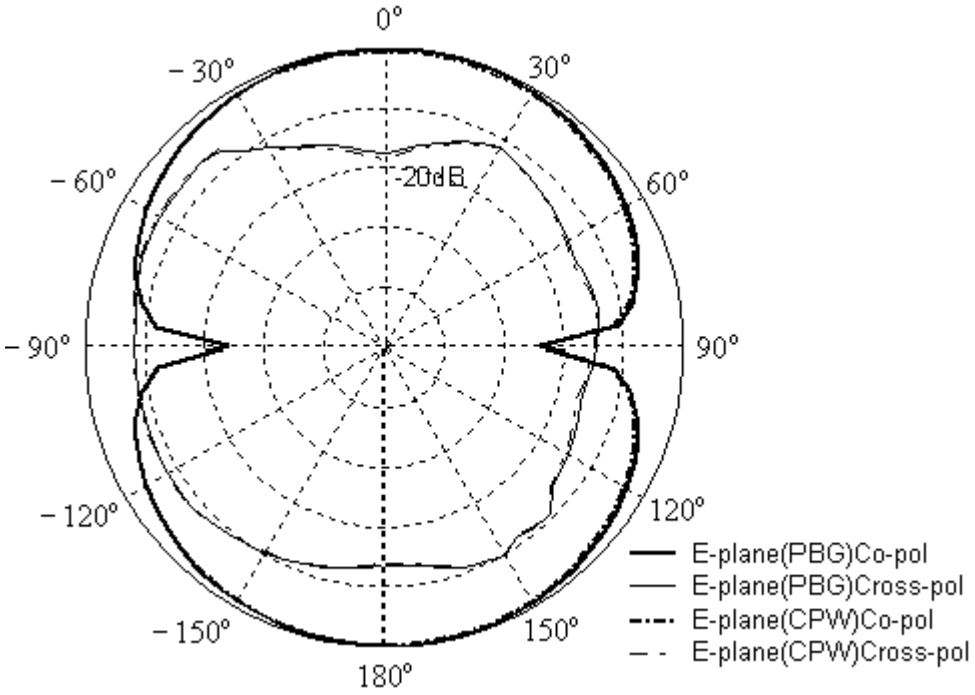

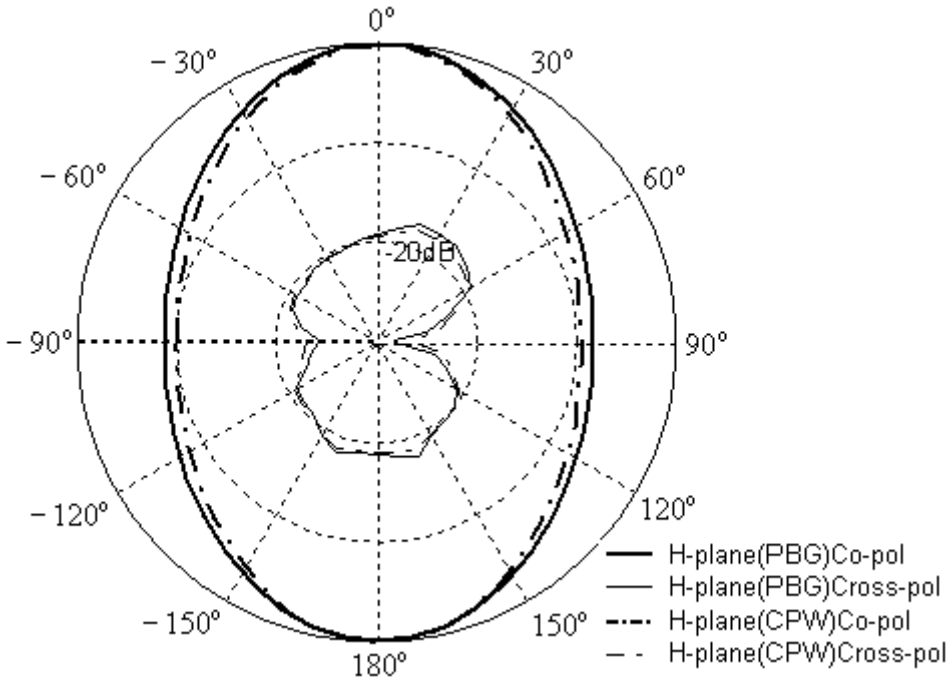

Figure 6.16 E-plane and H-plane at 1.9GHz

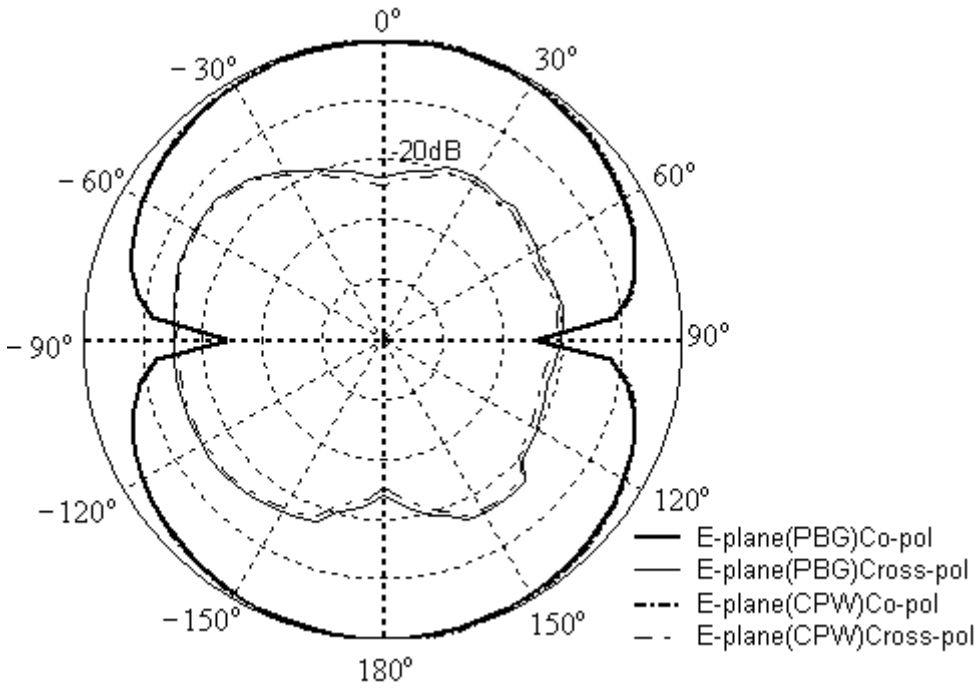

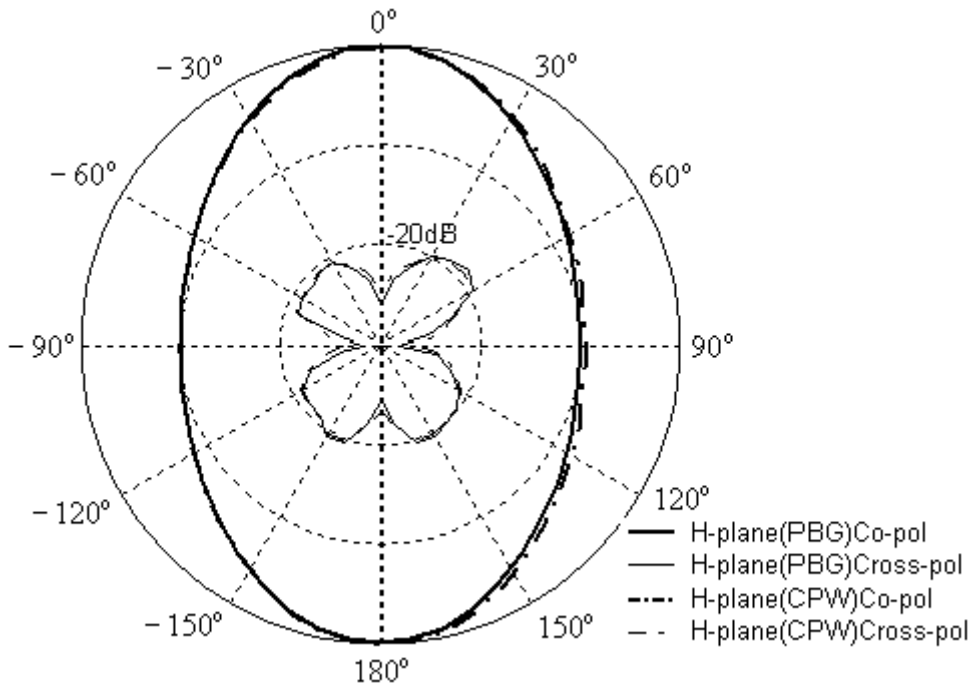

Figure 6.17 E-plane and H-plane at 2.4 GHz

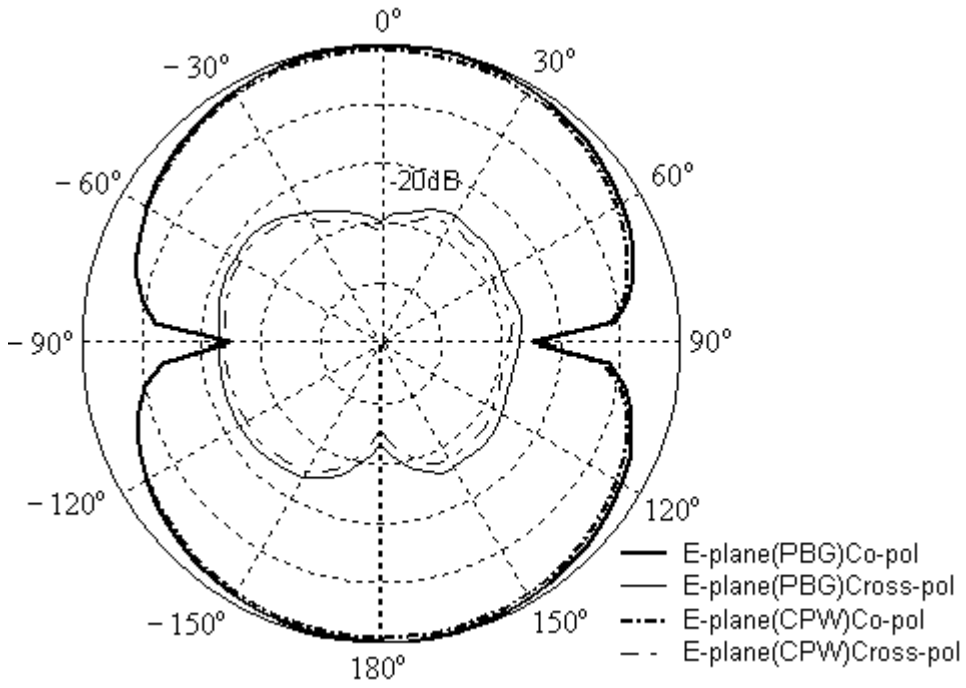

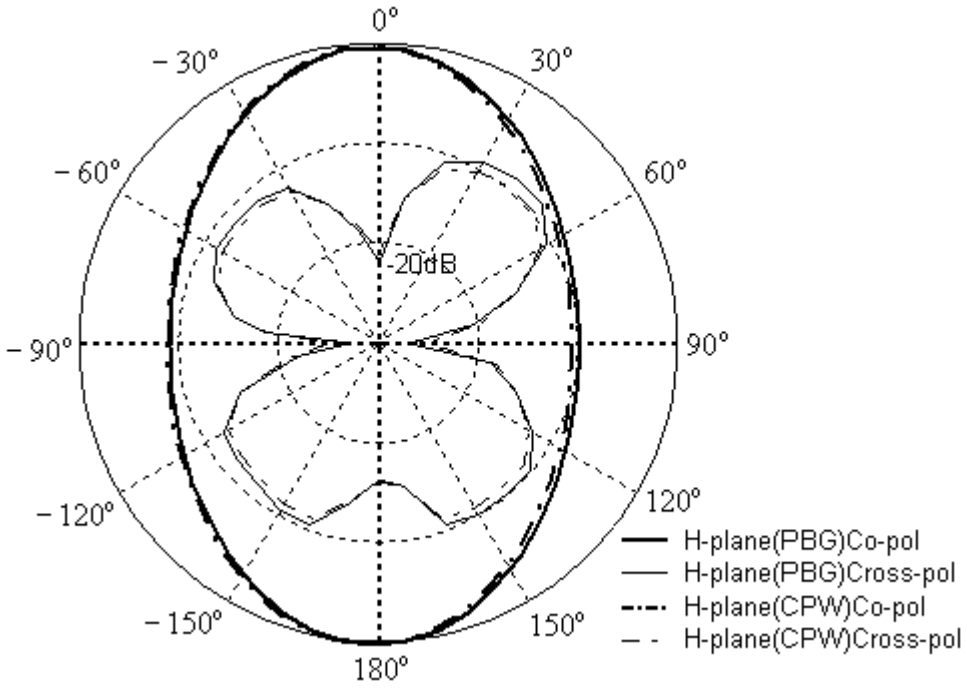

Figure 6.18 E-plane and H-plane at 3.3 GHz

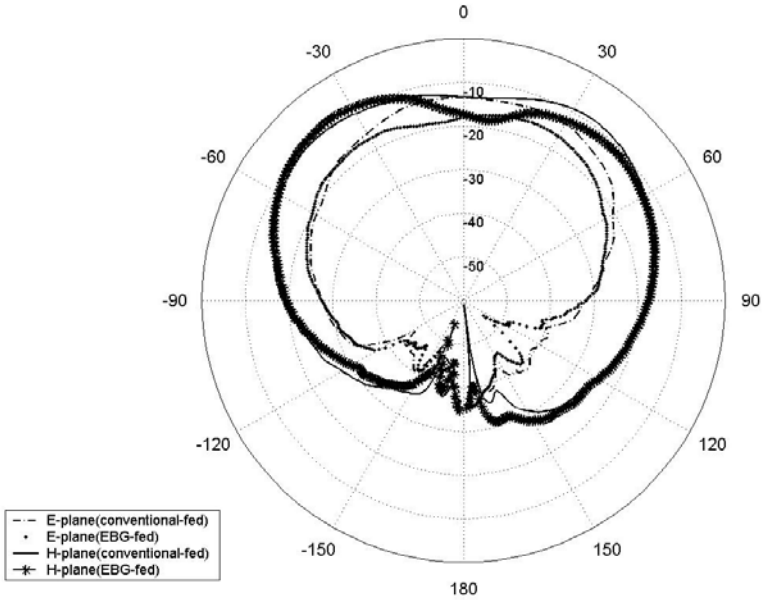

(a)

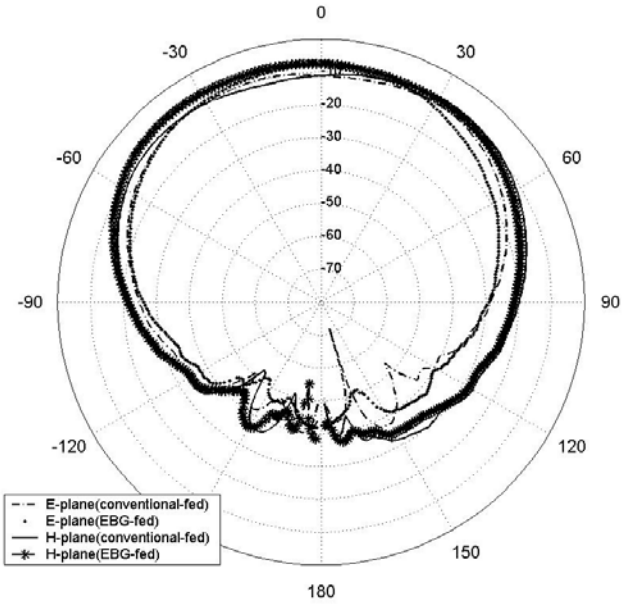

(b)

Figure 6.19 Comparison of the measured E-plane and H-plane co-polarization radiation patterns between the EBG-fed and conventional-fed antennas. (a) Radiation patterns measured at 1.8GHz. (b) Radiation patterns measured at 2.4GHz.

6.5 Design and Verification of Active Slot Antenna with EBG Feed

6.5.1 Model Verification

By applying the procedure for the extraction of the nonlinear model parameters already discussed, DC current model for several on-wafer transistors with different emitter length and width is extracted. Due to the good power performance, the GaAs HBT device has been selected to integrate with slot antenna. Figure 6.20 shows the photo of one of the GaAs HBT devices under the study. The DUT has a dimension of emitter width of 2 μm and length of 20 μm.

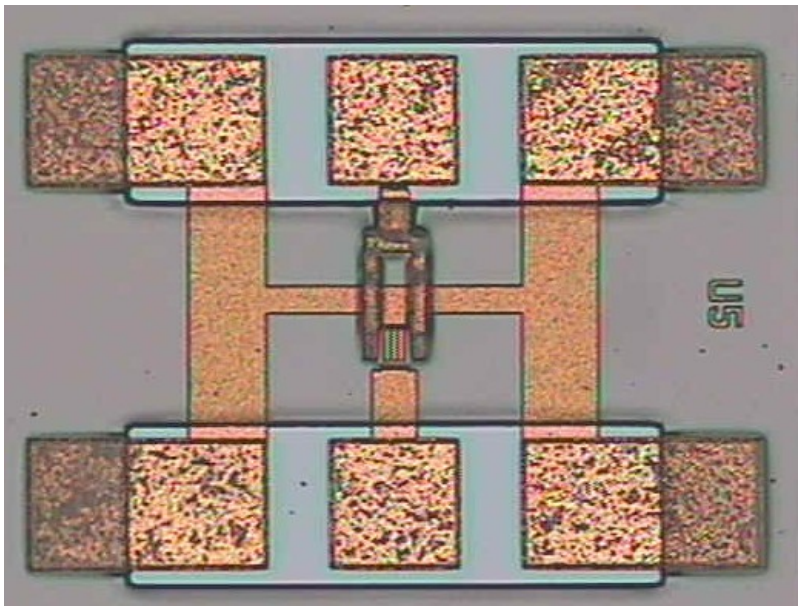

Figure 6.20 Photograph for the GaAs HBT device under test.

Figure 6.21 shows the measured and simulated DC IV characteristics for the GaAs HBT studied. Due to the thermal effect at high current, the DC IV characteristics exhibits negative slope as the current progressively increases. As discussed in Chapter 2, the thermal resistance is extracted to be 55200 K/W. The emitter resistance and collector resistance are extracted to be 153 Ω and 308 Ω, respectively. The breakdown behavior is modeled with good accuracy based on the modified VBIC avalanche model, as shown. Figure 6.21 further confirms the capability of the approaches employed to the extraction method and avalanche model modification to predict the DC current characteristics.

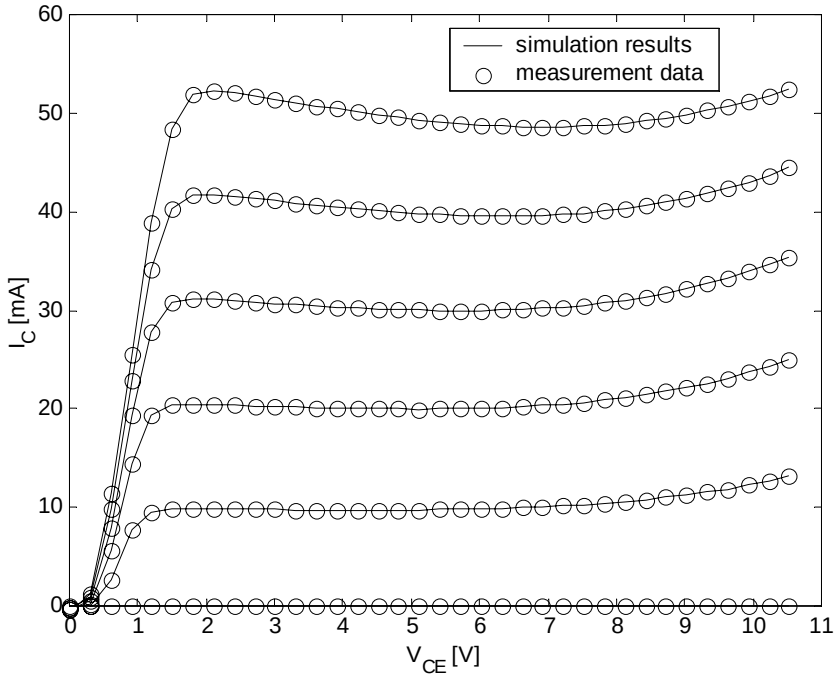

Figure 6.21 Measured and simulated DC IV characteristics for GaAs HBT showing all regions of operations (I_b: 0 μA-500 μA, step 100 μA).

The parasitic inductances and coupling capacitances are calculated using contour-integral method based on the HBT device layout as discussed in Chapter 3. For the HBT device studied, an excellent agreement on S-parameter was obtained for different biasing conditions, as shown in Figure 6.22 – Figure 6.24. Table 6.3 gives the values of the residual error quantifying the accuracy of the proposed extraction method according to the following defined error function:

$$\left\|\vec{\varepsilon}\right\| = \frac{1}{4N}\sum_{i,j=1}^{2}\sum_{k=1}^{N}\frac{\left|S_{ij}^{m}(f_k) - S_{ij}^{c}(f_k)\right|}{\max_k\left(\left|S_{ij}^{m}(f_k)\right|\right)}, \tag{6.39}$$

where N is the number of considered frequency points, $S_{ij}^{m}(f_k)$ is the measured S-parameter at the frequency f_k, and $S_{ij}^{c}(f_k)$ is the calculated corresponding S-parameters derived from the extracted values of model parameters.

Table 6.3 Residual data-fitting error for the extracted bias points

Bias Point	V_{CE}=5 V, I_C=18.12 mA, I_b= 220 µA.	V_{CE}=10 V, I_C=48.5 mA, I_b= 450 µA.	V_{CE}=2 V, I_C=101 mA, I_b=1.1 mA.
Residual Error	1.2%	0.98%	1.3%

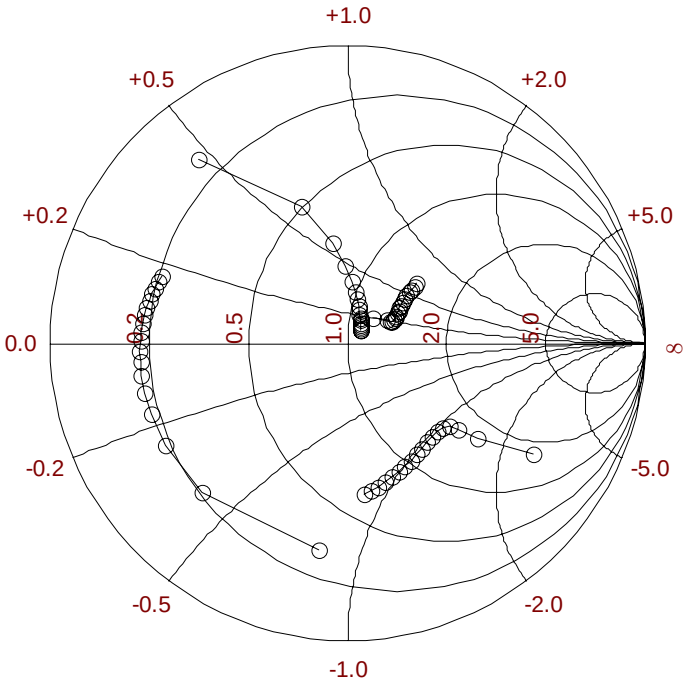

Figure 6.22 Measured and simulated S-parameters for GaAs HBT. (solid line: simulation data; circle line: measurement data; I_b=220 µA, V_{CE}=5V, I_C=18.12 mA, frequency: 1-18 GHz; S12*5, S21/20).

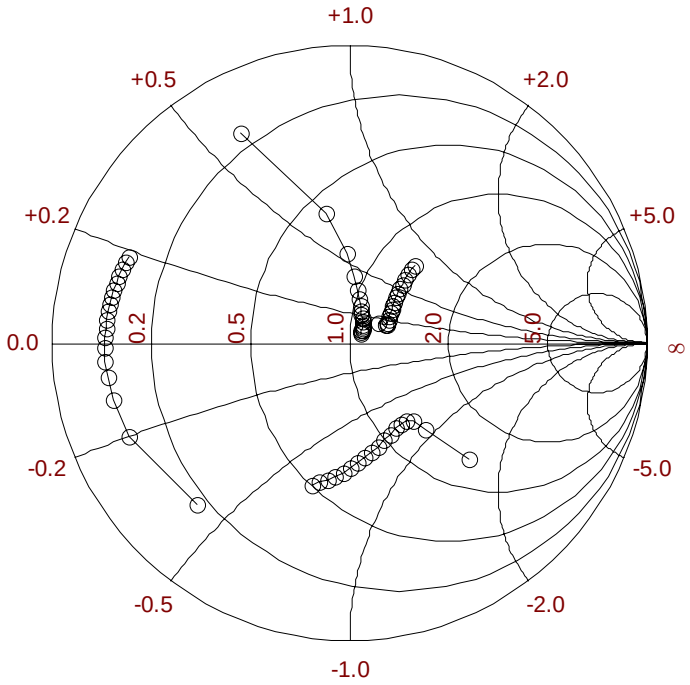

Figure 6.23 Measured and simulated S-parameters for GaAs HBT. (solid line: simulation data; circle line: measurement data; I_b=450 μA, V_{CE}=10V, I_C=48.5 mA, frequency: 1-18 GHz, S12*5, S21/20).

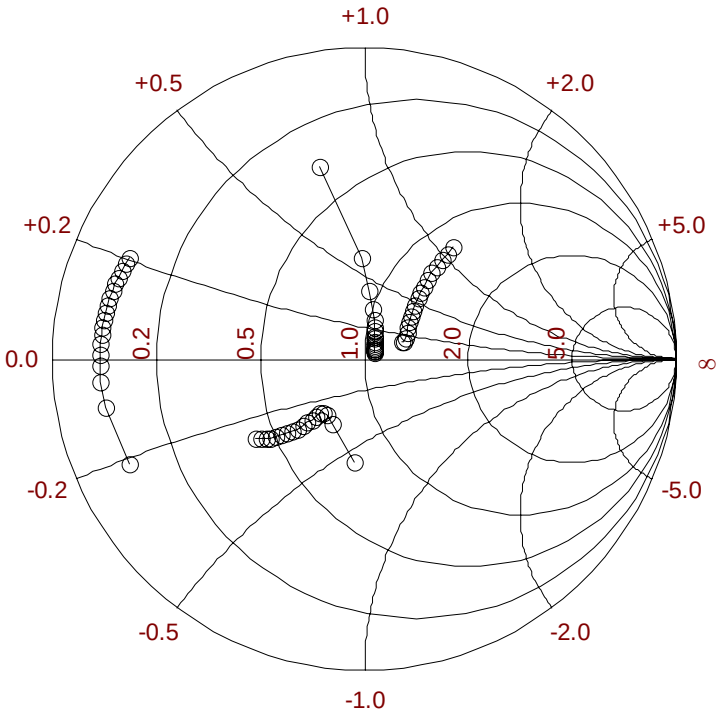

Figure 6.24 Measured and simulated S-parameters for GaAs HBT. (solid line: simulation data; circle line: measurement data; I_b=1.1 mA, V_{CE}=2V, I_C=101 mA, frequency: 1-18 GHz, S12*5, S21/20).

6.5.2 Wideband Power Amplifier Design and Verification

To verify the nonlinear model on the prediction of power performance, a hybrid single stage power amplifier using GaAs HBT device from KnowledgeOn Inc. is designed and fabricated it on the FR4 substrate. The purposes of the amplifier are to validate the correctness of the nonlinear model on circuit level and to integrate with the EBG-fed slot antenna. Thus, to simplify the matching network, only the matching circuits on the fundamental frequencies 1.9GHz, 2.45GHz and 3.5 GHz are designed without any harmonic termination circuits.

The HBT device used in the power amplifier has four emitter fingers with each emitter area of $2 \times 20\,\mu\text{m}^2$. The design simulation and layout are implemented in Agilent ADS. To improve the simulation accuracy, the parasitic inductance introduced by the bonding wire is also included into the design simulation. The input is conjugately matched at all times to provide as high as possible input power while the output matching network is optimized using load-pull simulation since, as it is well-known that the simultaneous conjugate matching can not provide the maximum output power. The output impedance using load-pull simulation is determined to be 48 +j92 Ω. To be compatible with the slot antenna, the matching network is implemented in CPW configuration, therefore no vias and transition is necessary. The open stubs are used in both the input and output matching circuit. The extra capacitive effect resulted from the CPW open end is included in the ADS distributed component model library. The nonlinear model for the transistor is implemented into Agilent ADS by the Symbolic Defined Device (SDD). Figure 6.25 is the photograph of fabricated power amplifier and Figure 6.26 shows the schematic of the designed power amplifier.

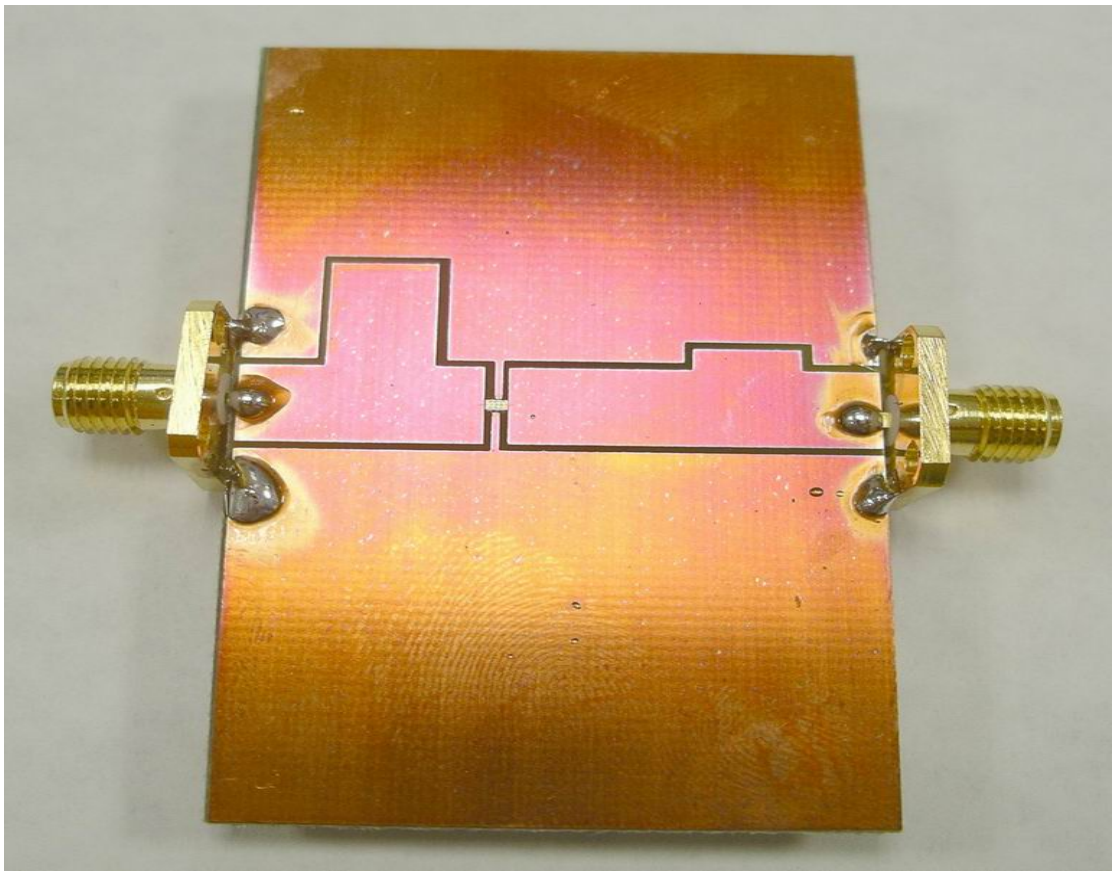

Figure 6.25 Photograph of fabricated one-stage HBT power amplifier.

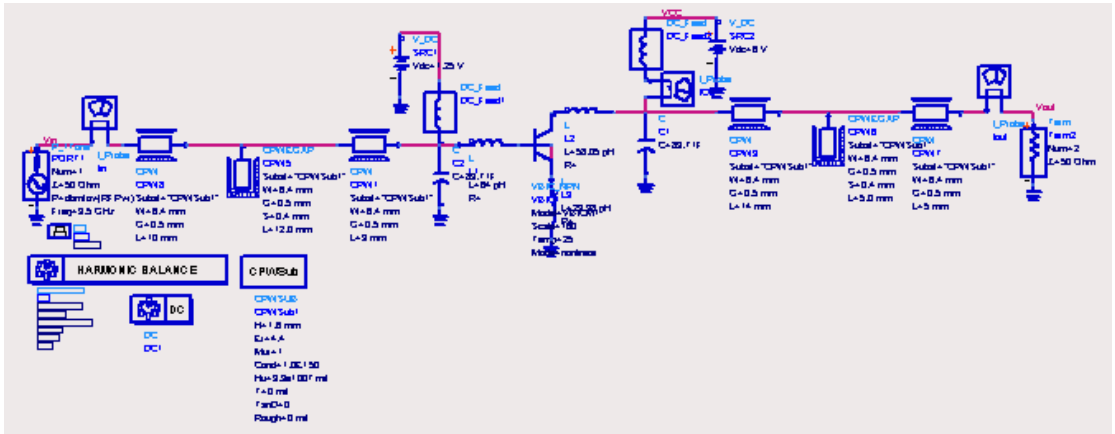

Figure 6.26 Schematic of one-stage wideband HBT power amplifier.

The measurement and test for the wideband power amplifier are accomplished by means of a probe station. The DC operating condition is provide by the DC probe with VBB=1.25 V and VCC=5.2 V. The S-parameters are measured by a HP8510C network analyzer and a power performance is measured by the spectrum analyzer.

The measurement results are as follows: at all operating frequencies, S11<-10 dB; S22< 6 dB; S21>22 dB; P_{1dB}>22 dBm; Power Added Efficiency @ P_{1dB} > 20%. Table 6.4 lists the measured power performance of the designed wideband power amplifier. As can be seen from Figure 6.27 and Figure 6.28, the agreement between the measured and the simulated results is excellent. The maximum discrepancy is less than 1dB for operating frequency at 3.5 GHz. The power gain in the entire operating band is well above 19 dB. The power added efficiency at 1.9GHz and 2.45 GHz are 40% and 42.4%, respectively. The lower PAE at 3.5GHz might be due to the FR4 substrate loss at higher frequency.

Table 6.4 Measured performance of the wideband power amplifier (VBB=1.25 V, VCC=5.2 V)

	P_{out} (dBm) @ P_{1dB}	Gain (dB)	PAE (%)
1.9 GHz	25.5	20.5	40
2.45 GHz	25.3	19.2	42.4
3.5 GHz	22.8	22.8	21

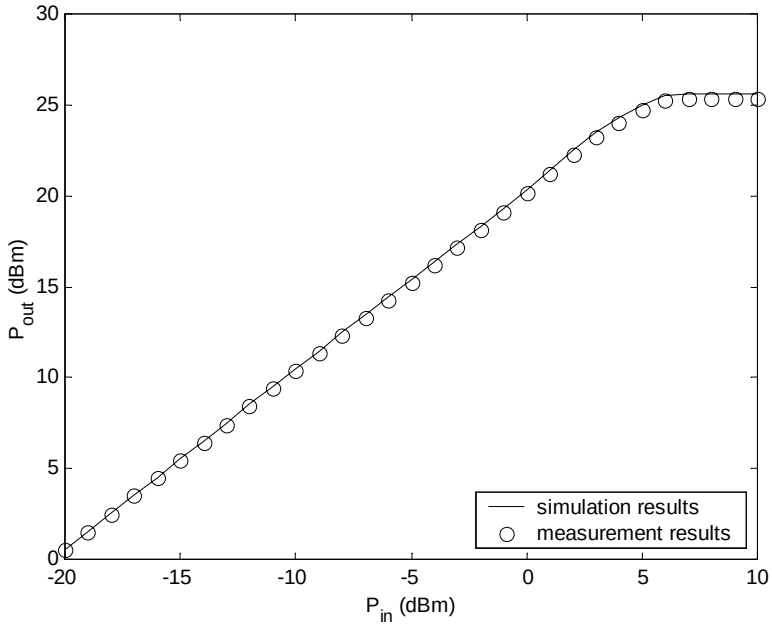

Figure 6.27 (a) Simulated and measured output power vs. input power at 1.9GHz.

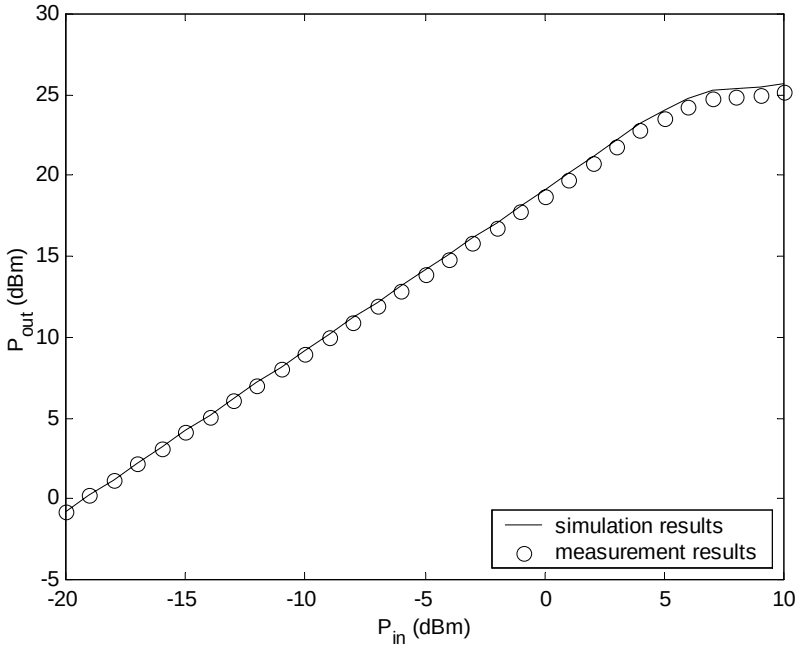

Figure 6.27 (b) Simulated and measured output power vs. input power at 2.45GHz.

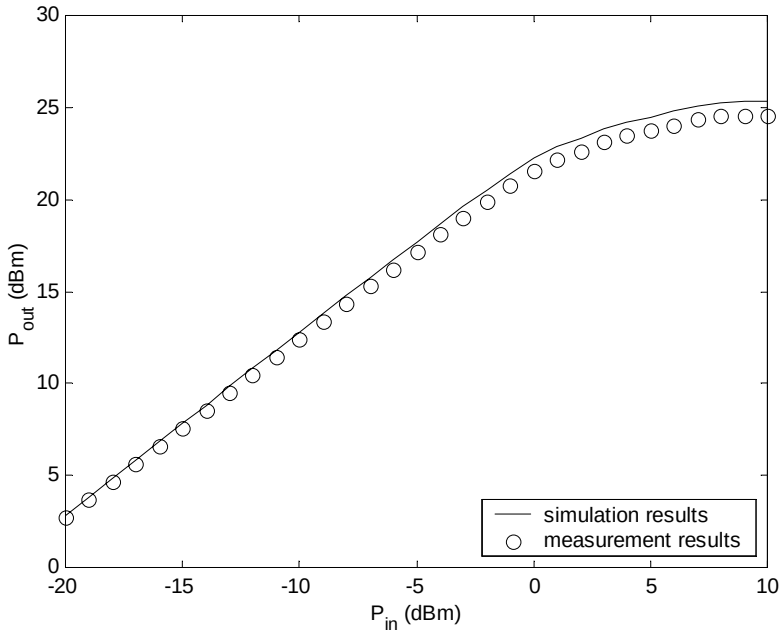

Figure 6.27 (c) Simulated and measured output power vs. input power at 3.5GHz.

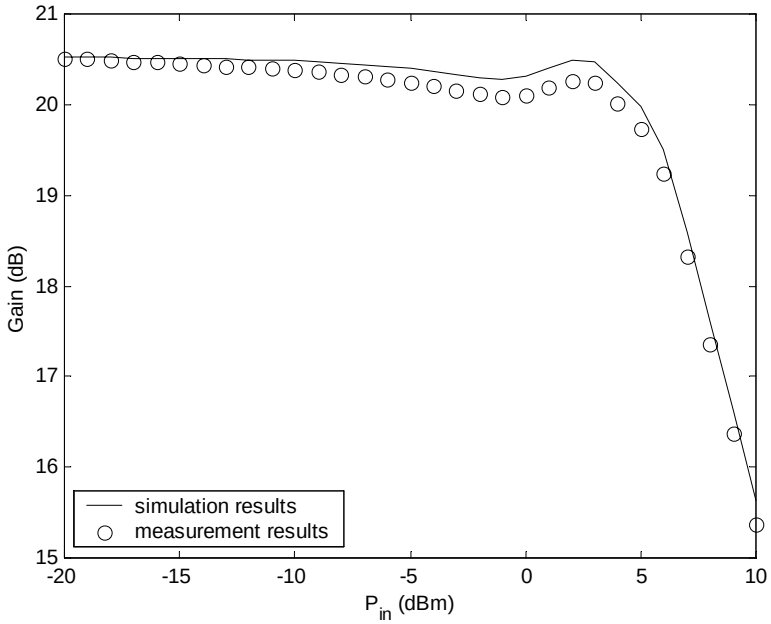

Figure 6.28 (a) Simulated and measured gain vs. input power at 1.9 GHz.

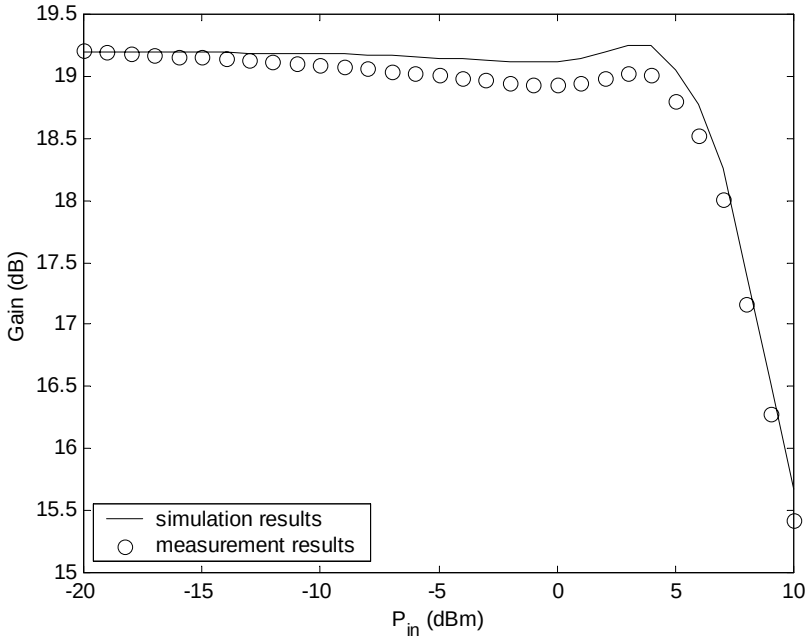

Figure 6.28 (b) Simulated and measured gain vs. input power at 2.45 GHz.

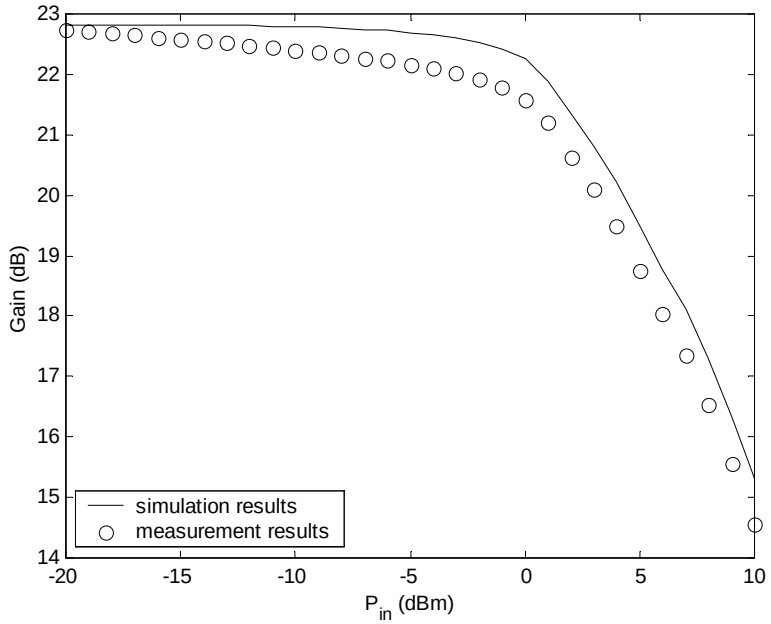

Figure 6.28 (c) Simulated and measured gain vs. input power at 3.5 GHz.

6.5.3 Active Integrated Antenna Design and Verification

The wideband power amplifier and slot antenna are designed and verified individually. Since both power amplifier and slot antenna have been designed with a characteristic impedance of 50 Ohm and are in the CPW configuration on the same substrate, designing an active integrated slot antenna is straightforward. Figure 6.29 shows the photograph of the fabricated multi-band active slot antenna with EBG feed.

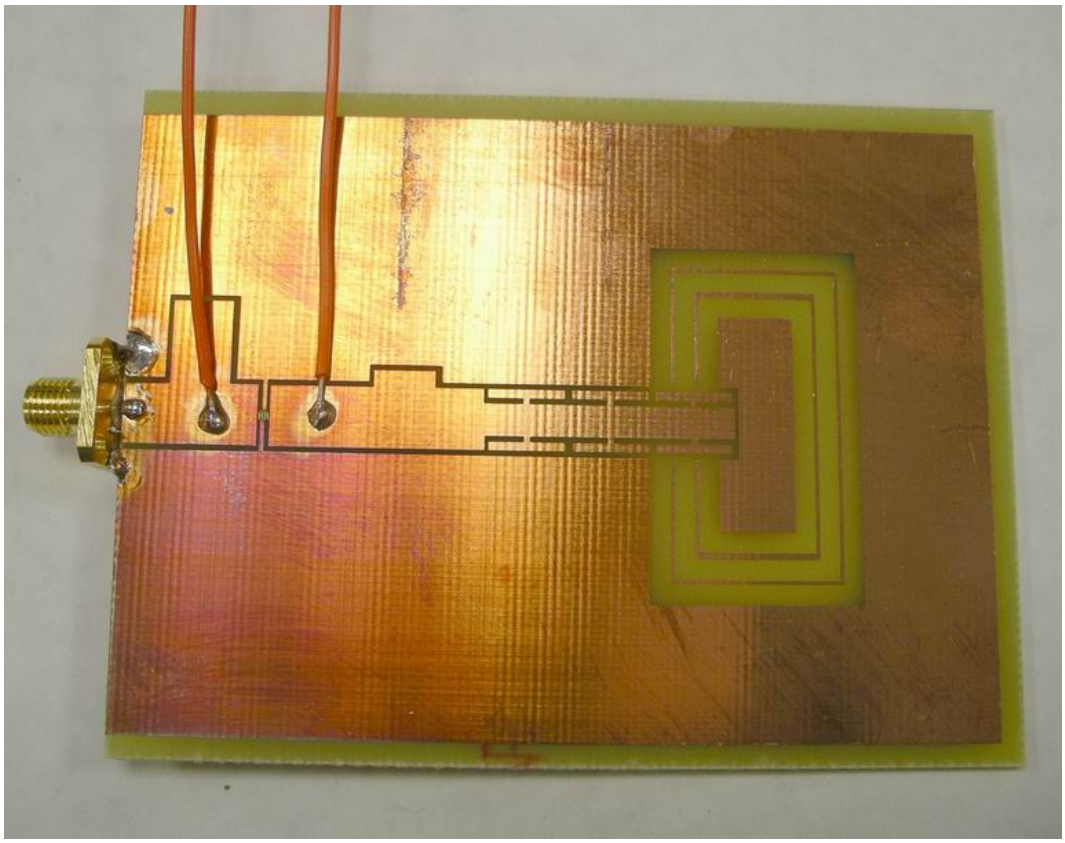

Figure 6.29 Photograph of fabricated active slot antenna with EBG feed.

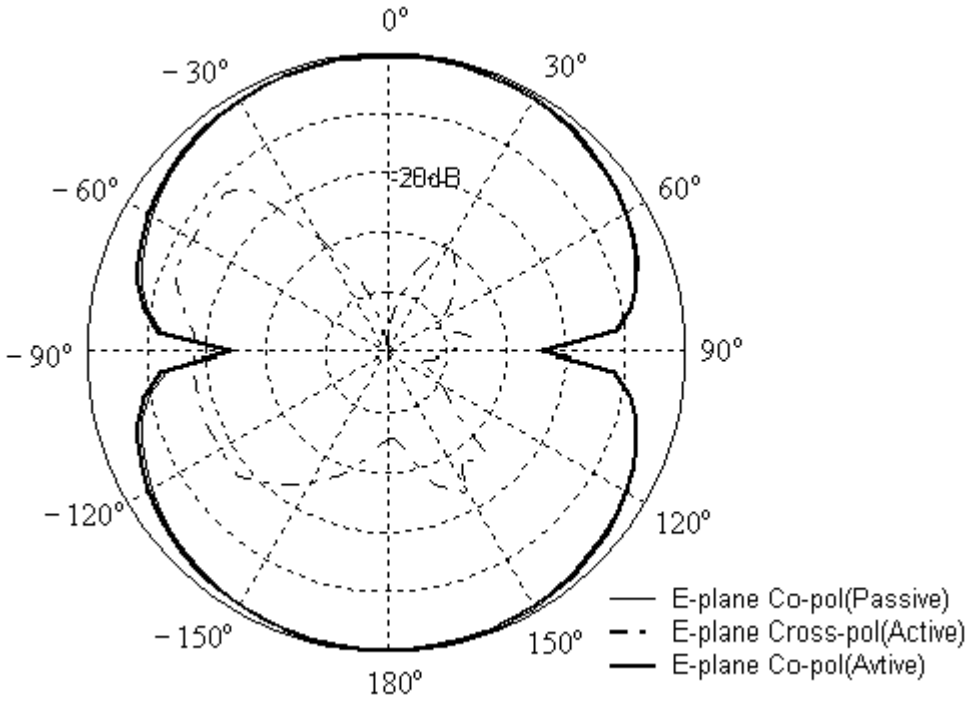

Figure 6.30(a) E-plane of multi-band active antenna at 1.9 GHz.

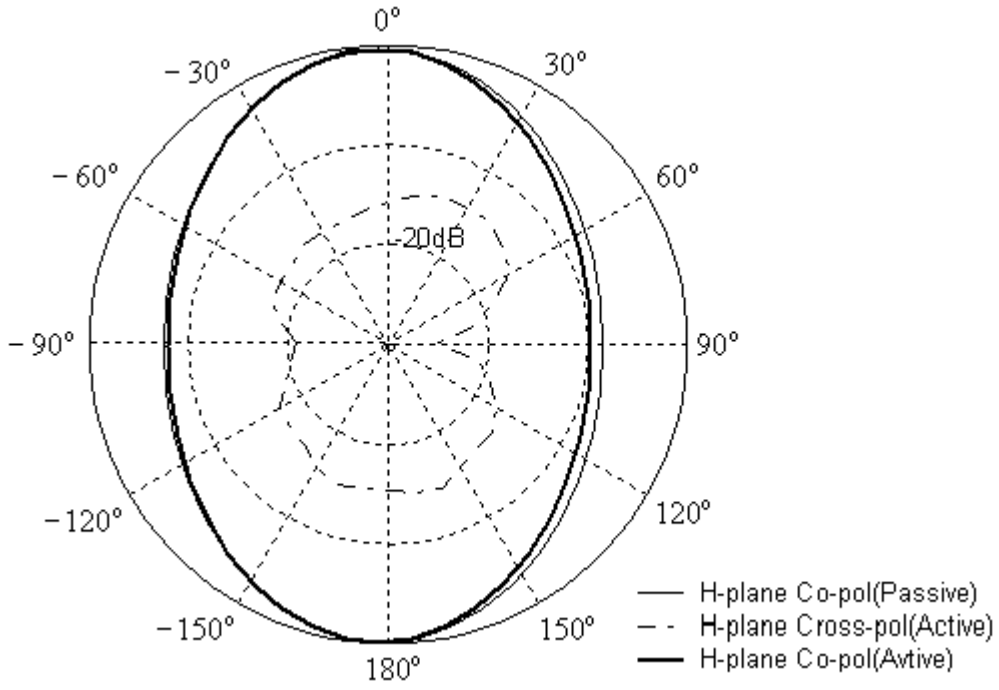

Figure 6.30(b) H-plane of multi-band active antenna at 1.9 GHz

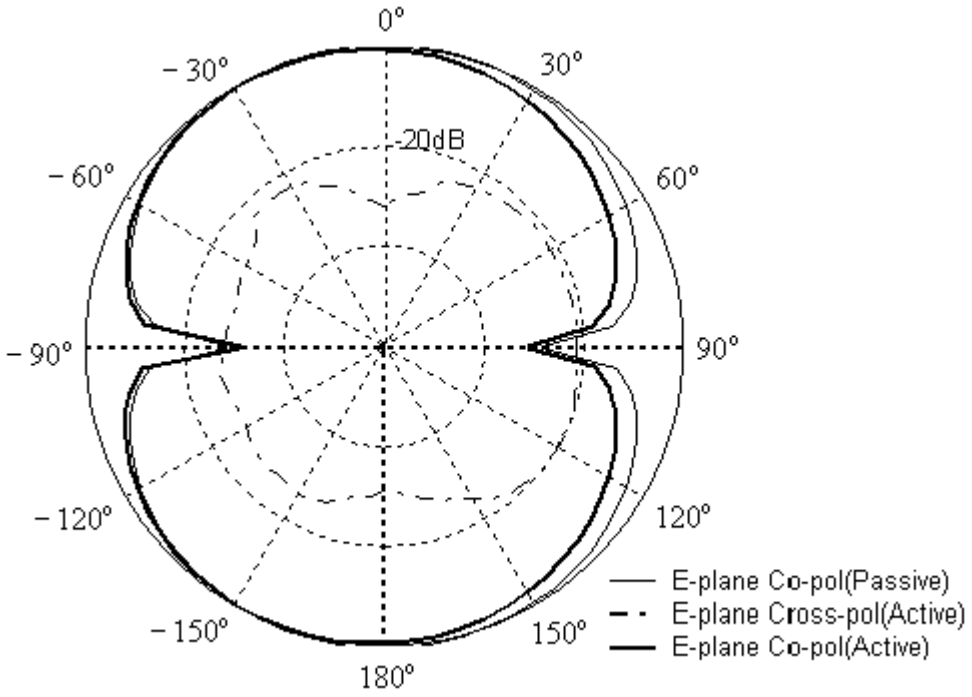

Figure 6.30(c) E-plane of multi-band active antenna at 2.45 GHz

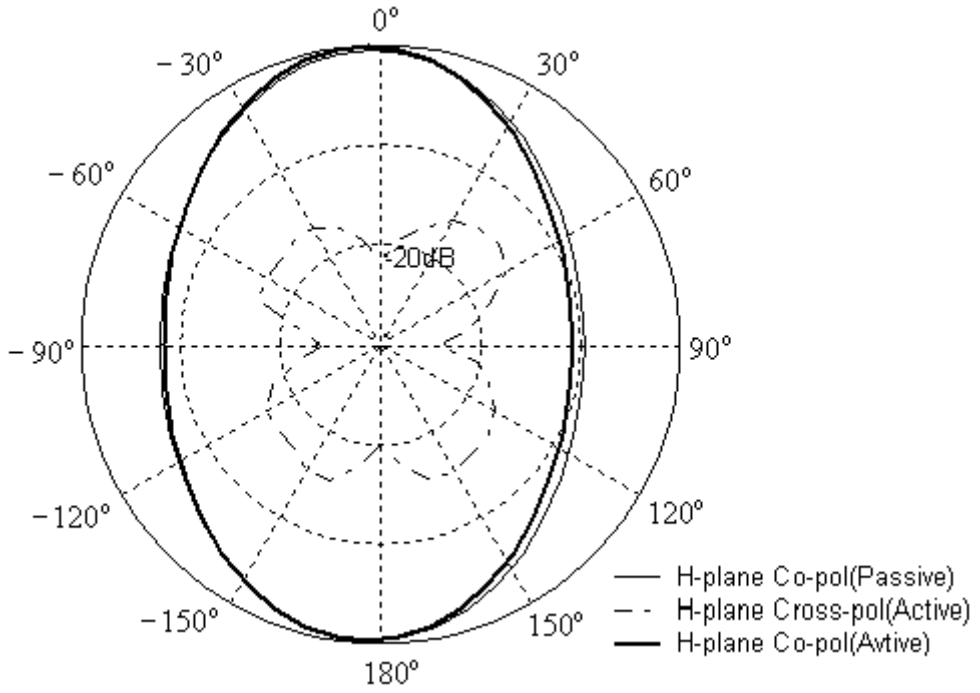

Figure 6.30(d) H-plane of multi-band active antenna at 2.45 GHz

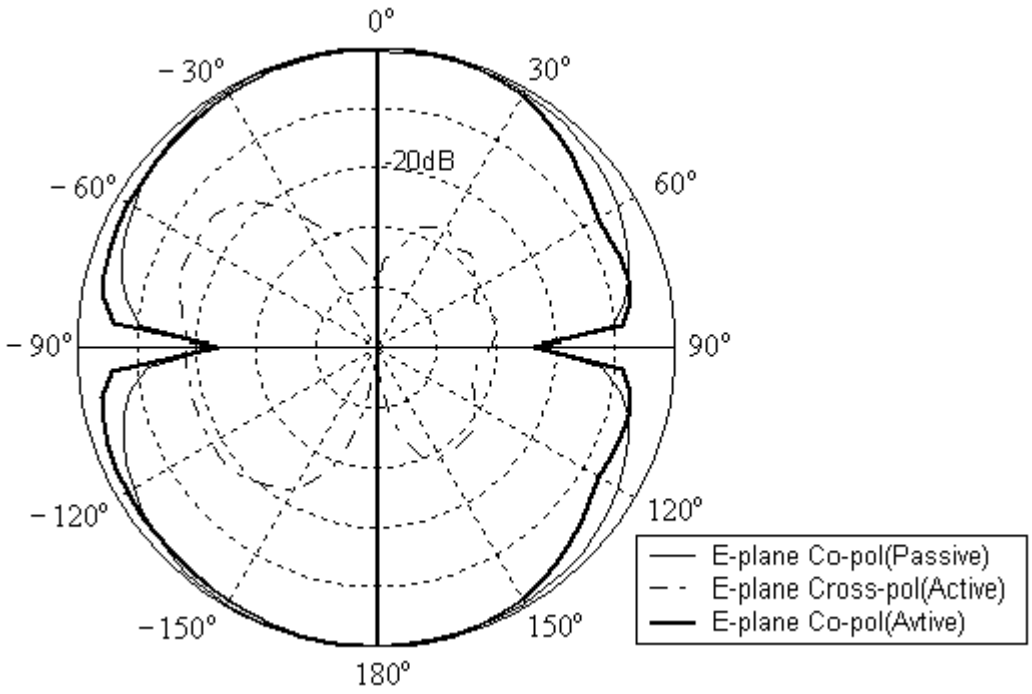

Figure 6.30(e) E-plane of multi-band active antenna at 3.5 GHz

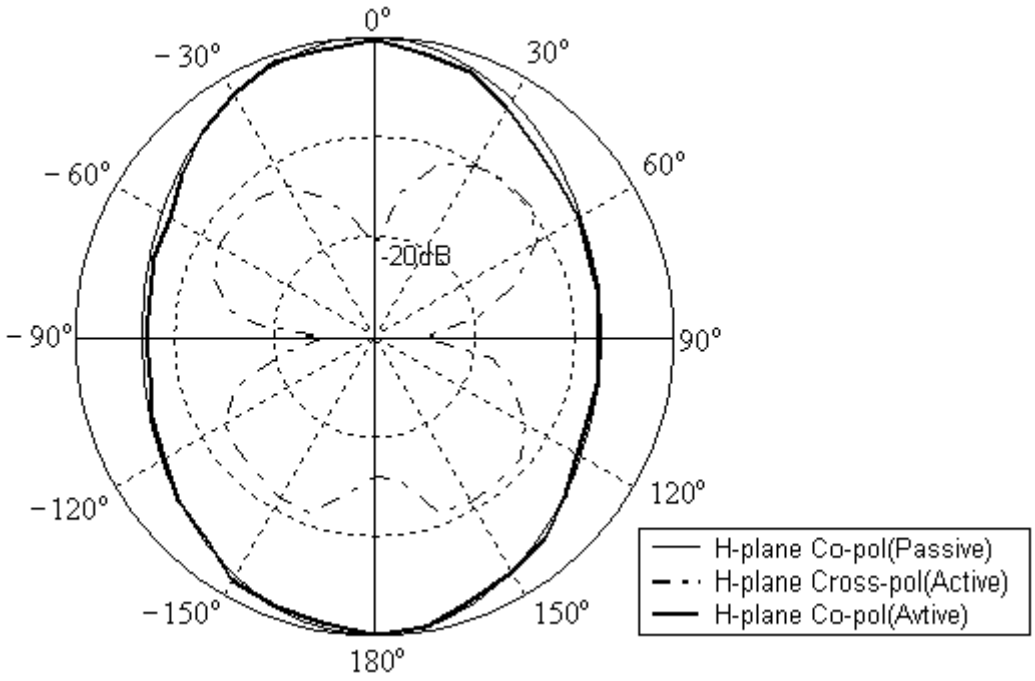

Figure 6.30(f) H-plane of multi-band active antenna at 3.5 GHz

Table 6.5 Measured gain vs. frequency for the integrated antenna

Frequency	1.9 GHz	2.45 GHz	3.5 GHz
Gain	24.5 dBi	23.6 dBi	28.1 dBi

The radiation patterns of fabricated active integrated antenna are measured and shown in Figure 6.30. The measurements are done in the anechoic chamber using the Friis free space formula. First, the gains of the passive antenna are measured at the broadside, with values of 4.3 dBi at 1.9GHz, 4.6 dBi at 2.45GHz and 5.5 dBi at 3.5 GHz. Then the passive antenna is substituted with the active integrated antenna. This measurement method eliminates any systematic errors. The E-plane and H-plane co-polarization patterns exhibit slight ripples due to the finite ground plane. The relative cross-polarization for both E-plane and H-plane is below –10 dB in all directions. Compared with the radiation pattern of passive slot antenna, a slight discrepancy is

observed. This is due to the parasitic radiation by the matching circuit of the amplifier.

By careful modeling the HBT device and designing the slot antenna separately, the performance and results of a uniplanar medium power (150 mW) EBG-fed slot-type multi-band active integrated antenna are successfully demonstrated. No vias is required, and the circuit is compatible with monolithic transistor technology. Thus, the design can be readily implemented in the established monolithic microwave circuit foundry.

Chapter 7

Conclusions and Suggestions for Future Works

7.1 Conclusions

The foregoing chapters are involved in the small-signal, large-signal and noise modeling and characterization of microwave HBTs for the application of multi-band active antenna. As the first step to obtain an accurate large-signal model, small-signal modeling based on the π-model equivalent circuit is carried out. The uniqueness of the approach in this thesis is that it determines the model parameters of small-signal model by the bi-directional optimization technique, thus reducing the number of optimization variables. Moreover, to accurately determine the parasitic resistance by eliminating the thermal effect, a fast and accurate method to extract the thermal resistance was proposed and consisted part of the extraction flow. It is demonstrated that the HBT thermal effect leads to the underestimation of the emitter resistance and overestimation of the collector resistance. S-parameters measurement has also verified the accuracy of the model, which is further validated in terms of bias-dependencies of extracted model parameters.

Due to the importance of parasitic inductance on the extraction of intrinsic elements and noise matching, the planar circuit approach and resonance-mode technique are, for the first time, applied to investigate the parasitic inductive effect

and its accurate extraction. It shows that in practical applications, only a finite number of cells are to be included in the equivalent circuit; such a number depends on the frequency range of interest and on the approximation required. In a low-frequency approximation, only the first two resonant modes can give sufficiently satisfied results. However, with the scaling down of the HBT device, more cells need to be included to improve the accuracy. Comparison with optimized values from measurements shows this technique is a valid method to extract the parasitic inductance without the tedious de-embedding and S-parameter measurements.

On the basis of HBT small-signal model, the noise behavior is studied thoroughly. Following the comparison of current available noise models, the wave approach is applied to analyze the device noise properties. To reliable perform the noise model by wave approach, the equivalent noise temperatures must be known. Therefore, a method to determine the equivalent noise temperature by using the small-signal model and minimum noise figure is proposed.

Based on Gummel-Poon model and VBIC model, large-signal modeling including self-heating effects is performed. The model is then compared with the measurement in terms of DC IV and small-signal S-parameters. The effect of various doping concentration on HBT high-current avalanche breakdown behavior can be explained by the change of maximum electric field in the intrinsic junction. Because of the complex nature of HBT breakdown behavior in the high current region, an empirical modification on the VBIC avalanche model is presented to improve the high current density breakdown behavior. The validity is also verified by the DC measurements up to high current densities. The good agreement between the model and the measurement has proven the validity of the proposed large-signal model.

Taking the inherent advantage of the coplanar waveguide, the planar slot antenna fed by coplanar waveguide is selected for the integration of active antenna. To simultaneously improve the impedance bandwidth of slot antenna, a novel feeding technique is proposed. The new antenna feed makes use of electromagnetic/photonic bandgap structure which effectively enhances the impedance bandwidth of multi-band slot antenna. Finally, based on the DC, small-signal verification of the HBT model, a wideband power amplifier is designed using the load-pull technique and integrated with the EBG-fed slot antenna. The measurement data on the power amplifier and active integrated antenna show the validity of the approaches thoughout this thesis.

7.2 Suggestions for Future Works

As the work presented in this thesis follows two major paths of modeling and aspects of HBT active integrated antenna, the suggestions for continued work can be divided into two directions.

For the completeness of the small-signal model, the impact of several physical parameters, like alloy grading of the base, dopant grading of the collector and emitter etc., should be further studied. Also different physical effects like base push-out and extreme forward biasing of the base emitter junction need to be investigated. Each parameter or physical process which will be included will require a thorough investigation and it is thus important to initially estimate the importance and benefits of such an approach.

As a large signal model with an emphasis on accounting for the physical processes within the transistor, the complexity of the model when simulating more complex structures may need to be decreased. It is then important to investigate what parameters have key importance for a certain approach. In addition, the modification

on the avalanche model presented in this thesis can be further improved to obtain the scalable breakdown model.

From the work on the RF noise of the HBT device, the low frequency noise model can be studied by wave approach. As a large signal model, it is also interesting to investigate the modeling of the optimal conversion of low frequency noise into, e.g., phase noise of an oscillator. For example, using the method of simulating low frequency noise in a SPICE-like simulator using only AC voltage and current sources, a model of the noise sources with a HBT should be realized and studied. Calculations of the input and output current noise and coherence between the signals should be calculated for a set of different signal levels of the individual noise sources. The HBT need not be in a common emitter configuration. Also different circuit configurations and a variation of parameters for external circuit elements, e.g., the base resistance termination in a common emitter configuration should be studied. By creating such a dataset, an increased understanding of the effects of the different noise sources and circuit configurations can be achieved which should simplify the study of new devices.

For continued research of the EM distribution inside the HBT device, a combination of planar circuit approach and multi-connection method can be used to find the scalable HBT RF model, which offers the advantages of both.

From the work on EBG-fed slot antenna, many interesting research directions, such as finding the optimal EBG lattice structure for planar antenna feed, are possible. Since the EBG feedline can offer more flexibility to design the matching network, the harmonic tuning circuit of the amplifier could be simplified and integrated with the feedline of the slot antenna. The HBT device can sometimes be mounted on a circuit with a microstrip configuration. Thus a study of a transition from microstrip to

coplanar waveguide and/or coplanar strip using EBG structure would be very interesting.

References

[1] K. Chang, R. A. York, P. S. Hall, and T. Itoh, “Active integrated antennas,” *IEEE Trans. Microwave Theory Tech.*, vol. MTT-50, No. 3, pp. 937-943, Mar. 2002.

[2] Y. Qian, and T. Itoh, “Progress in active integrated antennas and their applications,” *IEEE Trans. Microwave Theory Tech.*, vol. MTT-46, No. 11, pp. 1891-1900, Nov. 1998.

[3] J. A. Navarro and K. Chang, *Integrated active antennas and spatial power combining*, John Wiley & Sons, Inc., 1996.

[4] R. A. York and Z. B. Popovic, *Active and quasi-optical arrays for solid-state power combining*, John Wiley & Sons, Inc., 1997.

[5] B. K. Kormanyos, W. Harokopus, L. P. B. Katehi, G. M. Rebeiz, “CPW-fed active slot antennas,” *IEEE Trans. Microwave Theory Tech.*, vol. MTT-42, No. 4, pp. 541-545, Apr. 1994.

[6] P. Russer, P. M. So, and W. J. R. Hoefer, “Modeling of nonlinear active regions in TLM,” *IEEE Microwave Guided Wave Lett.*, vol. 1, pp. 10-13, Jan. 1991.

[7] W. Sui, D. A. Christensen, and C. H. Durney, “Extending the two-dimensional FDTD method to hybrid electromagnetic systems with active and passive lumped element,” *IEEE Trans. Microwave Theory Tech.*, vol. MTT-40, No. 4, pp. 724-730, Apr. 1992.

[8] B. Toland, B. Houshmand, and T. Itoh, “Modeling nonlinear active regions with the FDTD method,” *IEEE Microwave Guided Wave Lett.*, vol. 3, pp. 333-335, Sep. 1993.

[9] C. N. Kuo, B. Hushmond, and T. Itoh, "Full-wave analysis of packaged microwave circuits with active and nonlinear devices: An FDTD approach," *IEEE Trans. Microwave Theory Tech.*, vol. MTT-45, No. 3, pp. 819-826, Mar. 1997.

[10] K. Guillouard, M. F. Wong, V. F. Hanna, and J. Citerne, "A new global time domain electromagnetic analysis of a strongly coupled two-element active antenna," in *Proc. 27th European Microwave Conf.*, Jerusalem, Israel, pp. 866-869, Sep. 1997.

[11] B. Bayraktaroglu, "GaAs HBT's for microwave integrated circuits," *Proc. IEEE*, vol. 81, pp. 1762-1785, Dec. 1993.

[12] P. M. Asbeck *et al*., "GaAs-based heterojunction bipolar transistors for very high performance electronic circuits," *Proc. IEEE*, vol. 81, pp. 1709-1726, Dec. 1993.

[13] G. Vendelin, A. M. Pavio and U. L. Rohde, *Microwave Circuit Design Using Linear and Nonlinear Techniques*, New York: Wiley, 1990.

[14] E. L. Kollberg, Ed., *Microwave and Millimeter-Wave Mixers*. Piscataway, NJ: IEEE Press, 1984.

[15] U. L. Rohde, J. Whitaker and T. N. N. Bucher, *Communications Receivers*, 2nd ed. New York: McGraw-Hill, 1997.

[16] U. L. Rohde, *Microwave and Wireless Synthesizers: Theory and Design*. New York: Wiley, 1996.

[17] J. W. Bandler, R. M. Bienacki, Q. Cai, S. H. Chen, S. Ye, and Q. J. Zhang, "Integrated physics-oriented statistical modeling simulation and optimization," *IEEE Trans. Microwave Theory Tech.*, vol. MTT-40, pp. 1374-1400, 1992.

[18] S. G. Skaggs, J. Gerber, G. Bilbro, and M. B. Steer, "Parameter extraction of microwave transistors using a hybrid gradient decent and tree annealing approach," *IEEE Trans. Microwave Theory Tech.*, vol. MTT-41, pp. 726-729, 1993.

[19] T. Fernandez, Y. Newport, J. M. Zamanillo, A. Tazon and A. Mediavilla, “Extracting a bias-dependent large-signal MESFET model from pulsed I/V measurements,” *IEEE Trans. Microwave Theory Tech*., vol. MTT-44, no. 5, pp. 372-378, 1996.

[20] D. Costa, W. U. Liu, and J. S. Harris Jr., “Direct extraction of the AlGaAs/GaAs heterojunction bipolar transistor small-signal equivalent circuit,” *IEEE Trans. Electron Devices*, vol. 38, pp.2018-2024, Sep. 1991.

[21] D. R. Pehlke and D. Pavlidis, “Evaluation of the factors determining HBT high-frequency performance by direct analysis of S-parameter data,” *IEEE Trans. Microwave Theory Tech*., vol. MTT-40, pp. 2367-2373, Dec. 1992.

[22] U. Schaper and B. Holzapfl, “Analytic parameter extraction of the HBT equivalent circuit with T-like topology from measured S-parameter,” *IEEE Trans. Microwave Theory Tech*., vol. MTT-40, pp. 493-498, Mar. 1995.

[23] C. J. Wei and J. C. M. Hwang, “Direct extraction of equivalent circuit parameters for heterojunction bipolar transistors,” *IEEE Trans. Microwave Theory Tech*., vol. MTT-43, pp. 2035-2039, Sep. 1995.

[24] A. Samelis and D. Pavlidis, “DC to high-frequency HBT model parameter evaluation using impedance block conditioned optimization,” *IEEE Trans. Microwave Theory Tech*., vol. MTT-45, pp. 886-897, Jun. 1997.

[25] B. Li, S. Prasad, L. Yang, and S. C. Wang, “A semianalytical parameter-extraction procedure for HBT equivalent circuit,” *IEEE Trans. Microwave Theory Tech*., vol. MTT-46, pp. 1427-1435, Oct. 1998.

[26] R. Hajji and F. M. Ghannouchi, “Small-signal distributed model for GaAs HBT’s and S-parameter prediction at millimeter-wave frequencies,” *IEEE Trans. Electron Devices*, vol. 44, pp.723-731, May 1997.

[27] Y. Gobert, P. J. Tasker, and K. H. Bachem, “A physical, yet simple, small-signal equivalent circuit for the heterojunction bipolar transistor,” *IEEE Trans. Microwave Theory Tech*., vol. MTT-45, pp. 149-153, Jan. 1997.

[28] J. P. Roux, L. Escotte, R. Plana, J. Graffeuil, S. L. Delage and H. Blanck, “Small-signal and noise model extraction technique for heterojunction bipolar transistor at microwave frequencies,” *IEEE Trans. Microwave Theory Tech*., vol. MTT-43, pp. 293-298, Feb. 1995.

[29] A. Ouslimani, J. Gaubert, H. Hafdallah, A. Birafane, P. Pouvil and H. Leier, “Direct extraction of linear HBT-model parameters using nine analytical expression blocks,” *IEEE Trans. Microwave Theory Tech*., vol. MTT-50, pp. 218-221, Jan. 2002.

[30] T. S. Horng, J. M. Wu and H. H. Huang, “An extrinsic-inductance independent approach for direct extraction of HBT intrinsic circuit parameters,” *IEEE Trans. Microwave Theory Tech*., vol. MTT-49, pp. 2300-2304, Dec. 2001.

[31] S. Bousnina, P. Mandeville, A. B. Kouki, R. Surridge and F. M. Ghannouchi, “Direct parameter-extraction method for HBT small-signal model,” *IEEE Trans. Microwave Theory Tech*., vol. MTT-50, pp. 529-536, Feb. 2002.

[32] F. Lin and G. Kompa, “FET model parameter extraction based on optimization with multi-plane data-fitting and bi-directional search-a new concept” *IEEE Trans. Microwave Theory Tech*., vol. MTT-42, pp. 1114-1120, July 1994.

[33] W. R. Curtice and R. L. Camisa, “Self-consist GaAs FET models for amplifier design and device diagnostics,” *IEEE Trans. Microwave Theory Tech*., vol. MTT-32, pp. 1573-1578, Dec. 1984.

[34] T. H. Ning and D. D. Tang, “Method for determining the emitter and base series resistances of bipolar transistors,” *IEEE Trans. Electron Devices*, vol. ED-31, pp. 409-412, Apr. 1984.

[35] L. J. Giacoletto, “Measurement of emitter and collector series resistances,” *IEEE Trans. Electron Devices*, vol. 19, pp. 692-693, 1972.

[36] W. Filensky and H. Beneking, “New technique for determination of static collector and emitter series resistances of bipolar transistors,” *Electron. Lett*., vol. 17, no. 14, pp.503-504, 1981.

[37] W. D. Mack and M. Horowitz, “Measurement of series collector resistance in bipolar transistors,” *IEEE J. Solid-State Circuits*, vol. SC-17, pp. 767-773, Aug. 1982.

[38] J. S. Park, A. Neugroschel, V. Torre and P. J. Zdebel, “Measurement of collector and emitter resistances in bipolar transistors,” *IEEE Trans. Electron Devices*, vol. 38, no. 2, pp. 365-371, Feb. 1991.

[39] A. Z. Incecik, “Computer-aided determination of emitter and collector resistances of integrated bipolar transistors,” *IEEE J. Solid-State Circuits*, vol. SC-14, pp. 1108-1111, Dec. 1979

[40] J. S. Park and A. Neugroschel, “Parameter extraction for bipolar transistor,” *IEEE Trans. Electron Devices*, vol. 36, no. 1, pp. 88-95, Jan. 1989.

[41] M. G. Adlerstein and M. P. Zaitlin, “Thermal resistance measurement for AlGaAs/GaAs heterojunction bipolar transistors,” *IEEE Trans. Electron Devices*, vol. 38, pp. 1553-1554, Jun. 1991.

[42] D. E. Dawson, A. K. Gupta and P. M. Asbeck, “CW measurement of HBT thermal resistance,” *IEEE Trans. Electron Devices*, vol. 39, pp. 2235-2239, Oct. 1992.

[43] N. Bovolon, P. Baureis, J. E. Muller, P. Zwicknagl, R. Schultheis and E. Zanoni, “A simple method for the thermal resistance measurement of AlGaAs/GaAs heterojunction bipolar transistors,” *IEEE Trans. Electron Devices*, vol. 45, pp. 1846-1848, Aug. 1998.

[44] J. R. Waldrop, K. C. Wang and P. M. Asbeck, “Determination of junction temperature in AlGaAs/GaAs heterojunction bipolar transistors by electrical measurement,” *IEEE Trans. Electron Devices*, vol. 39, pp. 1248-1250, May 1992.

[45] D. Williams and P. Tasker, “Thermal parameter extraction technique using DC I-V data for HBT transistors,” *High Frequency Postgraduate Student Colloquium*, pp. 71-75, 2000.

[46] G. B. Gao, M. S. Unlu, H. Morkoc and D. L. Blackburn, “Emitter ballasting resistor design for, and current handling capability of AlGaAs/GaAs power heterojunction bipolar transistors,” *IEEE Trans. Electron Devices*, vol. 38, no. 2, pp. 185-196, Feb. 1991.

[47] D. L. Harame, J. H. Comfort, J. D. Cressler, E. F. Crabbe, J. Y. C. Sun, B. S. Meyerson, and T. Tice, “Si/SiGe epitaxial-base transistors-part II: process integration and analog applications,” *IEEE Trans. Electron Devices*, vol. 42, no. 3, pp. 469-482, Mar. 1995.

[48] A. R. Reid, T. C. Kleckner, M. K. Jackson, D. Marchesan, S. J. Kovacic, and J. R. Long, “Thermal resistance in trench-isolated Si/SiGe heterojunction bipolar transistors,” *IEEE Trans. Electron Devices*, vol. 48, no. 7, pp. 1477-1479, July 2001.

[49] C. Fager, L. J. Peter, and J. C. Pedro, “Optimal parameter extraction and uncertainty estimation in intrinsic FET small-signal models,” *IEEE Trans. Microwave Theory Tech.*, vol. MTT-50, no. 12, pp. 2797-2803, Dec. 2002.

[50] *8510C Network Analyzer Data Sheet*, Agilent Technologies, Palo Alto, CA, 1999.

[51] T. Okoshi, and T. Miyoshi, “Planar circuit - an approach to microwave integrated circuitry,” *IEEE Trans. Microwave Theory Tech.*, vol. MTT-20, no. 4, pp. 245-252, Apr. 1972.

[52] T. Okoshi, *Planar circuits for microwaves and lightwaves*, Springer-Verlag, 1985

[53] T. Okoshi, T. Imai, and K. Ito, "Computer-oriented synthesis of optimum circuit pattern of 3-dB hybrid ring by the planar circuit approach," *IEEE Trans. Microwave Theory Tech*., vol. MTT-29, no. 3, pp. 194-202, Mar. 1981.

[54] T. Miyoshi, and S. Miyauchi, "The design of planar circulators for wide-band operation," *IEEE Trans. Microwave Theory Tech*., vol. MTT-28, no. 3, pp. 210-214, Mar. 1980.

[55] T. Miyoshi, S. Yamaguchi, and S. Goto, "Ferrite planar circuits in microwave integrated circuits," *IEEE Trans. Microwave Theory Tech*., vol. MTT-25, no. 7, pp. 593-600, July 1977.

[56] K. R. Carver, and J. W. Mink, "Microstrip antenna technology," *IEEE Trans. Antennas Propagat*., vol. AP-29, pp. 2-24, Jan. 1981.

[57] T. Okoshi, Y. Uehara, and T. Takeuchi, "The segmentation method – an approach to the analysis of microwave planar circuits," *IEEE Trans. Microwave Theory Tech*., vol. MTT-24, no. 10, pp. 662-668, Oct. 1976.

[58] R. Chadha, and K. C. Gupta, "Segmentation method using impedance matrices for analysis of planar microwave circuits," *IEEE Trans. Microwave Theory Tech*., vol. MTT-29, no. 1, pp. 71-74, Jan. 1981.

[59] K. C. Gupta, and M. D. Abouzahra, *Analysis and design of planar microwave components*, IEEE Press, 1994.

[60] T. Itoh, *Numerical techniques for microwave and millimeter-wave passive structures*, John Willey & Sons, 1989.

[61] G. D'Inzeo, F. Giannini, C. M.Sodi, and R. Sorrentino, "Method of analysis and filtering properties of microwave planar networks," *IEEE Trans. Microwave Theory Tech*., vol. MTT-26, no. 7, pp. 462-471, Jan. 1978.

[62] J. Helszajn, *Green's function, finite elements and microwave planar circuits*, John Willey & Sons, 1996.

[63] K. C. Gupta, *et al*., *Microstrip lines and slotlines*, Artech House, 1996.

[64] G. Kompa, and R. Mehran, "Planar waveguide model for calculation of microstrip components," *Electron. Lett.*, vol. 11, pp. 459-460, 1975.

[65] R. Sorrentino, "Planar circuits, waveguide models, and segmentation method," *IEEE Trans. Microwave Theory Tech*., vol. MTT-33, no. 10, pp. 1057-1066, Oct. 1985.

[66] I. Woff, and N. Knoppik, "Rectangular and circular microstrip disk capacitors and resonators," *IEEE Trans. Microwave Theory Tech*., vol. MTT-22, no. 1, pp. 857-862, Oct. 1974.

[67] H. A. Wheeler, "Transmission-line properties of parallel strips separated by a dielectric sheet," *IEEE Trans. Microwave Theory Tech*., vol. MTT-13, no. 10, pp. 172-185, Mar. 1965.

[68] G. D'Inzeo, F. Giannini, and R. Sorrentino, "Wide-band equivalent circuits of microwave planar networks," *IEEE Trans. Microwave Theory Tech*., vol. MTT-28, no. 10, pp. 1107-1113, Oct. 1980.

[69] J. Dobrowolski, *Computer-aided analysis, modeling, and design of microwave networks: the wave approach*, Artech House, 1996.

[70] D. L. Harame, *et al*, "Current status and future trends of SiGe BiCMOS technology," *IEEE Trans. Electron Devices*, vol. 48, no. 11, pp.2575-2594, 2001.

[71] R. J. Hawkins, “Limitations of Nielson’s and related noise equations applied to microwave bipolar transistors, and a new expression for the frequency and current dependent noise figure,” *Solid-state Electron*., vol. 20, pp. 191-196, 1977.

[72] W. E. Ansley, J. D. Cressler and D. M. Richey, “Base-profile optimization for minimum noise figure in advanced UHV/CVD SiGe HBT’s,” *IEEE Trans. Microwave Theory Tech*., vol. MTT-46, no. 5, pp. 653-660, May 1995.

[73] A. van der Ziel, *Noise in Solid State Devices and Circuits*, New York, John Wiley & Sons, chap. 9.4, 1986.

[74] K. Aufinger, J. Bock, T. F. Meister and J. Popp, “Noise characteristics of transistors fabricated in an advanced bipolar technology,” *IEEE Trans. Electron Devices*, vol. 43, no. 9, pp.1533-1538, Sep. 2001.

[75] J. P. Roux, L. Escotte, R. Plana, J. Graffeuil, S. L. Delage, and H. Blanck, “Small-signal and noise model extraction technique for heterojunction bipolar transistor at microwave frequencies,” *IEEE Trans. Microwave Theory Tech*., vol. MTT-43, no. 2, pp. 293-297, Feb. 1995.

[76] L. Escotte, J. P. Roux, R. Plana, J. Graffeuil, and A. Gruhle, “Noise modeling of microwave heterojunction bipolar transistors,” *IEEE Trans. Electron Devices*, vol. 42, pp. 883-888, May 1995.

[77] S. P. Voinigescu, M. C. Maliepaard, J. L. Showell, G. E. Babcock, D. Marchesan, M. Schroter, P. Schvan, and D. L. Harame, “A scalable high-frequency noise model for bipolar transistors with application to optimal transistor sizing for low-noise amplifier design,” *IEEE J. Solid-State Circuits*, vol. 32, pp. 1430-1438, Sep. 1997.

[78] G. Niu, J. D. Cressler, S. Zhang, W. E. Ansley, C. S. Webster and D. L. Harame, "A unified approach to RF and microwave noise parameter modeling in bipolar transistors," *IEEE Trans. Electron Devices*, vol. 48, pp. 2568-2573, Nov. 2001.

[79] A. van der Ziel and A. G. Becking, "Theory of junction diode and junction transistor noise," *Proc. of IRE*, vol. 46, pp. 589-594, Mar. 1958.

[80] K. M. van Vliet, "General transport theory of noise in PN junction-like devices–I. Three–dimensional Green's function formulation," *Solid-State Electron.*, vol. 15, pp. 1033-1053, 1972.

[81] F. Herzel and B. Heinemann, "High frequency noise of bipolar devices in consideration of carrier heating and low temperature effects," *Solid-State Electron*, vol. 38, pp. 1905-1909, Nov. 1995.

[82] F. Herzel, P. Schley, B. Heinemann, U. Zilmann, D. Knoll, D. Temmler, and U. Erben, "Experimental verification and numerical application of the thermodynamic approach to high frequency noise on SiGe HBTs," *Solid-State Electron*, vol. 41, pp. 387-390, Mar. 1997.

[83] H. Rothe and W. Dahlke, "Theory of noisy four poles," *Proc. IRE*, vol. 44, pp. 811-818, June 1956.

[84] P. Penfield, "Wave representation of amplifier noise," *IRE Trans. Circuit Theory*, vol. CT-9, p. 84, Mar. 1962.

[85] J. A. Dobrowolski, "A CAD-oriented method for noise figure computation of two-ports with any internal topology," *IEEE Trans. Microwave Theory Tech.*, vol. MTT-37, no. 1, pp. 15-20, Jan. 1989.

[86] H. A. Haus, W. R. Atkinson, W. H. Fonger, W. W. Mcleod, G. M. Branch, W. A. Harris, E. K. Stodola, W. B. Davenport, Jr., S. W. Harrison, and T. E. Talpey, "Representation of noise in linear two ports," *Proc. IRE*, vol. 48, pp. 69-74, Jan. 1960.

[87] H. Hillbrand and P. H. Russer, "An efficient method for computer aided noise analysis of linear amplifier networks," *IEEE Trans. Circuits Sys*, vol. CAS-23, pp. 235-238, Apr. 1976.

[88] K. Hartmann, "Part I: theory of linear noisy networks – noise characterization of linear circuits," *IEEE Trans. Circuit Sys*., vol. CAS-23, no. 10, pp.581-590, Oct. 1976.

[89] K. Hartman, and M. Strutt, "Changes of the four noise parameters due to general changes of linear two-port circuits, " *IEEE Trans. Electron Devices*, vol. ED-20, pp. 874-877, Oct. 1973.

[90] R. P. Meys, "A wave approach to the noise properties of linear microwave devices," *IEEE Trans. Microwave Theory Tech*., vol. MTT-26, pp. 34-37, Jan. 1978.

[91] J. A. Dobrowolski, *Introduction to computer methods for microwave circuit analysis and design*, Artech House, Boston, 1991.

[92] K. B. Niclas, "The exact noise figure of amplifiers with parallel feedback and lossy matching circuits," *IEEE Trans. Microwave Theory Tech*., vol. MTT-30, pp. 832-835, May 1982.

[93] K. B. Niclas and B. A. Tucker, "On noise in distributed amplifiers at microwave frequencies," *IEEE Trans. Microwave Theory Tech*., vol. MTT-31, pp. 661-668, Aug. 1983.

[94] K. C. Gupta, R. Garg, and R. Chadha, *Computer-aided design of microwave circuits*, Artech House, 1981.

[95] V. A. Monato, and P. Tiberio, “Computer aided analysis of microwave circuits,” *IEEE Trans. Microwave Theory Tech*., vol. MTT-22, pp. 249-263, Mar. 1974.

[96] G. Gonzalez, *Microwave transistor amplifiers: analysis and design*, 2nd ed. Prentice-Hall, 1997.

[97] M. Garcia, J. Stenarson, H. Zirath and I. Angelov, “A direct extraction formula for the FET temperature noise model,” *Microwave Opt. Techno. Lett*., vol. 16, pp. 208-212, Nov. 1997.

[98] M. Garcia, J. Stenarson, K. Yhland, H. Zirath and I. Angelov, “A new extraction method for the two-parameter FET temperature noise model,” *IEEE Trans. Microwave Theory Tech*., vol. MTT-46, pp. 1679-1685, Nov. 1998.

[99] M. Garcia, J. Stenarson, H. Zirath and I. Angelov, “An algebraic method foe noise parameter analysis of temperature noise models,” *Microwave Opt. Techno. Lett*., vol. 17, pp. 287-291, Apr. 1998.

[100] J. J. Ebers, J. L. Moll, “Large-signal behavior of junction transistors,” *Proc. IRE*, pp. 1761-1772, Dec. 1954.

[101] H. K. Gummel, H. C. Poon, “An integral charge control model of bipolar transistors,” *Bell Sys. Tech. Journal*, vol. 49, pp.827-853, 1970.

[102] H. K. Gummel, “A charge control relation for bipolar transistor,” *Bell Sys. Tech. Journal*, vol. 49, pp.115-120, 1970.

[103] H. C. de Graaff, F. M. Klaassen, *Compact Transistor Modeling for Circuit Design*, Springer Verlag, Wien, 1990.

[104] C. C. McAndrew, J. A. Seitchik, D. F. Bowers, M. Dunn, M. Foisy, I. Getreu, M. McSwain, S. Moinian, J. Parker, D. J. Roulston, M. Schroter, P. Wijinen and L. Wagner, “VBIC95, the vertical bipolar inter-company model,” *IEEE J. Solid-State Circuits*, vol. 31, pp. 1476-1483, Oct. 1996.

[105] H. Stubing and H. M. Rein, “A compact physical large-signal model for high-speed bipolar transistors at high current densities-part I: one-dimensional model,” *IEEE Trans. Electron Devices*, vol. 34, no. 8, pp. 1741-1751, Aug. 1987.

[106] H. M. Rein and M. Schroter, “A compact physical large-signal model for high-speed transistors at high current densities-part II: two-dimensional model and experimental results,” *IEEE Trans. Electron Devices*, vol. 34, no. 8 pp. 1752-1761, Aug. 1987.

[107] H. M. Rein, H. Stubing and M. Schroter, “Verification of the integral charge-control relation for high-speed bipolar transistors at high current densities,” *IEEE Trans. Electron Devices*, vol. 32, pp. 1070-1076, Jun. 1985.

[108] M. Schroter, M. Friedrich and H. M. Rein, “A generalized integral charge-control relation and its application to compact models for silicon based HBTs,” *IEEE Trans. Electron Devices*, vol. 40, pp. 2036-2046, Nov. 1993.

[109] C. T. Kirk “A theory of transistor cutoff frequency (f_t) falloff at high current densities,” *IRE Trans. Electron Devices*, vol. 9, pp. 164-174, Mar. 1962.

[110] C. C. McAndrew and W. N. Laurence, “SPICE Early modeling,” *Proc. IEEE BCTM* pp. 144-147, 1994.

[111] C. C. McAndrew and W. N. Laurence, “Early effect modeling in SPICE,” *IEEE J. Solid-State Circuits*, vol. 31, no. 1, pp. 136-138, Jan. 1996.

[112] W. J. Kloosterman and H. C. de Graaff, “Avalanche multiplication in a computer bipolar transistor model for circuit simulation,” *in Proc. 1988 IEEE BCTM*, pp. 103-106.

[113] W. J. Kloosterman and H. C. de Graaff, “Avalanche multiplication in a computer bipolar transistor model for circuit simulation,” *IEEE J. Solid-State Circuits*, vol. 36, no. 7, pp. 1376-1380, July 1989.

[114] G. M. Kull, L. W. Nagel, S. W. Lee, P. Lloyd, E. J. Prendergast, and H. K. Dirks, "A unified circuit model for bipolar transistors including quasi-saturation effects," *IEEE Trans. Electron Devices*, vol. 32, no. 6, pp. 1103-1113, June 1985.

[115] P. Antognetti and G. Massobrio, "Semiconductor devices modeling with SPICE," McGraw-Hill, New York, 1987.

[116] J. M. M. Rios, L. M. Lunardi, S. Chandrashekhar and Y. Miyamoto, "A self-consistent method for complete small-signal parameter extraction of InP-based heterojunction bipolar transistors," *IEEE Trans. Microwave Theory Tech*., vol. 45, pp. 39-44, 1997.

[117] H. Cho, and D. E. Burk, "A three-step method for the de-embedding of high-frequency S-parameter measurements," *IEEE Trans. Electron Devices*, vol. 38, no. 6, pp. 1371-1375, June 1991.

[118] E. O. Johnson, *IEEE Int. Conf. Rec. Pt. 5*, p.27, 1965.

[119] E. O. Johnson, "Physical limitations on frequency and power parameters of transistors," *RCA Rev*., pp.163-177, June 1965.

[120] C. Wei, J. C. M. Hwang, W. J. Ho, and J. A. Higgins, "Large-signal modeling of self-heating, collector transit-time, and RF-breakdown effects in power HBT's", *IEEE Trans. Microwave Theory Tech*., vol. 44, no. 12, pp. 2641-2647, Dec. 1996.

[121] H. Wang *et al*., "Avalanche multiplication in InP/InGaAs double heterojunction bipolar transistors with composite collectors, " *IEEE Trans. Electron Devices*, vol. 47, pp. 1125-1133, Jun. 2000.

[122] G. Niu, *et al*., "Measurement of collector-base junction avalanche multiplication effects in advanced UHV/CVD SiGe HBT's," *IEEE Trans. Electron Devices*, vol. 46, pp. 1007-1015, May 1999.

[123] J. S. Hamel, “Separating the influence of neutral base recombination and avalanche breakdown on base current reduction in SiGe HBT’s,” *IEEE Trans. Electron Devices*, vol. 44, pp. 901-903, May 1997.

[124] J. J. Chen, *et al*., “Breakdown behavior of GaAs/AlGaAs HBT’s”, *IEEE Trans. Electron Devices*, vol. 36, pp. 2165-2172, Oct. 1989.

[125] G. Niu, *et al*., “Collector-base junction avalanche multiplication effects in advanced UHV/CVD SiGe HBT’s”, *IEEE Electron Device Lett.*, vol. 19, pp. 288-290, Aug. 1998.

[126] M. Schroter, *et al*., “A compact tunneling current collector breakdown model,” *IEDM Tech. Dig*., pp. 203-206, 1998.

[127] M. J. Kumer and D. J. Roulston, “Miller’s approximation in advanced bipolar transistors under nonlocal impact ionization conditions,” *IEEE Trans. Electron Devices*, vol. 41, pp. 2471-2473, Dec. 1994.

[128] E. F. Crabbe, *et al*., “The impact of non-equilibrium transport on breakdown and transit time in bipolar transistors,” *IEDM Tech. Dig*., pp. 463-466, 1990.

[129] W. J. Kloosterman, J. C. J. Paasschens and R. J. Havens, “A comprehensive bipolar avalanche multiplication compact model for circuit simulation,” *Proc. 2000 BCTM*, pp. 172-175.

[130] J. D. Joannopoulos, R. D. Meade, and J. N. Winn, “Photonic crystals: modeling the flow of light,” Princeton University Press, 1995.

[131] E. Yahlonovitch, “Inhibited spontaneous emission in solid state physics and electronics,” *Phys. Rev. Lett*., vol. 50, pp. 2059-2062, 1987.

[132] F. R. Yang, R. Coccioli, Y. Qian, and T. Itoh, “ Planar PBG structures: basic properties and applications,” *IEICE Trans. Electron.*, vol. E83-C, No. 5, May 2000.

[133] R. Coccioli, F. R. Yang, K. P. Ma, and T. Itoh, "Aperture-coupled patch antenna on UC-PBG substrate," *IEEE Trans. Microwave Theory Tech.*, vol. MTT-47, no. 11, pp. 2123-2130, 1999.

[134] Y. Hao, and C. G. Parini, "Microstrip antennas on various UC-PBG substrates," *IEICE Trans. Electron.*, vol. E86-C, No. 8, Aug. 2003.

[135] E. Yablanovitch, T. J. Gmitter, and K. M. Leung, "Photonic bandgap structure: the face-centered-cubic case employing nonspherical atoms, " *Phys. Rev. Lett.*, vol. 67, No. 17, pp. 2295-2298, Oct. 1991.

[136] *IEEE Trans. Microwave Theory Tech.*, vol. MTT-47, no. 11, 1999 (Special issue on electromagnetic crystal structures, design, synthesis and applications).

[137] *IEEE J. Lightwave Tech.*, vol. 17, No. 11, Nov. 1999 (Special issue on electromagnetic crystal structures, design, synthesis and applications).

[138] F. R. Yang, K. P. Ma, Y. Qian, and T. Itoh, "A uniplanar compact photonic-bandgap (UC-PBG) structure and its applications for microwave circuits," *IEEE Trans. Microwave Theory Tech.*, vol. MTT-47, no. 8, pp. 1509-1514, Aug. 1999.

[139] F. R. Yang, K. P. Ma, Y. Qian, and T. Itoh, "A novel TEM waveguide using uniplanar compact photonic-bandgap (UC-PBG) structure," *IEEE Trans. Microwave Theory Tech.*, vol. MTT-47, no. 11, pp. 2092-2098, Nov. 1999.

[140] M. J. Vaughan, K. Y. Hur, and R. C. Compton, "Improvement of microstrip patch antenna radiation patterns," *IEEE Trans. Antennas Propagat.*, vol. 42, pp. 882-885, June 1994.

[141] R. Gonzalo, De. Maggt, and M. Sorolla, "Enhanced patch antenna performance by suppressing surface waves using photonic bandgap substrates," *IEEE Trans. Microwave Theory Tech.*, vol. MTT-47, pp. 2131-2138, Nov. 1999.

[142] R. Gonzalo, De. Maggt, and M. Sorolla, “Improved patch antenna performance by using photonic bandgap substrates,” *Microwave and Optical Technology Lett.*, vol. 24, pp. 213-215, Feb. 2000.

[143] Y. Qian, R. Coccioli, D. Sievenpiper, V. Radisic, E. Yablonovitch, and T. Itoh, “A microstrip patch antenna using novel photonic bandgap structures,” *Microwave Journal*, pp.67-76, Jan. 1999.

[144] V. Radisic, Y. Qian, R. Coccioli, and T. Itoh, “Novel 2-D photonic bandgap structure for microstrip lines,” *IEEE Microwave and Guided Wave Lett.*, vol. 8, pp. 69-71, Feb. 1998.

[145] Y. Horii, and M. Tsutsumi, “Harmonic control by photonic bandgap on microstrip patch antenna,” *IEEE Microwave and Guided Wave Lett.*, vol. 9, pp. 13-15, Jan. 1999.

[146] V. Radisic, Y Qian, R. Coccioli, and T. Itoh, “Novel 2-D photonic bandgap structure for microstrip lines,” *IEEE Microwave and Guided Wave Lett.*, vol. 8, pp. 69-71, Feb. 1998.

[147] F. R. Yang, Y. Qian, R. Coccioli, and T. Itoh, “A novel low-loss slow wave microstrip structure,” *IEEE Microwave and Guided Wave Lett.*, vol. 8, pp. 372-374, Nov. 1998.

[148] K. Wu, D. Maurin, and R. Bosisio, “An explicit design technique for wide-band couplers and high quality filters using periodic topology,” in *IEEE MTT-S Int. Microwave Symp. Dig.*, vol. 2, June 1993, pp. 1085-1088.

[149] J. Sor, Y. Qian and T. Itoh, “Miniature low-loss CPW periodic structures for filter applications,” *IEEE Trans. Microwave Theory Tech.*, vol. MTT-49, pp. 2336-2341, Dec. 2001.

[150] Y. Eo, and W. Eisenstadt, “High-speed VLSI interconnect modeling based on S-parameter measurements,” *IEEE Trans. Comp., Hybrid, Manuf. Technol.*, vol. 16, no. 5, pp. 555-562, Aug. 1993.

[151] S. Gevorgian, L. J. P. Linner, and E. L. Kollberg, “CAD models for shielded multilayered CPW,” *IEEE Trans. Microwave Theory Tech*., vol. 43, pp. 772-779, Apr. 1995.

[152] R. N. Simons, *Coplanar waveguide circuits, components, and systems*, Wiley-Interscience, 2001.

[153] D. M. Pozar, *Microwave engineering*, John Wiley & Sons, Inc., 1998.

[154] R. Garg, P. Bhartia, I. Bahl, and A. Ittipiboon, *Microstrip antenna design handbook*, Artech House, 2001.

[155] R. W. Dearnley, and A. F. Barel, “A broad-band transmission line model for a rectangular microstrip antenna,” *IEEE Trans. Antennas and Propagat*., vol. 37, pp.6-15, Jan. 1989.

[156] J. S. Chen, and S.Y. Lin, “Triple-frequency rectangular-ring slot antennas fed by CPW and microstrip line,” *Microwave and Optical Technology Lett*., vol. 37, pp. 243-246, May 2003.